

Implementation of an active seismic isolation system for the AEI 10 m prototype

Von der Fakultät für Mathematik und Physik
der Gottfried Wilhelm Leibniz Universität Hannover

zur Erlangung des akademischen Grades

Doktor der Naturwissenschaften

Dr. rer. nat.

Genehmigte Dissertation von

M.Sc. Robin Kirchhoff

2021

Referent: Apl. Prof. Dr. Benno Willke
Korreferentin: Prof. Dr. Michèle Heurs
Korreferent: Prof. Dr. Kenneth Strain

Tag der Promotion: 03.12.2021

Abstract

The first direct observation of gravitational waves on the 14th September 2015 opened up a new window to the Universe. Since then, gravitational wave astronomy has provided highly valuable information about previously mostly unexplored astronomic events like the merger of two black holes; nevertheless, it is still in its infancy, with numerous phenomena to be discovered and investigated. This requires improved detectors, featuring higher sensitivities.

Seismic noise is among the most relevant noise sources for current gravitational wave detectors. Although featuring sophisticated seismic isolation systems, current detectors are directly and indirectly limited by seismic noise below 30 Hz; therefore, current and future detectors require novel isolation systems and strategies to achieve their design sensitivity.

The Albert Einstein Institute (AEI) 10 m prototype is a test facility for gravitational wave detectors to develop and study novel technology. The primary goal is to reach and surpass the interferometric Standard Quantum Limit (SQL) based on quantum noise. It requires significant suppression of all classical noise contributions in order to achieve the design sensitivity. AEI Seismic Attenuation Systems (AEI-SASs) isolate the sub-SQL interferometer against seismic noise and are used to develop and demonstrate novel techniques for gravitational wave detectors. The AEI-SASs combine passive isolation based on the principle of a harmonic oscillator and active isolation based on feedback loop suppression.

In the scope of this thesis, the active seismic isolation of the AEI-SASs is implemented and analyzed in detail. Two different isolation strategies are described, namely local seismic isolation and global seismic isolation. The former is predominantly used by current gravitational wave detectors and focuses on inertial isolation of each interferometer component individually. The latter is a mostly untested principle implemented in the AEI 10 m prototype in a unique realization. It focuses on the minimization of differential motion between the interferometer components.

All involved sensors are characterized, and their noise is calculated. The sensor noise is measured in so-called huddle tests with excellent agreement to the models, providing detailed insight into limitations of the sensors and the entire system. Requirements for precise huddle tests are investigated in measurements.

The application of local isolation techniques at the AEI 10 m prototype is described and novel methods for their improvement are demonstrated. An enhanced coordinate system transformation increases the decoupling between different degrees of freedom, resulting in better isolation performance. The sensitivity dependence on the sensor alignment is analyzed in a novel approach, enabling the capability of a sensitivity optimization and an improved system characterization. The combination of different sensors to exploit their most sensitive frequency regimes is optimized using a new calculation method. It is adapted for the purpose of global isolation by including inter-platform sensors and the coupling of motion of the globally isolated AEI-SASs to the sub-SQL interferometer. This method simultaneously provides detailed information about limitations of the isolation system, which is used to propose and analyze possible improvements for the global isolation. An optimization of digital filters is calculated to improve the seismic isolation by a factor of 1.4. A realistic upgrade of vertical sensors offers an additional improvement of up to a factor of 4.3. Some fundamental statements of global isolation are confirmed by measurements.

Furthermore, a noise budget of the AEI sub-SQL interferometer is simulated. Requirements on noise suppression and interferometric parameters are set by comparison to the SQL. Based on these requirements, a possible design for the anti-symmetric port photodetector is motivated, and its noise is analyzed.

Keywords: ground-based gravitational wave detector, AEI 10 m prototype, active seismic isolation, global seismic isolation

Zusammenfassung

Die erste direkte Detektion einer Gravitationswelle am 14. September 2015 öffnete ein neues Fenster in das Universum. Seitdem hat die Gravitationswellenastronomie eine Vielzahl an Informationen über bislang kaum erforschte Ereignisse, wie die Verschmelzung zweier schwarzer Löcher, geliefert. Dennoch befindet sie sich erst am Anfang ihrer Entwicklung. Viele unerforschte und unbekannte Phänomene sind das Ziel zukünftiger Forschung und verlangen nach sensitiveren Detektoren.

Seismisches Rauschen gehört zu den relevantesten Störquellen für aktuelle Gravitationswellendetektoren. Trotz der Verwendung hoch entwickelter Isolationssysteme limitiert seismisches Rauschen die Detektoren direkt oder indirekt unterhalb von 30 Hz. Daher benötigen aktuelle und zukünftige Detektoren neue Systeme und Strategien für das Erreichen ihrer Zielsensitivität.

Der Albert-Einstein-Institut (AEI) 10 m Prototyp ist eine Testeinrichtung für Gravitationswellendetektoren. Das Primärziel ist die Detektion und anschließend die Unterbietung des interferometrischen Standard Quanten Limits (SQL), welches auf Quantenrauschen basiert. Um dessen Zielsensitivität zu erreichen, wird eine signifikante Reduktion aller klassischen Rauschquellen benötigt. AEI Seismische Isolationssysteme (AEI-SAS) werden verwendet, um das AEI sub-SQL Interferometer gegen Seismik zu isolieren und um neue Techniken zur Verbesserung der Gravitationswellendetektoren zu erforschen. Sie kombinieren passive Isolation, basierend auf dem harmonischen Oszillator, mit aktiver Isolation, basierend auf einer Unterdrückung durch Rückkopplungskontrolle.

Im Rahmen dieser Doktorarbeit wird die aktive Seismikisolation implementiert und im Detail analysiert. Es werden zwei unterschiedliche Strategien beschrieben: lokale Seismikisolation und globale Seismikisolation. Die erstgenannte Strategie wird derzeit in großer Mehrheit von Gravitationswellendetektoren eingesetzt. Sie fokussiert sich auf die individuelle Isolation der Interferometeroptiken. Die zweitgenannte Strategie ist weitestgehend ungetestet und wird im AEI 10 m Prototypen in einer einzigartigen Umsetzung verwendet. Sie fokussiert sich auf die Minimierung differentieller Bewegung zwischen den Interferometeroptiken.

Alle involvierten Sensoren werden charakterisiert und ihr Rauschen wird berechnet. Das Rauschen wird zusätzlich in sogenannten huddle tests gemessen und liefert eine exzellente Übereinstimmung mit den Modellen. Dies ermöglicht eine detaillierte Einsicht in Limitierungen der Sensoren und des gesamten Systems. Außerdem werden Bedingungen für effektive huddle tests erarbeitet.

Lokale Isolationstechniken bilden die Basis für die globale Isolation und werden im Rahmen dieser Arbeit beschrieben und analysiert. Dabei werden neue Techniken für die Verbesserung der lokalen Isolation vorgestellt. Eine optimierte Koordinatentransformation verbessert die Entkopplung verschiedener Freiheitsgrade. Eine neuartige Analyse zur Positionierung von Sensoren ermöglicht eine Sensitivitätsoptimierung sowie eine verbesserte Charakterisierung des Systems. Die Kombination verschiedener Sensoren, mit dem Ziel ihre sensitivsten Frequenzbereiche bestmöglich auszunutzen, wird durch eine neue Simulation optimiert. Diese Simulation wird in adaptierter Form für die globale Isolation verwendet, indem inter-Plattform Sensoren und die Kopplung global isolierter AEI-SAS auf das sub-SQL Interferometer miteinbezogen werden. Gleichzeitig liefert die Simulation Informationen über Limitierungen des Systems, welche dazu verwendet werden, mögliche Verbesserungen zu motivieren und zu analysieren. Eine Optimierung digitaler Filter ergibt eine um den Faktor 1.4 verbesserte Isolationswirkung. Eine realistische Implementierung neuer vertikaler Sensoren ergibt eine zusätzliche Verbesserung um den Faktor 4.3. Grundsätzliche Zusammenhänge der globalen Isolation werden durch Messungen verifiziert.

Des Weiteren wird ein Rauschbudget für das AEI sub-SQL Interferometer aufgestellt. Anforderungen an Rauschunterdrückungen und interferometrische Parameter werden erarbeitet. Basierend auf diesen Anforderungen wird ein mögliches Design für den Fotodetektor des anti-symmetrischen Interferometerausgangs motiviert und das Rauschen wird analysiert.

Schlagwörter: erdgebundene Gravitationswellendetektoren, AEI 10 m Prototyp, aktive Seismikisolation, globale Seismikisolation

Abbreviations

<i>rms</i>	root mean square
aa	auto-alignment
AA	Anti-Aliasing
acc	accelerometer
ADC	Analogue-to-Digital Converter
AEI	Albert Einstein Institute
AEI-SAS	Albert Einstein Institute - Seismic Attenuation System
AI	Anti-Imaging
AOM	Acousto-Optic Modulator
ASD	Amplitude Spectral Density
BOSEM	Birmingham Optical Sensor and Electro-Magnetic Actuator
BSC-ISI	Basic Symmetric Chambers - Internal Seismic Isolation
CDS	Control and Data System
CPS	Capacitive Position Sensor
DAC	Digital-to-Analogue Converter
EIB-SAS	External Injection Bench - Seismic Attenuation System
ETM	End Test Mass
FIR	Finite Impulse Response
GaAs/AlGaAs	Gallium Arsenide/Aluminium Gallium Arsenide
GAS	Geometric Anti-Spring
gwinc	Gravitational Wave Interferometer Noise Calculator
HAM-ISI	Horizontal Access Module - Internal Seismic Isolation
HAM-SAS	Horizontal Access Module - Seismic Attenuation System
HEPI	Hydraulic External Pre-Isolator
HoQI	Homodyne Quadrature Interferometer
IIR	Infinite Impulse Response
IMC	Input Mode Cleaner
InGaAs	Indium Gallium Arsenide
ISS	Intensity Stabilization System
ITM	Input Test Mass
KAGRA	Kamioka Gravitational Wave Detector
LIGO	Laser Interferometer Gravitational-Wave Observatory
LISA	Laser Interferometer Space Antenna
LVDT	Linear Variable Differential Transformer
MultiSAS	Multistage Seismic Attenuation System
Nd:YAG	Neodymium-doped Yttrium Aluminium Garnet
NPRO	Non-Planar Ring Oscillator
OL	Optical Lever
OMC	Output Mode Cleaner
PCF	Photonic Crystal Fiber
PMC	Pre-Mode Cleaner
QPD	Quadrant Photodiode
RIN	Relative Intensity Noise
RoC	Radius of Curvature
SAT	Single Arm Test
SiO₂/Ta₂O₅	Silicon Dioxide/Tantalum Pentoxide
SPI	Suspension Platform Interferometer
SQL	Standard Quantum Limit
STS-2	Streckeisen Seismometer 2
TEM	Transverse Electro Magnetic

Contents

1	Introduction	1
1.1	Gravitational waves	1
1.2	Gravitational wave detections	2
1.3	Gravitational wave detectors	5
1.4	AEI 10 m prototype	8
1.5	Outline of this thesis	10
2	Noise sources and their countermeasures	13
2.1	Seismic noise	13
2.2	Electronic noise	15
2.3	Thermal noise	17
2.4	Laser intensity noise	19
2.5	Laser frequency noise	19
2.6	Mode mismatch and beam jitter	20
2.7	Scattering noise	24
2.8	Quantum noise	25
3	Seismic isolation	27
3.1	Principles of passive seismic isolation	27
3.2	Principles of active seismic isolation	30
3.2.1	Feedback control system	30
3.2.2	Feedforward control system	31
3.2.3	Stability criteria	31
3.3	The AEI-SAS	32
3.3.1	Motivation for seismic pre-isolation	32
3.3.2	Setup and passive isolation	34
3.4	Sensors and actuators	38
3.4.1	Data acquisition and processing	42
3.4.2	Linear Variable Differential Transformer	42
3.4.3	Geophone	47
3.4.4	Accelerometer	56
3.4.5	STS-2 seismometer	63
3.4.6	Optical lever	65
3.4.7	Suspension platform interferometer	69
3.4.8	Voice-coil actuator	73
3.4.9	Motorized blade springs	76
3.4.10	Comparison of sensors	77
3.5	Huddle test	79
3.5.1	Principles of huddle tests	79
3.5.2	Huddle test for geophones	79
3.5.3	Analysis on requirements for precise huddle tests	82
3.5.4	Huddle test for LVDTs	84
3.5.5	Huddle test for accelerometers	86
3.6	Concepts of active seismic isolation	86
3.7	Local active seismic isolation	87

3.7.1	Control scheme	87
3.7.2	Sensor calibration	89
3.7.3	Coordinate system transformation	89
3.7.4	Sensor positioning and alignment	92
3.7.5	Sensor blending	94
3.7.6	Sensor correction	97
3.7.7	Controller	99
3.7.8	Sensor blending optimization	100
3.7.9	Local isolation performance	105
3.7.10	Performance analysis	106
3.8	Global active seismic isolation	108
3.8.1	Control scheme	109
3.8.2	Coupling of AEI-SAS motion to the sub-SQL interferometer	111
3.8.3	Sensor blending optimization	126
3.8.4	Analysis of performance limitations	133
3.8.5	Global isolation performance	136
3.9	Concepts for improvements	140
3.9.1	Optimization of digital filters	140
3.9.2	Implementation of new sensors	148
4	FINESSE simulations	157
4.1	Model of the sub-SQL interferometer	157
4.1.1	Setup of the sub-SQL interferometer model	157
4.1.2	Optical gain	158
4.1.3	Noise budget	160
4.2	Jitter noise of input path optics	161
4.2.1	Influence of test mass misalignments on jitter noise	161
4.2.2	Noise budget	166
4.3	Dark fringe offset	167
4.4	Anti-symmetric port photodetector	167
5	Summary and outlook	173
	Appendices	177
A	Overview of further seismic isolation systems	177
A.1	Active seismic isolation of GEO600	177
A.2	Active seismic isolation of Advanced LIGO	177
A.3	Active seismic isolation of Advanced Virgo	183
A.4	Active seismic isolation of KAGRA	187
A.5	Global seismic isolation outside the AEI 10 m prototype	194
A.6	Comparison to the AEI-SAS	196
B	Schematics of amplifier electronics	199
C	Removal of L-22D geophones	204
D	Positioning of L-4C geophones	207
E	Sensor blending filter calculation	209
F	FINESSE script	211

Chapter 1

Introduction

1.1 Gravitational waves

Gravitational waves were predicted by Albert Einstein in his General Theory of Relativity from 1916 [Ein16]. They can be understood as the reaction of spacetime to accelerated masses, changing the spacetime curvature. The change of curvature travels with the speed of light in vacuum and carries information about the accelerated objects.

Due to the conservation of mass and momentum, the lowest order solution of the Einstein field equations is the quadrupole radiation. This requires a non-symmetric accelerated mass distribution given by, for example, two orbiting objects. The wave resulting from the quadrupole oscillates in orthogonal direction to propagation and can be decomposed into two components, the plus $+$ and cross \times polarization. The amplitude of each polarization and the phase between both polarization states depends on the relative position and orientation between observer and accelerated objects.

A passing gravitational wave stretches spacetime in one direction and shrinks it in the orthogonal direction. This is demonstrated in figure 1.1.1 for a ring of free-falling test masses with diameter L . The strength of a gravitational wave is described by its strain h , defined as

$$h = \frac{2\Delta L}{L}, \quad (1.1.1)$$

where ΔL describes the change of diameter caused by the gravitational wave.

The interaction between a gravitational wave and the environment is extremely low. This opens up the possibility of observing mostly undisturbed signals from events located far away, but significantly complicates detections in general. It requires the most energetic events in the Universe, like orbiting and merging black holes or neutron stars, to produce measurable gravitational waves. The first directly detected gravitational wave emitted by a binary black hole merger had a strain of roughly $h \leq 10^{-21}$. To give a descriptive example, these gravitational waves change the diameter of the whole earth ($L = 12742$ km) by less than four times the diameter of a free proton ($\Delta L \leq 6.37 \times 10^{-15}$ m). More information on this detection is provided in section 1.2.

To measure the effect of gravitational waves, a measurement device is required that does not stretch and shrink together with spacetime. This requirement is fulfilled by measuring the travelling time of a laser beam over a certain distance, since the speed of light in vacuum is unaffected by spacetime curvature. All modern gravitational wave detectors rely on exactly this principle. Details on the general setup and an overview of existing and future detectors is given in section 1.3.

Gravitational waves were first measured indirectly by Russel A. Hulse and Joseph H. Taylor in 1974 [HT75]. They observed the binary pulsar system PSR 1913+16 and discovered a decrease in the orbital period and hence a loss of energy of the

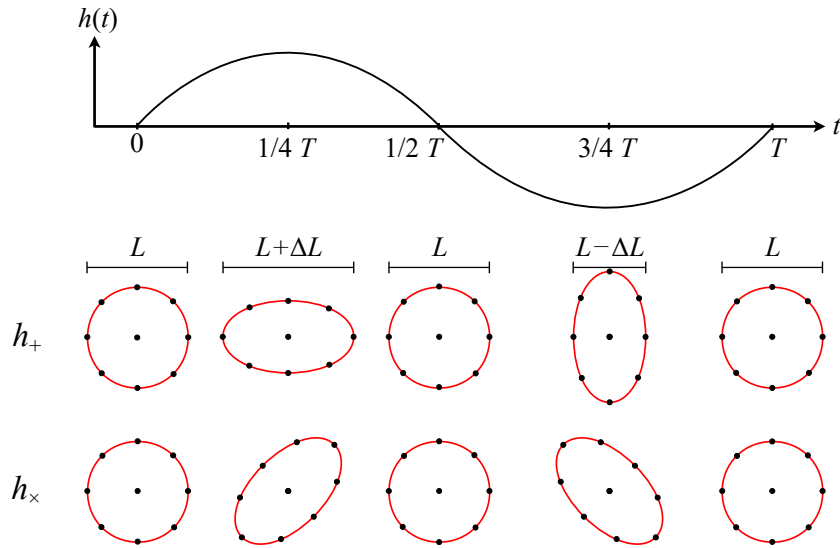


Figure 1.1.1: Effect of a passing gravitational wave on a ring of free-falling test masses with diameter L . The ring is stretched in one direction and shrunk in the orthogonal by the distance ΔL . The figure is adapted from [LN17].

system. The behavior exactly matched the effect due to energy loss by emission of gravitational waves, predicted by the General Theory of Relativity.

Roughly 100 years after their postulation by Einstein, gravitational waves were directly detected for the first time by the Advanced Laser Interferometer Gravitational-Wave Observatory (LIGO) detectors. Although the existence of gravitational waves was ultimately proven, this detection did not end the investigations, but started a new era of astronomy. The following section presents an overview of detected gravitational waves and motivates the necessity of increased sensitivity to learn more about the so far unknown.

1.2 Gravitational wave detections

The first direct detection of a gravitational wave succeeded on the 14th September 2015 by the two Advanced LIGO detectors [A⁺16b]. Two black holes with masses of 36_{-4}^{+5} and 29_{-4}^{+4} solar masses (later updated to 35_{-3}^{+5} and 30_{-4}^{+3} solar masses [A⁺16a]) merged to a final black hole with 62_{-4}^{+4} solar masses. The mass difference of $3_{-0.5}^{+0.5}$ solar masses was radiated as energy of gravitational waves. The peak strain of this event, referred to as GW150914, was 1×10^{-21} resulting in a false alarm rate estimated to be less than 1 event per 20300 years.

Figure 1.2.1 shows the measured signal of this event for both detectors in a timeline and spectrogram. Models reconstructing the signal are shown, and the difference between matched models and measurement is depicted. The models were updated later to reconstruct the signal more precisely [A⁺16a].

At the time of writing, this detection was followed by 49 further confirmed detections split in three observation runs O1, O2 [A⁺19a] and O3a [A⁺21a]. The second half of the third observation run O3b contributed with 23 public alerts [O'R21].

The detections so far include 46 binary black hole mergers, two binary neutron star mergers, one neutron star-black hole merger and one observation where the second object merging with a black hole is either a neutron star or a black hole. The involved masses span a wide and unforeseen range, which is depicted in figure 1.2.2. The purple and yellow dots symbolize black holes and neutron stars, which existence was known before from electromagnetic observations. Blue and orange show black holes and neutron stars involved in mergers that were detected by gravitational wave

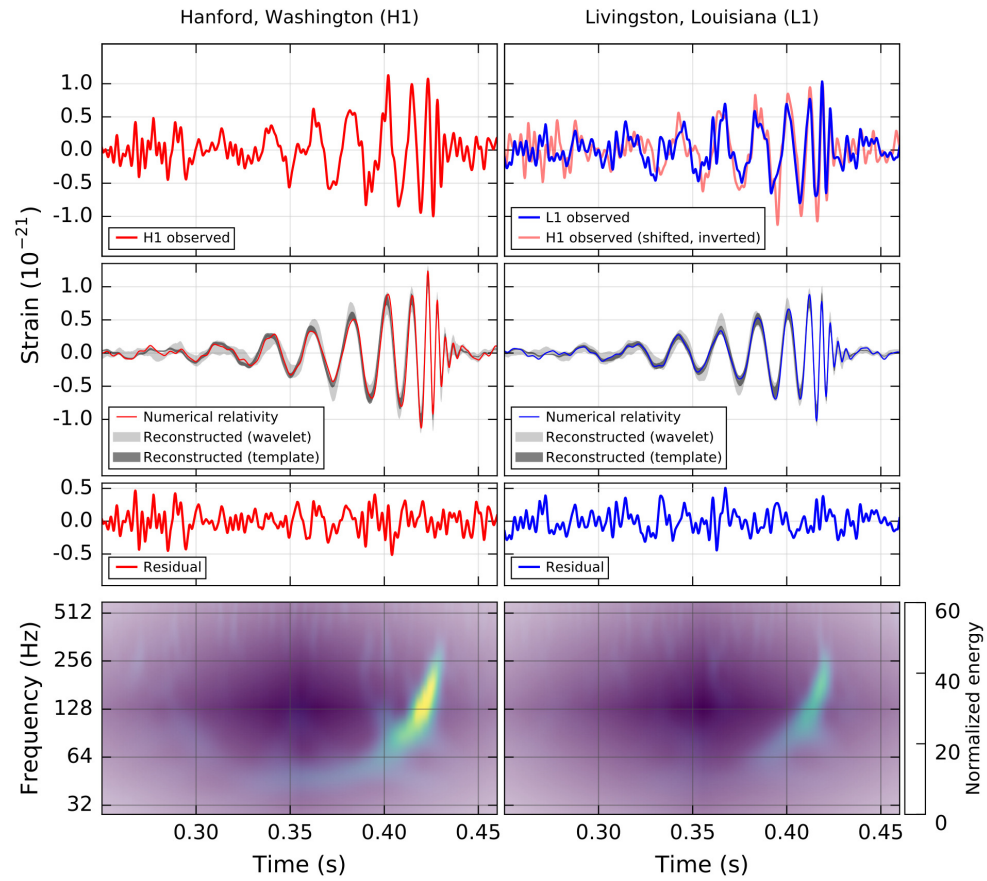


Figure 1.2.1: Measured signal and model reconstructions of the first detected gravitational wave GW150914 for both Advanced LIGO detectors. The figure is adapted from [A⁺16b].

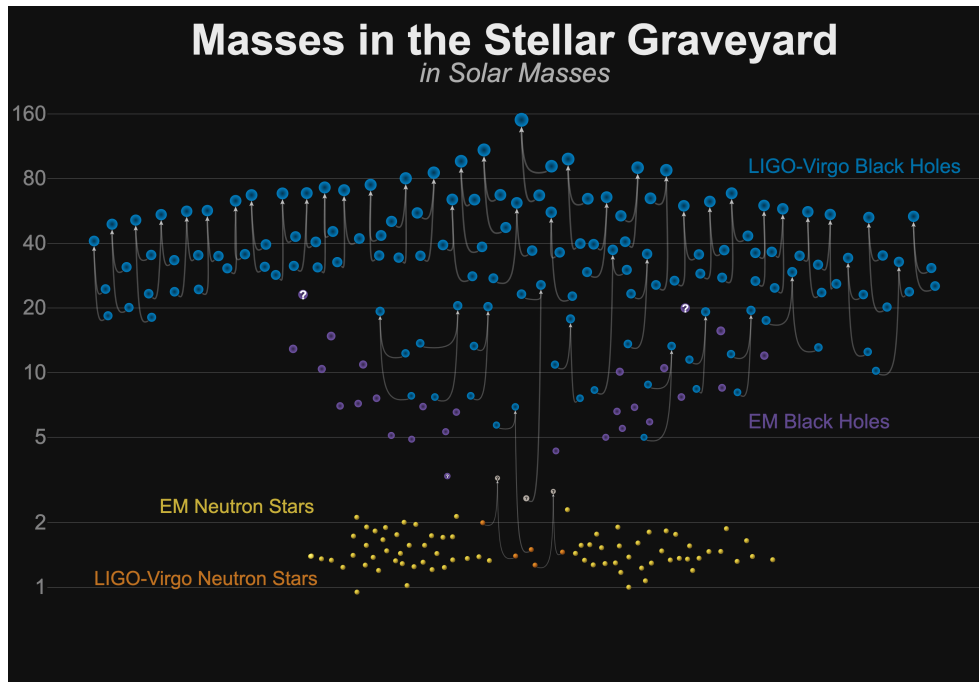


Figure 1.2.2: Masses of objects involved in all gravitational wave signals detected and confirmed so far. The public alerts of O3b are excluded. The purple and yellow dots symbolize black holes and neutron stars observed by electromagnetic radiation. The blue and orange dots show black holes and neutron stars detected via their gravitational waves with the arrows, indicating which objects merged. The figure is designed by F Elavsky and A Geller, Northwestern University, LIGO-Virgo collaboration [EG] based on data published in [A⁺21a].

measurements. The amount of black holes with a mass higher than 20 solar masses was unexpected given the population of black holes observed so far. Especially the merger GW190521 [A⁺20a] with black holes of 85_{-14}^{+21} and 66_{-18}^{+17} solar masses and a resulting black hole of 142_{-16}^{+28} solar masses arouse high interest. With a probability of 99% at least one initial black hole populated the pair-instability mass gap between 65–120 solar masses, arousing questions about its formation channel [A⁺20b]. The merger is the first ever directly or indirectly observed intermediate mass black hole [A⁺20b].

During O1 and the beginning of O2 only the two Advanced LIGO detectors were online and taking data. Advanced Virgo joined the network during O2 enabling a significantly better sky localization of detections [Fai09, Fai11b]. Some gravitational wave sources do not only produce gravitational waves but also gamma-ray, x-ray, optical, near-infrared, radio and neutrino counterparts. With a precise and rapid sky localization, the telescopes for these counterparts can be pointed in the right direction, providing comprehensive information about individual events.

The first detected gravitational wave signal from a non-binary black hole merger was GW170817, a binary neutron star merger [A⁺17a]. Due to the existing three detector network and the resulting precise sky localization, multiple electromagnetic counterparts were detected [A⁺17b]. The amount of data from various channels for this event lead to a so far unprecedented depth of analysis of neutron stars.

Still to be learned

There is still a lot to be learned from gravitational wave detections. Most of it cannot be investigated with current gravitational wave detectors due to their insufficient sensitivity. The list below provides some highlights of information that require improved detectors. The information is summarized from [ET 20].

- So far, the detected mergers only include black holes and neutron stars for a very limited range of masses and redshifts. Extending detections to a wider range of both parameters provides crucial information about populations, formation channels and dynamics of these objects.
- Detecting gravitational waves with higher sensitivity would allow for more precise parameter estimations and hence more precise testing of General Relativity.
- There are known sources of gravitational waves that could not be detected yet, like core collapse supernovae and continuous gravitational wave signals from rotating asymmetric neutron stars. Both detections would provide plenty of so far unknown information.
- Dark matter, dark energy and the stochastic gravitational wave background are concepts that were never directly measured and can be investigated with gravitational wave detections. Detection of dark matter would provide information of fundamental importance for astrophysics, fundamental physics and cosmology. Exploring dark energy could lead to modifications of General Relativity. Detection of the stochastic gravitational wave background would provide information about the earliest moments of the Universe inaccessible by electromagnetic and neutrino measurements, offering information beyond the standard model of physics.

This list clearly shows that the new, wide field of gravitational wave astronomy is still in its infancy.

1.3 Gravitational wave detectors

Measuring the time it takes a laser beam to pass a certain distance is an excellent tool for measuring gravitational waves. This principle is utilized in Michelson interferometers by current and planned gravitational wave detectors in a modified realization. Figure 1.3.1 depicts the principle. A laser beam is split into two orthogonal arms and reflected back. Both beams recombine at the beam splitter and interfere depending on the individual travelling times. A gravitational wave stretches one arm and shrinks the other, influencing the differential phase between the laser beams at the beam splitter and hence the interference pattern. This changes the laser power at the anti-symmetric port of the beam splitter, which is detected by a photodetector.

Despite being based on a Michelson interferometer, modern gravitational wave detectors include a variety of additional technologies to increase their sensitivity. [BBFS17] provides an overview of the principles of the key technologies.

Gravitational wave astronomy started with the so-called first generation of gravitational wave detectors including two initial LIGO detectors [A⁺09], initial Virgo [A⁺07], GEO600 [W⁺07] and TAMA300 [A⁺02]. Although not succeeding in gravitational wave detections, crucial knowledge was gained for future upgrades and new detectors. While GEO600 received minor upgrades and remained operating most of the time until now, LIGO and Virgo received extensive upgrades to form a new generation of gravitational wave detectors.

The second generation of detectors includes the two Advanced LIGO [A⁺15] detectors and the Advanced Virgo [A⁺14] detector, which are currently operating. The Kamioka Gravitational Wave Detector (KAGRA) [A⁺13] is categorized between second and third generation and recently joined the network of operating detectors. Upgrades for Advanced LIGO [MVF⁺15, Bar18, A⁺20c, LIG20] and Advanced Virgo, using current infrastructures, are planned. Furthermore, a third Advanced LIGO detector of the second generation is built in India [SRK⁺17], with the main goals of improving the sky localization and increasing the observation time of the detector network [Fai11a, S⁺21].

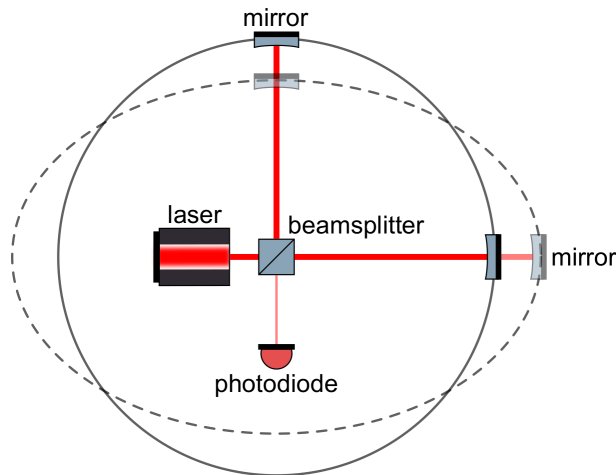


Figure 1.3.1: Principle description of a Michelson interferometer affected by a gravitational wave. The two arms are stretched and shrunk differentially, creating a changing laser power at the anti-symmetric port of the beam splitter. The figure is adapted from [HHP14].

The third generation of gravitational wave detectors is being planned, including two detectors: the Einstein Telescope [ET 20] and Cosmic Explorer [R⁺19]. In addition to having a long arm length of 10 km, the Einstein Telescope focuses on novel technologies and topologies to achieve an unprecedented sensitivity. Cosmic Explorer is planned to initially have a more traditional layout compared to the Einstein Telescope but with an even longer arm length.

A different type of planned gravitational wave interferometer is Laser Interferometer Space Antenna (LISA) [DR03] [AS⁺17], operated in space. It consists of three spacecrafts in an equilateral triangle, separated by 2.5 million kilometers. This detector will exploit the absence of seismicity in space and its long arm length to measure gravitational waves in the mHz regime. This will extend the window for gravitational waves significantly, allowing to observe different phenomena like mergers of massive black holes and providing early warning for ground based detectors [AS⁺17].

Figure 1.3.2 shows the sensitivities of current second generation detectors, planned third generation detectors and LISA. While the third generation is sensitive at roughly the same frequencies as current detectors, LISA covers a completely different frequency regime.

Future gravitational wave detectors will enable many more detections of so far undiscovered phenomena and provide a large amount of data to specify parameters more accurately, as discussed in section 1.2. To achieve their design sensitivity, significant progress in research and development in various areas needs to be made. This includes, for example, seismic isolation, coating thermal noise and quantum noise.

Figure 1.3.3 shows the noise budget of the Advanced LIGO Hanford detector during the third observation run. Above 30 Hz quantum noise is limiting. Below 30 Hz it is alignment control, auxiliary length control, beam jitter and the penultimate-mass actuator. All of these can be traced back to seismic noise as their origin, or can be lowered by attenuating seismic noise. Motion sensors and actuators, for example, would benefit from lower seismic noise by lower dynamical range requirements, leading to lower absolute noise.

Although utilizing state-of-the-art technology, the current Advanced LIGO detectors do not meet the design sensitivity, especially below 30 Hz. To do so, improvements in seismic isolation and the control system are necessary. Looking at third generation design sensitivities shows the demanding technology improvements that are required. At 8 Hz, for example, the Einstein Telescope requires a reduction of seismic noise of more than a factor 300 compared to the Advanced LIGO design, strongly rising to lower frequencies.

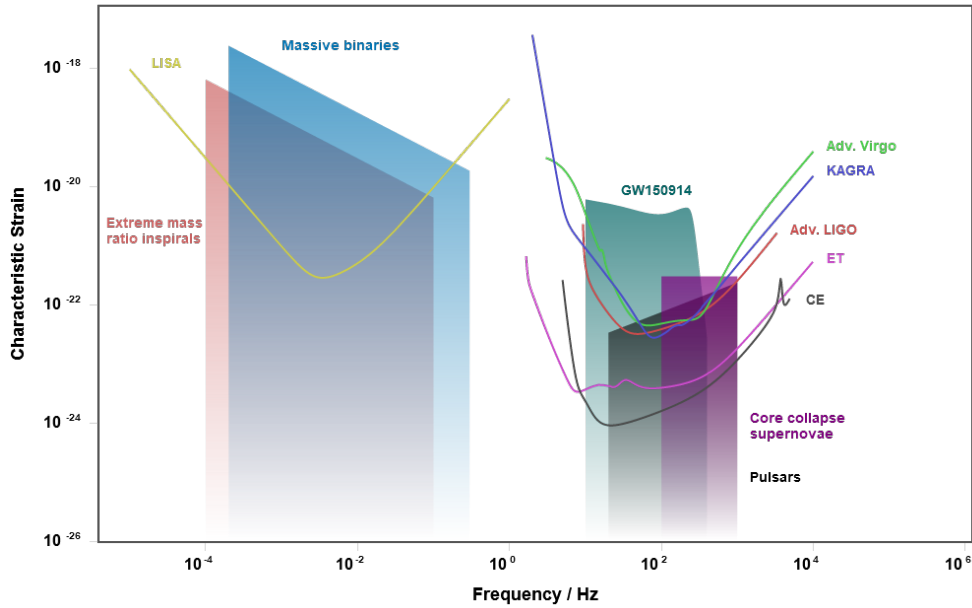


Figure 1.3.2: Sensitivity of current gravitational wave detectors and planned ground-based and space-born detectors. For reference, the strain sensitivities of some phenomena are shown. While ground-based detectors are bound to detections above roughly 1 Hz due to seismic motion, space-born detectors can exploit significantly lower frequency regimes. The figure is customized with the GWplotter tool [MCB18], based on data and calculations presented in [MCB14].

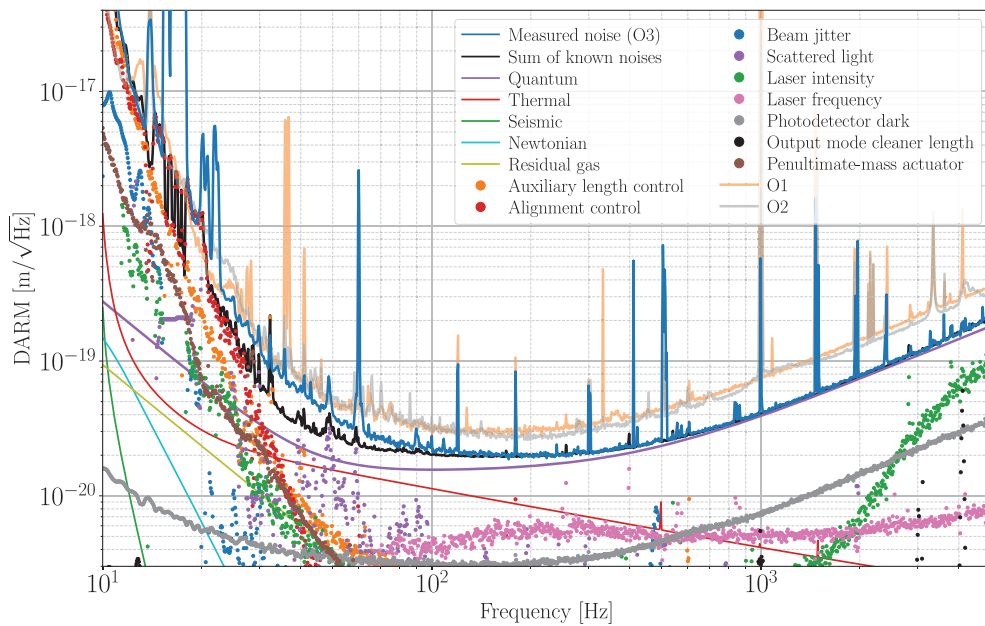


Figure 1.3.3: Noise budget of the Advanced LIGO Hanford detector in observation run 3. The noise is projected to Differential Arm length changes between both interferometer arms. Above 30 Hz quantum noise is mostly limiting. Below 30 Hz alignment control and auxiliary length control limit the total performance. The latter two noise contributions depend on seismic motion acting on the mirror suspensions. The figure is taken from [B⁺20].

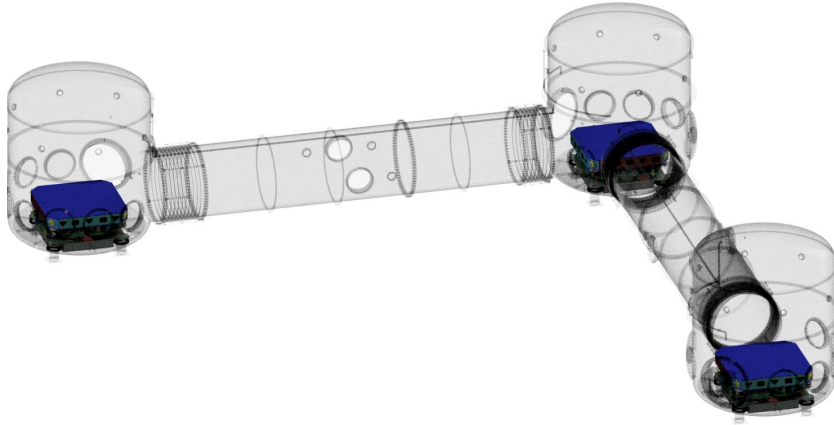


Figure 1.4.1: Vacuum system and AEI-SASs of the AEI 10 m prototype. The vacuum system has an L-shape and provides flexible working conditions by offering generous space and the capability of fast evacuation and venting. The AEI-SASs seismically isolate optical tables, which serve as a base for all sensitive interferometer components.

1.4 AEI 10 m prototype

Prototype and test facilities, like the AEI 10 m prototype, are required to develop and test novel technologies to improve gravitational wave detectors. The AEI 10 m prototype includes a roughly 10 m long L-shaped vacuum system, housing the sub-SQL interferometer [W⁺12]. This is designed to measure and subsequently surpass the Standard Quantum Limit (SQL), which is a fundamental noise limit in classical physics, based on quantum noise. More information about quantum noise and the SQL is provided in section 2.8.

In order to measure the SQL, various subsystems are required to lower all classical noise sources below quantum noise. Figure 1.4.1 shows the vacuum system and three seismic pre-isolation systems, the Albert Einstein Institute - Seismic Attenuation Systems (AEI-SASs). The AEI-SASs seismically isolate optical tables that serve as a base for all sensitive main and auxiliary interferometer components.

The most relevant optical components and subsystems of the final layout are shown in figure 1.4.2. The laser preparation and input path to the main interferometer are depicted with an orange beam. The main interferometer is shown with a red beam and the output path with a pink beam. The laser is fiber-coupled into the vacuum system onto the central AEI-SAS. First, its mode content is filtered by the Pre-Mode Cleaner (PMC), labelled with 1 (see section 2.6). A part of the beam coming out of the PMC is split and sent to the Intensity Stabilization System (ISS), labelled with 2, to stabilize the laser power (see section 2.4). The residual beam is split a second time with one part sent into the frequency reference cavity, labelled with 3, to stabilize the laser frequency (see section 2.5). The other part of the beam is steered to the south AEI-SAS, where its mode is filtered a second time by the Input Mode Cleaner (IMC), labelled with 4 (see section 2.6). The beam parameters are matched to the arm cavity eigenmodes using three steering mirrors. Three propagations between the south and central AEI-SASs enable small angles of incidence on the steering mirrors and large radii of curvature of the same to keep the distortion of the beam small. Afterwards, it enters the main interferometer, labelled with 5. The output of the interferometer contains the signal of interest and is steered to the west AEI-SAS, where it is guided into the Output Mode Cleaner (OMC), labelled with 6, to clean the laser mode once again (see section 2.6). The output of the OMC is detected by a photodetector, labelled with 7 (see section 4.4).

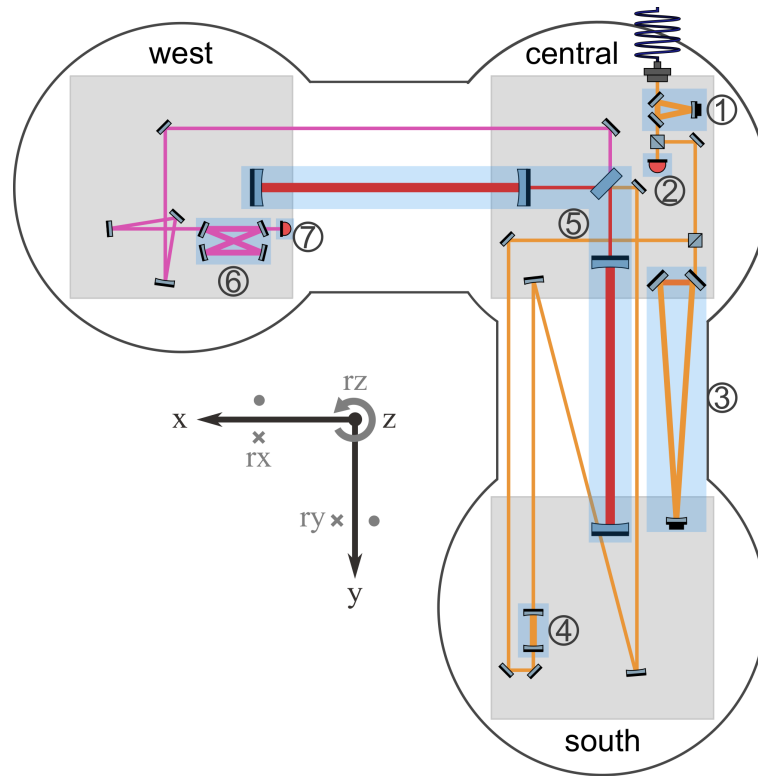


Figure 1.4.2: Optical layout of the AEI sub-SQL interferometer. The laser beam enters the vacuum system at the central AEI-SAS via an optical fiber. Its spacial mode is cleaned by the PMC (1). A part of the PMC output is split and sent to the ISS (2) to stabilize the laser intensity. The residual beam is split again, with one part entering the frequency reference cavity (3) to stabilize the laser frequency and the second part being steered to the south AEI-SAS, where it propagates through the IMC (4) to clean the spacial mode of the laser beam further. Afterwards, the laser beam is steered into the main interferometer (5). The anti-symmetric port of the interferometer is propagated to the west AEI-SAS and coupled into the OMC (6) to clean the spacial mode of the signal of interest. The OMC output is detected by a photodetector (7).

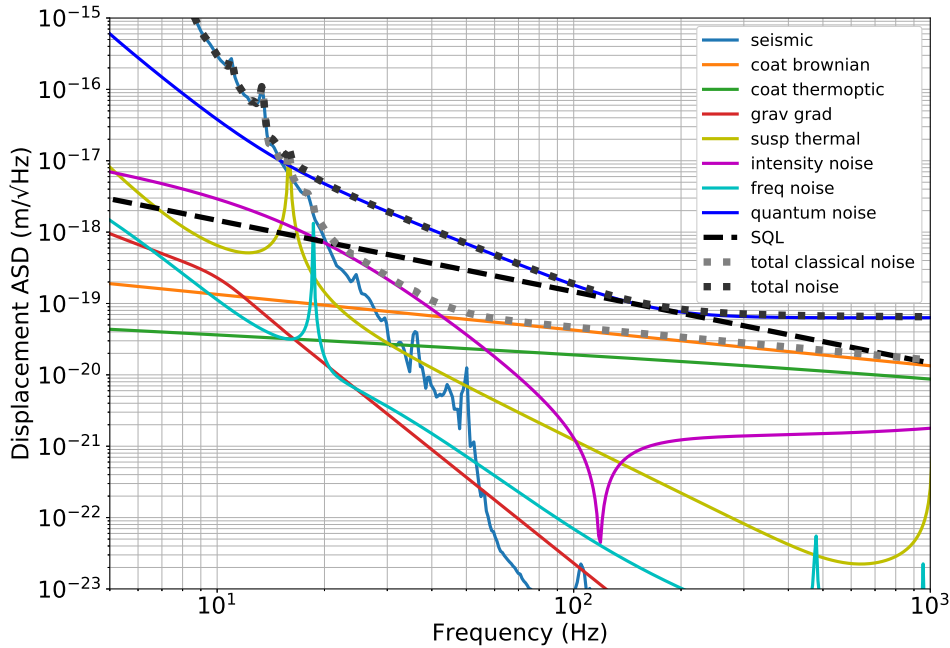


Figure 1.4.3: Noise budget for the AEI sub-SQL interferometer in units of $\text{m}/\sqrt{\text{Hz}}$. The noise is given for a laser input power of 3 W and for GaAs/AlGaAs coatings on the arm cavity mirrors.

At the time of writing, the sub-SQL interferometer is not fully assembled. The IMC is currently being built and will be installed soon. An ion beam sputter coating [RG05] was applied to a first set of mirrors for the Michelson interferometer. These mirrors will be installed in the near future. The manufacturing of the final optics with an Gallium Arsenide/Aluminium Gallium Arsenide (GaAs/AlGaAs) coating is being planned. More information on the two mirror sets is provided in section 2.3. One arm of the interferometer, called Single Arm Test (SAT), is assembled using another set of pilot optics to test the suspensions, verify control techniques and investigate noise sources. The OMC and the anti-symmetric port photodetector assembly is in progress. All other components exist and their functionality is verified.

Figure 1.4.3 shows a noise budget of the AEI sub-SQL interferometer for a laser input power of 3 W and GaAs/AlGaAs coatings. Detailed information about the different noise contributions is provided in chapter 2. Details about the simulation of this noise budget are provided in chapter 4. The noise is given as a displacement Amplitude Spectral Density (ASD), with units of $\text{m}/\sqrt{\text{Hz}}$. The functionality of sub-SQL techniques will be demonstrated by decreasing the total noise beyond the SQL, possibly down to the total classical noise.

Comparing the design noise budget of the AEI sub-SQL interferometer with current Advanced LIGO noise (figure 1.3.3) shows that a comparable displacement sensitivity is aimed for.

1.5 Outline of this thesis

Chapter 2 provides an overview of all relevant noise sources. Requirements for the AEI sub-SQL interferometer and specifically for seismic isolation are derived and countermeasures to the noise are described.

The primary focus of this thesis is on seismic isolation to reduce the coupling from

ground motion to the interferometer. More precisely, active seismic isolation of the pre-isolation systems AEI-SASs is motivated, described and analyzed in chapter 3. The work presented in this thesis is essential for the AEI sub-SQL interferometer to achieve its demanding requirements, and it is a valuable technology demonstrator for large scale gravitational wave detectors of current and future generations.

Sections 3.1 and 3.2 present principles of passive and active seismic isolation. This is followed by a motivation for the AEI-SASs and a description of the setup and passive isolation performance in section 3.3.

Section 3.4 presents all utilized sensors and actuators and derives their noise. This is followed by noise measurements in section 3.5, showing a remarkable overlap to calculations granting insight into limitations. Sections 3.6 and 3.7 describe the objectives of seismic isolation and the realization of local active seismic isolation. Active isolation techniques are analyzed with respect to performance and limitations. The resulting active isolation performance is depicted and analyzed using simulations of the AEI-SAS noise performance.

Sections 3.8 presents the concept, an analysis and the implementation of global seismic isolation. In this realization, it is firstly implemented in and utilized by the AEI 10m prototype, serving as a pioneer for possible future improvements of gravitational wave detectors. Section 3.9 demonstrates possible improvements for the global seismic isolation at the AEI 10m prototype.

Chapter 4 describes the simulation of a noise budget for the AEI sub-SQL interferometer. Different noise sources and interferometer parameters are investigated with respect to their influence on the total noise. Requirements on seismic isolation of input optics and the anti-symmetric port photodetector are set.

Chapter 2

Noise sources and their countermeasures

Two different definitions for noise are widely spread. One definition describes noise as purely stochastically random fluctuations. It is commonly used in many fields of research, for example in electronics and signal processing. The second definition describes noise as a summary of all unwanted contributions to a sensor output, including random fluctuations, cross talk from other channels and unwanted signals such that

$$X_s = x_s + n_s, \quad (2.0.1)$$

with X_s being the output of a sensor or system, x_s being the signal to be measured, and n_s being the noise disturbing the signal. Note that the capital X denotes the sensor output throughout this thesis while the lowercase x defines the sensor signal.

The input referred noise, indicated with a tilde, \tilde{n} is used to compare different noise sources among themselves and to signals. It is the result of a calculation transferring the noise from its source back to the input of a sensor or system under test and is calculated as

$$\tilde{n} = \frac{n}{T}, \quad (2.0.2)$$

where T is the transfer function from the input of the sensor or system to the source of the noise. Within this thesis, the input is usually seismic noise such that the input referred noise is a displacement equivalent noise. The classification as signal or noise depends on the sensor or system under observation. While seismic motion is signal for a seismometer, for example, it is noise for the interferometer.

The latter described definition of noise is commonly used in the experimental section of gravitational wave physics and hence is applied in this thesis. This section describes the most important noise sources for the Albert Einstein Institute (AEI) 10 m prototype with a focus on relevant noise sources for this thesis and summarizes the countermeasures utilized in the AEI 10 m prototype.

2.1 Seismic noise

Description and requirements

Seismic noise describes motion of the ground. It is usually divided up into motion below 1 Hz, called micro seismic, and motion above 1 Hz mainly resulting from anthropogenic sources. Micro seismic is mainly created by natural phenomena and features two characteristic peaks. The primary micro seismic peak has a frequency between 0.04–0.15 Hz and the secondary micro seismic peak has a frequency between 0.08–0.3 Hz. They result from ocean waves interacting with land and generate motion up to a few micrometers. For the purpose of this thesis, only the secondary micro

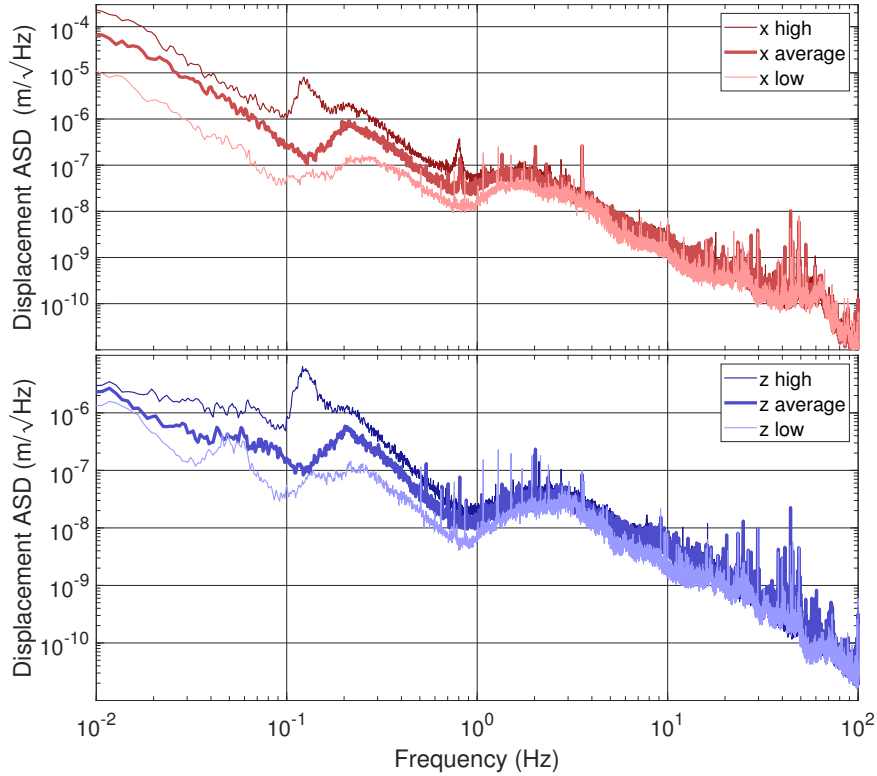


Figure 2.1.1: Horizontal (x) and vertical (z) translational seismic motion in the AEI 10 m prototype lab. The seismic motion is shown for a very windy day (“high”), creating high seismic motion, a day with average seismic activity (“mid”) and seismic motion in a calm night (“low”). The secondary micro seismic peak at roughly 0.2 Hz is visible. For high seismic activity there is another feature showing up at 0.12 Hz which is possibly linked to the micro seismic peak. Below 0.1 Hz the motion in x is dominated by tilt motion of the ground coupling to the horizontal readout sensor (see section 3.4.3); hence, the data does not resemble translational ground motion here.

seismic peak is relevant since its amplitude is significantly larger for the location of the AEI 10 m prototype.

This large low frequency motion disturbs the interferometer on several paths, for example, by reducing the duty cycle, by up-conversion in frequency into the measurement band and by introducing controls noise. This is described in more detail in section 3.3.1 and underlines the importance of seismic isolation not only in the measurement band but also at lower frequencies down to the micro seismic peak.

Figure 2.1.1 shows seismic motion in the basement of the AEI 10 m prototype lab, measured with an Streckeisen Seismometer 2 (STS-2). It includes seismic motion for a very windy day, creating high ground motion, a day with average ground motion and a night with low seismic activity. The micro seismic peak at 0.2 Hz is well visible. On the windy day, another peak at 0.12 Hz shows up which is possibly connected to the micro seismic peak. The transition between micro seismic and anthropogenic noise at 1 Hz is well visible. As expected, anthropogenic noise is similar for the high and average seismic activity measurements, taken at daytime, and lower for the low seismic activity measurement, taken at night.

Rotational ground motion can not be measured with a single STS-2. Measurements indicate that rotational ground motion around the vertical z axis is low enough to be negligible for the sub-SQL interferometer. Rotational ground motion around the horizontal axes x and y is significantly higher since it is created by vertical surface waves passing by. This was measured by positioning two identical and calibrated geo-

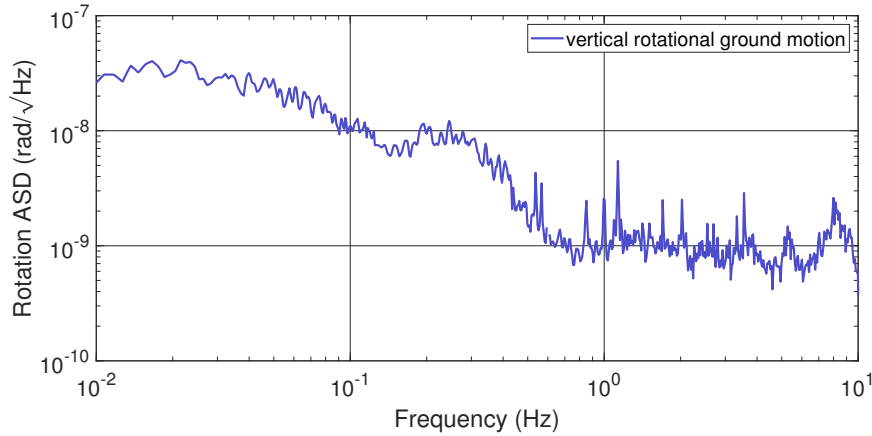


Figure 2.1.2: Vertical rotational ground motion in the AEI 10 m prototype lab. The measurement was taken using the subtraction of two L-4C geophone [Ser18] signals standing on the ground. Below 0.1 Hz the measurement was limited by sensor noise, which is why the rotational ground motion is inferred from the tilt-to-horizontal coupling to a horizontal ground motion measurement.

phones on the ground. They were separated by roughly 2 m and the differential signal was calculated. At high frequencies above 10 Hz, incoherence of the geophones prevents a tilt measurement. Below 0.1 Hz rotational ground motion cannot be measured by vertical geophones due to their sensor noise, but it can indirectly be measured by horizontal sensors because they are limited by the coupling of tilt motion referred to as tilt-to-horizontal coupling (see section 3.4.3). This effect was used to infer rotational ground motion from a horizontal measurement below 0.1 Hz. The result is shown in figure 2.1.2.

Environmental changes like wind speed, human activity or earthquakes induce a strong time dependence on seismic noise. This requires robust isolation systems capable of handling high variations in amplitude.

Detailed requirements for seismic isolation of the AEI-SAS below the measurements band were never set. They are evaluated in the process of building the interferometer. In the measurement band of the sub-SQL interferometer, seismic motion needs to be suppressed by a factor of approximately 10^{10} in order to achieve the target sensitivity.

Countermeasures

Two approaches are commonly utilized to isolate gravitational wave interferometers from seismic noise: passive isolation based on the principle of the harmonic oscillator and active isolation based on feedback control systems. In all current seismic isolation systems, both approaches coincide, but their realizations differ significantly. An overview of seismic isolation systems of current gravitational wave detectors is given in appendix A. Further information on passive isolation of the AEI 10 m prototype is provided in sections 3.1 and 3.3. Active seismic isolation of the AEI 10 m prototype is the main topics of this thesis and will be discussed in sections 3.2 and 3.4 – 3.9.

2.2 Electronic noise

Description and requirements

Electronic noise can be divided up into two categories. The first describes noise arising from external sources to the circuit under observation and is called extrinsic noise. It includes electromagnetic coupling from external transmitters, alternating magnetic fields from transformers or motors, capacitively coupled noise from nearby

conductors, seismic vibrations creating motion of cables and many more. The second category describes intrinsic noise having their origin within the circuit under observation. More details about definitions of electronic noise and descriptions of intrinsic and extrinsic noise are provided in [Fis17] and [Vas06a].

There are three prominent intrinsic noise types relevant for this thesis:

- Shot noise describes the random distribution of electrons in a flowing current across potential barriers, for example in semiconductors. It creates a frequency independent noise, referred to as white noise.
- Johnson noise, also called Johnson-Nyquist noise, describes thermally induced random motion of charges and also forms a white noise. It is always present, independent of a flowing current, and depends on the temperature of the system [Fis17].
- Flicker noise or $1/f$ noise describes noise with a power spectral density proportional to $1/f$. Its origin is poorly understood [Sch18]. Some information on Flicker noise in chosen electronic devices is provided in [Vas06a]. A theoretical description of Flicker noise is shown in [Mil95].

For all interior components of operational amplifiers, these three intrinsic noise sources are summarized as input referred amplifier voltage noise n_v and amplifier current noise n_c . Both are characteristic values of operational amplifiers and are usually provided by the manufacturer. Operational amplifiers have a corner frequency separating high frequencies, where white noise is dominant and low frequencies, where Flicker noise is dominant.

For this thesis, operational amplifier noise, shot noise and Johnson noise of resistors are relevant. Shot noise is calculated by

$$n_{\text{sh}} = \sqrt{2eI}, \quad (2.2.1)$$

with e being the elementary charge and I being the current. Johnson noise is calculated by

$$n_{\text{J}} = \sqrt{4k_{\text{B}}T\Re(Z)}, \quad (2.2.2)$$

where k_{B} is the Boltzmann constant, T is the temperature of the resistor, and $\Re(Z)$ is the real part of the impedance of the resistor. Calculations of electronic noise for the individual seismic sensors of the AEI-SAS will follow in section 3.4.

Requirements on electronic noise depend on the system or sensor under investigation. Electronic noise of seismic sensors should be lower than the minimum expected signal, which differs for the different sensors. Electronic noise of the anti-symmetric port photodetector for the sub-SQL interferometer must not limit future sub-SQL measurements, but be below the sum of all other classical noise sources. More details are provided in section 4.4.

Countermeasures

External electronic noise sources have to be tackled in different ways. If possible, signals should be amplified directly after the signal source to lift them above any external noise. If this is not possible, the choice of cable between signal source and amplifier is crucial. A grounded shield around the signal strands, acting as a Faraday cage, reduces the coupling of external fields to the signals. In case of differential signals, twisted signal strands ensure a common coupling of external fields to both signal wires and should be used in combination with a differential amplifier input stage to suppress this common noise. Additionally, sources of external fields should be shielded or located at a far distance to reduce their amplitude at the location of the system under observation. These techniques are utilized for every sensor and electronics design presented in this thesis.

Intrinsic noise is tackled by design of the amplifier input stage and the choice of electrical components. The input stage amplifies the signal to be above subsequent noise sources, such that only the noise of components in the input stage, like operational amplifiers and resistors, is relevant. The noise of operational amplifiers usually underlies a trade-off between a low corner frequency, granting low noise at low frequencies, and a low white noise, granting low noise at high frequencies. Consequently, operational amplifiers are chosen to match the system requirements. Section 3.4 and appendix B provide details about the amplifier electronics of seismic sensors within the AEI-SAS. General information about low noise circuit designs are provided in [Fis17, Vas06b].

2.3 Thermal noise

Description and requirements

Thermal noise results from random, thermally driven motion of molecules and atoms and is directly related to the dissipation of the system, described in the Fluctuation-Dissipation theorem [CW51, CG52]. It is relevant for the AEI 10 m prototype in various subsystems of the interferometer, some of which are:

- substrate thermal noise, driven by mechanical loss and thermal dissipation in the bulk material of the test masses,
- coating thermal noise, driven by mechanical loss and thermal dissipation in the high reflecting coating of the test masses,
- suspension thermal noise, driven by mechanical loss in the mirror suspensions,
- and suspension thermal noise, driven by mechanical loss in the suspensions of inertial seismic sensor.

While thermal noise in the substrate, coating and mirror suspension are of major interest in current research, they only find application for noise budget calculations described in section 4 in this thesis and will not be discussed in depth. Details about substrate and mirror thermal noise are provided in [Gor08, FMF⁺09]. Suspension thermal noise is discussed in [Sau90, Gon00]. Suspension thermal noise of inertial sensors is relevant and will be focused on in the following.

[Sau90] describes noise of the test mass $n_{\text{sus}}(\omega)$ driven by thermal suspension noise by the equation

$$|n_{\text{sus}}(\omega)| = \sqrt{\frac{4k_{\text{B}}T}{\omega^2}} \times \Re(Y), \quad (2.3.1)$$

with $\Re(Y)$ being the real part of the admittance. Thermal noise is directly connected to the loss and hence to the damping of the harmonic oscillator under test. There are two different damping mechanisms relevant for inertial sensors of the AEI-SAS: Viscous damping, i.e. velocity proportional damping, results from oscillation of the test mass in a medium, like air, or due to eddy current damping. Structural damping, i.e. velocity independent damping, results from internal friction and is always present in real systems. It becomes relevant, if viscous damping is low, for example, in cases of evacuation and the non-existence of eddy current damping. The admittance for these two types of damping is described by

$$\Re(Y_{\text{vis}}(\omega)) = \frac{\omega^2 v}{(k - m\omega^2)^2 + \omega^2 v^2}, \quad (2.3.2)$$

$$\Re(Y_{\text{struc}}(\omega)) = \frac{\omega k \phi}{(k - m\omega^2)^2 + k^2 \phi^2}, \quad (2.3.3)$$

where m is the mass of the test mass, k is the spring constant, v is the viscous damping factor, and ϕ is the structural damping factor. These parameters can be written to:

$$k = \omega_0^2 m, \quad (2.3.4)$$

$$v = \frac{m\omega_0}{Q}, \quad (2.3.5)$$

$$\phi = \frac{1}{Q}, \quad (2.3.6)$$

with ω_0 being the angular resonance frequency of the harmonic oscillator and Q being the quality factor, such that the viscous (n_{susv}) and the structural (n_{suss}) thermal suspension noise can be written as

$$|n_{\text{susv}}(\omega)| = \sqrt{\frac{4k_{\text{B}}T\omega_0}{mQ} \times \left[(\omega_0^2 - \omega^2)^2 + \left(\frac{\omega_0\omega}{Q} \right)^2 \right]^{-1}}, \quad (2.3.7)$$

$$|n_{\text{suss}}(\omega)| = \sqrt{\frac{4k_{\text{B}}T\omega_0^2}{\omega mQ} \times \left[(\omega_0^2 - \omega^2)^2 + \frac{\omega_0^4}{Q^2} \right]^{-1}}. \quad (2.3.8)$$

Countermeasures

Substrate thermal noise is reduced by the choice and quality of the material, by the dimensions of the substrate and by the surrounding temperature. While the first two options are considered for the AEI sub-SQL interferometer, a temperature control is not pursued. A common choice for interferometers operating at room temperature is fused silica because of its high optical quality, its ability to be excellently polished and its low intrinsic mechanical loss [FMF⁺09]. The type of fused silica used for the AEI 10 m prototype is Suprasil 3001 and is estimated to have a mechanical quality factor of about 10^6 .

Coating thermal noise is reduced by choice and quality of the material and by its design of the multiple layers. The AEI 10 m prototype has the goal to pioneer the use of GaAs/AlGaAs multilayer coatings which provide lower thermal noise than the commonly used Silicon Dioxide/Tantalum Pentoxide ($\text{SiO}_2/\text{Ta}_2\text{O}_5$) multilayer coatings [CZM⁺13]. As an intermediate step, mirrors with ion beam sputtered coatings, similar to the ones currently used by the large gravitational wave detectors [G⁺20], will be installed. The multiple layers are predominantly designed to achieve the target reflectivity; nevertheless, there are techniques to simultaneously reduce thermal noise [KGG11].

Suspension thermal noise of the mirror suspensions is as well reduced by choice and quality of the material and by design properties. The final suspension stage for the core optics of the AEI sub-SQL interferometer will consist of monolithic fused silica, similar to the final stage of the Advanced LIGO quadruple suspensions [A⁺12]. Careful design of the fibers and the connection points to the mirrors, called ears, is required for a low thermal noise [C⁺12].

Suspension thermal noise of inertial seismic sensors can, in principle, be reduced by the same countermeasures as listed for suspension thermal noise of the mirror suspensions. Its reduction played a minor role in the design of most seismic sensors, since other noise sources limit the sensor performance. It was only accounted for in the design of the monolithic accelerometers (see section 3.4.4) cut out of one aluminum block to minimize thermal noise [BDF⁺05]. Suspension thermal noise calculations find application for the noise characterization of some seismic sensors.

2.4 Laser intensity noise

Description and requirements

Fluctuations of laser intensity create noise in gravitational wave interferometers on two paths: The first path is direct coupling of intensity fluctuations to the interferometer output. This coupling is created by intended arm length differences, like the dark fringe offset (see chapter 4) and unintended arm differences, for example arising from seismic coupling to the test masses. The second path is a coupling of intensity fluctuations to phase fluctuations by exerting radiation pressure forces onto the suspended test masses. These phase fluctuations directly couple to the interferometer output, since the interferometer is designed to measure phase fluctuations present in its arms.

The AEI 10 m prototype utilizes a 35 W laser system with a wavelength of 1064 nm consisting of a commercial Neodymium-doped Yttrium Aluminium Garnet (Nd:YAG) Non-Planar Ring Oscillator (NPRO) manufactured by InnoLight GmbH [KB85], [FTW95] and a four stage amplifier [FSW⁺07]. The same laser system was used in the enhanced LIGO detector and is currently used in Advanced LIGO, where an additional amplifier stage was added. Relative Intensity Noise (RIN) of this laser system in the sub-SQL interferometer measurement band is between $10^{-6} - 10^{-5} \text{ Hz}^{-1/2}$ [FSW⁺07, JOW17]. The intensity stability requirements for the AEI sub-SQL interferometer are $10^{-8} \text{ Hz}^{-1/2}$ at 40 Hz and $3 \times 10^{-8} \text{ Hz}^{-1/2}$ at 100 Hz [KWD09]; consequently, the RIN needs to be reduced by a factor of $10^2 - 10^3$.

Countermeasures

An ISS was installed at the AEI 10 m prototype to reduce the RIN down to the requirements [JOW17]. Its design is adapted from the Advanced LIGO ISS [KWD09].

The main interferometer laser beam is propagated through a beam splitter, where about 320 mW are split off and propagated to an array of eight photodiodes, four in-loop and four out-of-loop. The signal of the in-loop PDs is processed and sent to an Acousto-Optic Modulator (AOM), located in the main interferometer beam in front of the beam splitter. This AOM controls the power in transmission by diffracting some power into the first diffraction order, removing it from the main beam.

2.5 Laser frequency noise

Description and requirements

There are two interferometers at the AEI 10 m prototype that suffer from fluctuations of the laser frequency: the sub-SQL interferometer and the Suspension Platform Interferometer (SPI), which is described in section 3.4.7. Both are based on measuring differential phase changes between two arms. Same as for intensity noise, frequency fluctuations would not couple to the interferometer output, if both arms were perfectly equal. The coupling predominantly arises from the Schnupp asymmetry, manifesting as unequal arm lengths. Calculations for the coupling of frequency noise to the Michelson interferometer output ports are provided in [SCKM06].

The main interferometer NPRO laser of the type Mephisto from InnoLight has a frequency noise $n_{\text{freq}}^{\text{Meph}}$ of

$$n_{\text{freq}}^{\text{Meph}} = \frac{10000 \text{ Hz}}{f} \frac{\text{Hz}}{\sqrt{\text{Hz}}}, \quad (2.5.1)$$

as measured for several InnoLight Mephisto NPRO lasers in [KW08]. The amplifier stage conserves this high frequency stability. The SPI uses an NPRO laser system of the type Prometheus, also from InnoLight. According to [SKP09] the frequency noise of the free running Prometheus laser system is

$$n_{\text{freq}}^{\text{Prom}} = \frac{1000 \text{ Hz}}{f} \frac{\text{Hz}}{\sqrt{\text{Hz}}}. \quad (2.5.2)$$

The displacement equivalent frequency noise \tilde{n}_{freq} is calculated by

$$\tilde{n}_{\text{freq}} = n_{\text{freq}} \times \frac{\lambda \Delta L}{c_0}, \quad (2.5.3)$$

$$\begin{aligned} \Rightarrow \tilde{n}_{\text{freq}}^{\text{Meph}} &\approx \frac{2 \times 10^{-12} \text{ m}}{f \sqrt{\text{Hz}}}, \\ \Rightarrow \tilde{n}_{\text{freq}}^{\text{Prom}} &\approx \frac{8 \times 10^{-11} \text{ m}}{f \sqrt{\text{Hz}}}, \end{aligned} \quad (2.5.4)$$

with $\lambda = 1064 \text{ nm}$ being the laser wavelength, c_0 being the speed of light in vacuum, and ΔL being the arm length difference of the two interferometer arms. For the sub-SQL interferometer, ΔL is 50 mm, set by the Schnupp asymmetry. For the SPI it is 23 m.

The requirement for frequency noise of the sub-SQL interferometer is to be below the sum of all other classical noise sources. Investigating the noise budget in figure 1.4.3 leads to the requirement of roughly

$$\tilde{n}_{\text{freq}}^{\text{SQL}} \leq \frac{10^{-18} \text{ m}}{f \sqrt{\text{Hz}}}. \quad (2.5.5)$$

Comparing this to equation 2.5.4 shows that a suppression of frequency noise by a factor of roughly 10^6 is required. This is relaxed strongly below the measurement band.

[DHW⁺12] states frequency independent requirements for the frequency noise of the SPI to be

$$\tilde{n}_{\text{freq}}^{\text{SPI}} = 10^{-11} \frac{\text{m}}{\sqrt{\text{Hz}}}, \quad (2.5.6)$$

above 10 mHz; hence, a suppression of frequency noise of $8 \times f^{-1} \text{ Hz}$ is necessary.

Countermeasures

The laser frequency can be stabilized by locking the laser to a stable frequency reference. The requirements for the sub-SQL interferometer are demanding in the measurement band, while for the SPI they are low in the measurement band but concentrate on frequencies below 1 Hz; hence, two different frequency references are chosen:

- For the sub-SQL interferometer the frequency reference is a triangular shaped optical cavity with mirrors suspended by three stages. The resonance condition is determined by the length of the cavity and by the frequency of the laser. For frequencies in the measurement band, the suspended optics grant a high length stability and hence a high sensitivity for the laser frequency. More information and a noise budget is given in [K⁺09, Han18].
- For the SPI interferometer, a commercial stabilization unit type I2 MTS V2.0 from InnoLight is utilized. It is based on highly stable hyperfine transitions of an iodine cell at 532 nm, providing a good low frequency reference for a frequency doubled Nd:YAG laser.

Using these techniques, the requirements on frequency noise for both interferometers (equations 2.5.5 and 2.5.6) are fulfilled.

2.6 Mode mismatch and beam jitter

Description and requirements

Higher order modes are present in the input and output path of the interferometer. In the interferometer input, higher order modes do not match the resonance conditions

of the arm cavities and are reflected. This causes intensity noise at the interferometer output port, if the ratio of laser power within the fundamental and higher order modes is time dependent. In the interferometer output, higher order modes mask the effect of quantum radiation pressure on the test masses, which is the signal of interest for the sub-SQL interferometer. Sources of higher order modes are

- 1) an imperfect output beam of the laser source,
- 2) seismic motion rotating or translating the laser source,
- 3) seismic motion rotating or translating auxiliary optics,
- 4) imperfect interference conditions on the beam splitter,
- 5) and motion of the cavity mirrors.

Motion of the cavity mirrors is neglected due to their large seismic isolation and the interferometer control loops. The first three sources create higher order modes in the input beam, while sources 3 and 4 create higher order modes in the output beam. Requirements for the output path are currently evaluated and not topic of this thesis. Requirements for the input path are investigated in the following.

[And84] provides calculations for the coupling of beam jitter and mode mismatches to higher order modes at a single resonant cavity. These calculations can be utilized to set requirements for the motion of input path optics. Four different degrees of freedom for misalignment are differentiated: the transverse position, the angular tilt, the waist size and the waist axial position, as pictured in figure 2.6.1. The resulting relative intensity noise terms RIN_{trans} , RIN_{rot} , RIN_{wsize} and RIN_{wpos} for these degrees of freedoms are calculated by

$$RIN_{\text{trans}} = \frac{x_{\text{beam}}}{w_0}, \quad (2.6.1)$$

$$RIN_{\text{rot}} = \frac{r_{\text{beam}}\pi w_0}{\lambda}, \quad (2.6.2)$$

$$RIN_{\text{wsize}} = \frac{w'_0}{w_0} - 1, \quad (2.6.3)$$

$$RIN_{\text{wpos}} = \frac{\lambda b}{2\pi w_0^2}, \quad (2.6.4)$$

where x_{beam} is the displacement of the beam at the waist position, w_0 is the initial beam waist size, r_{beam} is the rotation of the beam around the waist position, λ is the laser wavelength, w'_0 is the changed waist size due to mode mismatch, and b is the changed waist position along the cavity axis due to mode mismatch.

The requirements on relative intensity noise due to jitter and mode mismatch are set to be equal to the ISS requirements at 40 Hz:

$$\sqrt{RIN_{\text{trans}}^2 + RIN_{\text{rot}}^2 + RIN_{\text{wsize}}^2 + RIN_{\text{wpos}}^2} \leq 10^{-8} \frac{1}{\sqrt{\text{Hz}}}. \quad (2.6.5)$$

The requirement is only evaluated at 40 Hz, since this is the lower end of the sub-SQL interferometer measurement band, and it is more challenging to meet the requirements than for higher frequencies. This equation assumes incoherence between the individual noise contributions. In order to set requirements including some safety margin on motion of the laser source and input steering and mode matching optics, each of the four RIN terms is required to fulfil

$$RIN \leq 5 \times 10^{-9} \frac{1}{\sqrt{\text{Hz}}}. \quad (2.6.6)$$

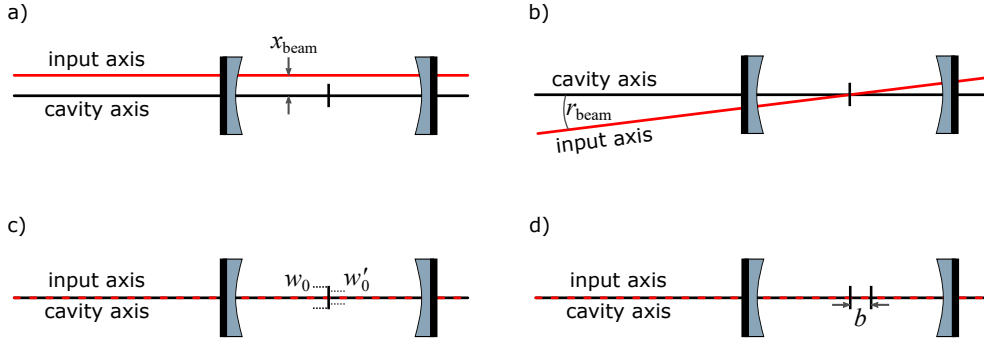


Figure 2.6.1: Possible types of misalignment of an input beam to a cavity axis. a) shows a translation of the input axis; b) shows a rotation of the input axis; c) shows a change in waist diameter of the input beam; d) shows a translation of the input beam waist along the cavity axis.

x_{beam} and r_{beam} are caused by translations and rotations of input optics x_{opt} and r_{opt} . The worst case couplings are described by

$$\begin{pmatrix} x_{\text{beam}} \\ r_{\text{beam}} \end{pmatrix} = \begin{pmatrix} d/f & d \\ 0 & 1 \end{pmatrix} \times \begin{pmatrix} x_{\text{opt}} \\ r_{\text{opt}} \end{pmatrix}, \quad (2.6.7)$$

where $d = 22\text{ m}$ describes the length of the lever between the first steering mirror and the waist position inside the cavity, and $f = 8\text{ m}$ is the focal length of the first steering mirror. Combining equations 2.6.1, 2.6.2 and 2.6.7 yields to requirements for displacement and rotation of input optics as

$$2.75 x_{\text{opt}} + 22 r_{\text{opt}} = RIN_{\text{trans}} \omega_0 \quad (2.6.8)$$

$$r_{\text{opt}} = \frac{RIN_{\text{rot}} \lambda}{\pi \omega_0}. \quad (2.6.9)$$

Assuming that translations and rotations of the input optics are about equal in amplitude and inserting $\lambda = 1064\text{ nm}$, $\omega_0 = 321\text{ }\mu\text{m}$ and equation 2.6.6 gives

$$x_{\text{opt}} \leq 2.7 \times 10^{-13} \frac{\text{m}}{\sqrt{\text{Hz}}}, \quad (2.6.10)$$

$$r_{\text{opt}} \leq 2.7 \times 10^{-13} \frac{\text{rad}}{\sqrt{\text{Hz}}}, \quad (2.6.11)$$

at 40 Hz.

Comparing these requirements to the seismic motion in figure 2.1.1 shows that a suppression of a factor 10^4 is necessary.

The intensity noise caused by mode mismatch RIN_{wsize} and RIN_{wpos} results from translation of mode matching optics along the direction of propagation. This translation is simulated using the ABCD-matrix formalism. The resulting requirements are

$$x_{\text{opt}} \leq 2.21 \times 10^{-9} \frac{\text{m}}{\sqrt{\text{Hz}}}, \quad (2.6.12)$$

which is automatically fulfilled when satisfying the requirements for beam translation and rotation.

These calculations are based on simplifications of the real setup. It is, for example, not considered that a displaced beam hitting a curved input mirror converts to rotation and vice versa. A more complex simulation of jitter noise is provided in section 4.

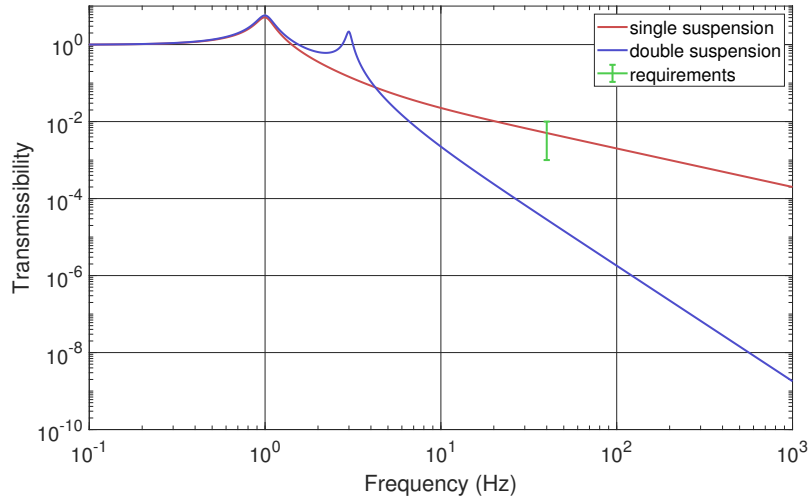


Figure 2.6.2: Transmissibility of a single and a double suspension and the isolation requirement for jitter noise of input optics. The model includes a realistic damping, reducing the isolation to $1/f$ for the single suspension and $1/f^3$ for the double suspension above 5 Hz.

Countermeasures

Higher order modes already present in the output beam of the laser source or created by motion of the laser source are filtered by the Photonic Crystal Fiber (PCF) guiding the laser into the vacuum system. This filtering effect is not sufficient and additionally, motion of the PCF creates higher order mode content, exceeding the ISS requirements; therefore, a Pre-Mode Cleaner is installed. The PMC consists of a triangular cavity inside a rigid SuperInvar block. More information on the concept of a pre-mode cleaner is provided in [RSS⁺81]. The realization for the AEI 10 m prototype is described in [Ali13] and [Wes16].

Recent investigations show that the PMC does not sufficiently suppress higher order modes; hence, a second mode cleaner, the Input Mode Cleaner (IMC), is being installed at the time of writing. It will consist of a Fabry-Perot cavity with optics suspended by double stage pendulums. It is assumed that the IMC suppresses jitter of all components earlier in the laser path effectively, such that jitter at the output of the IMC is limited by the IMC motion itself.

Higher order modes resulting from motion of the IMC and input path optics located in between the IMC and the Input Test Masses (ITMs) are reduced by isolating the optics from ground motion; therefore, all input optics including the IMC are installed on the AEI-SASs. The AEI-SAS is optimized to isolate at frequencies below the measurement band of the sub-SQL interferometer. Isolation at 40 Hz and above is about a factor $10^1 - 10^2$, such that additional suspensions are required.

Figure 2.6.2 shows the evaluated requirements and the transfer functions of a single suspension and a double suspension, each with a resonance frequency of 1 Hz. The models for the suspensions contain realistic damping of the resonances, reducing the isolation to $1/f$ for the single suspension and $1/f^3$ for the double suspension above 5 Hz. The single suspension does not fully meet the requirements while the double suspension exceeds them, giving a safety margin of a factor 300. These results are confirmed by the FINESSE simulations presented in section 4.

2.7 Scattering noise

Description and requirements

Scattering noise was first noticed and investigated in 1979 [BMR⁺79, BWS⁺81] and is still topic of current research [ZATA19, LBP⁺20]. It usually requires three different unwanted processes to create scattering noise [VBB96].

- 1) Fractions of laser light leave the beam and take a different path. Scattered light can have two different forms: It can be mostly collimated parasitic beams, resulting from, for example, reflections on back surfaces of optics, photodiodes or view ports, and it can be uncollimated, resulting from rough optic surfaces or defects.
- 2) The scattered light hits a different object, like the vacuum tube, and picks up a phase depending on the relative position between the object and the relevant interferometer optics [A⁺10a]. From this object, the light is scattered or reflected back onto one of the interferometer optics.
- 3) The scattered light incident on the optic is scattered back into the main laser beam path and creates time-varying interferences due to the differential motion between optics and object. Same as in process 1), this effect depends on the surface and bulk material quality of the optics and on the amount of scattered light incident on the optics. Another effect creating noise in this third process is the time-varying momentum transfer of scattered light onto the main optics, resulting in increased radiation pressure noise.

There are two different types of interferences, which differ by the amplitude of the relative motion between optics and the object hit by the stray light [OFW12]. If the motion is small compared to the laser wavelength of 1064 nm, the interaction is linear and creates noise at the same frequency as that of the relative motion; hence, for this effect only motion in the measurement band is relevant. If the amplitude of motion is not small compared to the laser wavelength, the effect called “fringe wrapping” converts the light modulated at a certain frequency to interference effects at higher frequencies. Ground motion at the micro seismic peak usually exceeds 10^{-6} m, such that motion at frequencies far below the measurement band become relevant as well.

[OFW12] calculates the impact of scattered light on gravitational wave interferometers. A study of requirements for scattering noise at the AEI 10 m prototype is currently investigated.

Countermeasures

Scattering noise is attenuated by three different measures. Firstly, optics within the interferometer are polished to extremely high surface quality. This reduces the amount of light scattering out of the laser beam, described by process 1). Additionally, it reduces the amount of light scattering back into the laser path, described by process 3). Especially the intra-cavity mirrors are polished to very high surface qualities [P⁺17, BYZ17] but a careful choice and treatment of all optics is required.

Secondly, scattered light is dumped by beam dumps and baffles. Beam dumps effectively absorb focused stray light beams from unwanted reflections and transmissions. They are designed to trap the beam, such that multiple reflections are required for the beam to leave the beam dump. The beam dump material and the surface orientation at Brewster angle are chosen to give maximal absorption. Baffles are designed to absorb the diffuse stray light from rough surfaces and defects. They cover large areas around the main interferometer optics, but are also located around other optics and inside the vacuum tubes to prevent reflections from the tube entering the interferometer beam. Their material is chosen to give maximal absorption as well. Their surface orientation is designed to trap as much stray light as possible [DPPS20, TSS⁺04, A⁺16c].

The third measure to reduce scattering noise is most relevant for this thesis. In the AEI 10 m prototype, all objects close to the interferometer optics are isolated by

the AEI-SASs. This reduces the relative velocity and hence the scattering noise. The reduction of relative velocity is utilized as a requirement in sections 3.7.8 and 3.8.3 to optimize active isolation parameters.

2.8 Quantum noise

Description and requirements

Quantum noise is a non-classical noise source based on the quantum nature of laser light. It can be described by vacuum fluctuations entering the interferometer through open ports. In the context of gravitational wave detectors, these vacuum fluctuations manifest in two different ways: Quantum shot noise $\tilde{n}_{\text{sh}}(f)$ results from phase fluctuations of the laser light within the arm cavities. These phase fluctuations are converted to an intensity noise on the anti-symmetric port photodetector via the interference on the interferometer beam splitter. Quantum radiation pressure noise $\tilde{n}_{\text{rp}}(f)$ results from intensity fluctuations within the arm cavities. These intensity fluctuations exert a force onto the suspended interferometer mirrors and hence create phase fluctuations of the laser light by changing the path length. Same as for shot noise, the phase fluctuations are converted to intensity noise on the photodetector by the interference on the beam splitter. As the randomness in amplitude and phase are statistically independent, the resulting total quantum noise is given by the incoherent sum of both, calculated by

$$\tilde{n}_{\text{q}}(f) = \sqrt{\tilde{n}_{\text{sh}}(f)^2 + \tilde{n}_{\text{rp}}(f)^2}. \quad (2.8.1)$$

The displacement amplitude spectral density of quantum shot noise in $\text{m}/\sqrt{\text{Hz}}$ can be written as

$$\tilde{n}_{\text{sh}}(f) = \sqrt{\frac{\hbar c \lambda}{2\pi P_{\text{in}}}}, \quad (2.8.2)$$

with \hbar being the reduced Planck constant and P_{in} being the input laser power of the interferometer.

Quantum radiation pressure noise is frequency dependent with a $1/f^2$ slope due to the susceptibility of the free-falling test masses to a force. The displacement amplitude spectral density in $\text{m}/\sqrt{\text{Hz}}$ can be written as

$$\tilde{n}_{\text{rp}}(f) = \frac{1}{m f^2} \sqrt{\frac{\hbar P_{\text{in}}}{2\pi^3 c \lambda}}, \quad (2.8.3)$$

with m being the mass of the test masses.

Quantum shot noise is inversely proportional to the square root of the laser power, while quantum radiation pressure noise is proportional to the same. By varying the laser power, the minimal quantum noise for each frequency forms a line called the Standard Quantum Limit (SQL). The SQL is an expression of the Heisenberg uncertainty relation [Hei83]. It is described by the equation

$$\tilde{n}_{\text{SQL}}(f) = \frac{1}{\pi f} \sqrt{\frac{2\hbar}{m}}. \quad (2.8.4)$$

Figure 2.8.1 shows the quantum noise of the sub-SQL interferometer for three different laser input powers and the SQL.

Significance for the AEI 10 m prototype

In gravitational wave detectors, effects from quantum fluctuations mask the gravitational wave signals and hence they are considered as noise. For the AEI 10 m prototype, quantum fluctuation and especially the SQL is the signal to be measured. In contrast to gravitational wave detectors, the AEI 10 m prototype test masses are

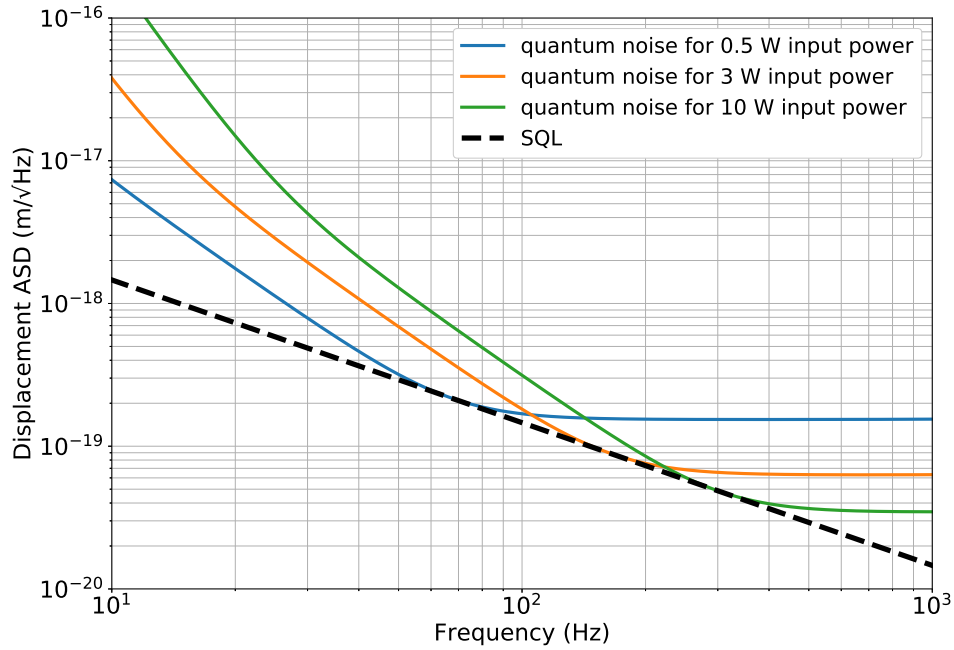


Figure 2.8.1: Quantum noise and the SQL for the AEI sub-SQL interferometer in units of $m/\sqrt{\text{Hz}}$. The noise is simulated using FINESSE, described in chapter 4.

very light-weight with a mass of 100 g to increase the effect of quantum radiation pressure noise.

For classical, i.e. coherent states of light, the SQL is a fundamental limit for the sensitivity of an interferometer. Only with non-classical techniques, it is possible to surpass the SQL. [CM04] describes the significance of quantum noise for gravitational wave interferometers and presents some techniques and ideas to reduce quantum noise and surpass the SQL. The implementation of such techniques and the verification of their functionality is the final goal of the AEI sub-SQL interferometer, but exceeds the scope of this thesis.

Chapter 3

Seismic isolation

Seismic isolation for gravitational wave interferometers can be divided up into two fundamentally different concepts: passive seismic isolation, based on the principle of the harmonic oscillator, and active seismic isolation, based on feedback control loops.

This chapter presents the principles and the realization of both concepts, with a strong focus on active isolation. All involved sensors are characterized with a focus on their noise, which is compared to noise measurements. Local seismic isolation and global seismic isolation are presented as two active isolation concepts. The involved techniques are described and improvements are elaborated. Final performance measurements are compared to simulations to analyze limitations. This is utilized to propose concepts for future improvements.

3.1 Principles of passive seismic isolation

Passive seismic isolation is based on the principle of the harmonic oscillator. The ideal harmonic oscillator consists of a mass m connected to the surroundings via a spring. The spring transmits a force $F_{\text{HO}}(t)$ from the surroundings to the mass, described by

$$F_{\text{HO}}(t) = m\ddot{x}(t) = -k \times \delta x(t), \quad (3.1.1)$$

with k being the spring constant and $\delta x(t)$ being the differential motion between the surroundings x_g and the test mass x . In case of a real harmonic oscillator a damping force opposing the restoring force is present. The two different forms of damping are viscous damping and structural damping, described in section 2.3. Viscous damping is described by the viscous damping factor v and the differential velocity between surroundings and test mass $\delta \dot{x}(t)$. Structural damping is described by the imaginary part $i\phi$ of the complex spring constant $k_s = k(1 + i\phi)$. $F_{\text{HO}}(t)$ for a real harmonic oscillator can be written as

$$F_{\text{HO}}(t) = -k_s \delta x(t) - v \delta \dot{x}(t). \quad (3.1.2)$$

The Fourier transform of equation 3.1.2 is

$$\omega^2 x(\omega) = \omega_0^2 (1 + i\phi) \delta x(\omega) - \frac{iv\omega}{m} \delta x(\omega), \quad (3.1.3)$$

where ω is the angular frequency and $\omega_0^2 = k/m$ is the resonance frequency. This equation can be rewritten to describe the transfer function from ground motion to motion of the test mass $T_{\text{HO}}(\omega)$ to

$$T_{\text{HO}}(\omega) = \frac{x(\omega)}{x_g(\omega)} = \frac{\omega_0^2 (1 + i\phi) + \frac{iv\omega}{m}}{\omega_0^2 (1 + i\phi) - \omega^2 + \frac{iv\omega}{m}}. \quad (3.1.4)$$

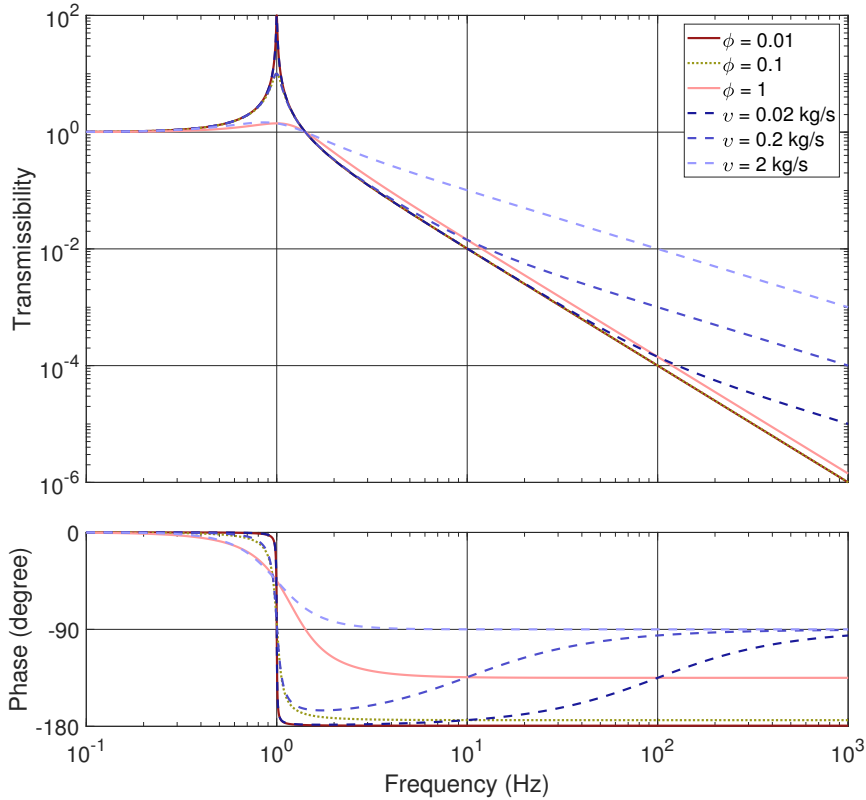


Figure 3.1.1: Transmissibility and phase of a damped harmonic oscillator for three different structural damping coefficients without viscous damping and three different viscous damping coefficients without structural damping.

Figure 3.1.1 shows the transfer function of a damped harmonic oscillator for three different structural damping coefficients without viscous damping and for three different viscous damping coefficients without structural damping. Structural damping reduces the height of the resonance peak and slightly lifts the amplitude above resonance in cases of high damping. The phase delay is 180° for low structural damping and is reduced for high structural damping. Viscous damping reduces the height of the resonance peak and reduces the attenuation from $1/\omega^2$ to $1/\omega$ above a corner frequency, depending on the viscous damping factor. The phase delay depends on the viscous damping factor and approaches 90° for high frequencies.

More information on the principles of passive isolation systems are provided in [Wan13, Ber18].

A stronger isolation above resonance frequency can be achieved by stacking harmonic oscillators. The slope above the resonance frequencies for n stages of ideal harmonic oscillators follows $1/f^{2n}$. In cases of viscous damping it is reduced to $1/f^n$, equivalent to the single stage harmonic oscillator. Figure 3.1.2 shows some examples for single, double and triple suspensions for a structural damping factor of 0.1 without viscous damping and for a viscous damping factor of 0.1 kg/s without structural damping.

Viscous damping from gases or liquids can be mostly neglected for the passive isolation systems of the sub-SQL interferometer since they are located inside a vacuum system; nevertheless, viscous damping is introduced by eddy current damping of suspension stages and lossy materials like the Viton[®] stage and the resonant dampers (see section 3.3). Geophones are viscously damped since they operate in a chamber filled with air. Structural damping is always present and is the predominant damping mechanism for the passive isolation of the sub-SQL interferometer.

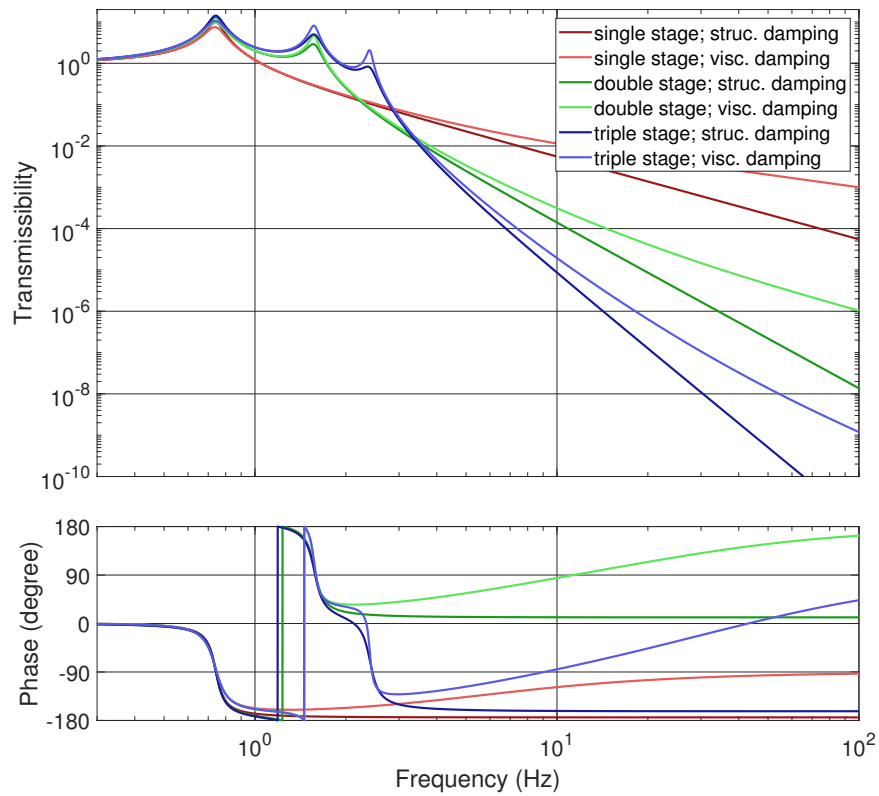


Figure 3.1.2: Transmissibility and phase of single, double and triple stage damped harmonic oscillators for a structural damping factor of 0.1 without viscous damping and for a viscous damping factor of 0.1 without structural damping. The resonance frequencies are realistic values for the triple suspensions that are utilized in the AEI sub-SQL interferometer.

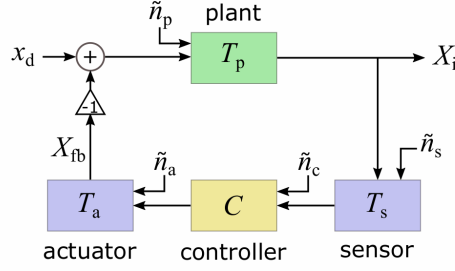


Figure 3.2.1: Block diagram for an idealized feedback control system. T_p : transfer function of the plant; T_s : transfer function of the sensor; T_a : transfer function of the actuator; C : gain of the controller; x_d : disturbance signal; $X_i = x_i + n_i$: plant output to be minimized, with the plant signal x_i and the noise n_i ; $X_{fb} = x_{fb} + n_{fb}$: feedback loop output, with the feedback signal x_{fb} and the noise n_{fb} ; \tilde{n} : noise of the different components.

The response of a harmonic oscillator to motion of the surroundings, differs from the response of a harmonic oscillator to an external force F_{ext} , directly acting on the test mass. With a similar calculation as presented earlier in this section, the transfer function from an external force acting on the mass to motion of the mass is described by

$$T_{\text{HOext}} = \frac{x_m}{F_{\text{ext}}} = \frac{1}{m \left(\omega_0^2 (1 + i\phi) - \omega^2 + \frac{i\nu\omega}{m} \right)}. \quad (3.1.5)$$

3.2 Principles of active seismic isolation

Active seismic isolation of current gravitational wave detectors and of the sub-SQL interferometer is based on feedback loop configurations, but also contains feedforward features. This section will describe the principles of these two types of control systems. The last section describes stability criteria in the context of the previously described techniques.

3.2.1 Feedback control system

Feedback control systems have the purpose of minimizing an output parameter while a disturbance signal and noise is present. Figure 3.2.1 shows a block diagram for a basic feedback control system. A disturbance signal x_d is incident on the plant with transfer function T_p . The resulting output of the plant $X_i = x_i + n_i$ is the signal of interest and consists of the plant signal x_i and the noise n_i , as defined in equation 2.0.1. X_i is measured by a sensor with transfer function T_s , which sends the signal to the controller. The controller shapes the signal with its filter C , depending on the requirements of the control loop, and sends it to the actuator with transfer function T_a . The resulting feedback $X_{fb} = x_{fb} + n_{fb}$ is applied to the plant to counteract the disturbance and minimize X_i . Input referred noise \tilde{n} is present at every component in the loop.

To calculate the open and closed loop gain, all noise components are neglected. x_i is given by

$$x_i = (x_d - x_{fb})T_p \quad (3.2.1)$$

with

$$\begin{aligned} x_{fb} &= x_i T_s C T_a, \\ \Rightarrow x_i &= x_d T_p - x_i T_s C T_a T_p. \end{aligned} \quad (3.2.2)$$

The closed loop transfer function describes the suppression of the disturbance and is expressed by

$$G_{cl} = \frac{x_i}{x_d} = \frac{T_p}{1 + T_s C T_a T_p}, \quad (3.2.3)$$

$$= \frac{T_p}{1 + G}, \quad (3.2.4)$$

with G_{cl} being the closed loop gain and G being the open loop gain. A suppression of the disturbance is only provided if the open loop gain is large. This is usually achieved by having a large controller gain C .

The noise of the different components have different significance for the system output X_i . Considering only noise sources, n_i can be written as

$$\begin{aligned} n_i &= \frac{\tilde{n}_p T_p - \tilde{n}_s T_s C T_a T_p - \tilde{n}_c C T_a T_p - \tilde{n}_a T_a T_p}{1 + T_s C T_a T_p}, \\ &= \frac{\tilde{n}_p}{G_{cl}} - \frac{\tilde{n}_a T_a}{G_{cl}} - \frac{\tilde{n}_c C T_a}{G_{cl}} - \frac{\tilde{n}_s T_s C T_a}{G_{cl}}. \end{aligned} \quad (3.2.5)$$

Equation 3.2.5 shows that the coupling from controller noise and sensor noise to the system output includes a multiplication by the usually large controller gain C , whereas the coupling of actuator and plant noise do not include the controller gain; therefore, most attention is paid to controller and sensor noise reduction, while the other noise sources often have less relevance for the AEI 10 m prototype.

3.2.2 Feedforward control system

Figure 3.2.2 displays a block diagram of a feedforward control system. It consists of a disturbance x_d , incident on the plant and a signal or disturbance x_r , which is measured by a reference sensor and processed by a reference controller C_r . x_r can be independent on, dependent on or equal to x_d . The feedforward output $X_{ff} = x_{ff} + n_{ff}$, with the feedforward signal x_{ff} and the noise n_{ff} , is combined with x_d to minimize or manipulate the plant output X_i .

Calculations of gain and noise are analogous to the calculations presented in section 3.2.1.

3.2.3 Stability criteria

Feedback control loops must fulfil certain criteria in order to be stable. If the stability criteria are not fulfilled, the system's output signal x_i slowly drifts to infinity or oscillates with an amplitude that increases to infinity. There are various stability criteria, utilizing different methods and describing different types of control systems. For control systems within gravitational wave detectors and the AEI sub-SQL interferometer, Bode diagrams are commonly used to analyze the loop stability. They are applicable for linear time-invariant systems in the Laplace domain. Bode diagrams consist of split plots, one showing the real part or amplitude of the open loop gain G over frequency and the other showing the imaginary part or phase between input and output ϕ over frequency.

In Bode plots, three different frequency ranges are differentiated. The separation can be motivated by looking at the closed loop gain from equation 3.2.4:

1. Well below the unity gain frequency, where $G \gg 1$, the denominator becomes very large granting a high loop suppression, independently of the phase. The loop is unconditionally stable here.

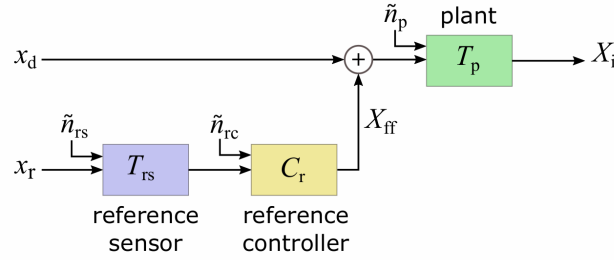


Figure 3.2.2: Basic feedforward system. T_p : transfer function of the plant; T_{rs} : transfer function of the reference sensor; T_a : transfer function of the actuator; C_r : gain of the reference controller; x_d : disturbance signal; $X_i = x_i + n_i$: plant output with x_i : output signal and n_i : noise at output; X_r : reference signal; $X_{ff} = x_{ff} + n_{ff}$: feedforward output with x_{ff} : feedforward signal and n_{ff} : noise in feedforward output; \tilde{n} : noise of the different components.

2. Well above the unity gain frequency, where $G \ll 1$, the denominator is approximately 1, such that the loop is unconditionally stable but does not provide any suppression.
3. At and around unity gain, where $G \approx 1$, the denominator can vary between 0–2 depending on the phase between input and output. Three different scenarios can be considered:
 - 3.1 $\phi > -180^\circ$: The denominator is unequal zero and the loop is stable. The closer ϕ approaches -180° , the less suppression is given and a “servo bump” is forming, which is an increased amplitude of the system’s output X_i around the unity gain frequency.
 - 3.2 $\phi \approx -180^\circ$: The denominator is approximately zero, which results in an infinite feedback signal quickly amplifying X_i to infinity.
 - 3.3 $\phi < -180^\circ$: The denominator is unequal zero, but the system is still unstable. A certain feature A in the disturbance signal creates a feature A' in the feedback signal that misses A by more than 180° ; therefore, it does not suppress feature A but amplifies a following feature B . This process continuously increases the amplitude of oscillation to infinity.

[AC00] provides exemplary calculations for a feedback system disturbed by a pulse with different bandwidths, to graphically demonstrate the different behaviors of the system in time domain.

3.3 The AEI-SAS

The concepts of passive and active isolation, described in sections 3.1 and 3.2, find application in the Albert Einstein - Institute Seismic Attenuation System (AEI-SAS). This section will motivate the necessity of this pre-isolation system, describe its setup and provide details on the realization of passive isolation.

An overview of seismic isolation systems used for gravitational wave detectors and a comparison to the AEI-SAS is provided in appendix A.

3.3.1 Motivation for seismic pre-isolation

Without seismic isolation, ground motion would mask the SQL by about 10 orders of magnitude in the measurement band of the sub-SQL interferometer. Predominantly, seismic isolation in the measurement band is provided by multiple stage suspensions.

Diagram 3.1.2 shows a realistic transfer function of the triple suspensions with structural damping utilized to isolate the main interferometer optics. At the lower end of the measurement band at 50 Hz they isolate by a factor of approximately 10^{10} which is already sufficient to achieve the target sensitivity.

The necessity for an additional pre-isolation system is not primarily motivated by direct coupling of seismic motion to the main interferometer optics, but by looking at second order noise effects and lock acquisition:

Mode mismatch and beam jitter

Sections 2.6 and 4.2 describe how mode mismatch and beam jitter create noise at the interferometer output. These effects result from seismic motion coupling to the various main and auxiliary optics in the interferometer input and output paths. Without a seismic pre-isolation system, requirements on the suspensions for the various optics would be significantly stricter, partly enforcing triple suspensions instead of double or single suspensions with significantly higher complexity.

Scattering noise

Section 2.7 describes how scattered light modulated at low frequencies and re-entering the interferometer beam is upconverted in frequency and creates noise in the measurement band. The noise amplitude is proportional to the relative velocity between the object modulating the scattered light and the interferometer optics. Especially components close to the main optics are strong candidates for the creation of scattering noise since it only requires small angle scattering for the light on those object to re-enter the interferometer beam. By placing all those components on a pre-isolation system and isolating them at low frequencies, especially at the micro seismic peak, the relative velocity between object and optic is reduced, lowering the scattering noise.

Controls noise

Rough positioning and control of the optics requires comparatively large forces. Without a seismic pre-isolation system, these large forces would be applied within the suspensions; hence, the suspension control loops would require high unity gain frequencies. Noise from the utilized sensors and actuators would couple strongly to the test masses, which would limit the interferometer sensitivity in the measurement band. In fact, although multiple stage pre-isolation is utilized, the Advanced LIGO interferometers are still limited by exactly this effect in the lower measurement band (see figure 1.3.3). When applying large forces in a pre-isolation system, the noise contributions are filtered by the whole suspension chain, reducing the noise coupling in the measurement band.

Lock acquisition

Lock acquisition is the process of positioning and controlling the main interferometer optics to resonantly enhance the light inside the cavities and tune the interferometer to the desired output light. Especially at the suspension resonances, large motion is transferred to the optics, which makes locking of the interferometers very challenging or impossible. Additionally, static positioning with large actuation range is required, which is difficult to achieve with the current design of suspension sensors and actuators. The pre-isolation systems focus on low frequency isolation to provide the best possible pre-isolation for the suspension resonances. They also include large range sensors and actuators to enable a positioning within a range of several millimeters.

Direct seismic isolation

Although not being the primary motivation, pre-isolation systems still provide some seismic isolation in the measurement band. This relaxes requirements on the suspensions.

3.3.2 Setup and passive isolation

The AEI-SASs consist of four stages, connected by three different applications of harmonic oscillators. Detailed information on the setup of the system, all its components and especially the isolation systems is provided in [Wan13, B⁺17, Ber18]. The setup and passive isolation are based on the LIGO Horizontal Access Module - Seismic Attenuation System (HAM-SAS) design [BDG⁺06] with only minor differences. A detailed comparison between the mechanics of the two systems and many other pre-isolation systems for gravitational wave detectors is provided in [Ber18]. This section gives a summary of the AEI-SAS setup and its passive isolation.

Setup

Figure 3.3.1 shows three schematic overviews of the AEI-SASs. Overview a) shows the location of the three AEI-SAS in the L-shaped vacuum system, together with a coordinate system. Overview b) shows a side view of the AEI-SAS in the z - x -plane to demonstrate the vertical positions of the four stages and the passive isolators, which are labelled and marked by color. Overview c) shows top views in the x - y -plane of all four AEI-SAS stages to demonstrate the horizontal positioning. Figure 3.3.2 shows a picture of the west AEI-SAS inside the vacuum system in side view.

The baseplate is stiffly connected to earth and sets the base of the AEI-SAS. It carries three inverted pendulum legs, which form the main horizontal isolation stage. By choosing the correct payload on top, the inverted pendulum stage can be tuned close to instability, granting very low resonance frequencies. As a compromise between low frequency isolation and stability in presence of non-stationary disturbances, 0.1 Hz is chosen as resonance frequency in the horizontal translational degrees of freedom x and y . The resonance frequency of the horizontal rotational degree of freedom rz is strongly dependent on the distance of the payload to the z axis, which changes during assembly of the interferometer. Resonance frequencies between 0.09–0.3 Hz are typical.

The inverted pendulum stage carries the springbox, which consists of two plates interconnected by a stiffening structure. [B⁺17] describes in detail how the softness of the springbox creates internal resonances, disturbing the isolation performance. The west AEI-SAS was equipped with an additional stiffening structure to shift these resonances to higher frequencies and dampen them. The springbox supports three Geometric Anti-Spring (GAS) filters, which provide most of the vertical isolation. They consist of eight blade springs bent horizontally and connected to a key stone in their center. When displaced from rest, the key stone experiences an anti-restoring force resulting from the horizontal tension of the GAS filter blades, which, when carefully tuned, results in very low resonance frequencies. As a compromise between low frequency isolation and stability, 0.3 Hz were chosen for the resonance frequency of the vertical translational degree of freedom z . The vertical rotational degrees of freedom rx and ry depend on the distance of the payload to the corresponding axes x and y . Without further measures they would be very close to instability, which is why an additional stiffening structure is added, shifting the resonances to 0.3–0.5 Hz.

The GAS filters are connected to the intermediate plate, which supports three Viton[®] pads. These were installed to dampen internal resonance of the GAS filters and springbox and provide a second isolation stage in all degrees of freedom above their resonance frequency of ≈ 10 Hz.

The Viton[®] pads carry the optical table, which serves as a base for all main and auxiliary interferometer components installed in the vacuum system. It is stiffened by a honeycomb structure to maintain the distances and orientations of optics, also for higher frequencies.

Besides these mechanical components, there is a multitude of different sensors and actuators installed in each stage of the AEI-SAS. They are presented in section 3.4.

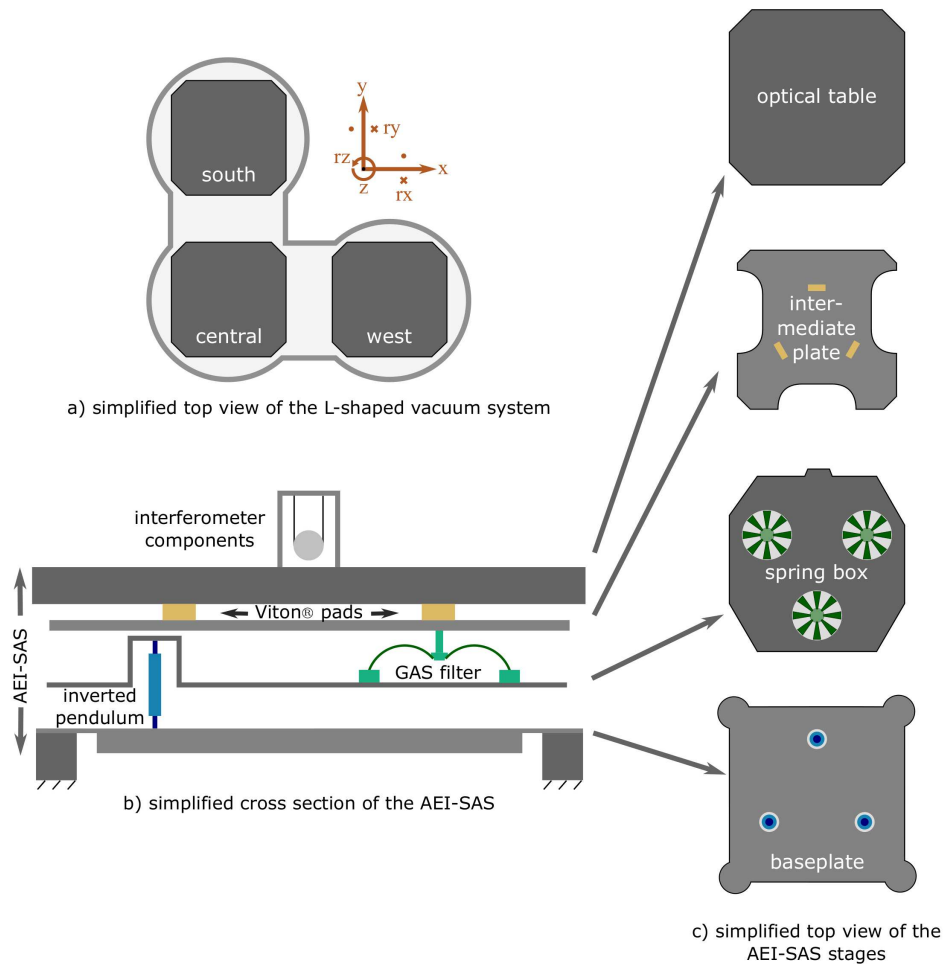


Figure 3.3.1: Schematic drawings of the AEI-SAS illustrating: a) their positions in the vacuum system; b) a side view in the z-x-plane to show the vertical positions of the different stages and passive isolation components; c) top views in the x-y-plane of the different AEI-SAS stages to show the horizontal positions of the passive isolation components. The passive isolators are marked by color in illustration b) and c). The figure is adapted from [K⁺20].

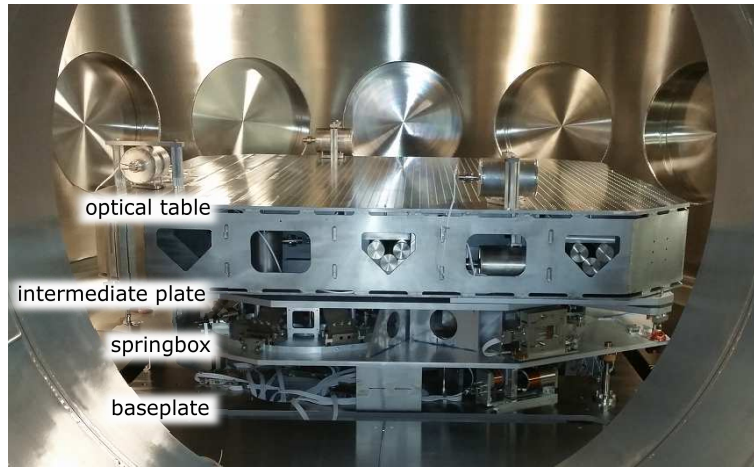


Figure 3.3.2: Picture of the west AEI-SAS after installation inside the vacuum system. The four different stages are visible and labelled. The optical table is only equipped with three horizontal L-4C geophones. Suspensions, auxiliary optics and other interferometer components are not yet installed.

Transmissibility

Figure 3.3.3 shows the transmissibilities of the west AEI-SAS in each degree of freedom. The transmissibilities of the central and south AEI-SAS are similar. For these measurements, the optical table was actively damped in all degrees of freedom but the one under investigation, to reduce cross coupling. In the translational directions x , y and z the transmissibilities are mostly constant over time since the resonance frequencies are mechanically tuned. In the rotational directions rx , ry and rz the resonance frequencies depend on the mass distribution on the AEI-SAS and hence change during the process of setting up the AEI sub-SQL interferometer.

All transmissibilities feature a wide notch above 4 Hz and an increasing magnitude above. These features do not show up in other, indirect measurements of the transmissibilities, like the open loop gain measurement (see figure 3.7.12) and are hence not expected to describe the real behavior.

Cross coupling

Cross coupling can be observed between x and y as well as between rx and ry . This is a result of imperfect mechanical tuning. A fundamental cross coupling exists from x or y motion of the springbox to ry or rx motion of the optical table and vice versa. This cross coupling depends on the stiffness of the GAS filters and is explained in general in figure 3.3.4. On the left, three examples are depicted: Example 1 shows the response of the optical table to a horizontal springbox motion for vertically stiff springs. Example 2 shows the same for low stiffness and example 3 for medium stiffness. The table at the top right shows amplitudes of the four involved variables qualitatively. The diagram at the bottom right shows transfer functions for the three examples from horizontal springbox motion to rotational optical table motion.

These transfer functions can be calculated by

$$T_{x \rightarrow ry} = C_{x \rightarrow ry} \times (1 - T_{ry}), \quad (3.3.1)$$

with $T_{x \rightarrow ry}$ being the transfer function from springbox x motion to optical table ry motion, $C_{x \rightarrow ry}$ being a coupling factor, and T_{ry} being the transfer function of the passively isolated AEI-SAS in ry . The coupling factor depends on some parameters like the vertical distance between springbox and optical table and the stiffness of the GAS filters and defines the height of the plateau above the resonance frequency. The coupling from springbox y motion to optical table rx motion is calculated analogously.

$T_{x \rightarrow ry}$ was analyzed for the AEI-SASs by Sara Al-Kersh, a student of the group at the time of writing, using the Euler-Lagrange-formalism. The calculation did not

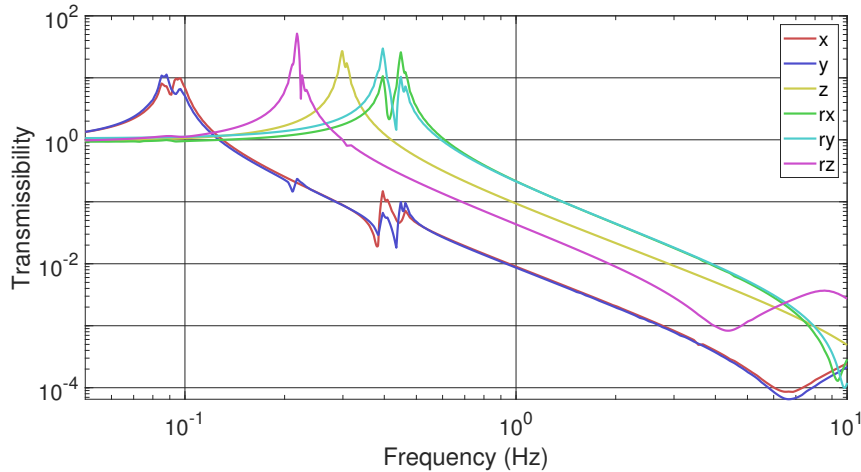


Figure 3.3.3: Transmissibilities from ground motion to optical table motion for the west AEI-SAS. The fundamental resonances are clearly visible. Some smaller resonances indicate cross coupling from other degrees of freedom. The transmissibilities of the central and south AEI-SASs are similar.

include an additional stiffening structure of the AEI-SASs for rx and ry (see [Wan13] and [Ber18]). This resulted in lower resonance frequencies, which were corrected to match reality. The according plateau above the resonance has a value of roughly 0.092 rad/m .

An analogous coupling exists from rotational motion of the springbox to translational motion of the optical table, having the exact same transfer function. Both couplings are used in section 3.7.10 and explain the observed motion of the AEI-SASs in x , y , rx and ry above 6 Hz.

Stiffness optimization

The stiffness values among all inverted pendulum legs and among all GAS filters within one AEI-SAS need to be equal in order to minimize cross couplings.

The stiffness of the inverted pendulum legs is predominantly set by the thickness of their flexures, which can not be adapted after machining. Small differences of the flexures and other mechanical parts result in small misalignment of the inverted pendulum legs from being perfectly straight. This results in different stiffness values for different degrees of freedom and in cross coupling. By rotating all three legs correctly, this can partly be compensated for.

The stiffness of the GAS filters can be tuned by modifying the horizontal compression of the GAS filter blades (see [Ber18]).

During construction and commissioning of the first two AEI-SASs, only little effort was made to optimize the inverted pendulum and GAS filter stiffness. After the installation inside the vacuum system, it became difficult and delicate to redo this optimization, with the result that it was never performed. An optimization was executed for the third (west) AEI-SAS.

Figure 3.3.5 shows the horizontal position changes of the three AEI-SAS optical tables during and after ventilation of the vacuum system. Due to a change in buoyancy, a vertical displacement is expected, but the horizontal positions should stay constant if horizontal stiffnesses are perfectly tuned. The ventilation starts at roughly $t = 300 \text{ s}$ and ends at $t = 950 \text{ s}$. Afterwards, the drifts result from thermalization. The west optical table (solid lines) moves significantly less by roughly a factor 12 compared to the south (dotted lines) and especially the central (dashed lines) optical tables, indicating a significantly better tuned stiffness.

In the vertical rotational degrees of freedom, all three optical tables drift by roughly the same amount. This either indicates that the GAS filter stiffnesses are, in

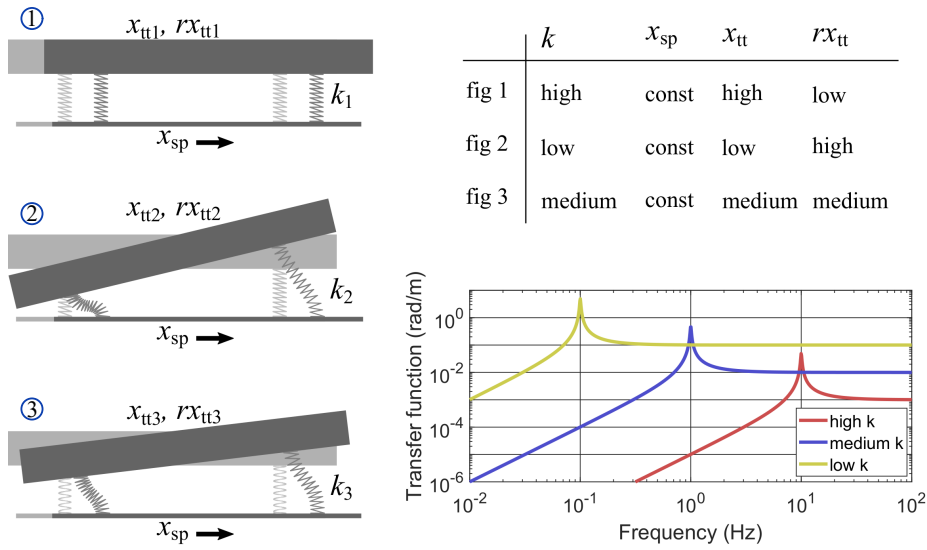


Figure 3.3.4: Graphical and tabular explanations for the fundamental coupling from horizontal motion of the springbox to rotational coupling of the optical table. On the left, three examples are depicted for differently high stiffness of the GAS filters: first with a high stiffness, second with a low stiffness and third with a medium stiffness. Relevant parameters are the stiffness of the GAS filters k , the springbox motion x_{sp} and the translational and rotational optical table motion x_{tt} and rx_{tt} . They are qualitatively summarized in the table at the top right. The diagram at the bottom right shows qualitative transfer functions from x_{sp} to rx_{tt} for the three examples.

fact, equally well tuned, or that the drifts are dominated by a different effect. One promising candidate could be cables hanging from the vacuum system onto the optical tables. Care was taken to hang them in a soft connection but during large changes of the z position, the cables presumably introduce tilt to the optical tables.

Passive isolation performance

Figures 3.3.6 and 3.3.7 show the horizontal and vertical passive isolation performance of the west AEI-SAS. The performances of the central and south AEI-SAS are similar. For comparison, the ground motion in x and z are shown, to demonstrate the attenuation. The resonance frequencies and the $1/f^2$ isolation above resonance are clearly visible. The noise of the readout sensors is shown, indicating that the measurement is limited by readout noise over a wide frequency range. In the horizontal degrees of freedom, the inertial sensors suffer from tilt-to-horizontal coupling, which increases the noise drastically. More detailed information is provided in section 3.4.3.

3.4 Sensors and actuators

Active seismic isolation is based on sensors, measuring the motion of interest and actuators, applying forces to minimize the motion of interest. This section presents the data acquisition and processing and all sensors and actuators utilized in the AEI-SASs in detail.

Figure 3.4.1 displays two illustrations of the AEI-SAS: a) showing a side view in the z - x -plane, to demonstrate the vertical positions of all sensors and actuators and b) showing three top views of the baseplate, springbox and optical table in the x - y -plane, to show the horizontal positions of all sensors and actuators. The baseplate is equipped with three horizontal Linear Variable Differential Transformers (LVDTs) (L_H), measuring the horizontal relative motion between baseplate and springbox. They are co-located with three horizontal voice-coil actuators (V_H), responsible for the

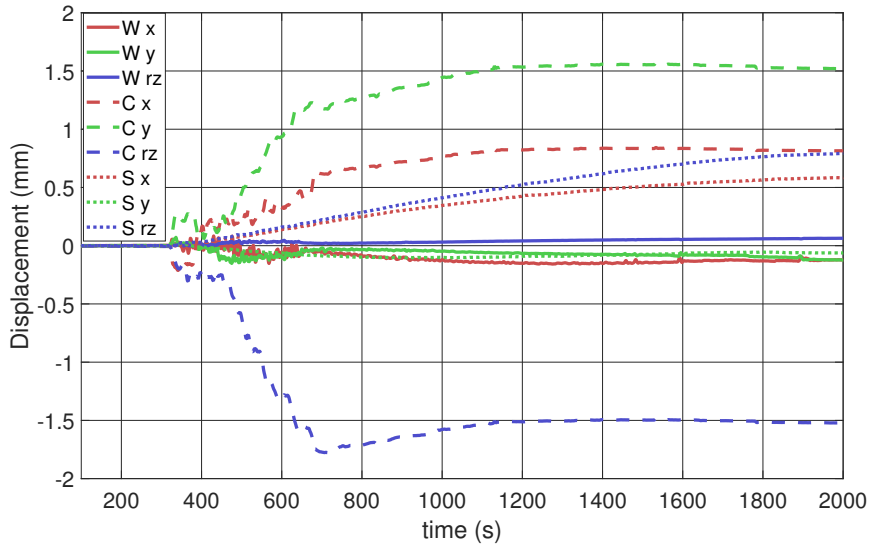


Figure 3.3.5: Displacement of the three AEI-SAS optical tables in the horizontal degrees of freedom during ventilation of the vacuum system. The ventilation starts at roughly $t = 300$ s and ends at $t = 950$ s. Optimally, the optical tables should not move horizontally but only in the z direction due to a changing buoyancy. The west AEI-SAS (solid lines) moves significantly less compared to the south AEI-SAS (dotted lines) and especially the central AEI-SAS (dashed lines).

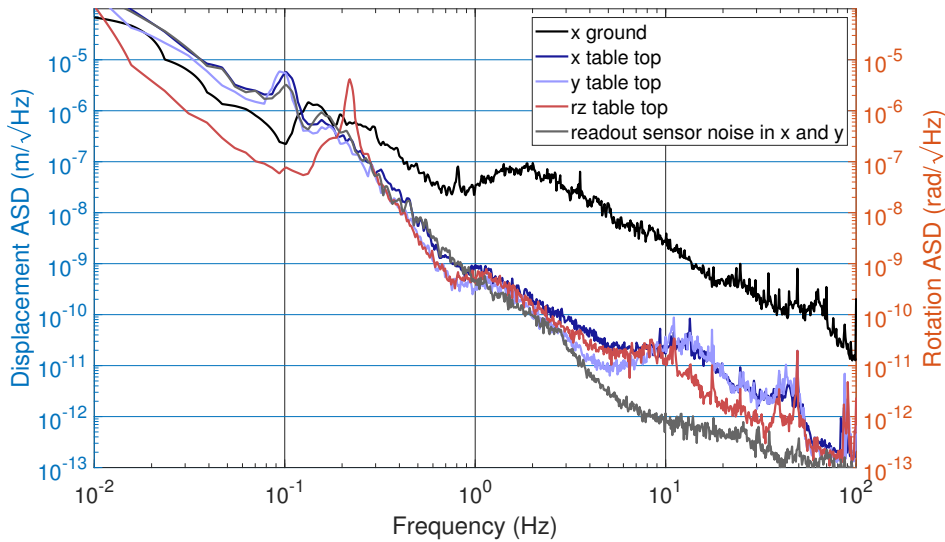


Figure 3.3.6: Passively isolated optical table motion in the horizontal degrees of freedom. The horizontal ground motion, measured with an STS-2, is shown for comparison. The readout sensor noise suffers from tilt-to-horizontal coupling, which limits the measurements below 4 Hz. Each degree of freedom was investigated in separate measurements. The AEI-SAS was free in the degree of freedom under test and actively damped in the other degrees of freedom to reduce cross coupling effects. rz motion is given as a rotation ASD, all other curves are depicted as displacement ASD.

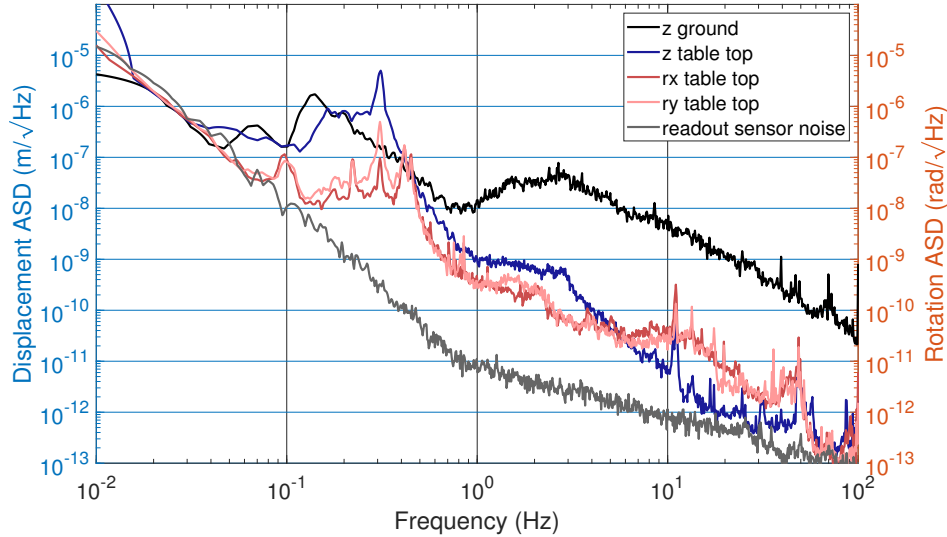


Figure 3.3.7: Passively isolated optical table motion in the vertical degrees of freedom. Below 0.05 Hz the measurements are limited by readout sensor noise. For the z measurement, the AEI-SAS was free in z and actively damped in the other degrees of freedom to reduce cross coupling effects. For the rx and ry measurements, the AEI-SAS was free in all degrees of freedom, which is why cross coupling is visible. Damping the other degrees of freedom introduced broad band noise, masking the actual optical table motion, and was therefore not used. rx and ry motion is given as rotation ASD, all other curves are depicted as displacement ASD.

horizontal feedback loop actuation. Moreover, there are three horizontal motorized springs (B_H) used for the coarse positioning of the optical table in the horizontal directions. These actuators are not used in-loop because of their high noise. All the three mentioned sets of sensors or actuators are separated by 60° and positioned next to the inverted pendulum legs.

Vertical versions of the LVDTs (L_V), voice-coil actuators (V_V) and motorized springs (B_V) are located on the springbox. LVDTs and voice-coil actuators are positioned below the key stone of the GAS filters and are as well separated by 60° . The vertical motorized springs are located at the rim of the table and count four devices. Besides these, three inertial horizontal accelerometers (accs) (A_H) are located in the springbox and measure its inertial motion in all horizontal degrees of freedom x , y and rz .

The optical table carries L-4C geophones [Ser18] in vertical (G_V) and horizontal (G_H) versions. The positions in the figure are only symbolic since space constrains require different positions of the sensors for all three AEI-SASs. A detailed overview of the positioning of the L-4Cs is provided in appendix D. The geophones measure inertial motion of the optical tables in all degrees of freedom. Furthermore, there are optical sensors installed on the AEI-SASs. Optical Levers (OLs) propagate a laser beam from one optical table to another and are read out by a Quadrant Photodiode (QPD) to measure rotations of the optical tables. Suspension Platform Interferometers (SPIs) consist of a Mach-Zehnder interferometer to measure the relative distance between two optical tables. The positions of both optical sensors vary for the different AEI-SASs.

All sensors and actuators, as well as their electronics, are described in detail in the following subsections.

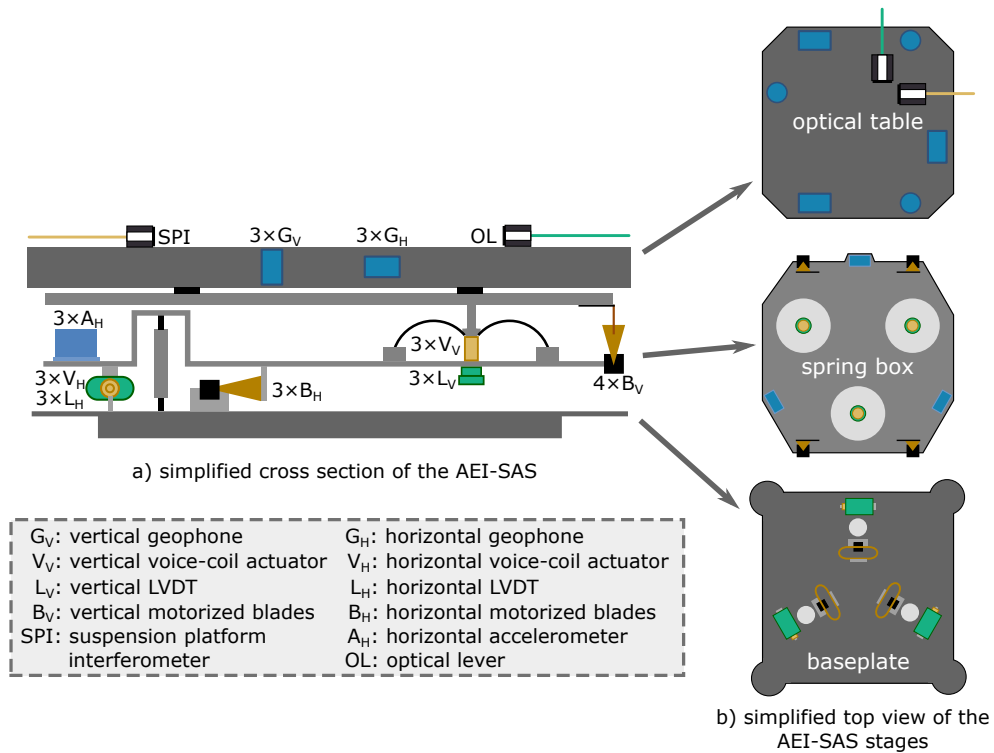


Figure 3.4.1: Schematic drawings of the AEI-SAS illustrating: a) a side view in the z - x -plane to show the vertical positions of the sensors and actuators; b) top views in the x - y -plane of the relevant AEI-SAS stages to show the horizontal positions of the sensors and actuators. Positions and numbers of the geophones, the optical levers and the SPIs are only symbolic and vary for the different AEI-SASs. The figure is adapted from [K⁺20].

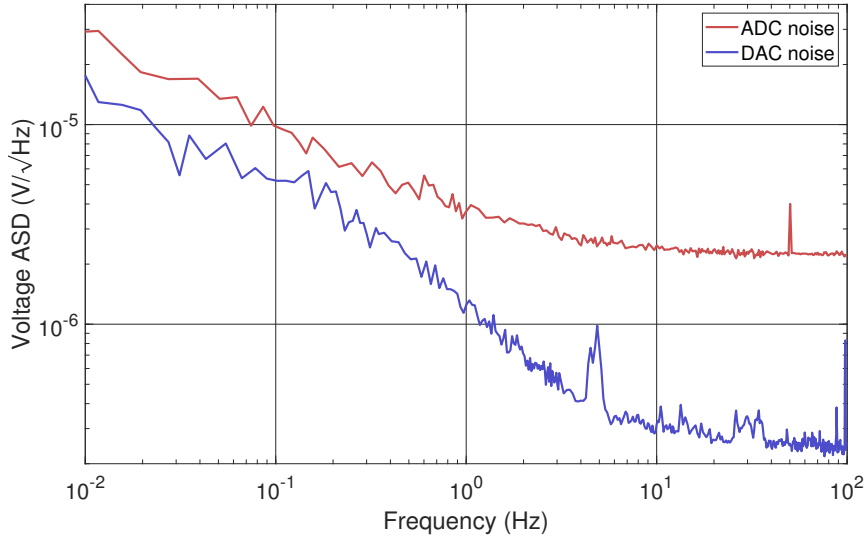


Figure 3.4.2: Measured amplitude spectral densities of ADC and DAC noise. This figure is adapted from [K⁺20].

3.4.1 Data acquisition and processing

Active isolation of the AEI 10 m prototype includes digital processing of the sensor and actuator signals to enable high flexibility and simple testing capabilities. To avoid digitalization noise effects, the analogue sensor signals are applied to Anti-Aliasing (AA) filters. They consist of two Sallen-key low pass filters with a corner frequency of 10 kHz, to filter out high frequency content. Afterwards, the filtered sensor signals are converted by Analogue-to-Digital Converters (ADCs) with a resolution of 16 bits and a sampling rate of 1 kHz, down-sampled from 64 kHz. The digital signals are processed with the Control and Data System (CDS) [BABH01] developed for the LIGO gravitational wave detectors. Digital-to-Analogue Converters (DACs) generate analogue actuation signals, which are filtered by Anti-Imaging (AI) filters to avoid noise effects from this conversion.

The described filters and converters introduce noise to the control loop, summarized as ADC noise for the input and DAC noise for the output, as shown in figure 3.4.2.

The maximal dynamic range of the CDS input for differential signals is ± 20 V, while for the output it is ± 10 V. In digital units of counts, this is equal to ± 32768 counts in the input and output such that

$$\begin{aligned} T_{\text{ADC}} &= 1638.4 \frac{\text{counts}}{\text{V}}, \\ T_{\text{DAC}} &= (3276.8)^{-1} \frac{\text{V}}{\text{counts}}, \end{aligned} \quad (3.4.1)$$

with T being the transfer functions of the ADC and DAC.

3.4.2 Linear Variable Differential Transformer

Functionality

LVDTs measure relative displacement between two stages of the AEI-SAS, using an inductive readout. All relevant variables and parameters within this section are described in table 3.4.1. Figure 3.4.3 shows a schematic drawing of a horizontal LVDT on the left-hand side and a vertical LVDT on the right-hand side. An excitation voltage x_{mod} at a frequency of 15 kHz is applied to an emitter coil, which is connected to the springbox in case of the horizontal LVDT and to the intermediate plate in case

Table 3.4.1: Overview, description and values of all relevant variables and parameters of section 3.4.2 Linear Variable Differential Transformer.

Variable	Description
x_g	translational ground motion
x_{sp}	springbox motion
x_{int}	intermediate plate motion
x_{opt}	optical table motion
δx	relative displacement between two stages
x_{mod}	modulation signal
$x_{LVDTmod}$	modulated LVDT readout signal
x_{LVDT}	demodulated LVDT readout signal

Parameter	Description	Value
T_{ind}	TF from displacement to induced voltage	vertical: 24.7 V/m horizontal: 13.9 V/m
T_{el}	TF of sensing electronics	vertical: 1364 V/V horizontal: 570 V/V
T_{ADC}	TF of ADC	1638.4 counts/V
C_{sense}	calibration filter	vert.: 1.87×10^{-8} m/counts hor.: 7.32×10^{-8} m/counts
\tilde{n}_J	input referred Johnson noise	
\tilde{n}_v	input referred voltage noise	
\tilde{n}_c	input referred current noise	see figures 3.4.6 and 3.4.7
\tilde{n}_{ADC}	input referred ADC noise	
\tilde{n}_{LVDT}	input referred total LVDT noise	
k_B	Boltzmann constant	1.38×10^{-23} J/K
T	temperature	293.15 K
$\Re(Z)$	real part of the receiver coil impedance	vertical: 462 Ω horizontal: 455 Ω

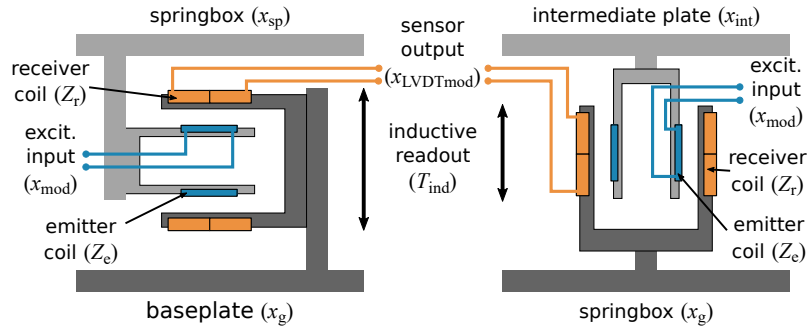


Figure 3.4.3: Schematic drawing of a horizontal (left) and vertical (right) LVDT. The components are labelled with all relevant parameters for the calculation of the LVDT transfer function and sensor noise. The baseplate motion for the horizontal LVDT and the springbox motion for the vertical LVDT are both labelled with ground motion x_g since in the relevant degrees of freedom, both stages move in common with ground.

of the vertical LVDT. A larger receiver coil, consisting of two counter-wound coils, is positioned around the emitter coil. The receiver coil is connected to the baseplate in case of the horizontal LVDT and to the springbox in case of the vertical LVDT. At zero position, both coils are perfectly centered to each other, such that the induction in the counter-wound parts of the receiver coil cancel each other, resulting in zero signal. A relative displacement δx of the two stages along the sensitive direction results in a modulated sensor signal x_{LVDTmod} proportional to the displacement, such that

$$x_{\text{LVDTmod}} = x_{\text{mod}} T_{\text{ind}} \delta x, \quad (3.4.2)$$

with T_{ind} being the transfer function from displacement to the induced voltage. After electrical demodulation with the excitation signal, the sensor signal x_{LVDT} is described by

$$x_{\text{LVDT}} = \frac{x_{\text{LVDTmod}}}{x_{\text{mod}}} = T_{\text{ind}} \delta x. \quad (3.4.3)$$

The LVDT output describes differential horizontal motion between baseplate and springbox for the horizontal version and differential vertical motion between springbox and optical table for the vertical version. Since GAS filters are horizontally stiff, inverted pendulums are vertically stiff and the Viton[®] stage is stiff below 10 Hz, this is approximated to be differential motion between ground and optical table, such that

$$x_{\text{LVDT}} \approx T_{\text{ind}} (x_g - x_{\text{opt}}), \quad (3.4.4)$$

with x_{opt} being the optical table motion.

[T⁺02b] offers detailed information on the design and functionality of LVDTs.

Electronics

LVDT electronics serve several purposes. A simplified overview is provided in figure 3.4.4. It can be divided up into the following stages:

- The **input stage** uses an INA103 differential amplifier [Tex98b] and amplifies the LVDT sensor output by a factor of 31, provides common mode rejection to reduce extrinsic noise sources (see section 2.2), and converts the differential LVDT output to a single-ended output.
- The **local oscillator** processes a 15 kHz sine wave oscillation to provide a modulation signal for the emitter coil of the LVDT and to provide a demodulation signal for the mixer.

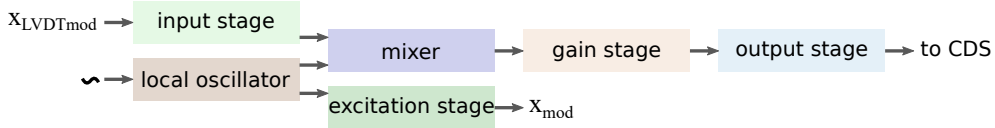


Figure 3.4.4: Overview of the LVDT amplifier electronics, divided up into different stages. The labels and descriptions refer to the explanations given in the text.

- The **excitation stage** converts the single-ended excitation signal from the local oscillator to a differential signal using a THAT1646 [THA15].
- The **mixer** of type AD630 [Ana16b] demodulates the amplified LVDT output using the local oscillator signal and provides a gain of 2.
- The **gain stage** provides a gain of 11 for vertical LVDTs and 4.6 for horizontal LVDTs and utilizes two OP270 operational amplifiers.
- The **output stage** prepares the signal for acquisition with CDS by buffering, converts it to a differential output and adds a gain of 2 using one OP270 and a THAT1646 driver [THA15].

The total gain of the LVDT output signal sums up to 1364 for vertical LVDTs and 620 for horizontal LVDTs. The difference accounts for larger horizontal motion compared to vertical motion, optimizing the dynamical range. Schematics of the electronics are shown in Appendix B.

Noise performance

Figure 3.4.5 shows the block diagram of an LVDT, its electronics and its CDS calibration. The sensor signal and all investigated noise contributions are included, revealing information about the coupling paths of the noise to the signal. The input referred noise \tilde{n}_{LVDT} in $\text{m}/\sqrt{\text{Hz}}$ can be calculated by either following the chain to the left, where differential motion is sensed by the LVDT, or to the right, where the sensor output is calibrated with the controller filter

$$C_{\text{sense}} = (T_{\text{ind}}T_{\text{el}}T_{\text{ADC}})^{-1}, \quad (3.4.5)$$

where T_{ind} is the transfer function of the inductive readout and T_{el} is the transfer function of the sensing electronics. All these transfer functions are flat in the relevant frequency range below 100 Hz and differ slightly in amplitude for the different LVDTs, due to mechanical and electrical differences.

The investigated noise contributions for LVDTs are listed below. The variables and parameters are listed in table 3.4.1.

- Johnson noise, as derived in equation 2.2.2, is present in the receiver coil. The input referred Johnson noise is calculated as

$$\tilde{n}_J = \frac{n_J}{T_{\text{ind}}} = \frac{\sqrt{4k_B T \Re(Z)}}{T_{\text{ind}}}, \quad (3.4.6)$$

with n_J being the Johnson noise at the receiver coil, k_B being the Boltzmann constant, T being the temperature and $\Re(Z)$ being the real part of the receiver coil impedance including and two resistors in the input of the electronics. $\Re(Z)$ is 694Ω for the vertical LVDT and 842Ω for the horizontal LVDT.

- Voltage and current noise is only relevant for the INA103 in the input stage of the sensing path due to its amplification of a factor of 30. Analogous to the Johnson noise, the input referred voltage and current noise contributions are calculated as

$$\tilde{n}_v = \frac{n_v}{T_{\text{ind}}}, \quad (3.4.7)$$

$$\tilde{n}_c = \frac{n_c R}{T_{\text{ind}}}, \quad (3.4.8)$$

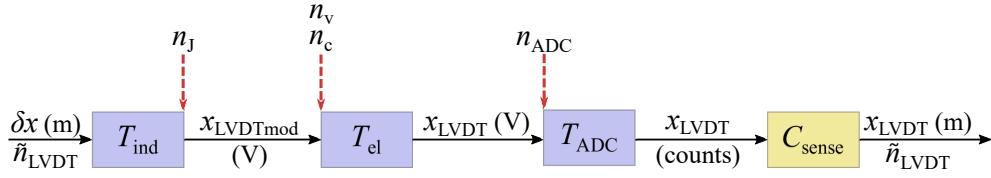


Figure 3.4.5: Block diagram of an LVDT, its electronics and its CDS calibration, displaying the path of the sensor signal and noise contributions.

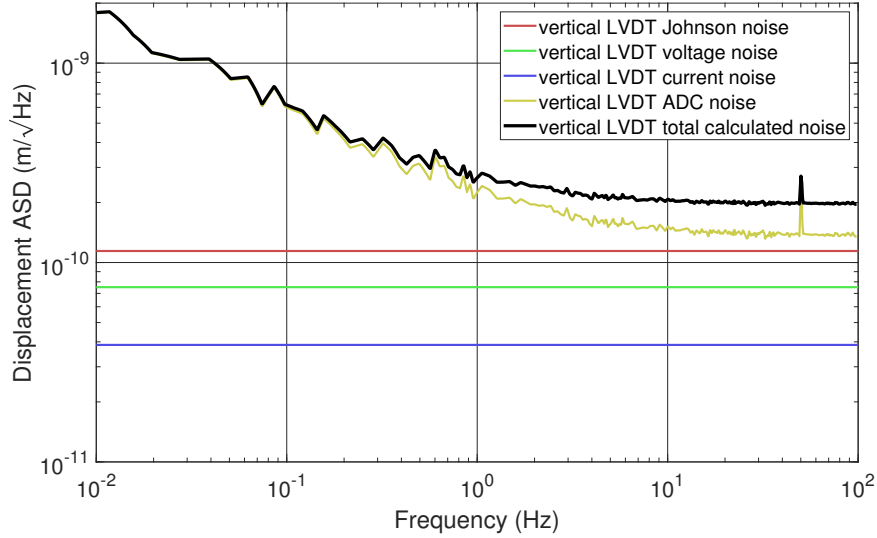


Figure 3.4.6: Input referred noise contributions and total input referred noise of a vertical LVDT. The total noise is limited by ADC noise from 0.01–100 Hz, with Johnson noise contributing significantly above 1 Hz.

with R being the sum of the resistances of the receiver coil and the two input resistors R1 and R2. Amplifier noise in the excitation path is assumed to be negligible.

- ADC noise is presented in section 3.4.1 and adds to the signal in the digitalization process. Its input referred contribution is calculated by

$$\tilde{n}_{ADC} = n_{ADC} T_{ADC} C_{sense}. \quad (3.4.9)$$

Calculations of all noise contributions are shown in figures 3.4.6 and 3.4.7. The total noise is calculated by taking the incoherent sum of all contributions. Both, vertical and horizontal LVDT noise, are limited by ADC noise from 0.01–100 Hz. Above 1 Hz, also Johnson noise contributes significantly to the vertical LVDT total noise.

Seismic contribution to LVDT noise

Seismic motion couples linearly to the LVDT signal, as described in equation 3.4.4. This coupling is a special form of LVDT noise since it varies for different degrees of freedom and with time, and its declaration as noise is frequency dependent. For some degrees of freedom, the active isolation aims at minimizing the inertial AEI-SAS motion, while for other degrees of freedom the relative motion between the optical tables needs to be minimized. This is explained in more detail in section 3.8. In the prior case, the full ground motion is considered as noise since it is a deviation from the inertial frame. In the latter case, ground motion is only considered as noise above some threshold frequency, which is estimated to be 0.3 Hz. This frequency was determined based on different measurements and observations. Below 0.3 Hz,

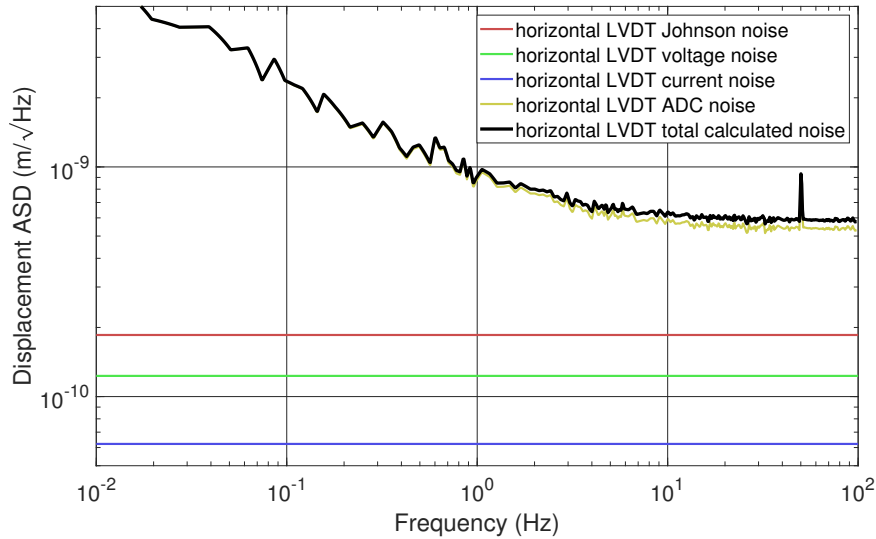


Figure 3.4.7: Input referred noise contributions and total noise of a horizontal LVDT. The total noise is limited by ADC noise over the entire frequency band.

the large period of seismic waves results in common ground motion, affecting all three AEI-SASs equally; hence, ground motion below this threshold does not result in relative optical table motion. Above this frequency the ground motion starts to be uncommon for the different AEI-SASs and the AEI-SAS transmissibilities also start to deviate from each other. Therefore, ground motion creates relative optical table motion above approximately 0.3 Hz and is considered as noise.

Furthermore, the control technique called sensor correction is applied to reduce seismic noise coupling to the LVDT output. Details on the theory and application of sensor correction in the AEI 10 m prototype are discussed in section 3.7.6.

The two different requirements of inertial and relative isolation result in two different LVDT noise curves for vertical and horizontal degrees of freedom each: inertial LVDT noise and relative LVDT noise. Figure 3.4.8 and 3.4.9 show both noise versions for the vertical and horizontal directions, respectively. The figures also include the corresponding ground motion and the LVDT electronic noise.

The dependence on seismic motion results in large variations of the noise over time and degrees of freedom; hence, the shown noise curves are only examples.

3.4.3 Geophone

Functionality

A geophone is an inertial sensor which is based on a harmonic oscillator. Figure 3.4.10 shows a schematic setup. A test mass together with a coil are suspended by a spring. The spring is attached to a case, which is stiffly connected to the surroundings. A magnet is attached to the case and the coil attached to the test mass is wrapped around the magnet. A relative motion between coil and test mass induces a current in the coil which is proportional to their relative velocity. Together with the transfer function of a harmonic oscillator, the overall geophone transfer function has an f^3 slope below resonance and an f slope above.

All relevant variables and parameters for this section are listed in table 3.4.2. In the absence of noise, the geophone signal in units of volts is described by differential motion between ground x_g and test mass x_m multiplied by the inductive readout

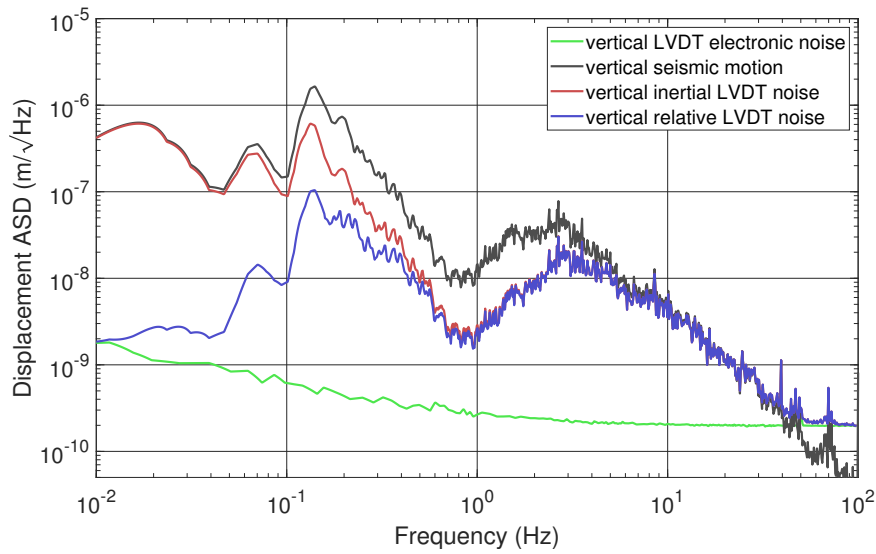


Figure 3.4.8: Input referred inertial and relative noise of a vertical LVDT, including seismic coupling and sensor correction. The inertial LVDT noise deviates from ground motion between 0.04–7 Hz because of sensor correction. This is described in detail in section 3.7.6. The relative noise is strongly reduced at low frequencies, because seismic motion is not considered as noise below 0.3 Hz.

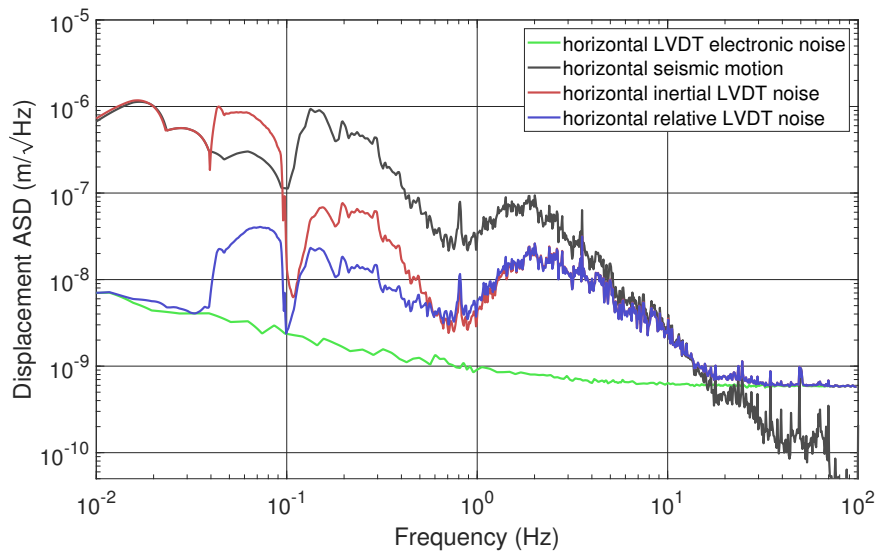


Figure 3.4.9: Input referred inertial and relative noise of a horizontal LVDT, including seismic coupling and sensor correction. The inertial LVDT noise deviates from ground motion between 0.04–7 Hz because of sensor correction. The increased noise between 0.04–0.09 Hz is caused by the ripple of the high pass filter. This is described in detail in section 3.7.6. The relative noise is strongly reduced at low frequencies, because seismic motion is not considered as noise below 0.3 Hz.

Table 3.4.2: Overview, description and values of all relevant variables and parameters of section 3.4.3 Geophone.

Variable	Description	
x_{geo}	geophone signal	
x_{g}	translational ground motion	
x_{m}	test mass motion	
rx_{g}	rotational ground motion	

Parameter	Description	Value
T_{ind}	Inductive readout efficiency	L-22D: 75.5 Vs/m \times f L-4C: 277 Vs/m \times f
T_{HO}	TF of the harmonic oscillator	
f_0	resonance frequency	L-22D: 2 Hz L-4C: 1 Hz
$\omega_0 = 2\pi f_0$	angular resonance frequency	
Q	quality factor	L-22D: 0.5 L-4C: 2
T_{geo}	TF from ground motion to geophone readout	see figure 3.4.11
\tilde{n}_{J}	input referred Johnson noise	
\tilde{n}_{v}	input referred voltage noise	
\tilde{n}_{c}	input referred current noise	see figures 3.4.14 and 3.4.15
\tilde{n}_{s}	input referred suspension thermal noise	
\tilde{n}_{geo}	total input referred geophone noise	
\tilde{n}_{tth}	input referred tilt-to-horizontal noise	see figure 3.4.17
k_{B}	Boltzmann constant	1.38×10^{-23} J/K
T	temperature	293.15 K
$\Re(Z)$	real part of the coil impedance	see figure 3.4.13
m	weight of the test mass	L-22D: 0.073 Kg L-4C: 0.96 Kg
g	gravitational constant	9.81 m/s
T_{HOext}	TF of the HO to external forces	

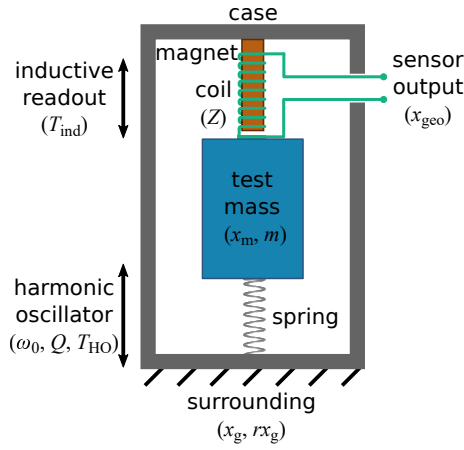


Figure 3.4.10: Schematic drawing of a geophone. The components are labelled with all relevant parameters for the calculation of the geophones transfer function and its sensor noise.

efficiency T_{ind} , as

$$\begin{aligned} x_{\text{geo}} &= (x_m - x_g)T_{\text{ind}}, \\ &= (x_g T_{\text{HO}} - x_g)T_{\text{ind}}, \end{aligned} \quad (3.4.10)$$

with T_{HO} being the transfer function of the harmonic oscillator. The transfer function of the geophone T_{geo} from input signal x_g to readout signal x_{geo} in volts is described by

$$T_{\text{geo}} = \frac{x_{\text{geo}}}{x_g} = (T_{\text{HO}} - 1)T_{\text{ind}}. \quad (3.4.11)$$

Inserting the transfer function of a viscously damped harmonic oscillator from equation 3.1.4 leads to

$$T_{\text{geo}} = \frac{\omega^2}{\omega_0^2 - \omega^2 + \frac{i\omega_0\omega}{Q}} T_{\text{ind}}, \quad (3.4.12)$$

with ω_0 being the resonance frequency, ω being the angular frequency and Q being the quality factor.

There are two different geophone types installed in the AEI-SAS. Vertical L-22D geophones [Ser18] were originally utilized for the vertical inertial isolation. Due to their high noise, additional vertical and horizontal L-4C geophones were installed, having a better signal-to-noise ratio. Table 3.4.2 shows the relevant parameters of both geophone types to calculate their transfer functions, which are shown in figure 3.4.11.

The L-22D geophones were removed from the central AEI-SAS optical table in order to save their mass load. This required major efforts and is described in appendix C. They are still implemented in the south AEI-SAS and can be removed if required, following the same procedures.

Electronics

The geophone amplifier electronics consist of an input stage, which provides common mode rejection to minimize extrinsic noise sources (see section 2.2); further, the input stage converts the differential sensor signal to a single-ended signal and amplifies it. A second stage, called gain stage, adds another frequency independent gain. Comparing the transfer functions of geophones from figure 3.4.11 with the natural slope of seismic noise from figure 2.1.1 shows an inverse behaviour; hence, the geophone acts as a natural whitening filter, which is why additional whitening is not required. The last stage is a differential output stage, buffering the signals.

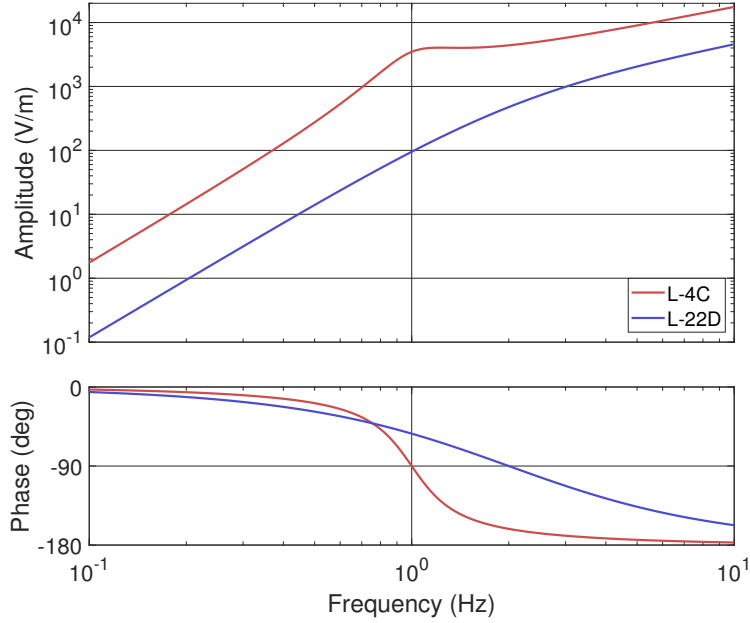


Figure 3.4.11: Transfer functions of the L-4C and L-22D geophones. The L-4C transfer function amplitude is higher, due to a higher inductive readout efficiency T_{ind} and a lower resonance frequency ω_0 .

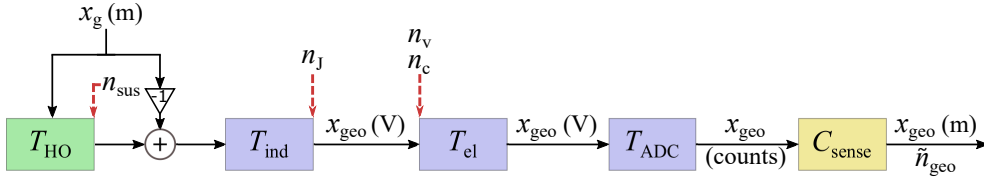


Figure 3.4.12: Block diagram of a geophone, its electronics and its CDS calibration, displaying the path of the sensor signal and noise contributions.

The L-22D geophones are amplified by INA128 differential amplifiers [Tex95] in the input stage, with a gain of 100. In the gain stage, OP270 operational amplifiers [Ana15] add another gain of 9. Differential output is provided by THAT1646 differential drivers [Tex98a], with a gain of 2. This results in an overall gain of 1800. Schematics of the L-22D geophone amplifier electronics are provided in Appendix B.

The L-4C geophones are amplified by a configuration of three OPA188 operational amplifiers [Tex13], with a gain of 101 in the input stage. Another OPA188 amplifies the signal in the gain stage by a factor of 36. Three OPA188 amplifier provide a differential output and add a factor 2, such that the total gain is 7272. Schematics of the L-4C geophone amplifier electronics are provided in Appendix B.

Noise performance

Figure 3.4.12 shows a block diagram of the geophone including all relevant noise contributions, except for tilt-to-horizontal coupling, which is investigated later in this subsection. The other relevant contributions are Johnson noise n_J of the coil, voltage and current noise n_v and n_c of the amplifiers used in the first amplifier stage and viscous suspension thermal noise n_{sus} . For the geophones used in the AEI sub-SQL interferometer, viscous damping is the primary damping source because they are installed inside individual vacuum enclosures filled with air. The parameters required to calculate the noise contributions are provided in table 3.4.2.

- Johnson noise of the geophone coil is present directly in the output of the

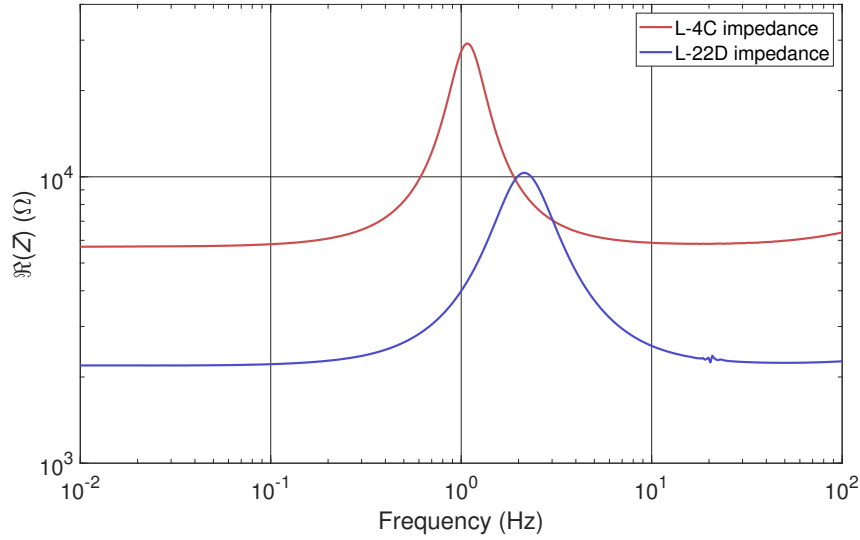


Figure 3.4.13: Real parts of the geophone impedances. A small voltage was applied to the geophones while they were exposed to ground motion in order to measure the impedance. The figure is adapted from [K⁺17].

geophone; hence, the input referred Johnson noise is calculated by dividing n_J by T_{geo} :

$$\tilde{n}_J = \frac{n_J}{T_{\text{geo}}} = \frac{\sqrt{4k_B T \Re(Z)}}{T_{\text{geo}}}. \quad (3.4.13)$$

The real parts of the impedances were measured for the two different geophone types; therefore, a small voltage was applied to the geophones, while they were exposed to ground motion. Figure 3.4.13 shows the results. [Lan05] provides a theoretical derivation of the impedance of geophones. Johnson noise of other resistors is negligibly low.

- Amplifier voltage and current noise are both present at the input of the first operational amplifiers. Due to the gain of the input stage of about 100, noise of other amplifiers does not contribute significantly. The input referred noise is calculated by dividing the voltage noise n_v and current noise n_c by T_{geo} :

$$\tilde{n}_v = \frac{n_v}{T_{\text{geo}}}, \quad (3.4.14)$$

$$\tilde{n}_c = \frac{n_c \Re(Z)}{T_{\text{geo}}}, \quad (3.4.15)$$

According to the data sheet of the INA128 [Tex95], n_v and n_c are $8 \text{ nV}/\sqrt{\text{Hz}}$ and $0.3 \text{ pA}/\sqrt{\text{Hz}}$. Measurements show a lower voltage and current noise of about $4 \text{ nV}/\sqrt{\text{Hz}}$ and $0.15 \text{ pA}/\sqrt{\text{Hz}}$, which will be utilized for further calculations. The data sheet of the OPA188 [Tex13] gives values of $n_v = 8.8 \text{ nV}/\sqrt{\text{Hz}}$ and $n_c = 7 \text{ fA}/\sqrt{\text{Hz}}$ with a corner frequency of the voltage noise at about 0.03 Hz. This corner frequency is remarkably low, which is why the OPA188 is an excellent choice for low frequency seismic measurements. No information about the corner frequency of the current noise is provided. [Hoy16] verifies values for the voltage noise of the OPA188 with measurements, while the setup was not sensitive enough to measure the current noise.

- Suspension thermal noise is not present at the output of the geophone, but at the test mass. For consistency with the other noise sources, it is first propagated to the output and then divided by the geophone transfer function to calculate the input referred noise, such that

$$\tilde{n}_{\text{sus}} = \frac{n_{\text{susv}} T_{\text{ind}}}{T_{\text{geo}}}. \quad (3.4.16)$$

Inserting the viscous suspension thermal noise from equation 2.3.7 and the geophone transfer function from equation 3.4.12 into equation 3.4.16, this yields to

$$\tilde{n}_{\text{sus}} = \frac{1}{\omega^2} \sqrt{\frac{4k_{\text{B}} T \omega_0}{mQ}}, \quad (3.4.17)$$

with k_{B} being the Boltzmann constant and T being the temperature.

The total input referred noise of a geophone \tilde{n}_{geo} is calculated by taking the incoherent sum of the individual contributions. Figures 3.4.14 and 3.4.15 show the individual input referred noise contributions for the L-22D and the L-4C geophones and their total noise. The L-22D is mostly limited by voltage noise from 0.01–100 Hz. Below 0.03 Hz current noise contributes a significant amount of noise, between 1–6 Hz suspension thermal noise is relevant and above 6 Hz Johnson noise is roughly equal to voltage noise. An improvement in total noise could be achieved by using lower noise amplifiers, but since the L-22D geophones were replaced by the L-4C geophones, this change will not be executed. The L-4C geophones are limited equally by Johnson noise of the coil and voltage noise. Only around the resonance frequency of 1 Hz, suspension thermal noise contributes significantly. Compared to L-22D noise, L-4C noise is lower by a factor 10 at 1 Hz, rising to a factor of 100 at 0.01 Hz.

The input referred noise demonstrates that geophones have better performance frequencies above their resonance, while their noise at lower frequencies rises strongly. The noise of horizontal geophones rises even stronger at low frequencies, due to an effect called “tilt-to-horizontal coupling”, which will be explained in the following.

Tilt-to-horizontal coupling

Tilt-to-horizontal coupling describes the effect of tilt motion on horizontal inertial sensors [CJFC⁺12, ME15]. It is a special form of sensor noise, caused by seismic motion. Figure 3.4.16 demonstrates the principle. A tilt of the surroundings and the case of the geophone rx_{g} also tilts the sensitive direction of the sensor; consequently, gravity partly acts along the sensitive direction of the sensor as an external force. The response of the test mass to this force for very small angles is calculated by

$$x_{\text{m}} = mgT_{\text{HOext}} \times rx_{\text{g}}, \quad (3.4.18)$$

with m being the mass, g being the gravitational constant, and T_{HOext} being the response of the harmonic oscillator to an external force as defined in equation 3.1.5. The test mass motion resulting from tilt-to-horizontal coupling is considered as noise. The sensor output resulting from this noise is described by

$$n_{\text{tth}} = mgT_{\text{HOext}} T_{\text{ind}} \times rx_{\text{g}}. \quad (3.4.19)$$

The input referred tilt-to-horizontal noise is again calculated by dividing by the geophone transfer function.

$$\tilde{n}_{\text{tth}} = \frac{n_{\text{tth}}}{T_{\text{geo}}} = \frac{g \times rx_{\text{g}}}{\omega^2}. \quad (3.4.20)$$

Since this noise is dependent on tilt, it varies strongly with the position of the sensor on the AEI-SAS, with the utilized control state, and with time. Figure 3.4.17 shows an exemplary noise budget for horizontal geophones, including tilt-to-horizontal noise. For the calculation of \tilde{n}_{tth} , tilt motion of the AEI-SAS in a “high gain, inertial local control state” was utilized (see section 3.7.1). Tilt-to-horizontal noise strongly limits the sensor’s sensitivity below 2 Hz.

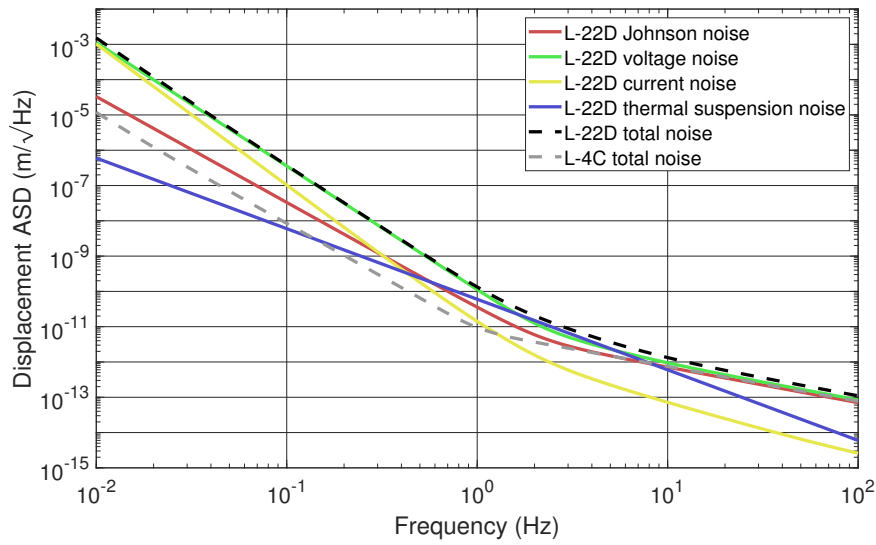


Figure 3.4.14: Input referred noise contributions and total input referred noise of an L-22D geophone. The noise is mostly limited by voltage noise over the entire frequency range of interest. Current noise below 0.03 Hz, suspension thermal noise from 1–6 Hz and Johnson noise above 6 Hz contribute a relevant amount of noise. The total input referred noise of an L-4C geophone using an OPA188 amplifier is shown for comparison.

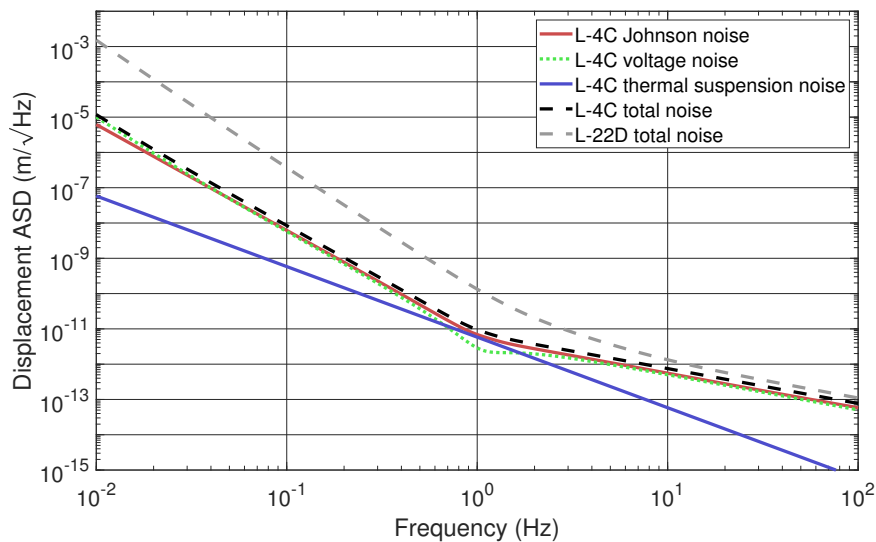


Figure 3.4.15: Input referred noise contributions and total input referred noise of an L-4C geophone. The noise is equally limited by voltage noise and Johnson noise over the entire frequency range of interest, only around the resonance frequency suspension thermal noise contributes significantly. The total input referred noise of an L-22D geophone is shown for comparison.

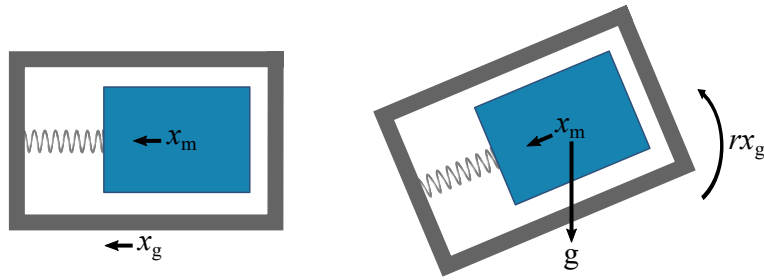


Figure 3.4.16: Visualization of tilt-to-horizontal coupling from tilt of the ground to the sensor output of horizontal inertial sensors. The left-hand side shows the ideal case with purely horizontal motion, while the right-hand side shows the effect of tilt of the ground, where gravity acts along the sensitive direction of the sensor.

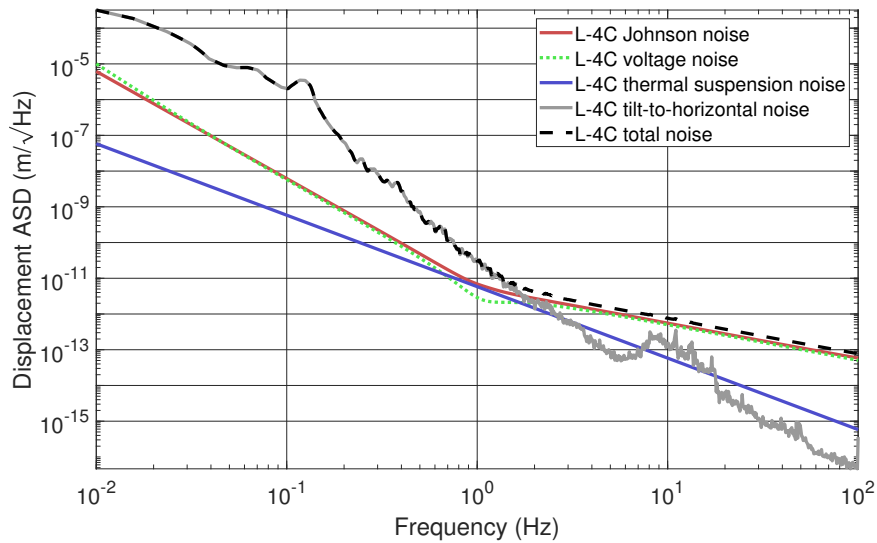


Figure 3.4.17: Input referred noise contributions for an L-4C geophone, including tilt-to-horizontal noise. To get a realistic estimate of tilt-to-horizontal noise, tilt motion of the optical table in a high gain inertial local isolation state (see section 3.7.1) is assumed. Tilt-to-horizontal noise limits the sensor performance below 2 Hz.

3.4.4 Accelerometer

Functionality

An accelerometer is an inertial sensor, which is based on a Watt's linkage. This is a setup, in which a test mass is suspended from a case by a pendulum on one side and an inverted pendulum on the other side. The center of mass of the test mass is tuned to be on the pendulum side, in order to have a stable harmonic oscillator. Tuning the center of mass close to the geometric center between pendulum and inverted pendulum lowers the resonance frequency, which increases the sensitivity. The left-hand side of figure 3.4.18 shows the mechanical setup. All relevant variables and parameters for this section are listed in table 3.4.3.

The transfer function of a structurally damped harmonic oscillator is derived in section 3.1. Analogous to equations 3.4.10–3.4.12 for the geophone, the transfer function from ground motion to relative motion between test mass and ground is described by

$$\frac{x_g - x_m}{x_g} = \frac{-\omega^2}{\omega_0^2 - \omega^2 + \frac{i\omega_0^2}{Q}}. \quad (3.4.21)$$

The relative motion is read out by a small LVDT (see section 3.4.2). Different to the inductive readout of the geophone, the LVDT readout is frequency independent, which results in a lower increase of the accelerometer noise towards low frequencies.

The accelerometer is operated in a force-feedback configuration, which is based on a feedback control as explained in section 3.2.1. Figure 3.4.18 shows a block diagram. Ground motion, which is the signal to be measured, is incident on the Watt's linkage. The relative motion between the test mass and ground motion is measured by an LVDT and the sensor output is processed by a controller. The controller output is used as the feedback signal to minimize the relative motion between test mass and ground. This way, very small linear dynamic ranges of the LVDT are required. The sensor output x_{acc} consists of the residual motion x_{res} , measured by the LVDT, and the feedback signal x_{sup} that describes the suppressed motion. Both, x_{res} and x_{sup} , are calibrated to equivalent ground motion in $\text{m}/\sqrt{\text{Hz}}$ using the additional calibration filters C_{res} and C_{sup} .

C_{res} is calculated by neglecting the feedback signal x_{fb} . For x_{res} it is required that

$$\begin{aligned} x_{\text{res}} &= (x_g T_{\text{HO}} - x_g) T_{\text{LVDT}} C_{\text{res}} \stackrel{!}{=} x_g, \\ \Rightarrow C_{\text{res}} &= \frac{1}{(T_{\text{HO}} - 1) T_{\text{LVDT}}}. \end{aligned} \quad (3.4.22)$$

C_{sup} is defined, such that the accelerometer output is calibrated to ground motion, leading to

$$\begin{aligned} x_{\text{acc}} &= x_{\text{res}} + x_{\text{sup}}, \\ &= [(x_g - x_{\text{fb}}) T_{\text{HO}} - x_g] T_{\text{LVDT}} (C_{\text{res}} + C C_{\text{sup}}) \stackrel{!}{=} x_g, \end{aligned} \quad (3.4.23)$$

where C is the controller filter and x_{fb} is the feedback signal, calculated by

$$\begin{aligned} x_{\text{fb}} &= ((x_g - x_{\text{fb}}) T_{\text{HO}} - x_g) T_{\text{LVDT}} C T_{\text{a}}, \\ \Rightarrow x_{\text{fb}} &= \frac{x_g T_{\text{LVDT}} C T_{\text{a}} (T_{\text{HO}} - 1)}{1 + G}. \end{aligned} \quad (3.4.24)$$

The open loop gain G is described by

$$G = T_{\text{HO}} T_{\text{LVDT}} C T_{\text{a}}. \quad (3.4.25)$$

Inserting equations 3.4.22, 3.4.24 and 3.4.25 into equation 3.4.23 and reordering the equation results in

$$C_{\text{sup}} = \frac{G}{(T_{\text{HO}} - 1) T_{\text{LVDT}} C} = \frac{T_{\text{HO}} T_{\text{a}}}{T_{\text{HO}} - 1}. \quad (3.4.26)$$

Table 3.4.3: Overview, description and values of all relevant variables and parameters of section 3.4.4 Accelerometer.

Variable	Description
x_g	translational ground motion
x_m	test mass motion
x_{acc}	accelerometer output signal
x_{res}	accelerometer residual motion signal
x_{sup}	accelerometer suppressed motion signal
x_{fb}	accelerometer feedback signal
rx_g	rotational ground motion

Parameter	Description	Value
T_{HO}	TF of the harmonic oscillator	
ω_0	angular resonance frequency	≈ 0.4 Hz
Q	quality factor	40
C_{res}	residual motion calibration filter	see figure 3.4.19
C_{sup}	suppressed motion calibration filter	
T_{LVDT}	TF of the accelerometer sensing path	
T_a	TF of the accelerometer actuation path	
C	controller filter	
G	open loop gain	see figure 3.4.20
T_{ind}	TF of the inductive LVDT readout	vertical: 23.9 V/m horizontal: 14.6 V/m
T_{els}	TF of the sensing electronics	9534 V/V
T_{ADC}	TF of the ADC	1638.4 counts/V
T_{DAC}	TF of the DAC	1/3276.8 V/counts
T_{ela}	TF of the actuation electronics	1/1325 A/V
T_{act}	TF of actuation in m/N	
\tilde{n}_J	input referred Johnson noise	
\tilde{n}_v	input referred voltage noise	
\tilde{n}_c	input referred current noise	
\tilde{n}_s	input referred suspension thermal noise	see figures 3.4.22
\tilde{n}_{ADC}	input referred ADC noise	
\tilde{n}_{DAC}	input referred DAC noise	
\tilde{n}_{acc}	total input referred accelerometer noise	
n_{res}	residual motion path noise	
n_{sup}	suppressed motion path noise	
n_{fb}	feedback signal noise	
k_B	Boltzmann constant	1.38×10^{-23} J/K
T	temperature	293.15 K
$\Re(Z)$	real part of the coil impedance	1482 Ω
T_{fbi}	TF of the force-feedback loop for noise i	
\tilde{n}_{tth}	tilt-to-horizontal noise	see figure 3.4.23
g	gravitational constant	9.81 m/s

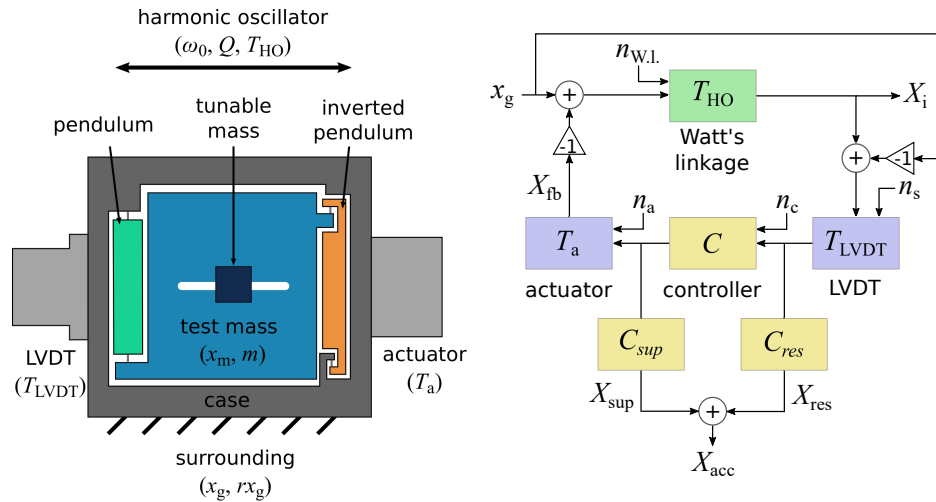


Figure 3.4.18: left: Schematic drawing of the accelerometer mechanics. The components are labelled with all relevant parameters for the calculation of the accelerometers transfer function and its sensor noise. The test mass, suspended by a pendulum on one side and an inverted pendulum on the other side, forms a Watt's linkage. The center of mass can be shifted to tune the Watt's linkage close to instability, to achieve a low frequency resonance.

right: Block diagram of the control loop of the accelerometer. The accelerometer is operated in a force-feedback configuration. Ground motion is incident on the Watt's linkage. The relative motion between the plant and the case is measured by an LVDT. This signal is processed by a controller and sent to a voice-coil actuator that locks the test mass to its null position. The residual motion measured by the LVDT is $X_{res} = x_{res} + n_{res}$, with the residual signal x_{res} and the noise n_{res} . The suppressed motion by the actuator is $X_{sup} = x_{sup} + n_{sup}$, with the suppressed signal x_{sup} and the noise n_{sup} . Both are combined to form the accelerometer output $X_{acc} = x_{acc} + n_{acc}$, with the measured signal x_{acc} and the noise n_{acc} , which resembles ground motion x_g .

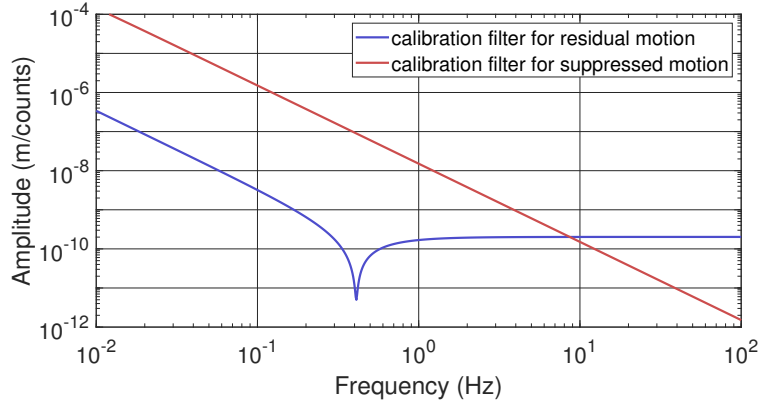


Figure 3.4.19: Transfer function amplitudes of the calibration filters C_{res} and C_{sup} for the accelerometer.

C_{res} and C_{sup} were measured and fitted for each accelerometer, with the results shown in figure 3.4.19. The open loop gain G is shown in figure 3.4.20. The loop has a unity gain frequency of 20.86 Hz with a phase margin of 49° .

The design of these monolithic, custom-made accelerometers is described in more detail in [BDF⁺05, Ber01]

Electronics

The electronics of the accelerometers are mostly the same as of the LVDT (see section 3.4.2) and the voice-coil actuator (see section 3.4.8), resulting from the fact that an LVDT reads out the test mass position and a voice-coil actuator stabilizes it.

The input stage provides a gain of 121, using the differential amplifier INA103 [Tex98b]. The mixer provides a gain of 2, the gain stage has a gain of 1 in the relevant frequency band and the output stage provides a gain of 39.4. This results in an overall gain of 9534 for the accelerometer sensing electronics. The gain of the actuation electronics is $1/1325$ A/V in the relevant frequency range. The schematics are provided in Appendix B.

Noise performance

All noise contributions of the accelerometer couple to both, the residual motion signal X_{res} and the suppressed motion signal X_{sup} . Figure 3.4.21 shows another block diagram of the accelerometer force-feedback configuration, but with a focus on all relevant noise contributions. The total input referred accelerometer noise is labelled with \tilde{n}_{acc} . The sum of all noise sources in the residual motion signal and the suppressed motion signal are labelled with n_{res} and n_{sup} and the noise of the feedback signal is named n_{fb} . T_{ind} , T_{els} and T_{ADC} are the transfer functions of the inductive readout, the amplifier electronics in the sensing path and the ADC, which were formerly summarized as T_{LVDT} . Similarly, the transfer functions of the DAC T_{DAC} , the amplifier electronics in the actuation path T_{ela} , and the actuator T_{act} were formerly summarized as T_{a} .

The relevant noise contributions are described and calculated in the following. The relevant variables and parameters are listed in table 3.4.3.

- Johnson noise of the receiver coil is described by

$$\tilde{n}_{\text{J}} = \frac{n_{\text{J}}}{T_{\text{fbJ}}} = \frac{\sqrt{4k_{\text{B}}T\Re(Z)}}{T_{\text{fbJ}}}, \quad (3.4.27)$$

where \tilde{n}_{J} is the input referred Johnson noise, n_{J} is the Johnson noise at its source, T_{fbJ} is the transfer function of the feedback loop for the Johnson noise, k_{B} is the Boltzmann constant, T is the temperature and $\Re(Z)$ is the real part of the impedance, including two input resistors of the electronics.

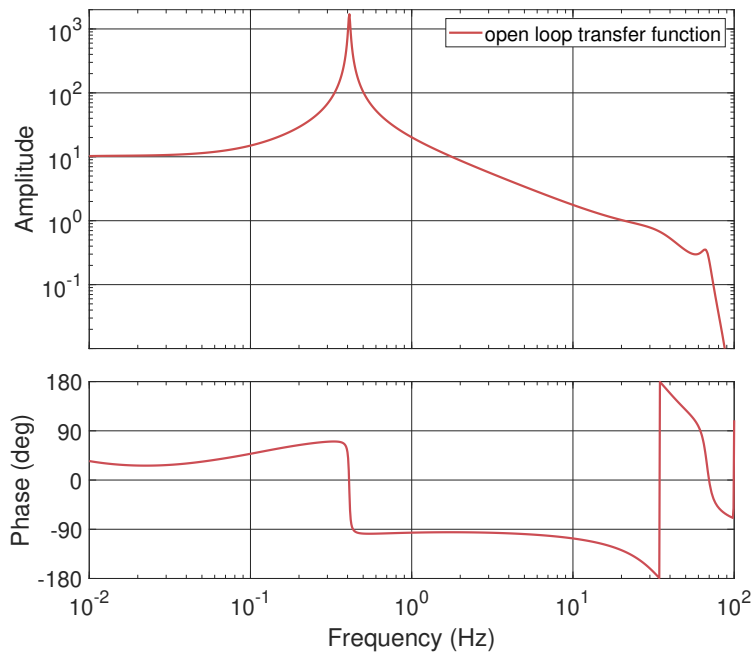


Figure 3.4.20: Open loop transfer function of the internal feedback loop of the accelerometer. The unity gain frequency is at 21 Hz with a phase margin of 51° .

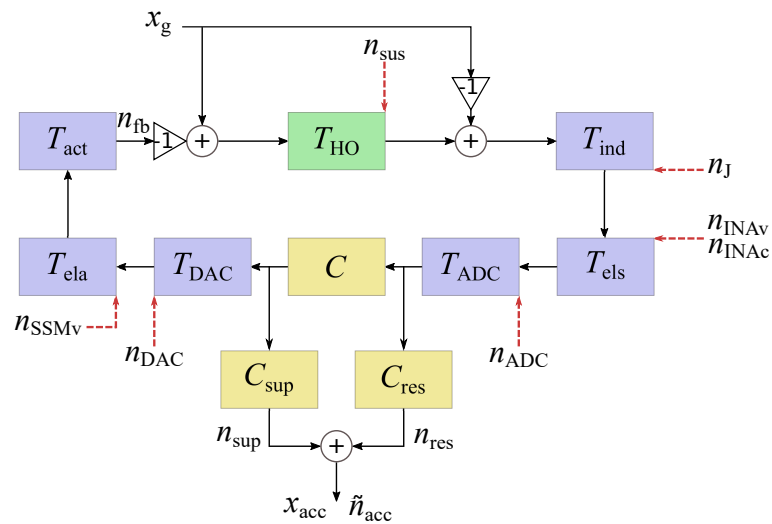


Figure 3.4.21: Block diagram of the accelerometer force-feedback configuration, including all relevant noise contributions.

- Amplifier noise is relevant for the INA103 in the sensing path and for the SSM2141 in the actuation path. Voltage noise of both amplifiers is provided by the manufacturer, while current noise is only provided for the INA103. The input referred noise contributions are described by

$$\begin{aligned}\tilde{n}_{\text{INAv}} &= \frac{n_{\text{INAv}}}{T_{\text{fbINA}}}, \\ \tilde{n}_{\text{INAc}} &= \frac{n_{\text{INAc}}R}{T_{\text{fbINA}}}, \\ \tilde{n}_{\text{SSMv}} &= \frac{n_{\text{SSMv}}}{T_{\text{fbSSM}}},\end{aligned}\quad (3.4.28)$$

with n_{INAv} , n_{INAc} and n_{SSMv} being the voltage and current noise of the INA103 [Tex98b] and SSM2141 [Ana07]. T_{fbINA} and T_{fbSSM} are the transfer functions of the force-feedback loop for the INA103 and SSM2141 noise. R is the effective resistance of the receiver coil and the input resistors of the electronics (see figure B.0.1).

- Suspension thermal noise of the accelerometer is dominated by structural damping, as described in equation 2.3.8. The input referred suspension thermal noise is calculated as

$$\tilde{n}_{\text{sus}} = \frac{n_{\text{suss}}}{T_{\text{fbsus}}} = \sqrt{\frac{4k_{\text{B}}T\omega_0^2}{mQ\omega} \times \left[(\omega_0^2 - \omega^2)^2 + \frac{\omega_0^4}{Q^2} \right]^{-1}} \times \frac{1}{T_{\text{fbsus}}}, \quad (3.4.29)$$

with n_{suss} being the structural suspension thermal noise and T_{fbsus} being the transfer function of the force-feedback loop for the suspension thermal noise.

- ADC and DAC noise is presented in section 3.4.1. Their input referred noise contributions are described by

$$\begin{aligned}\tilde{n}_{\text{ADC}} &= \frac{n_{\text{ADC}}}{T_{\text{fbADC}}}, \\ \tilde{n}_{\text{DAC}} &= \frac{n_{\text{DAC}}}{T_{\text{fbDAC}}},\end{aligned}\quad (3.4.30)$$

with T_{fbADC} and T_{fbDAC} being the transfer functions of the force-feedback loop for the ADC and DAC noise.

The transfer functions of the force-feedback loop T_{fb} for each noise contribution is calculated exemplarily for the ADC noise. The ADC noise contributions to n_{res} and n_{sup} are added coherently, described by

$$\tilde{n}_{\text{acc}} = n_{\text{res}} + n_{\text{sup}}. \quad (3.4.31)$$

Considering only ADC noise, n_{res} is described by

$$n_{\text{res}} = (n_{\text{ADC}} - n_{\text{fb}}T_{\text{HO}}T_{\text{ind}}T_{\text{els}})T_{\text{ADC}}C_{\text{res}}. \quad (3.4.32)$$

The corresponding noise of the feedback signal is calculated as

$$\begin{aligned}n_{\text{fb}} &= n_{\text{ADC}}T_{\text{ADC}}CT_{\text{DAC}}T_{\text{ela}}T_{\text{act}} - n_{\text{fb}}G, \\ \Rightarrow n_{\text{fb}} &= \frac{n_{\text{ADC}}T_{\text{ADC}}CT_{\text{DAC}}T_{\text{ela}}T_{\text{act}}}{1 + G},\end{aligned}\quad (3.4.33)$$

which results in a coupling of ADC noise to the residual motion signal of

$$n_{\text{res}} = n_{\text{ADC}}T_{\text{ADC}}C_{\text{res}} \left(1 - \frac{G}{1 + G} \right). \quad (3.4.34)$$

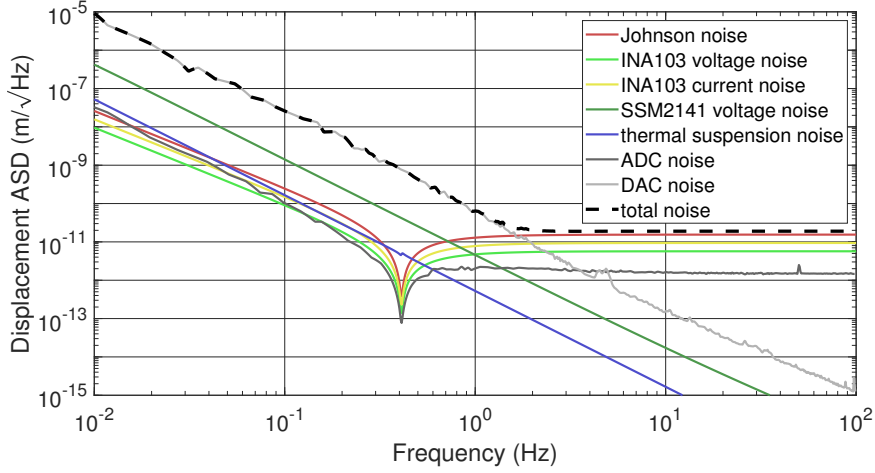


Figure 3.4.22: Input referred noise contributions and total noise of an accelerometer. Every noise source includes its coupling to the residual motion and the suppressed motion. DAC noise limits the total noise below 1.7 Hz, while Johnson noise limits above.

The coupling of ADC noise to the suppressed motion signal is described by

$$\begin{aligned} n_{\text{sup}} &= n_{\text{res}} \frac{CC_{\text{sup}}}{C_{\text{res}}}, \\ &= n_{\text{ADC}} T_{\text{ADC}} CC_{\text{sup}} \left(1 - \frac{G}{1+G}\right). \end{aligned} \quad (3.4.35)$$

The transfer function of the force-feedback loop for the ADC noise is described by inserting equations 3.4.34 and 3.4.35 into equation 3.4.31 and dividing by n_{ADC} , such that

$$T_{\text{fbADC}} = (C_{\text{res}} + CC_{\text{sup}}) T_{\text{ADC}} \left(1 - \frac{G}{1+G}\right). \quad (3.4.36)$$

T_{fb} is calculated for each noise source and inserted into the equations derived within this section, together with the values from table 3.4.1. This results in a total noise as shown in figure 3.4.22. The individual contributions describe the sum of their coupling to the residual motion and suppressed motion signal. Below 1.7 Hz, DAC noise is the limiting noise source, above 1.7 Hz it is Johnson noise. ADC noise is, in principle, not fundamental for the sensor. By increasing the gain in the sensing electronics, the ADC noise would decrease linearly by the same factor. Johnson noise could be reduced by removing the resistors R1 and R2 in the input. Both changes would not improve the overall active isolation performance significantly, since electronic accelerometer noise is not limiting the seismic isolation. This is proven in section 3.8.3.

Tilt-to-horizontal coupling

Same as the horizontal geophones, accelerometers suffer from coupling of tilt motion of the ground to horizontal translation of the test mass, called tilt-to-horizontal noise. The input referred tilt-to-horizontal noise for the accelerometer is described by

$$\tilde{n}_{\text{tth}} = \frac{mgT_{\text{HOext}} \times rx_{\text{g}}}{T_{\text{fbtth}}}, \quad (3.4.37)$$

with T_{HOext} being the transfer function of a harmonic oscillator to an external force, as described in equation 3.1.5, rx_{g} being the rotation of the ground, and T_{fbtth} being the transfer functions of the force-feedback loop for the tilt-to-horizontal noise.

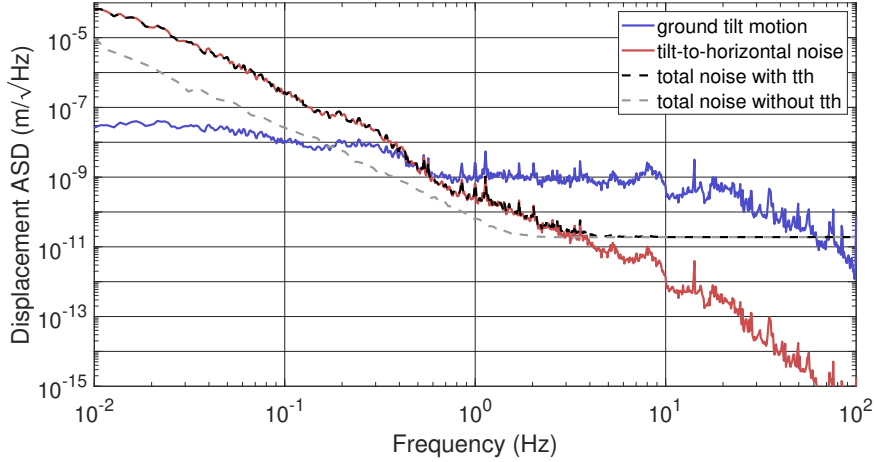


Figure 3.4.23: Ground tilt motion, input referred tilt-to-horizontal noise and total accelerometer noise with and without tilt-to-horizontal motion.

Analogously to equation 3.4.36, this is given by

$$T_{\text{fbtth}} = (C_{\text{res}} + CC_{\text{sup}})T_{\text{ind}}T_{\text{els}}T_{\text{ADC}}\left(1 - \frac{G}{1+G}\right). \quad (3.4.38)$$

Figure 3.4.23 shows the rotational ground motion rx_g , as presented in section 2.1, the input referred tilt-to-horizontal noise, the total accelerometer noise without tilt coupling and the total accelerometer noise with tilt coupling. \tilde{n}_{tth} limits the total noise below 3 Hz.

3.4.5 STS-2 seismometer

Functionality

The Streckeisen Seismometer 2 (STS-2) [AG95] is a triaxial force-feedback sensor capable of measuring motion in all three translational degrees of freedom. Figure 3.4.24 shows a schematic view of the mechanical setup as presented in [Wie12]. Three inverted pendulums have a rest position at 54.7° relative to the surface and are held in position with a force-feedback loop as described for the accelerometers in section 3.4.4. Motion of the three test masses is measured in the directions of u , v and w . The resulting signals are processed internally and converted into the Cartesian degrees of freedom as described by the equation

$$\begin{pmatrix} x \\ y \\ z \end{pmatrix} = \frac{1}{\sqrt{6}} \begin{pmatrix} -2 & 1 & 1 \\ 0 & \sqrt{3} & -\sqrt{3} \\ \sqrt{2} & \sqrt{2} & \sqrt{2} \end{pmatrix} \times \begin{pmatrix} u \\ v \\ w \end{pmatrix}. \quad (3.4.39)$$

Electronics

The force-feedback electronics and a calibration of the signal is provided by the manufacturer and is implemented in the interior of the STS-2. It is described in the STS-2 manual [AG95] but not further investigated in the scope of this thesis.

Noise performance

The STS-2 noise was measured at the Conrad Observatory in Austria and the Albuquerque Seismological Laboratory [RSHG14] with very similar results. Figure 3.4.25 shows a fit to their measurement data, converted to units of $\text{m}/\sqrt{\text{Hz}}$.

Tilt-to-horizontal coupling

Tilt-to-horizontal coupling is described in section 3.4.3 and affects the STS-2 in the horizontal degrees of freedom. Figure 3.4.26 shows the resulting noise. The calculation includes ground motion in tilt direction as shown in figure 2.1.2.

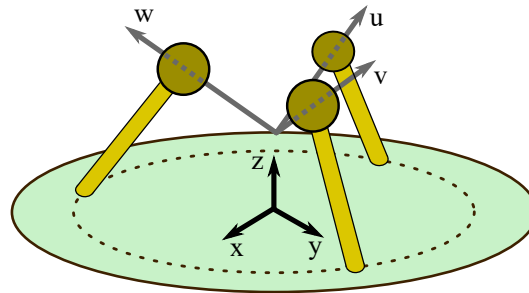


Figure 3.4.24: Schematic drawing of an STS-2 seismometer from Streckeisen [AG95] as presented in [Wie12]. It consists of three identical inverted pendulums at an angle of 54.7° relative to the surface. They are read out in the directions of u , v and w and hold in position by a force-feedback loop.

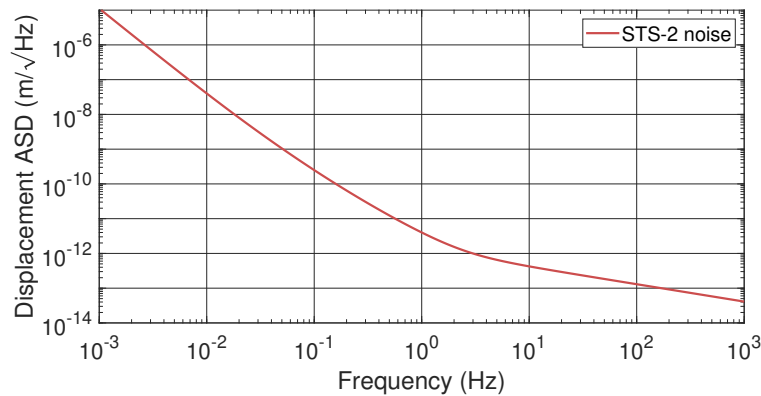


Figure 3.4.25: Fit to the measured noise of an STS-2 by the Conrad Observatory in Austria and the Albuquerque Seismological Laboratory [RSHG14].

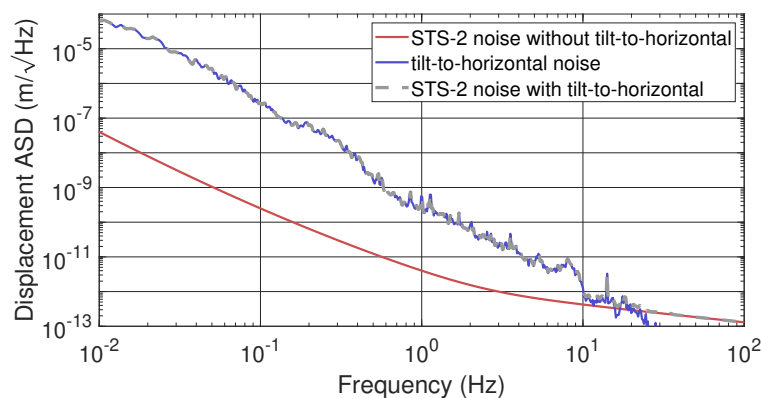


Figure 3.4.26: STS-2 noise, tilt-to-horizontal noise and the total STS-2 noise including tilt-to-horizontal noise. The STS-2 noise without tilt-to-horizontal coupling is a fit to measurements by the Conrad Observatory in Austria and the Albuquerque Seismological Laboratory [RSHG14]. In the horizontal degrees of freedom, the STS-2 is limited by tilt-to-horizontal coupling below ≈ 20 Hz.

Table 3.4.4: Overview, description and values of all relevant variables and parameters of section 3.4.6 Optical lever.

Variable	Description	
Q_i	QPD quadrant number i	
$rx_p; rx_y$	rotational ground motion in pitch or yaw	
δx	differential translational motion between two AEI-SAS	

Parameter	Description	Value
T_{ij}	TF from rx_g to beam displacement on QPD	$\pm l$
l	length of the lever	11.5 m
T_{QPD}	TF from beam motion on QPD to current	
T_{el}	TF of the electronics	see figure 3.4.29
C_{cal}	optical lever calibration filter	
T_{ADC}	TF of the ADC	
Q_{sum}	sum of calibrated signal of all four quadrants	
\tilde{n}_{sh}	input referred shot noise	
\tilde{n}_{v}	input referred voltage noise	see figures 3.4.30
\tilde{n}_{ADC}	input referred ADC noise	
\tilde{n}_{OL}	total input referred optical lever noise	
\tilde{n}_{x}	translational motion noise	see figure 3.4.31
e	elementary charge	1.6022×10^{-19} C
I	photocurrent	$17.26 \mu\text{A}$
$R1$	input resistor of electronics	33 k Ω
k_{B}	Boltzmann constant	1.38×10^{-23} J/K
T	temperature	293.15 K

3.4.6 Optical lever

Description

Optical levers measure rotations of the optical tables by utilizing an inter-table setup. A laser beam propagates from the optical table of one AEI-SAS to a second AEI-SAS, where its position is detected with a QPD. The signal contains the rotation of the initial AEI-SAS, amplified by the lever of roughly 11.5 m and the relative translations between both AEI-SAS, which are not amplified by the lever. This grants a high sensitivity for rotations. Table 3.4.4 lists all relevant variables and parameters for this section.

Figure 3.4.27 shows the optical lever arrangement for all three AEI-SAS. South and west AEI-SAS have one optical lever to measure two rotational degrees of freedom. The central AEI-SAS has two optical levers, one propagating to the west and one to the south; hence, all three rotational degrees of freedom are sensed. Expressed in degrees of freedom typically used for mirrors, all optical tables are sensed in pitch and yaw with reference to the interferometer mirrors they support. The central AEI-SAS has two pitch degrees of freedom, called “pitch to south” and “pitch to west”, because it supports two interferometer mirrors.

Figure 3.4.28 shows a block diagram of an optical lever, including the noise sources and the calculation path to pitch and yaw measurements. The rotational motion rx_i couples to the quadrants of the QPD by displacing the laser beam from its center.

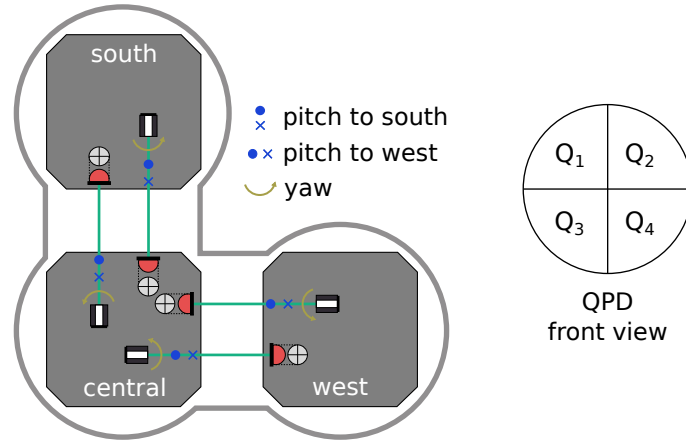


Figure 3.4.27: left: Setup of the optical levers for all three AEI-SASs. The sensitive degrees of freedom are indicated in color. The south and west AEI-SAS have one optical lever to measure two rotational degrees of freedom, while the central AEI-SAS has two optical levers measuring all three rotational degrees of freedom. The measurement of horizontal rotation of the central AEI-SAS of one optical lever is redundant. right: Labelling of the QPD quadrants.

Table 3.4.5: Sign of coupling factor T_{ij} , which describes the transfer function from AEI-SAS rotation to the signal on the optical lever QPD quadrants.

	$j = Q_1$	$j = Q_2$	$j = Q_3$	$j = Q_4$
$i = p$	-	-	+	+
$i = y$	+	-	+	-

The transfer function T_{ij} from rotation of the laser source to displacement of the beam on the QPD is defined as

$$\begin{aligned}
 |T_{ij}| &= l, \\
 i &\in \{p, y\}, \\
 j &\in \{Q_1, Q_2, Q_3, Q_4\},
 \end{aligned} \tag{3.4.40}$$

where $l = 11.5$ m is the length of the lever, p and y describe the degrees of freedom pitch and yaw, and $Q_1 - Q_4$ describe the four quadrants as shown in figure 3.4.27. The sign of T_{ij} depends on i and j and is shown in table 3.4.5.

The beam displacement changes the power on each quadrant, which is converted to a current, depending on the photodiode responsivity. Both effects are summarized as the QPD transfer function T_{QPD} . The current is converted to a voltage, amplified and whitened by the electronics with the transfer function T_{el} , and digitized by the ADC. Afterwards, the signals are multiplied by a calibration filter C_{cal} . The calibrated quadrant outputs are divided by the sum of all four quadrants P , to decouple the outputs from intensity and frequency noise of the laser. The pitch and yaw motion is calculated by addition or subtraction of the quadrant outputs as shown in figure 3.4.28.

The calibration filter inverts all these effects, which leads to

$$C_{\text{cal}} = \frac{P}{4T_{ij}T_{\text{QPD}}T_{\text{el}}T_{\text{ADC}}}. \tag{3.4.41}$$

Note that the calibration filter C_{cal} is a constant; hence, it does not inject intensity and frequency noise.

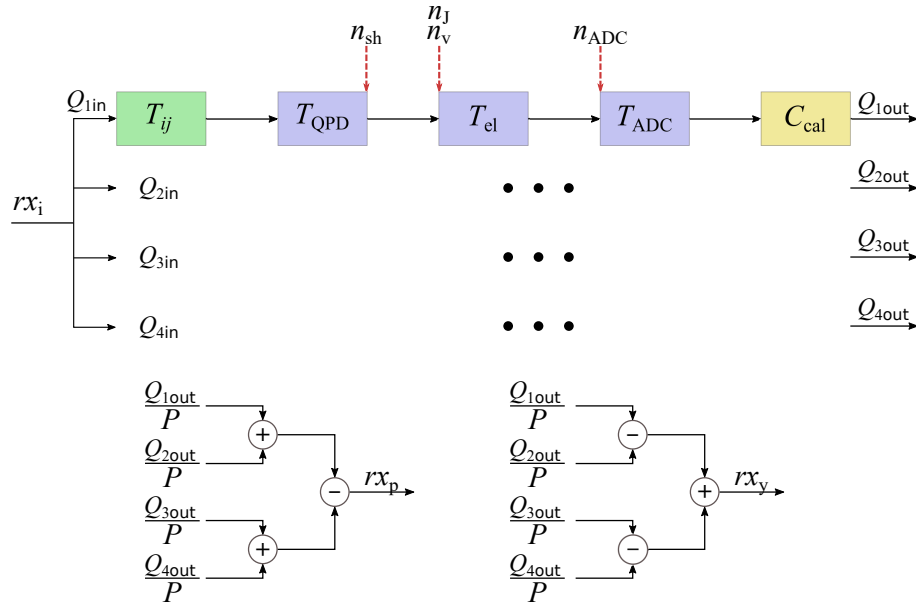


Figure 3.4.28: Block diagram displaying the functionality, signal calculations and noise contributions of the optical lever. Rotational motion couples to the motion of the beam on the QPD by multiplication with the lever T_{ij} . The laser beam is detected by the quadrants, converted, amplified and whitened by the electronics, digitized by the ADC and calibrated digitally. The calibrated quadrant outputs are normalized by the sum and added or subtracted from each other to calculate pitch and yaw signals.

Further technical information about the optical levers is provided in [Köh18].

Electronics

The optical lever electronics are shown in figure B.0.4 and consist of three stages:

- The first stage is a trans-impedance amplifier (TIA) using an OP177 amplifier [Ana16a], which converts the current signal of the photodiode into a voltage. The conversion is calculated as: $U = R_{TIA}I$, with the trans-impedance resistor $R_{TIA} = 274 \text{ k}\Omega$.
- A whitening stage with corner frequencies at 0.33 Hz and 33 Hz provides an amplification of the signal at higher frequencies by a factor 100, also using an OP177 amplifier [Ana16a].
- The output stage converts the single-ended signal to a differential signal and adds a gain of 2 using two LT1124 amplifiers [Lin92].

Figure 3.4.29 shows the total transfer function of the optical lever electronics in units of V/A.

Noise performance

Four different noise contributions are investigated to calculate the total optical lever noise \tilde{n}_{OL} . They couple to each of the QPD quadrants incoherently. The calculation of the input referred noise contributions is explained below, with the values shown in table 3.4.4.

- Shot noise n_{sh} is present in the photo current, calculated by

$$n_{sh} = \sqrt{2eI}, \quad (3.4.42)$$

where e is the elementary charge and I is the photo current. The input referred

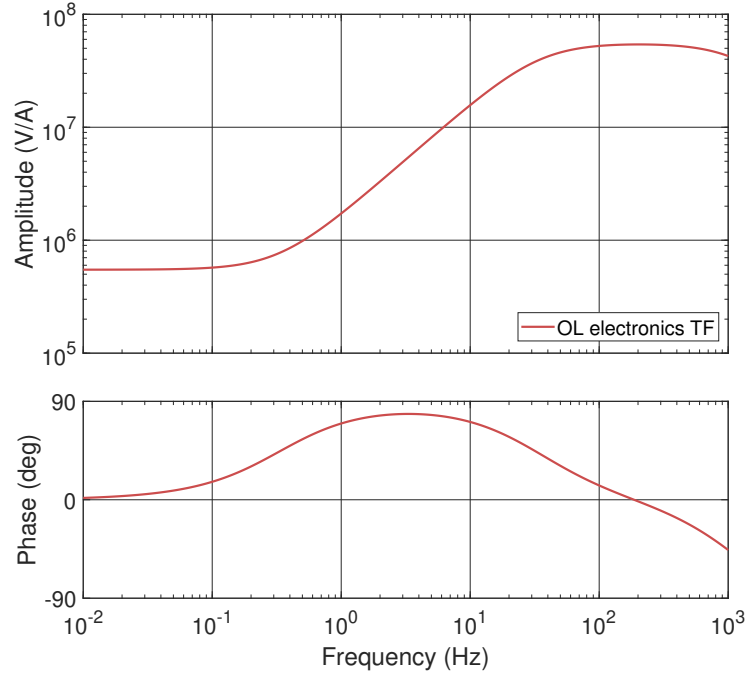


Figure 3.4.29: Transfer function of the optical lever electronics.

shot noise is calculated by

$$\tilde{n}_{\text{sh}} = 2 \frac{n_{\text{sh}} T_{\text{el}} T_{\text{ADC}} C_{\text{cal}}}{P}, \quad (3.4.43)$$

where the factor 2 accounts for the incoherent summation of all four quadrants.

- Johnson noise of the input resistor with resistance $r_1 = 33000 \Omega$, (see figure B.0.4) is present at the input of the electronics and calculated by

$$n_{\text{J}} = \sqrt{4k_{\text{B}} T r_1}, \quad (3.4.44)$$

with k_{B} being the Boltzman constant and T being the temperature. n_{J} is converted to a current by dividing by the input resistor and converted to an input referred noise by multiplying by the electronics transfer function:

$$\tilde{n}_{\text{J}} = 2 \frac{n_{\text{J}} T_{\text{el}} T_{\text{ADC}} C_{\text{cal}}}{r_1 P} \quad (3.4.45)$$

- Voltage noise of the electronics is dominated by the trans-impedance amplifier of the type OP177 [Ana16a]. The input referred voltage noise is calculated as

$$\tilde{n}_{\text{v}} = 2 \frac{n_{\text{v}} T_{\text{el}} T_{\text{ADC}} C_{\text{cal}}}{r_1 P}. \quad (3.4.46)$$

- ADC noise is presented in section 3.4.1. The input referred ADC noise is calculated by

$$\tilde{n}_{\text{ADC}} = 2 \frac{n_{\text{ADC}} T_{\text{ADC}} C_{\text{cal}}}{P}. \quad (3.4.47)$$

Figure 3.4.30 presents all noise contributions and the total optical lever noise. ADC noise is limiting the performance below roughly 2 Hz, above this frequency it is shot noise.

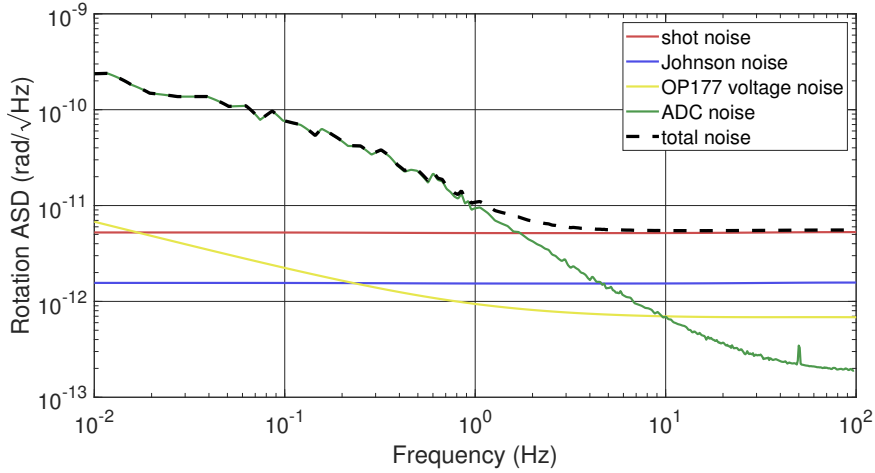


Figure 3.4.30: Input referred noise contributions and total noise of an optical lever. ADC noise is limiting the total noise below 2 Hz, above 2 Hz it is shot noise.

Translational motion noise

A special form of noise for the optical levers is differential translational motion of the two AEI-SAS perpendicular to the laser beam, labelled as \tilde{n}_x . This relative motion creates a displacement of the laser beam on the QPD. z motion creates noise for the pitch measurement, and x or y motion create noise for the yaw measurement. The input referred noise \tilde{n}_x is calculated as

$$\tilde{n}_x = \frac{\delta x}{l}, \quad (3.4.48)$$

where δx is the differential motion between the AEI-SASs and l is the length of the lever. Motion of the optical tables is assumed to be differential above the fundamental resonance frequencies in z , x and y . To calculate the noise created by differential motion, the inertial optical table motion is multiplied with a second order high pass filter with corner frequencies at 0.3 Hz or 0.1 Hz, respectively. Since this noise depends on the optical table motion, it strongly varies with time and the utilized control scheme and is therefore classified as a special form of optical lever noise.

Figure 3.4.31 shows the input referred noise contributions and total noise, including an example of translational motion noise in z . The translational motion was measured on a day with middle to high seismic activity, with the optical tables in a “high gain inertial control state” (see section 3.7.1), including optical levers (see section 3.8.1). \tilde{n}_x limits the total noise from 0.05–5 Hz.

3.4.7 Suspension platform interferometer

Description

The Suspension Platform Interferometer (SPI) is a heterodyne Mach-Zehnder interferometer that measures the distance between two AEI-SASs. It consists of a frequency stabilized laser beam (see section 2.5) that is split into two equal parts. Both beams propagate through AOMs, which shift the laser frequency by roughly 80 MHz, but with a small difference between the two arms, creating a beat signal. A phase lock loop stabilizes this beat signal at a frequency of 15.34 kHz. The laser beams are guided into the vacuum system to the central AEI-SAS using optical fibers. One of the two beams propagates to the second AEI-SAS and is reflected back, while the other beam stays local on the central AEI-SAS. The beams are recombined using a second beam splitter and detected by a phasemeter [H⁺04b]. A measurement of the differential motion δx between the two AEI-SAS is provided by the phase change $\delta\phi$

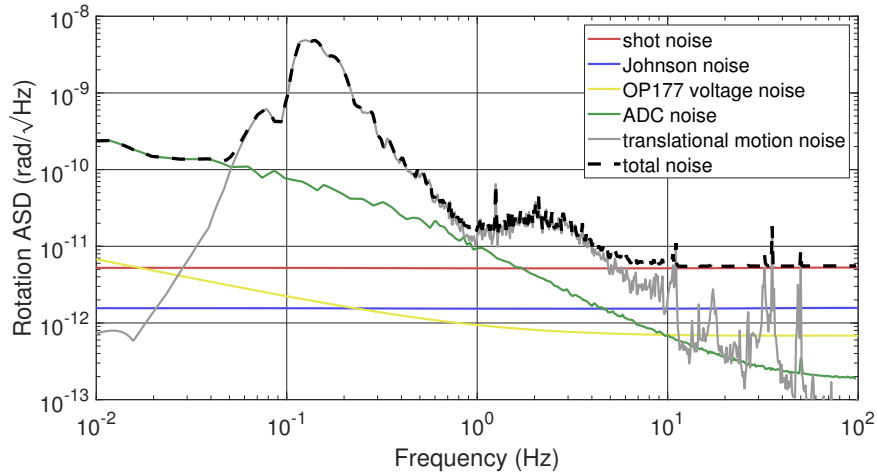


Figure 3.4.31: Input referred noise contributions and total noise of an optical lever in pitch, including an example of translational motion noise.

Table 3.4.6: Overview, description and values of all relevant variables and parameters of section 3.4.7 Suspension platform interferometer.

Variable	Description
δx	differential longitudinal motion between two AEI-SAS
$\delta\phi$	phase change between local and global SPI beam
$rx_p; rx_y$	rotational ground motion in pitch or yaw

Parameter	Description	Value
λ	laser wavelength	1064 nm
η_c	contrast between local and global SPI beam	
\tilde{n}_f	input referred frequency noise	see figure 3.4.33
ΔL	length difference local/global SPI beam	23 m
c_0	speed of light in vacuum	2.998×10^8 m/s
\tilde{n}_{RIN}	input ref. rel. intensity noise (0.01–10 Hz)	$\approx 10^{-11}$ m/ $\sqrt{\text{Hz}}$
$n_{RIN\phi}$	phase fluctuations from rel. intensity noise	
$\tilde{n}_{P1}; \tilde{n}_{P2}$	power noise of local and global SPI beam (at 10 mHz)	$0.0044/\sqrt{\text{Hz}}$; $0.0147/\sqrt{\text{Hz}}$
$P_1; P_2$	power of local and global SPI beam	1 mW
η_{het}	heterodyne efficiency	
\tilde{n}_{sh}	input referred shot noise	W: 7.9×10^{-15} m/ $\sqrt{\text{Hz}}$ S: 1.7×10^{-14} m/ $\sqrt{\text{Hz}}$
$n_{sh\phi}$	phase fluctuations from shot noise	
e	elementary charge	1.6022×10^{-19} C
R_{pd}	photodiode responsivity	0.7 A/W

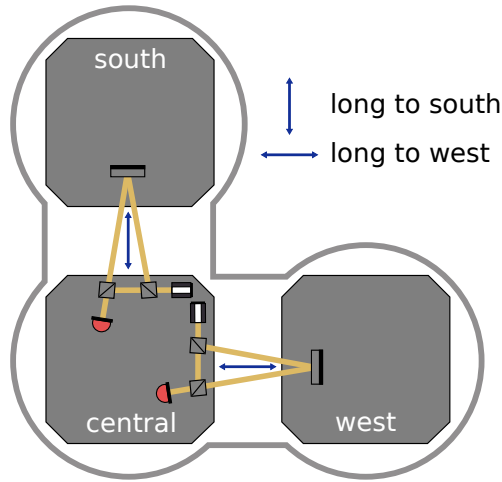


Figure 3.4.32: Setup of the SPI interferometers measuring differential longitudinal motion between the central and south AEI-SAS and central and west AEI-SAS. The sensitive degrees of freedom are indicated in blue.

between the two beams, described by the equation

$$\delta x = \frac{\lambda \delta \phi}{2\pi}, \quad (3.4.49)$$

with λ being the laser wavelength. All relevant variables and parameters for this section are listed in table 3.4.6.

Different to the other sensors, the SPI does not measure motion of one AEI-SAS but a combination of the motion of two AEI-SASs. Figure 3.4.32 shows the setup of the two SPIs, measuring the distance between central and south AEI-SAS and central and west AEI-SAS. The two signals are utilized in a leader-follower control scheme. The central AEI-SAS is controlled with local sensors and the south and west AEI-SASs follow the central AEI-SAS in the longitudinal degree of freedom, using the SPI signal.

Design, setup and analysis of the SPI interferometer was the topic of one paper and two PhD theses [DHW⁺12, Dah13, Köh18] and is not discussed in detail here. A summary of noise calculations and measures to reduce the noise below the target sensitivity of $100 \text{ pm}/\sqrt{\text{Hz}}$ is provided below. Table 3.4.6 provides the required values for the calculations.

Noise performance

- Thermal noise

To achieve low thermal noise at low frequencies, the SPI setup inside the vacuum system was planned to be fully monolithic. Due to imperfect alignment of the monolithic setup, the best achieved contrast for the two south SPI beams is $\eta_c \approx 30\%$, for the west SPI beams it is only $\eta_c \approx 8\%$; hence, the west SPI obtained additional non-monolithic steering mirrors and photodiodes, resulting in a contrast of $\eta_c \approx 65\%$ but increased thermal noise (see [Köh18], page 25).

- Frequency noise

The free-running frequency noise of the Prometheus NPRO laser exceeds the noise requirements and needs an additional frequency stabilization. As presented in section 2.5, a commercial iodine stabilization is utilized. [DHW⁺12], page 36–37, presents a measurement of the resulting frequency noise executed by the LISA group of the AEI Hanover. For this measurement, the beat note of two iodine-stabilized laser systems equal to the SPI laser was measured. The

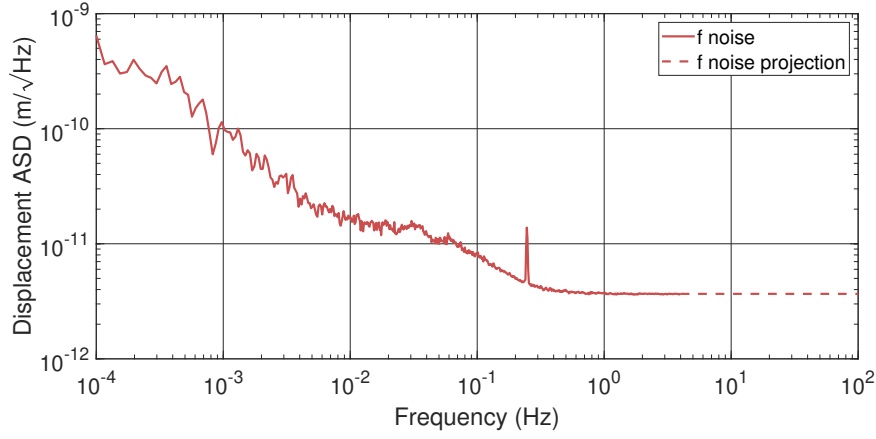


Figure 3.4.33: Input referred frequency noise of the iodine-stabilized laser system used for the SPI. The measurement was taken by the LISA group of the AEI in Hanover.

resulting frequency noise n_f in units of $\text{Hz}/\sqrt{\text{Hz}}$ is converted to an equivalent path length noise \tilde{n}_f with the equation

$$\tilde{n}_f = \frac{n_f \Delta L \lambda}{c_0}, \quad (3.4.50)$$

with $\Delta L = 23 \text{ m}$ being the arm length difference of the two arms, λ being the laser wavelength and c_0 being the speed of light in vacuum. Figure 3.4.33 shows the results. The measurement provided by the LISA group had a maximum frequency of 4 Hz. The data hints towards a flat noise above 0.5 Hz, which is why a projection of this noise up to 100 Hz is included in the figure.

- Phase meter noise
[DHW⁺12], pages 101–102, provides measurements of the phase meter noise for a high and low contrast of 0.81 and 0.045 between two phase meter input signals. This noise includes all electronic noise sources of the readout and has values of roughly $7 \times 10^{-14} \text{ m}/\sqrt{\text{Hz}}$ and $1 \times 10^{-12} \text{ m}/\sqrt{\text{Hz}}$, respectively. The contrast values of the two SPI interferometers are well within the range of the two tested contrast configurations, such that phase meter noise is assumed to be below $10^{-12} \text{ m}/\sqrt{\text{Hz}}$.

- Relative intensity noise
A calculation of Relative Intensity Noise (RIN) for a heterodyne Mach-Zehnder interferometer is presented in [Bar15], pages 39–40 and executed for the SPI in [Dah13], pages 52–54. The phase noise resulting from RIN is calculated by

$$n_{\text{RIN}\phi} = \sqrt{\frac{(n_{P1}P_1)^2 + (n_{P2}P_2)^2}{2\eta_{\text{het}}P_1P_2}}, \quad (3.4.51)$$

where n_{P1} and n_{P2} are the relative power noise of the local and global beams, $P_1 = P_2 = 1 \text{ mW}$ are the powers of both beams, and η_{het} is the heterodyne efficiency. The relative power noise of the individual beams was measured to be $n_{P1} = 0.0044/\sqrt{\text{Hz}}$ and $n_{P2} = 0.0147/\sqrt{\text{Hz}}$ at 10 mHz [Dah13]. The heterodyne efficiency depends on the contrast η_c as described by

$$\eta_{\text{het}} = \frac{\eta_c^2(P_1 + P_2)^2}{4P_1P_2}. \quad (3.4.52)$$

Phase fluctuations from RIN are converted to an equivalent path length noise \tilde{n}_{RIN} by applying equation 3.4.49. The results for the south and west SPI at 10 mHz are $6.1 \times 10^{-9} \text{ m}/\sqrt{\text{Hz}}$ and $3.5 \times 10^{-9} \text{ m}/\sqrt{\text{Hz}}$, respectively. This noise is far off the requirements and is not expected to decrease sufficiently for frequencies above 10 mHz; hence, countermeasures are implemented.

To reduce phase noise originating from the out-of-vacuum setup, the fiber, the fiber coupler and the first in-vacuum optics, another interferometer is installed. It uses the same input path but stays fully local on the central AEI-SAS. This reference interferometer signal is subtracted from the south and west SPI signal to subtract the noise contributions of the input path.

This subtraction of noise is supplemented by an optical path length stabilization, fixing the beat note phase of the reference interferometer [Köh18], pages 21–23. Since both main SPI interferometers use the same input path as the reference interferometer, they are stabilized as well.

Using both techniques the noise of the reference interferometer is suppressed down to roughly $10^{-11} \text{ m}/\sqrt{\text{Hz}}$ from 0.01–10 Hz.

- Shot noise

A calculation of shot noise for a heterodyne Mach-Zehnder interferometer is provided in [Bar15], pages 39–40. The phase fluctuations on the beat note due to shot noise are given by

$$n_{\text{sh}\phi} = \sqrt{\frac{2e(P_1 + P_2)}{R_{\text{pd}}\eta_{\text{het}}P_1P_2}}, \quad (3.4.53)$$

with e being the elementary charge and $R_{\text{pd}} = 0.7 \text{ A/W}$ being the responsivity of the photodiode.

These phase fluctuations due to shot noise are converted to an input referred shot noise \tilde{n}_{sh} in units of $\text{m}/\sqrt{\text{Hz}}$ by applying equation 3.4.49. The resulting shot noise for the south SPI with a contrast of 0.3 is $1.7 \times 10^{-14} \text{ m}/\sqrt{\text{Hz}}$, for the west SPI with a contrast of 0.65 it is $7.9 \times 10^{-15} \text{ m}/\sqrt{\text{Hz}}$.

- Total noise estimate

The investigations within this section hint towards frequency noise and residual RIN as the major noise sources for the SPI; nevertheless, there might be additional noise not being investigated or deviations of the real noise from theory; hence, it is useful to measure the real noise directly.

A good noise estimate for the final SPI performance, including most noise sources, can be obtained by utilizing another fully local interferometer, also using the same input path. The differential signal of both local interferometers includes all relevant noise contributions, except for frequency noise. Figure 3.4.34 shows this measurement labelled with “total noise w/o f noise” and additionally the frequency noise as shown in figure 3.4.33. The incoherent sum of both measurements is assumed to be the total SPI noise.

3.4.8 Voice-coil actuator

Description

Voice-coil actuators are utilized to actively isolate the AEI-SAS from ground motion. They consist of an actuation coil and permanent magnets, magnetizing a frame around the coil. All relevant variables and parameters for this section are listed in table 3.4.7. An electro-magnetic force is exerted by applying a current to the coil. Figure 3.4.35 shows a schematic setup of the horizontal (left) and vertical (right) voice-coil actuators. The horizontal voice-coil actuator applies a horizontal force of

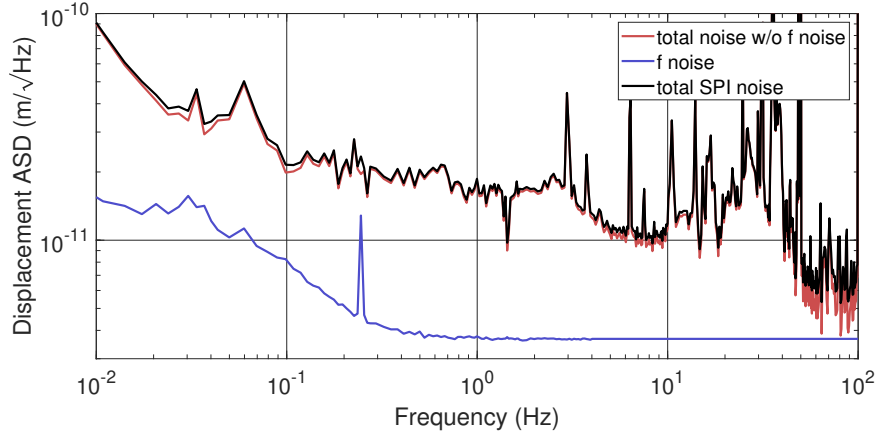


Figure 3.4.34: Total expected SPI noise excluding frequency noise, input referred frequency noise and total noise of the SPI. The total noise without frequency noise is obtained by subtracting the signal of two fully local SPI interferometers from each other.

Table 3.4.7: Overview, description and values of all relevant variables and parameters of section 3.4.8 Voice-coil actuator.

Variable	Description
F_{vc}	Force of voice-coil actuator on test mass
x_{act}	actuation signal
x_{sp}	springbox motion

Parameter	Description	Value
T_{em}	electro-magnetic force per current	horizontal: 5 N/A vertical: 7 N/A
T_{HOext}	TF from external force to test mass motion	see figure 3.4.36
T_{el}	TF of the actuation electronics	horizontal: 0.06 A/V vertical: 0.01 A/V
\tilde{n}_{DAC}	input referred DAC noise	
\tilde{n}_v	input referred voltage noise	see figure 3.4.38
\tilde{n}_J	input referred Johnson noise	
\tilde{n}_{vc}	total input referred voice-coil actuator noise	
T_{DAC}	TF of the DAC	1638.4 counts/V
k_B	Boltzmann constant	1.38×10^{-23} J/K
T	temperature	293.15 K
$\Re(Z)$	real part of the coil impedance	horizontal: 138 Ω vertical: 45 Ω

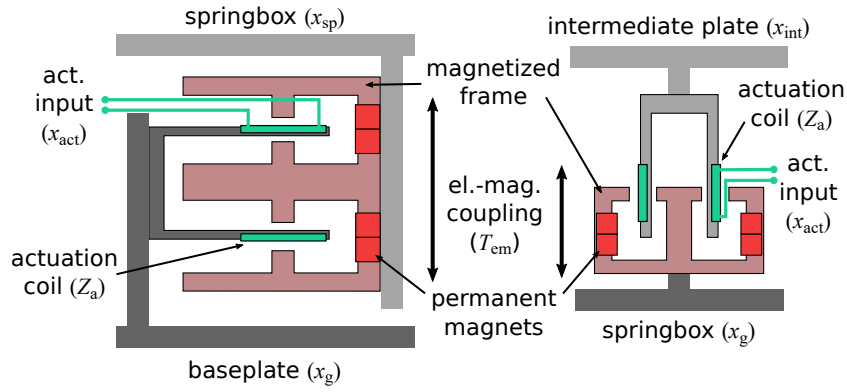


Figure 3.4.35: Schematic drawing of a horizontal (left) and vertical (right) voice-coil actuator. The components are labelled with all relevant parameters for the calculation of the actuator transfer function and noise. The baseplate motion for the horizontal actuator and the springbox motion for the vertical actuator are equal to ground motion due to a stiff connection.

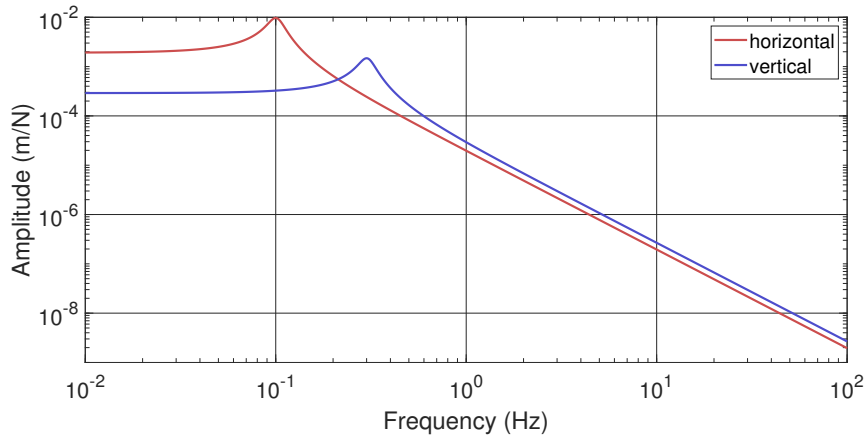


Figure 3.4.36: Transfer functions from force to displacement for the vertical and horizontal voice-coil actuators. The zero frequency values are $300 \mu\text{m}/\text{N}$ in vertical and $2 \text{ mm}/\text{N}$ in horizontal direction.

$T_{\text{em}} = 5 \text{ N/A}$ between baseplate and springbox, while the vertical actuator applies a vertical force of $T_{\text{em}} = 7 \text{ N/A}$ between springbox and intermediate plate.

[WTD⁺02] motivates the design of the voice-coil actuators and provides a detailed characterization. The shape of the magnetized frame is optimized to offer a highly position-independent coupling. In the desired degree of freedom, the actuator has a constant force coupling over a range of more than 10 mm. In the other degrees of freedom, the coupling is zero over a wide range.

The force of the voice-coil actuator F_{vc} directly acts on the AEI-SAS stage to be controlled. Using equation 3.1.5 it can be described by

$$F_{\text{vc}} = x_{\text{act}} T_{\text{em}} = \frac{x_{\text{sp}}}{T_{\text{HOext}}}, \quad (3.4.54)$$

with x_{act} being the actuation signal in units of A, T_{em} being the electro-magnetic coupling of the voice-coil actuator in units of N/A, x_{sp} being the motion of the springbox, and T_{HOext} being the transfer function for external forces acting directly onto the test mass.

Electronics

The coil driver for the voice-coil actuators consists of a differential amplifier type

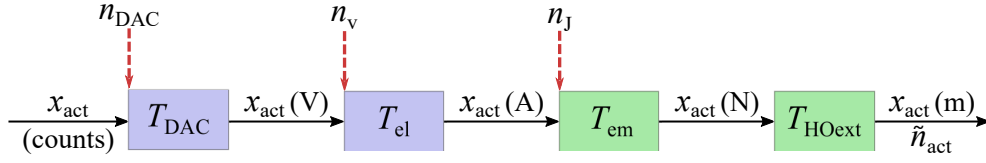


Figure 3.4.37: Block diagram of a voice-coil actuator, its electronics, and its CDS calibration, displaying the path of the actuation signal and noise contributions.

SSM2141 [Ana07] and an operational amplifier OP27 providing a gain of 0.01 A/V in vertical and 0.06 A/V in horizontal direction. Its schematics are shown in Appendix B.

The DAC maximum output in vertical direction is 10 V for each actuator, in horizontal direction it is limited to 1.17 V each. This results in a total range of 611 μm in vertical and 2 mm in horizontal direction.

Noise performance

Figure 3.4.37 shows a block diagram of the voice-coil actuator, containing the path from digital actuation signal to the resulting AEI-SAS motion. The actuation signal x_{act} in counts is converted to a voltage by the DAC. The actuation electronics with transfer function T_{el} converts the actuation signal into a driving current, which is sent to the actuation coil. The current is converted to a force via the electro-magnetic coupling factor T_{em} and results in motion of the suspended stage, depending on the mechanical transfer function T_{HOext} .

There are three relevant noise sources for the voice-coil actuators:

- DAC noise is presented in section 3.4.1 and couples to the input referred actuation noise as

$$\tilde{n}_{\text{DAC}} = n_{\text{DAC}} T_{\text{DAC}} T_{\text{el}} T_{\text{em}} T_{\text{HOext}}. \quad (3.4.55)$$

- Noise of the electronics is dominated by the voltage noise of the operational amplifier SSM2141 [Ana07]. The input referred noise is calculated as

$$\tilde{n}_{\text{v}} = n_{\text{v}} T_{\text{el}} T_{\text{em}} T_{\text{HOext}}. \quad (3.4.56)$$

- Johnson noise is present at the actuation coil. Following equation 2.2.2 the input referred Johnson noise is calculated as

$$\tilde{n}_{\text{J}} = n_{\text{J}} T_{\text{em}} T_{\text{HOext}} = \sqrt{4k_{\text{B}} T \Re(Z)} T_{\text{em}} T_{\text{HOext}}. \quad (3.4.57)$$

It is assumed that $\Re(Z)$ is sufficiently approximated by the resistance due to the small resistor values of 45 Ω in vertical and 138 Ω in horizontal direction.

Figure 3.4.38 shows the different noise contributions and their incoherent sum \tilde{n}_{vc} . The total noise is limited by DAC noise for the vertical and the horizontal actuator from 0.01 – 100 Hz.

3.4.9 Motorized blade springs

The optical table positions of the AEI-SASs strongly depend on temperature changes of the environment and pressure changes during the pumping and venting processes. Temperature changes influence the stiffness of the GAS filters, which influences their equilibrium position. [Ber18], pages 105 – 110, provides theory and measurements of this dependence. Pumping and venting of the vacuum system does not only change the optical table position in vertical direction due to the missing air load, but also rotates the optical tables due to inconsistent stiffness of the passive isolators (see figure 3.3.5).

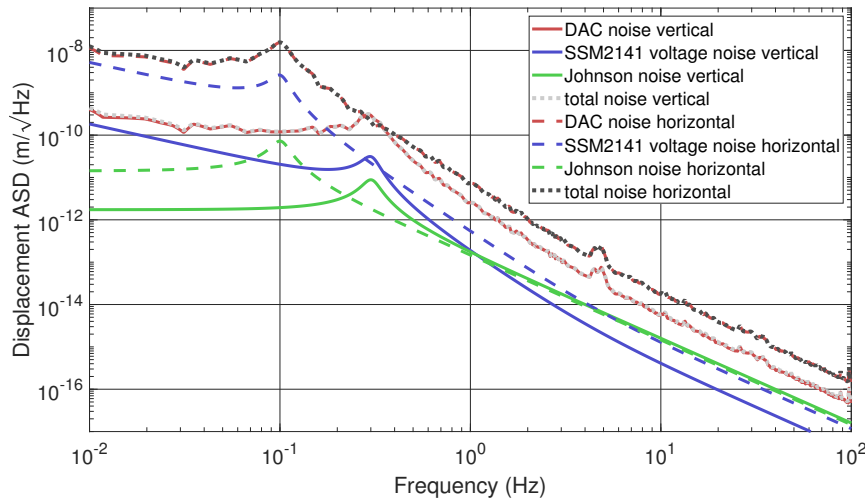


Figure 3.4.38: Input referred noise contributions and total noise of a vertical and a horizontal voice-coil actuator. The total noise is limited by DAC noise over the entire frequency band.

Both described effects cause displacements of the optical tables that exceed the voice-coil actuator range. Re-leveling by changing the mass distribution on the optical tables works fine for vertical degrees of freedom in a vented state, but it is not possible for horizontal degrees of freedom or if the vacuum system is evacuated; therefore, motorized blade springs are implemented.

The motorized blade springs are utilized to provide a coarse positioning of the optical tables with a range of several millimeters and a precision of roughly $50 \mu\text{m}$. They consist of a stepper motor that drives a sleeve, with a soft blade connecting the sleeve and the suspended stage of the AEI-SAS. A soft blade is required in order to maintain a soft connection between ground and optical table. Details on the mechanical design is provided in [Wan13], pages 109–110 and [Ber18], pages 69–70.

In operation, the stepper motors introduce high displacement noise due to current noise; hence, they are not included into the feedback control system and switched off for sensitive measurements.

3.4.10 Comparison of sensors

Figure 3.4.39 shows the input referred displacement noise of all previously described sensors. Translational motion coupling to the optical levers, tilt coupling to the geophones, accelerometers and STS-2 and seismic coupling to the LVDTs are not included in this figure. As explained in the corresponding sections, they strongly depend on the control system, the positioning of the sensors and the magnitude of seismic motion; hence, they change with time. These effects are exemplarily included in figure 3.4.40 for the control states and seismic activity described in the respective sections. Voice-coil actuator noise is not included in the figures because of its different role for the control system, making a noise comparison to sensors pointless.

acLVDTs are favorable over geophones and accelerometers at low frequencies and vice versa. Optical levers and the SPI beat LVDTs at low frequencies and are worse than geophones at high frequencies. The STS-2 is the best performing inertial sensor; nevertheless, it is only used for sensor correction of the LVDTs (see section 3.7.6) due to its high costs.

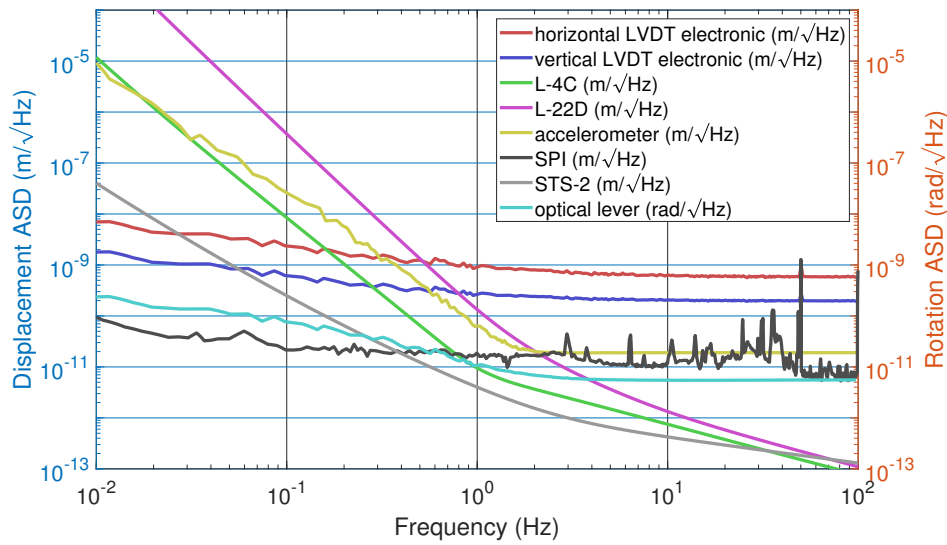


Figure 3.4.39: Input referred displacement or rotation noise of all sensors implemented in the AEI-SASs. Translational motion coupling to optical levers, tilt coupling to inertial horizontal sensors and seismic coupling to the LVDTs are not included, because they strongly depend on the control system, the positioning of the sensors, and on the changing seismic activity.

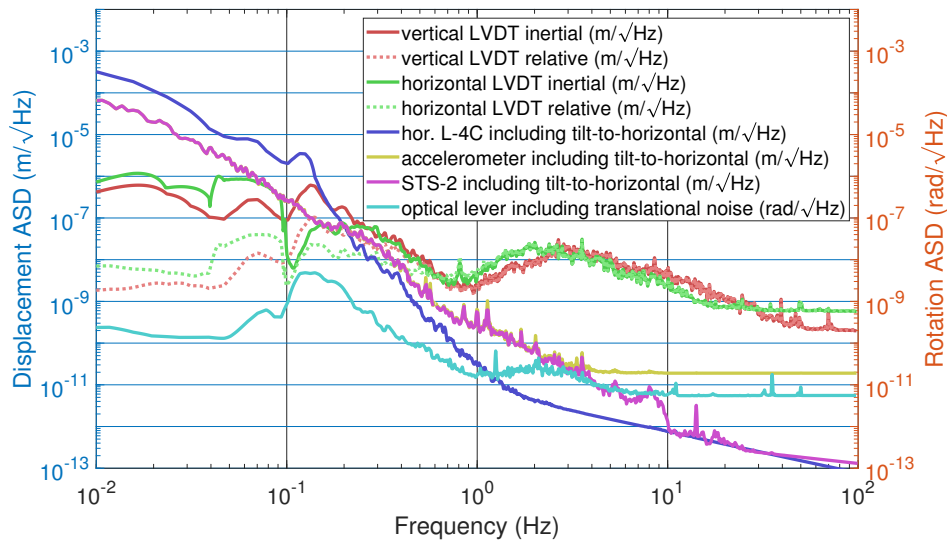


Figure 3.4.40: Input referred displacement or rotation noise of all sensors implemented in the AEI-SASs. Translational motion coupling to optical levers, tilt coupling to inertial horizontal sensors and seismic coupling to the LVDTs are included here exemplarily. Medium seismic activity is assumed to calculate the LVDT, the accelerometer, and the STS-2 noise. The tilt coupling to horizontal L-4C geophones is calculated for a “high gain local control state”. The optical lever translational coupling is calculated for a “high gain control state” with additional use of optical levers.

3.5 Huddle test

Section 3.4 presents noise calculations of the sensors implemented in the AEI-SAS. To confirm that the calculations match the reality, it is important to measure the sensor noise. If measurement and calculation overlap to a high extent, the calculation is assumed to be precise, which gives a detailed insight into the limitations of the sensors.

A direct measurement of noise of seismic sensors is often impossible, because it is at least partly masked by the sensor signal. The so-called huddle test is a technique to subtract the large seismic contribution from the sensor output, revealing its noise. This section describes the principles of huddle tests and presents huddle test results for L-22D geophones, L-4C geophones, accelerometers and LVDTs, with a comparison to the calculated sensor noise. Requirements for successful huddle tests are derived and analysed based on measurements.

3.5.1 Principles of huddle tests

In a huddle test, the sensor under test, referred to as the main sensor, and multiple reference sensors are located close to each other. The sensors are clamped to a rigid underground in order to maximize the equality of the detected seismic motion. This results in a high coherence of the seismic signal for all sensors, while the sensor noise is always incoherent. By subtracting the coherent common mode signal between main and reference sensors from the main sensor, its uncommon sensor noise is revealed.

Mathematical description

For the huddle tests described in this thesis, the data was processed using a MATLAB script called “Multi-Channel Coherent Subtraction” (see supplementary material of [K⁺17]). It was developed by Brian Lantz and Wensheng Hua and is based on the method presented in [AHO99].

At first, the script converts time series of all involved sensors into the frequency domain using Fast Fourier Transform (FFT). Next, the noise of the main sensor is estimated using the equation

$$\bar{n}_m(\omega) = X_m(\omega) - \sum_{i=1}^N T_{mi}(\omega) \times Y_i(\omega), \quad (3.5.1)$$

where \bar{n}_m is the estimated sensor noise of the main sensor, referred to as huddle test result, X_m is the main sensor output including its noise and the seismic signal, Y_i is the sensor output of the i -th reference sensor out of a total of N reference sensors, and T_{mi} is a transfer function that calibrates the reference sensor output to the main sensor output. By doing so, differences in the sensor response, the amplitude of the incident seismic motion, and the calibration are removed to provide the optimal subtraction. The script searches for the best possible T_{mi} for each reference sensor, while taking the coherence to the main sensor into account.

In the last step, the script applies a correction factor to the estimated sensor noise to account for the statistical chance that random signals, like noise, are coherent [AHO99, Hua05, BP10].

3.5.2 Huddle test for geophones

Three different types of geophones are installed in the AEI-SAS and tested in a huddle test: vertical L-22D geophones, vertical L-4C geophones and horizontal L-4C geophones. The huddle test for both vertical geophone types was done in one experiment and is published in [K⁺17], while the horizontal L-4Cs were tested separately.

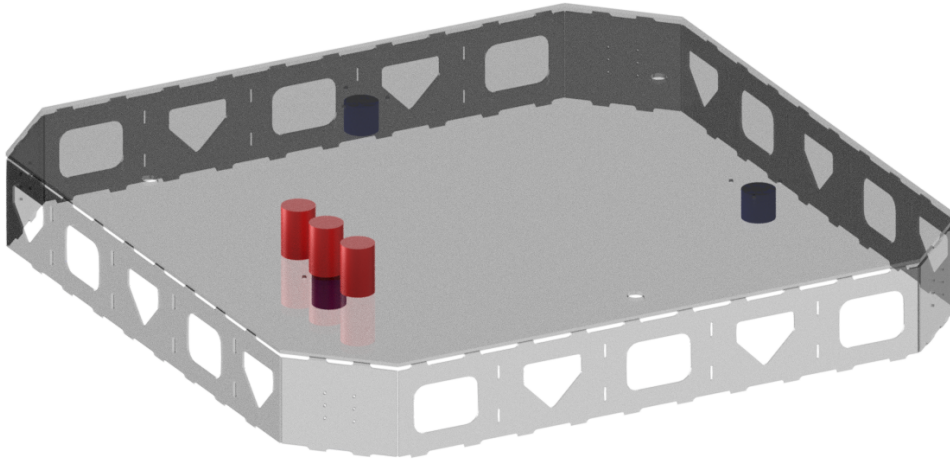


Figure 3.5.1: Setup of the huddle test for the vertical L-22D and L-4C geophones. The gray structure shows the optical table of an AEI-SAS. Three large red cylinders show the positions of the L-4C geophones on top of the optical table. Three smaller blue cylinders show the positions of the L-22D geophones installed inside the optical table in a triangle.

Vertical L-22D and L-4C geophones

Figure 3.5.1 shows the setup of the huddle test for the vertical L-22D and L-4C geophones. Three L-4C geophones, shown in red, are mounted onto the optical table (gray structure) of the AEI-SAS. Three L-22D geophones, shown in blue, were pre-installed in a triangular arrangement inside the optical table. For the L-4C huddle test, the middle L-4C was assigned as the main sensor, while for the L-22D huddle test, the L-22D right below the L-4Cs was assigned as the main sensor. The optical table was passively isolated, supported by active damping of the fundamental AEI-SAS resonances.

Figure 3.5.2 shows the results of the huddle test. The figure includes the amplitude spectral density of the main sensor during the test, its measured noise and, for comparison, the calculated noise from section 3.4.3. Measurement and theory overlap to a very high extent over the entire frequency range of interest. Only around 0.3 Hz the measured noise is slightly higher than theory predicts. At frequencies below 0.2 Hz for the L-22Ds and 0.1 Hz for the L-4Cs, the amplitude spectral densities follow the noise, indicating that the sensor output is noise limited at these frequencies.

Horizontal L-4C geophones

Figure 3.5.3 shows the setup of the huddle test for the horizontal L-4C geophones. Five horizontal L-4Cs are located close to each other on top of the optical table, one of which is assigned as main sensor. One horizontal L-4C is located inside the optical table, and three vertical L-4C geophones were pre-installed inside the optical table. The vertical sensors are utilized to subtract cross coupling from vertical degrees of freedom. The AEI-SAS was passively isolated, integrated to the zero position to remove tilt, and the fundamental resonances were damped.

Figure 3.5.4 shows the amplitude spectral density of the main sensor output, the measured noise resulting from the huddle test and the theoretically calculated noise from section 3.4.3, for comparison. Theory and measurement overlap excellently over the entire investigated bandwidth. The amplitude spectral density does not match the measured noise at low frequencies, because it is limited by tilt-to-horizontal coupling (see figure 3.4.17), which is common for all horizontal L-4Cs and hence subtracted in the huddle test.

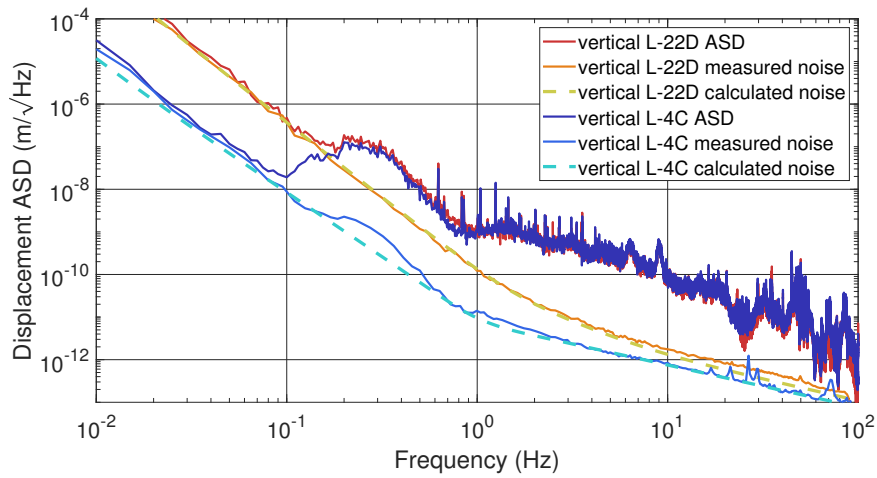


Figure 3.5.2: Amplitude spectral density, measured noise resulting from the huddle test and calculated noise of the vertical L-22D and L-4C geophone.

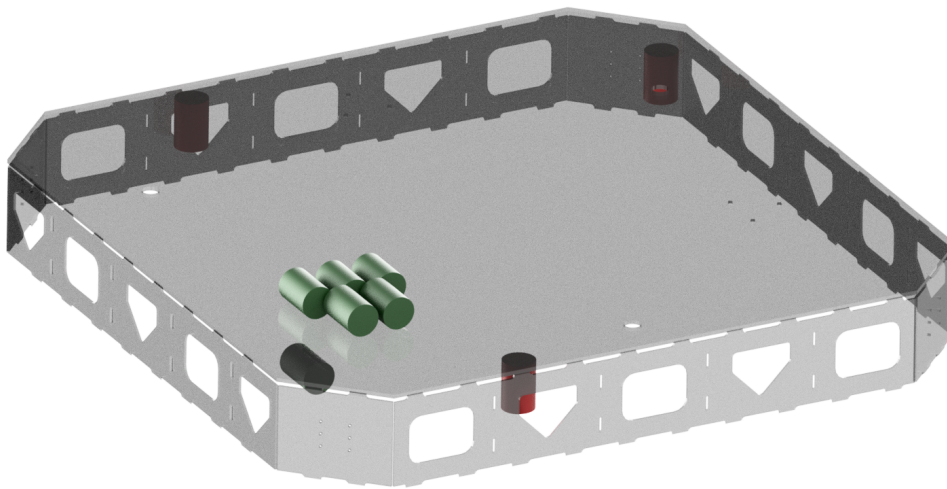


Figure 3.5.3: Setup of the huddle test for the horizontal L-4C geophones. The gray structure shows the optical table of an AEI-SAS. Six green cylinders show the positions of the horizontal L-4Cs, one inside the optical table (bottom left) and five on top of the optical table. Three red cylinders show the positions of the vertical L-4C geophones inside the optical table. They were used to subtract cross coupling from the vertical degrees of freedom.

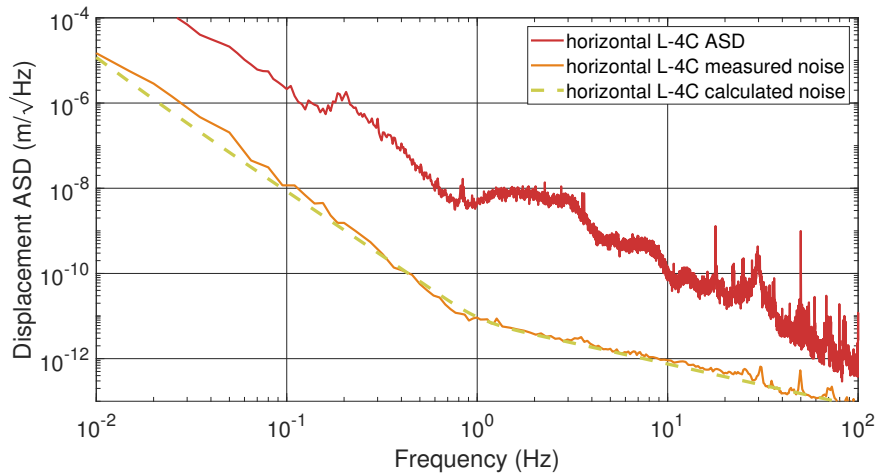


Figure 3.5.4: Amplitude spectral density, measured noise resulting from the huddle test and calculated noise of the horizontal L-4C geophone. Measurement and theory overlap to a very high extent over the entire frequency range of interest.

3.5.3 Analysis on requirements for precise huddle tests

There are several requirements to achieve good results in huddle tests:

- The main and reference sensors must be positioned as close to each other as possible and/or must be stiffly mounted on a rigid structure.
- At least some reference sensors must have a similar or better sensitivity as the main sensor.
- There should be at least 2 reference sensors. More reference sensors provide better results.
- The difference in amplitude between the common signal, here seismic motion, and the sensor noise, must not be too high. For the huddle tests in this thesis, seismic pre-isolation of the AEI-SAS was utilized to lower the common seismic signal.

The latter two bullet points are analyzed in more detail below.

Importance of the number of reference sensors

Although all reference sensors should, in principle, measure the same common signal as the main sensor, only using one or two reference sensors for subtraction delivers imprecise results. Figure 3.5.5 shows huddle test results for the horizontal L-4C geophones for using one to five of the horizontal L-4Cs as reference sensors and, in the last step (“all reference sensors”), also including the vertical reference sensors. The ASD and the calculated noise are shown for comparison. All five horizontal reference sensors improve the huddle test result over wide frequency ranges. This behavior is independent on the assignment of reference sensors as number one to five, i.e. changing the order of reference sensors gives roughly the same results. The more reference sensors are used, the better is the result. Adding vertical reference sensors for subtraction removes or lowers some peaks between 20–100 Hz, indicating that these peaks origin from vertical cross coupling.

Importance of seismic pre-isolation

The subtraction of common motion from the main sensor is never perfect but limited, for example, by non-linear differences between reference sensors and the main sensor. This leaves residues of seismic motion in the subtracted data, potentially

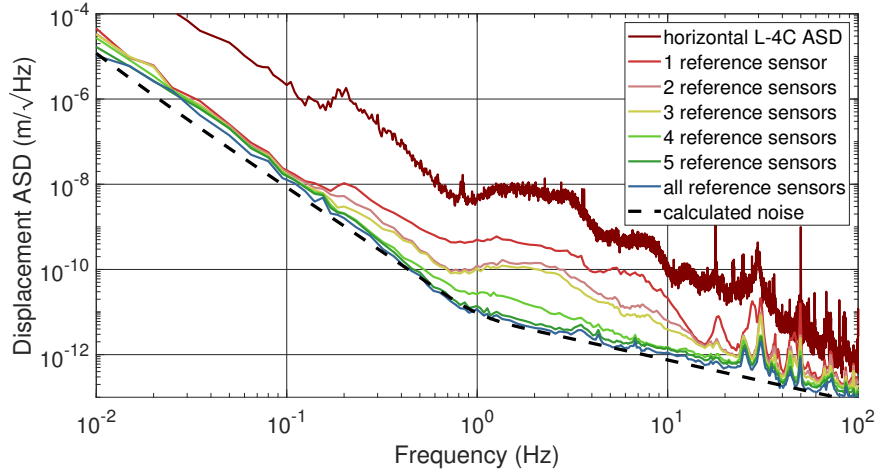


Figure 3.5.5: Huddle test results for the horizontal L-4C geophones for different numbers of reference sensors. The results are compared to the main sensor ASD and the calculated noise.

masking the sensor noise. The estimated sensor noise of the main sensor from equation 3.5.1 can be described by

$$\bar{n}_m(\omega) = n_m(\omega) + x_m^{\text{res}}(\omega), \quad (3.5.2)$$

$$x_m^{\text{res}}(\omega) = T_{\text{diff}}x_g, \quad (3.5.3)$$

with n_m being the real sensor noise, x_m^{res} being the residual seismic signal spoiling the subtraction, T_{diff} being a factor that describes non-linear differences between the sensors or other disturbances, preventing a perfect subtraction, and x_g being the seismic motion. A huddle test is precise, if $x_m^{\text{res}} < n_m$.

T_{diff} can be reduced by following the requirements for a successful huddle test listed earlier in this section; nevertheless, for the huddle tests of geophones described in this thesis, it is as well necessary to reduce the seismic motion.

Another setup was utilized to demonstrate this effect. Three vertical L-4C geophones were positioned close to each other on an optical table. For the first huddle test, the optical table was rigidly connected to ground motion, resulting in large common seismic signals. In the second measurement, the optical table was isolated passively with damping of the fundamental resonances, as it was done for the huddle test of the vertical geophones.

Figure 3.5.6 shows the results. Without seismic pre-isolation, the ASD of the seismic motion is about a factor 30 larger for frequencies above 1 Hz, compared to the pre-isolated case. The huddle test result follows the shape of the seismic spectrum, deviating significantly from the underlying sensor noise.

From the huddle test measurement without seismic pre-isolation, it is possible to estimate T_{diff} for this setup, by dividing the noise by the ASD. This gives a factor 0.01–0.001 between 0.2–20 Hz. Consequently, the underlying sensor noise can only be revealed, if it is at most a factor of 100–1000 below the seismic signal. This factor changes for different setups. A larger number of reference sensors, more sensitive reference sensors or a more rigid platform, on which the sensors are mounted, are possibilities to improve the subtraction.

The measurement with pre-isolation is assumed to have the same T_{diff} , because the same sensors are utilized in the same configuration. This enables an estimation of x_m^{res} for the seismically pre-isolated huddle test, which is compared to the actual huddle test result in figure 3.5.7. The curve “huddle test result with pre-isolation” is taken from figure 3.5.6. The curve “estimated accuracy limit of huddle test” describes the

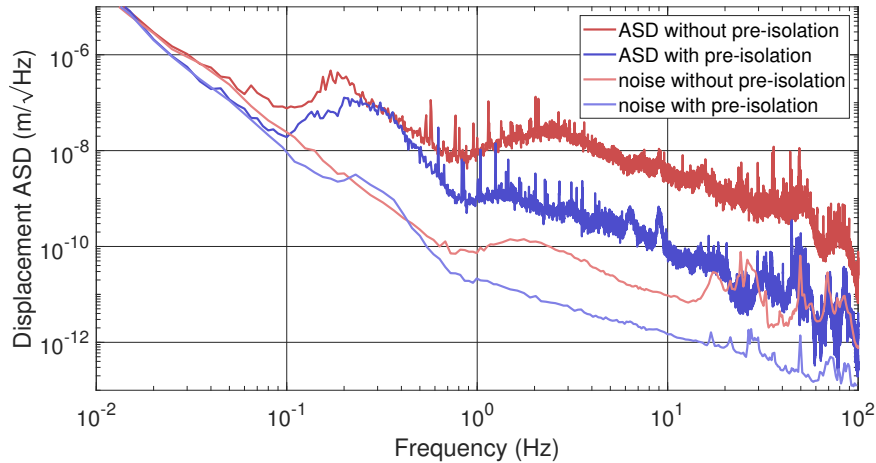


Figure 3.5.6: ASD and estimated noise for a huddle test without seismic pre-isolation and a huddle test with seismic pre-isolation. The estimated noise without pre-isolation strongly deviated from the real sensor noise. It follows the slope of the large common seismic signal due to imperfect subtraction.

estimated $x_{\text{in}}^{\text{res}}$. This curve is just below the calculated sensor noise, partly peaking through. The setup used for this huddle test was just good enough to provide an estimated sensor noise that comes close to the real noise. A higher optical table motion would have resulted in an imprecise huddle test. The deviation between measured and calculated noise at 0.3 Hz and above roughly 15 Hz can be explained by residual seismic contributions.

3.5.4 Huddle test for LVDTs

The noise of the horizontal and vertical LVDTs was measured in separate huddle tests. Different to the geophone huddle tests, the measurement did not require multiple sensors mounted close to each other, but it was executed with the usual sensor arrangement of the AEI-SAS shown in figure 3.4.1. For the horizontal LVDT huddle test, the two other horizontal LVDTs, the three accelerometers, the three horizontal L-4Cs and the STS-2 X and Y readout were utilized as reference sensors. For the vertical LVDT huddle test, the other two vertical LVDTs, the three vertical L-4Cs, the three accelerometers and the STS-2 X, Y and Z readout were utilized as reference sensors. The horizontal reference sensors helped to subtract motion from cross coupling. The inverted pendulum stage and GAS filter stage were bridged by mechanical clamping, such that the optical table was rigidly clamped to ground. Since LVDTs measure relative motion between ground and optical table, this resulted in low LVDT outputs, promising for precise huddle test results as described in section 3.5.3.

Figure 3.5.8 shows the huddle test results for the horizontal LVDTs. The ASD is already very close to the calculated noise, requiring only small subtractions of seismic signal by the huddle test. The measured noise matches the calculation to a high extent.

Figure 3.5.9 shows the huddle test results for the vertical LVDTs. The ASD deviates significantly from the noise, with a maximum factor of roughly 100 at 4 Hz. This differential motion is estimated to be caused by the comparably soft intermediate plate, loaded by the heavy optical table. This leads to soft internal resonances. The measured noise matches the calculation roughly. The peaks in the ASD at 4 Hz and 50 Hz were not subtracted perfectly in the huddle test and show up as small peaks in the noise measurement.

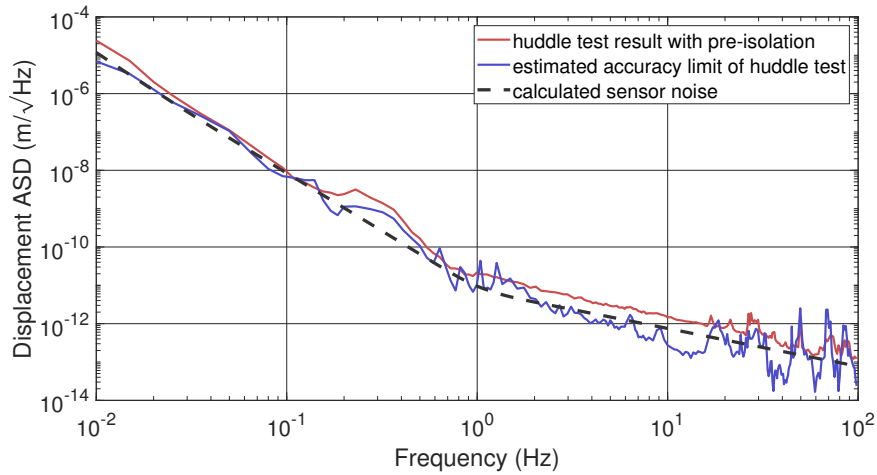


Figure 3.5.7: Huddle test result with pre-isolation, estimated accuracy limit to the huddle test from imperfect subtraction x_m^{res} and calculated sensor noise. Three vertical L-4C sensors are utilized for these huddle tests. The diagram shows that the seismic pre-isolation was just good enough to attenuate seismic contributions to the huddle test result below the real sensor noise at most frequencies.

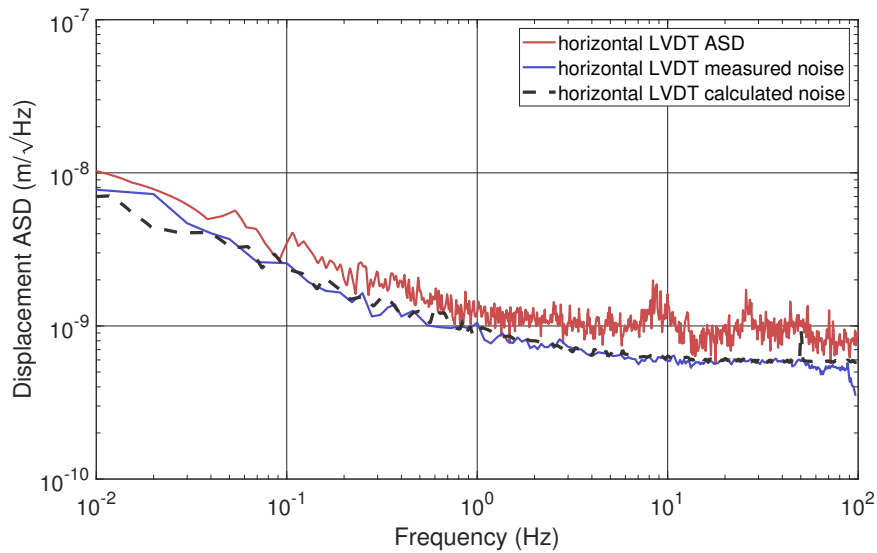


Figure 3.5.8: Amplitude spectral density, measured noise resulting from the huddle test and calculated noise of the horizontal LVDTs. The inverted pendulum stage of the AEI-SAS was mechanically clamped to minimize the differential motion between ground and optical table.

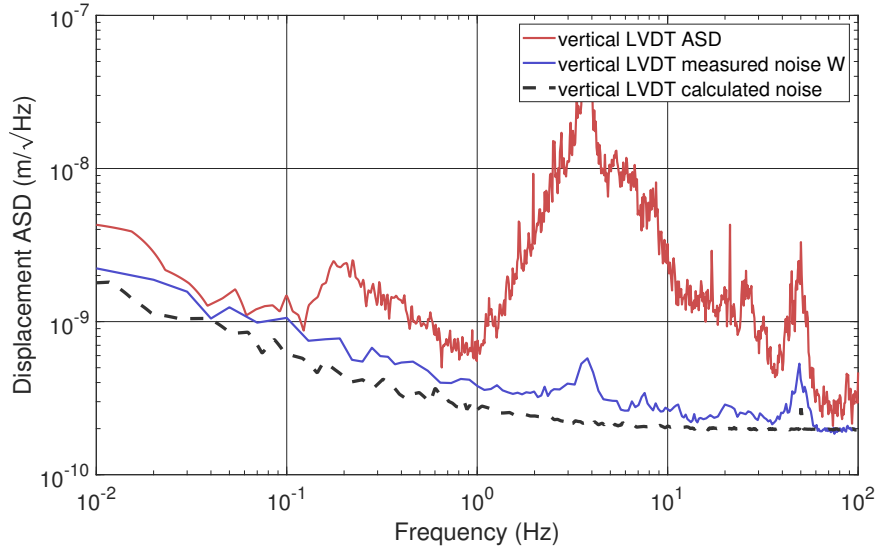


Figure 3.5.9: Amplitude spectral density, measured noise resulting from the huddle test and calculated noise of the vertical LVDTs. The GAS filter stage of the AEI-SAS was mechanically clamped to minimize the differential motion between ground and optical table. The ASD features a high peak at roughly 4 Hz, presumably created by internal resonances of the soft intermediate plate, loaded by the heavy optical table.

3.5.5 Huddle test for accelerometers

The noise of the accelerometers was measured in another huddle test. As with the LVDTs, the standard sensor arrangement shown in figure 3.4.1 was utilized, with one additional accelerometer positioned on the optical table. This additional accelerometer was assigned as the main sensor, while the three accelerometers and the three horizontal L-4Cs were used as reference sensors. The optical table was passively isolated.

Figure 3.5.10 shows the ASD of the main accelerometer, the huddle test result and the calculated noise. Measurement and calculation match very well below 1 Hz, while they have a slightly different slope above. This results in deviations of a factor of ≈ 2 . The ASD resembles the measured noise above 4 Hz closely, hinting towards the measured noise being more precise than the calculated noise.

3.6 Concepts of active seismic isolation

The active isolation of the AEI-SAS can be separated into two different concepts: local active isolation and global active isolation.

- **Local active isolation** is well known since it is used for the large gravitational wave interferometers worldwide. This concept aims at minimizing the inertial motion of the suspended mirrors, which is achieved by isolating each optical table separately; thereby, control loops gain data from sensors within one pre-isolation system and feed the signals to actuators within the same.
- **Global active isolation** is a comparatively unexplored concept. It does not primarily aim at minimizing the inertial motion of the mirrors, but at minimizing the relative motion between them; therefore, control loops force both mirrors to move in common.

There are some attempts in the gravitational wave community outside the AEI 10m prototype that make use of global isolation techniques. These are described

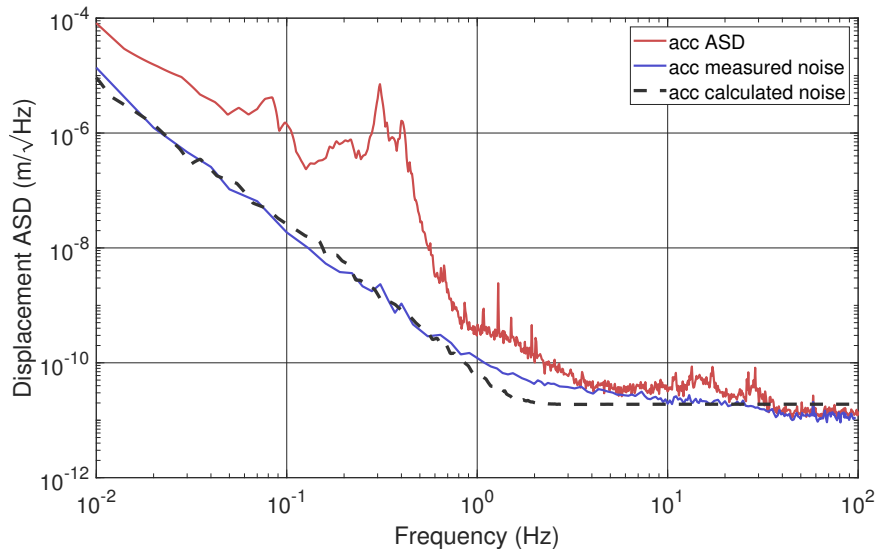


Figure 3.5.10: Amplitude spectral density, measured noise resulting from the huddle test and calculated noise of the accelerometers. Measured and calculated noise match precisely below 1 Hz and have a slightly different slope above, resulting in small deviations of a factor of ≈ 2 .

in appendix A.5. Seismic isolation of the AEI 10 m prototype is the only isolation system worldwide that primarily focuses on global isolation. It is implemented using two types of sensors: the SPI interferometers stabilize differential motion in long and the optical levers stabilize differential pitch and yaw motion, if used in pairs on two AEI-SASs. Details are described in section 3.8.

The other degrees of freedom are primarily isolated inertially using local sensors and actuators; nevertheless, they include techniques and considerations to minimize differential mirror motion.

Local active isolation sets the foundations for the more sophisticated global isolation techniques, and is investigated in detail in the following section. Global seismic isolation is described in section 3.8.

3.7 Local active seismic isolation

This section describes the implementation of local active isolation at the AEI-SASs. The control scheme is adapted from the Advanced LIGO control scheme for the HAM-SAS [S⁺09] and the Horizontal Access Module - Internal Seismic Isolation (HAM-ISI) [M⁺15b]. Basic principles, like sensor blending and sensor correction, are well known and used in many pre-isolation systems worldwide. They are adapted to the circumstances at the AEI 10 m prototype and improved with novel techniques. The final local active isolation performance is depicted and analyzed with a noise model based on SimulinkNB [Wip14].

3.7.1 Control scheme

Figure 3.7.1 shows the control scheme for local active isolation in one degree of freedom. Ground motion x_g acts on the AEI-SAS, which is labelled as plant. The AEI-SAS filters the motion with its transfer function T_p and the optical table moves with the signal of interest X_i . The inertial optical table motion is sensed by a set of inertial sensors (geophones or accelerometers) and the differential motion between optical table and ground is measured by a set of relative sensors (LVDTs).

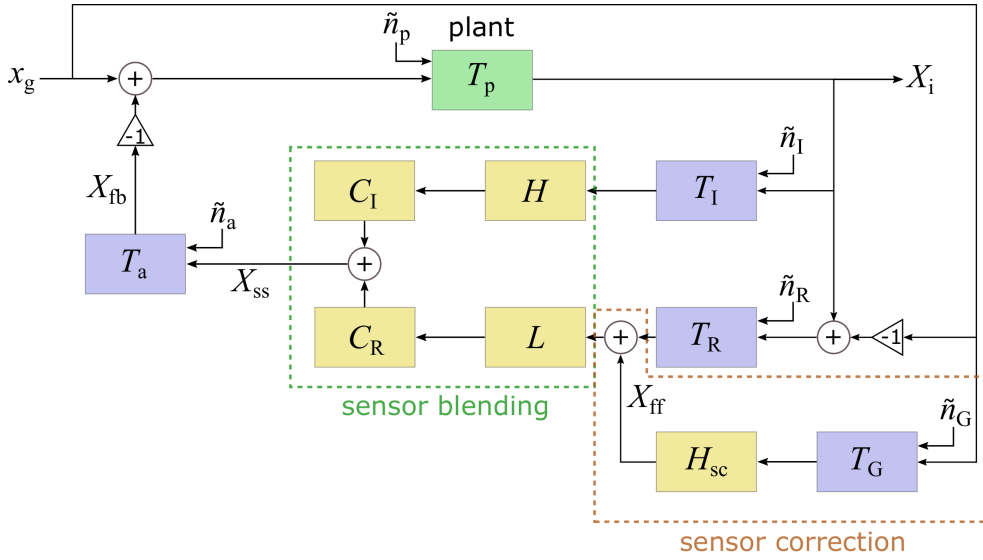


Figure 3.7.1: Block diagram of the control scheme for local active isolation of the AEI-SAS. Each translational degree of freedom is isolated using this control scheme. The rotational degrees of freedom do not include sensor correction. T_p : transfer function of the plant; T_I : transfer function of the inertial sensor; T_R : transfer function of the relative sensor; T_G : transfer function of the ground sensor; H : high pass filter; L : low pass filter; H_{sc} : high pass filter for sensor correction; T_a : transfer function of the actuator; C_I : gain of inertial sensor controller; C_R : gain of relative sensor controller; x_g : ground motion; $X_i = x_i + n_i$: plant output with x_i : output signal and n_i : noise at output; $X_{ss} = x_{ss} + n_{ss}$: super sensor output with x_{ss} : super sensor signal and n_{ss} super sensor noise; $X_{fb} = x_{fb} + n_{fb}$: feedback output with x_{fb} : feedback signal and n_{fb} : noise in feedback output; \tilde{n} : input referred noise of the sensors and actuator.

Ground motion in the translational degrees of freedom is detected by the ground motion sensor STS-2. It is multiplied with a digital high pass filter and subtracted from the relative sensor output to construct an inertial signal. This technique is called sensor correction and is explained in section 3.7.6. Ground motion in the rotational degrees of freedom is not measured and hence, the LVDT outputs in these degrees of freedom are not corrected.

The corrected relative sensor signal and the inertial sensor signal are multiplied with complementary low and high pass filters and added together to a so-called super sensor. This technique is called sensor blending and aims at finding a super sensor with the lowest possible noise given the available sensors. Sensor blending is described in more detail in section 3.7.5.

The controller filters C_I and C_R are exemplarily included and symbolize a larger set of filters for calibration (see section 3.7.2), coordinate system transformation (see section 3.7.3) and the controller, setting the loop gain (see section 3.7.7). The super sensor signal is sent to the actuators, which exert a force onto the AEI-SAS to minimize X_i .

The control system of the AEI 10 m prototype is very flexible. Different control states can be activated digitally to investigate different features. In the best possible local isolation state, all degrees of freedom use the control scheme described in figure 3.7.1. This operation state is referred to as “high gain local inertial isolation”. Another often used state is “damping of the resonances”, only using LVDTs with low gain. A third common option is a fully “passive isolation”, by opening the feedback control loop.

3.7.2 Sensor calibration

After acquisition of the sensor signals with CDS, they are calibrated to units of meter to provide comparability among the sensors, actuators and ground motion. The calibration filters are theoretically derived in section 3.4, but due to small perturbations in the sensor mechanics and the electronics, a measurement of the calibration filter is required for confirmation.

There are three different calibration methods that were tested for sensors of the AEI-SAS:

- Calibration of the sensors prior to installation.

The LVDTs were calibrated using a test stand with the option to shift the sensing coil inside the excitation coil by defined values. The inertial sensors were calibrated by comparison to the STS-2, which was calibrated by the manufacturer.

After installation, the calibration prior to installation turned out to be imprecise. The sensor calibration depends on the exact setup and orientation of the sensors, which slightly differs for each installation.

- Calibration of the LVDTs to the STS-2 after installation and subsequent calibration of the inertial sensors to the LVDTs.

The AEI-SASs were put into a “high gain inertial control state”, such that the LVDT signals were dominated by ground motion. The LVDT output was compared to the calibrated STS-2 signal and equalized. In the next step, the isolated AEI-SAS stages were actuated with the voice-coil actuators and the inertial sensor outputs were calibrated to the LVDT signals.

This calibration technique strongly depends on an equal seismic motion at the STS-2 and the AEI-SAS for calibration of the LVDTs. Over the distance of about 11 m between west/south AEI-SASs and the STS-2, the seismic amplitude varies significantly. Consequently, this calibration method turned out to be imprecise.

- Calibration of the LVDTs with μm -screws and subsequent calibration of the inertial sensors to the LVDTs.

The optical tables of all AEI-SASs were displaced using μm -screws in different degrees of freedom multiple times and the LVDT response was measured. The resulting calibration factors for the LVDTs were highly repeatable, verifying their reliability. The inertial sensors were calibrated by actuation of the isolated stages with voice-coil actuators and comparison to the calibrated LVDTs. This technique achieved the highest accuracy.

The actuators were calibrated to the LVDTs at zero frequency by equalizing an actuation signal to its LVDT response.

3.7.3 Coordinate system transformation

Each set of local AEI-SAS sensors counts three devices, each of which has one sensitive direction. The alignment of the sensors is chosen such that each set either measures AEI-SAS motion in all horizontal or vertical degrees of freedom.

After calibration of the sensor signals to units of meter, the signals of each sensor set are converted to global Cartesian degrees of freedom by linear combination. This allows for intuitive operation of the experiment and interpretation of the data. The coordinate system transformation for the horizontal sensors is described by

$$\begin{pmatrix} x \\ y \\ rz \end{pmatrix} = \mathbb{M} \cdot \begin{pmatrix} H_1 \\ H_2 \\ H_3 \end{pmatrix}, \quad (3.7.1)$$

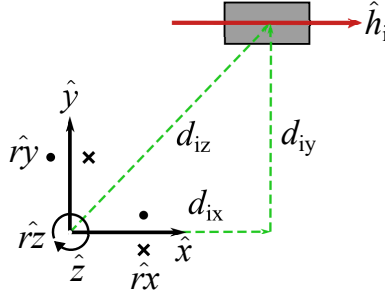


Figure 3.7.2: Depiction of a horizontal sensor i , a Cartesian coordinate system and all relevant parameters to calculate the transformation matrix entries for this sensor.

with

$$\mathbb{M} = \begin{pmatrix} H_{1x} & H_{2x} & H_{3x} \\ H_{1y} & H_{2y} & H_{3y} \\ H_{1rz} & H_{2rz} & H_{3rz} \end{pmatrix}, \quad (3.7.2)$$

where x, y, rz describe the Cartesian degrees of freedom, H_1, H_2, H_3 describe the local sensor degrees of freedom of sensor 1, 2 and 3, \mathbb{M} is the transformation matrix and H_{ij} are the matrix entries describing the contribution of sensor i to the Cartesian degree of freedom j . The transformation for the vertical degrees of freedom is analogous.

Determination of the transformation matrix entries

The entries of matrix \mathbb{M} were determined with two different approaches. In the **first approach**, the orientation of the sensors to the axes and their distances to the origin were measured with a length scale. Figure 3.7.2 shows the relevant parameters. $\hat{x}, \hat{y}, \hat{z}, \hat{r}_x, \hat{r}_y$ and \hat{r}_z are the unit vectors in the Cartesian degrees of freedom and the rotations around them, \hat{h}_i is the unit vector pointing into the sensitive direction of sensor i and d_{ix}, d_{iy} and d_{iz} are the distances of sensor i to the axes.

The transformation matrix is calculated by inverting a matrix \mathbb{M}' , defined as

$$\mathbb{M} = (\mathbb{M}')^{-1} = \begin{pmatrix} H'_{1x} & H'_{1y} & H'_{1rz} \\ H'_{2x} & H'_{2y} & H'_{2rz} \\ H'_{3x} & H'_{3y} & H'_{3rz} \end{pmatrix}^{-1}, \quad (3.7.3)$$

with the matrix entries calculated as

$$\begin{aligned} H'_{ix} &= \hat{h}_i \cdot \hat{x}, \\ H'_{iy} &= \hat{h}_i \cdot \hat{y}, \\ H'_{irz} &= (\hat{h}_i \cdot \hat{r}_z) d_{iz}. \end{aligned} \quad (3.7.4)$$

$\hat{h}_i \cdot \hat{x}$, $\hat{h}_i \cdot \hat{y}$ and $\hat{h}_i \cdot \hat{r}_z$ are the projections of the sensitive direction of sensor i onto the axes.

Figure 3.7.3 shows the orientations and distances to the axes of all horizontal sensors installed in the west AEI-SAS. Choosing the horizontal L-4C geophones as an example, the transformation matrix is calculated to be

$$\mathbb{M} = (\mathbb{M}')^{-1} = \begin{pmatrix} -1 & 0 & 0.815 \\ 0 & 1 & 0.8 \\ 0 & -1 & 0.8 \end{pmatrix}^{-1} = \begin{pmatrix} -1 & 0.509 & 0.509 \\ 0 & 0.5 & -0.5 \\ 0 & 0.625 & 0.625 \end{pmatrix}. \quad (3.7.5)$$

This calculation was executed for all sensor sets on each AEI-SAS. Some measurements indicated that the matrix entries are slightly imprecise, leading to increased cross-coupling between different degrees of freedom. This was investigated in more detail by measuring tilt-to-horizontal coupling in the x and y degrees of freedom with the horizontal L-4Cs and comparing the measurement to the rz degree of freedom.

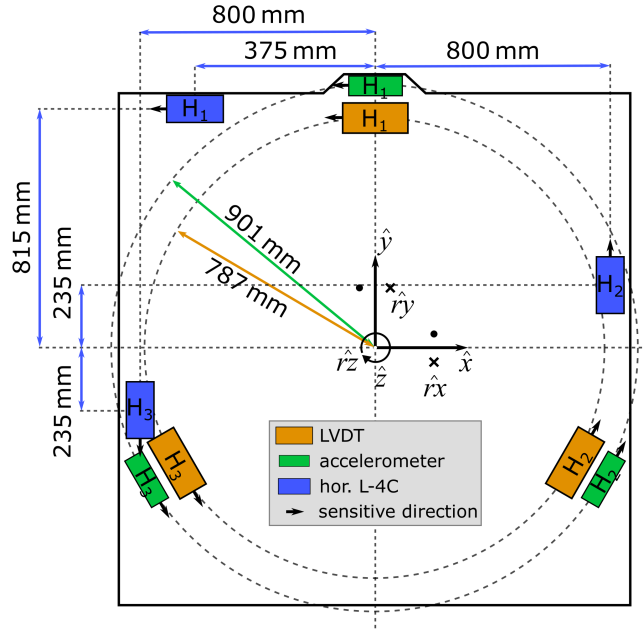


Figure 3.7.3: Positions of the horizontal sensors on the west AEI-SAS. The figure shows all relevant distances to calculate the transformation matrix entries. It is adapted from [K⁺20].

In principle, rz should not be affected by tilt-to-horizontal coupling; nevertheless, the top left diagram in figure 3.7.4 shows that the optical table rz motion measurement is clearly above L-4C noise following the slope of tilt-to-horizontal noise. This noise is assumed to couple to the rz measurement due to an inaccurate transformation matrix for the horizontal L-4C geophones. The bottom diagram in the same figure shows the ratio between rz and x . This ratio describes the clearance between x and rz measurement and is a factor of ≈ 10 below 0.08 Hz.

One likely reason for an inaccurate coordinate transformation matrix is the fact that L-4Cs are no point objects, and it is not clear, to which part of the L-4Cs the distance has to be measured. Also, the calibration of the L-4Cs can be imprecise.

To increase the suppression of tilt-to-horizontal noise in the rz measurement, a **second approach** was tested to optimize the transformation matrix. For this approach, it is assumed that the LVDT transformation matrix is precise. This is correct to a high extent, since LVDT positions are mechanically constrained by design of the AEI-SAS. The optical table was actuated in rz direction using the voice-coil actuators. This led to high coherence between the LVDT rz measurement and each individual horizontal L-4C. The transfer functions from LVDT rz to the L-4C signals contain information about the distance of the L-4Cs to the z axis and their orientation, directly providing the third column entries of M' :

$$M = (M')^{-1} = \begin{pmatrix} -1 & 0 & 1.088 \\ 0 & 1 & 1.197 \\ 0 & -1 & 1.145 \end{pmatrix}^{-1} = \begin{pmatrix} -1 & 0.465 & 0.465 \\ 0 & 0.489 & -0.511 \\ 0 & 0.427 & 0.427 \end{pmatrix}. \quad (3.7.6)$$

This second approach has two big advantages: it does not rely on a correct definition of the L-4C position to measure distances, and it automatically corrects for imprecise sensor calibrations. The top right diagram in figure 3.7.4 shows the optical table x motion limited by tilt-to-horizontal coupling, the optical table rz motion, ground motion in x for reference and the L-4C noise. The optical table rz motion has

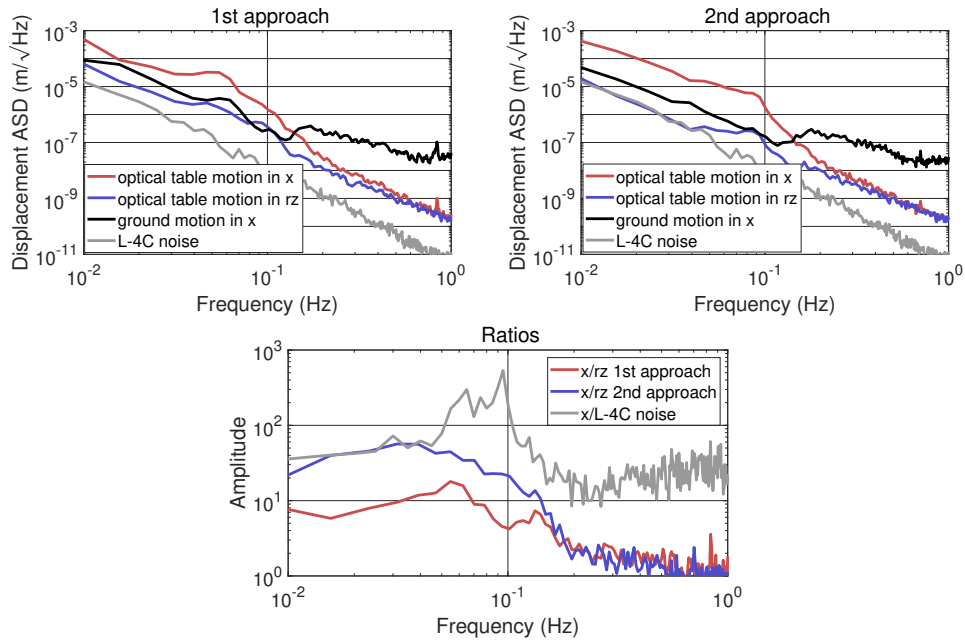


Figure 3.7.4: Top diagrams: Amplitude spectral densities of the optical table x and rz motion for two calibration methods explained in the text. The optical table motion was measured with the horizontal L-4C geophones. For comparison, the ground motion in x and the L-4C noise are included. The second approach leads to a higher clearance between x and rz motion, limited by L-4C noise.

Bottom diagram: Ratios between x and rz optical table motion and between x optical table motion and L-4C noise. The first approach results in a ratio of roughly 10 below 0.08 Hz while the second approach reaches a ratio of 56 below 0.045 Hz, limited by L-4C noise.

a higher clearance from the x motion. Below 0.045 Hz, the rz motion is limited by L-4C noise preventing an even higher clearance. The bottom diagram shows a ratio between rz and x motion of up to a factor 56, limited by L-4C noise.

The second approach to measure and calculate the transformation matrix entries by actuation provided significantly better results. Tilt-to-horizontal coupling to the optical table rz measurement is lowered by more than a factor 3 compared to the first approach. Higher improvements might be achieved, but are masked by L-4C noise.

The transformation matrix for the vertical degrees of freedom is calculated accordingly. The matrix entries were determined using the actuated measurement approach.

3.7.4 Sensor positioning and alignment

The main requirement on sensor positioning and alignment is to cover all relevant degrees of freedom with each sensor set. A secondary argument is the optimization of signal-to-noise ratios. A simple thought experiment helps to understand the influence of sensor positioning and alignment on the signal-to-noise ratio:

Consider the setup of horizontal L-4C geophones shown in figure 3.7.3 and a motion in x direction. This motion is only sensed by L-4C H_1 , since the sensitive directions of H_2 and H_3 are orthogonal to this motion. Equation 3.7.6 shows that all three L-4Cs contribute to the measurement of x motion, though. This is required to subtract a possible rz motion, which would otherwise be interpreted as x motion by H_1 . The sensor output of only one L-4C contains signal, while all three L-4Cs contribute with their noise. Hence, the signal-to-noise ratio in this degree of freedom is decreased.

The signal-to-noise ratio snr_j in a degree of freedom $j = \{x, y, rz\}$ is calculated

Table 3.7.1: Multiplication factors T_j for the horizontal LVDTs, accelerometers and the horizontal L-4Cs as positioned on the west AEI-SAS. The LVDTs and accelerometers are positioned equally on each AEI-SAS, whereas the L-4C alignment changes due to space constrains.

Sensor type	T_x	T_y	T_{rz}
hor. LVDTs	1.225	1.225	1.363
accelerometers	1.225	1.225	1.561
hor. L-4Cs	0.836	1.414	1.13

Table 3.7.2: Multiplication factors T_j for the vertical LVDTs and L-4Cs as positioned on the west AEI-SAS. The LVDTs are positioned equally on each AEI-SAS, whereas the L-4C alignment changes due to space constrains.

Sensor type	T_z	T_{rx}	T_{ry}
vert. LVDTs	1.732	0.643	0.643
vert. L-4Cs	1.647	1.151	1.085

as

$$snr_j = \frac{x_j}{\tilde{n}_s} \times T_j. \quad (3.7.7)$$

x_j is the signal in degree of freedom j , \tilde{n}_s is the input referred noise of one sensor of the sensor set under investigation and T_j is a multiplication factor, depending on the alignment and positioning of the sensor under investigation to the degree of freedom j .

T_j for the horizontal degrees of freedom is calculated by

$$T_x = \sum_{i=1}^3 \frac{H_{ix} \cdot (\hat{x} \cdot \hat{h}_i)}{\sqrt{(H_{1x})^2 + (H_{2x})^2 + (H_{3x})^2}} \quad (3.7.8)$$

$$T_y = \sum_{i=1}^3 \frac{H_{iy} \cdot (\hat{y} \cdot \hat{h}_i)}{\sqrt{(H_{1y})^2 + (H_{2y})^2 + (H_{3y})^2}} \quad (3.7.9)$$

$$T_{rz} = \sum_{i=1}^3 \frac{H_{irz} \cdot (\hat{r}z \cdot \hat{h}_i)}{\sqrt{(H_{1rz})^2 + (H_{2rz})^2 + (H_{3rz})^2}} \quad (3.7.10)$$

where $i = \{1, 2, 3\}$ labels the sensors, H_{ij} describes the entries of \mathbb{M} , \hat{x} , \hat{y} and \hat{z} define unit vectors in x , y and z and \hat{h}_i is the unit vector pointing into the sensitive direction of sensor i . The quantities $\hat{x} \cdot \hat{h}_i$, $\hat{y} \cdot \hat{h}_i$ and $\hat{r}z \cdot \hat{h}_i$ are projections of the sensitive direction of the sensors onto the degree of freedom under investigation.

Table 3.7.1 shows the multiplication factors T_j for the horizontal LVDTs, the accelerometers and the horizontal L-4Cs, as positioned on the west AEI-SAS (see figure 3.7.3). T_x and T_y are equal for the LVDTs and accelerometers, while T_{rz} differs for both sensor types due to the different distances to the z axis. The horizontal L-4C alignment is advantageous for the y direction and disadvantageous for the x direction, as predicted by the thought experiment.

The calculations of T_j for the vertical sensors are executed analogously. The results are shown in table 3.7.2. The vertical LVDT positioning is highly beneficial for the z degree of freedom compared to rx and ry . This results from the short distances between the sensors and the z axis.

The results for the vertical LVDTs are verified by a huddle test measurement shown in figure 3.7.5. The same setup is utilized as for the vertical LVDT huddle test

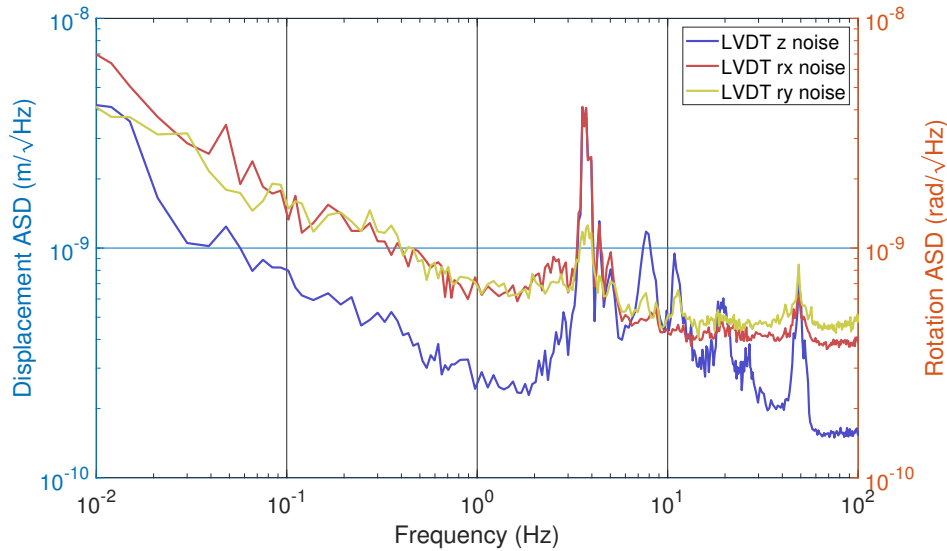


Figure 3.7.5: Huddle test measurements for the vertical LVDT signals of the west AEI-SAS, converted to Cartesian degrees of freedom. The measurements show a lower noise in z compared to rx and ry by a factor of 2–2.5 besides the resonances. This verifies the calculations of T_j , which predict a lower noise in z by a factor of 2.7 compared to rx and ry . The noise in z is given as displacement ASD, while the other curves are given as rotation ASDs.

measurement, described in section 3.5.4. This time, the time series to be analyzed are converted to Cartesian degrees of freedom. Since all three vertical LVDTs contribute to each vertical degree of freedom, they can not be used as reference sensors. This decreases the precision of the huddle test, but the tendency is still clearly visible. Besides the resonances between 2–60 Hz, the noise in z is a factor of 2–2.5 below the noise in rx and ry . Table 3.7.2 predicts a factor of about 2.7. The small difference can be explained by the measurement imprecision. This measurement verifies the principle of setup dependent signal-to-noise ratios, described in this section.

The calculations show that sensor positioning and alignment can be optimized to maximize the signal-to-noise ratio in certain degrees of freedom. Space constrains and the standardized AEI-SAS design prevents an optimization of sensor positioning and alignment for the AEI 10 m prototype; nevertheless, the calculations of T_j are required for precise noise estimations, and find application, for example, in section 3.7.10. Future projects should investigate the influence of sensor positioning on the signal-to-noise ratios and design their isolation system accordingly.

3.7.5 Sensor blending

Section 3.2.1 underlines the importance of sensor noise for an effective feedback control loop. Most sensors are specialized to a certain frequency band in terms of their noise performance, depending on their functionality and readout; hence, they enable good feedback loop suppression at a certain frequency band but poor suppression for other frequencies. Sensor blending is a technique to combine two or more sensors together, to form a so-called super sensor. If blending parameters are chosen correctly, the super sensor combines the good signal-to-noise ratios of the different sensors and enables good feedback loop suppression over a widely extended frequency range.

In the following, a very basic sensor blending for a relative and an inertial sensor is described. The inertial sensor has a better high frequency noise performance, the relative sensor has a better low frequency noise performance; hence, they are multiplied with a high pass filter H and a low pass filter L , accordingly. Afterwards,

the two signals are combined to form the super sensor signal X_{ss} . Figure 3.7.6 shows a block diagram of a basic sensor blending scheme. Other noise sources than sensor noise are neglected here. The open loop gain is described by

$$G = (T_I H C_I + T_R L C_R) T_a T_p. \quad (3.7.11)$$

L and H are complementary filters, such that

$$L(s) + H(s) = 1, \quad (3.7.12)$$

where s is the Laplace variable. For a stable sensor blending, it is required that

$$T_R C_R \approx T_I C_I \approx \frac{1}{2} T_s C_s \quad (3.7.13)$$

in the frequency range around the blending frequency. T_s and C_s represent an effective sensor and controller. For the open loop gain, this leads to

$$G \approx T_s C_s T_a T_p, \quad (3.7.14)$$

which is approximately equal to the open loop gain in a simple feedback loop (see equation 3.2.4); hence, to a good approximation, sensor blending does not influence the output signal of the system.

The difference to a standard feedback control system becomes visible by investigating the sensor noise, being filtered by low and high pass filters. The noise at the system's output n_i depends on the sensor noise by

$$n_i = -\frac{G}{1+G}(\tilde{n}_I H(s) + \tilde{n}_R L(s)). \quad (3.7.15)$$

Other noise sources than the input referred relative and inertial sensor noise are neglected here. If the blending filters are chosen correctly, the high noise of both sensors is filtered out such that the total resulting noise is significantly lower than for a single sensor.

There are three relevant parameters for a basic sensor blending with two sensors:

- the blending frequency ω_b that determines the crossing frequency at which both filters have equal amplitude,
- the filter order of the low pass filter l that determines the steepness of the filter to high frequencies,
- and the filter order of the high pass filter h that determines the steepness of the filter to low frequencies.

$L(s)$ and $H(s)$ depend on l and h each, such that $L(s) \rightarrow L_{lh}(s)$ and $H(s) \rightarrow H_{lh}(s)$. The calculation of blending filters is demonstrated exemplarily in appendix E.

Figure 3.7.7 shows three pairs of blending filters with low and high pass orders of 2-2, 2-3 and 4-4. The blending frequency is at 1 Hz for each filter set. Around the blending frequency, the filters have an amplitude > 1 , which is called ripple. The ripple increases with higher filter orders. If a coherent signal, like seismic motion, dominates the output of both blended sensors, the out-of-phase addition results in a total transfer function for the super sensor of 1 and the ripple has no influence. If noise limits the output of at least one sensor, the phase of this sensor is strongly distorted and the ripple amplifies this noise; hence, if noisy signals are blended together, a compromise between a higher roll-off and lower ripple around the blending frequency has to be found.

Section 3.7.8 presents a calculation method to find the optimal sensor blending parameters for each degree of freedom.

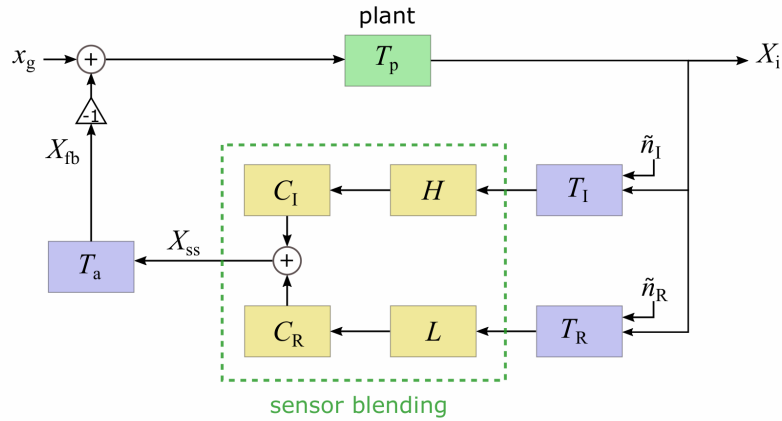


Figure 3.7.6: Feedback control loop including sensor blending. Two different sensors measure the same signal x_p . The inertial sensor has low noise at high frequencies, the relative sensor has low noise at low frequencies; therefore, they are multiplied with a high pass filter and low pass filter, before being combined to the super sensor. Noise is only shown for the sensors and neglected for other components. T_p : transfer function of the plant; T_I : transfer function of inertial sensor; T_R : transfer function of relative sensor; T_a : transfer function of the actuator; C_I : gain of inertial controller; C_R : gain of relative controller; x_g : ground motion; $X_i = x_i + n_i$: plant output with x_i : output signal and n_i : noise at output; $X_{ss} = x_{ss} + n_{ss}$: super sensor output with x_{ss} : super sensor signal and n_{ss} noise of super sensor signal; $X_{fb} = x_{fb} + n_{fb}$: feedback output with x_{fb} : feedback signal and n_{fb} : noise in feedback output; \tilde{n} : noise of the two sensors.

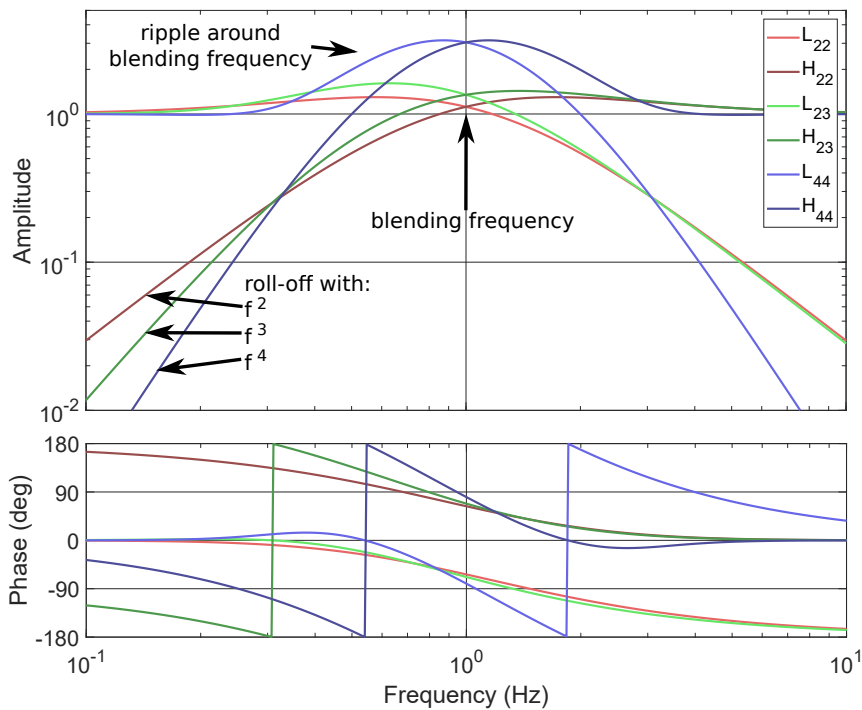


Figure 3.7.7: Bode diagram of three pairs of blending filters with low and high pass orders of 2-2, 2-3 and 4-4. The blending frequency is at 1 Hz.

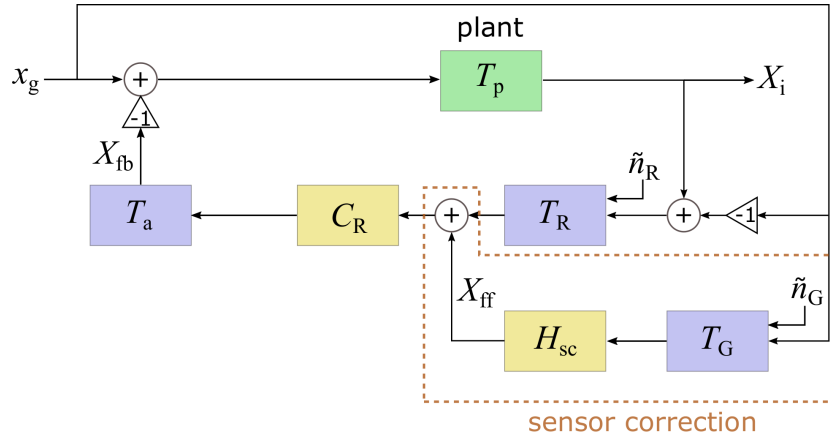


Figure 3.7.8: Feedback control loop, including a feedforward system that provides sensor correction. The LVDT measures the differential motion between the plant and the ground. The ground motion is also measured by a ground motion sensor, multiplied with a high pass filter and then added to the LVDT output to subtract the ground motion contribution. T_p : transfer function of the plant; T_R : transfer function of the relative sensor; T_G : transfer function of the ground sensor; T_a : transfer function of the actuator; C_R : controller filter of the relative sensor; H_{sc} : sensor correction high pass filter; x_g : ground motion signal; $X_i = x_i + n_i$: plant output with x_i : output signal and n_i : noise at output; $X_{ff} = x_{ff} + n_{ff}$: feedforward output with x_{ff} : feedforward signal and n_{ff} : noise in feedforward output; $X_{fb} = x_{fb} + n_{fb}$: feedback output with x_{fb} : feedback signal and n_{fb} : noise in feedback output; \tilde{n} : noise of the two sensors.

3.7.6 Sensor correction

Seismic isolation of the AEI-SAS includes LVDTs that do not measure motion with respect to an inertial frame but with respect to ground. Feedforward techniques are used to subtract the ground motion signal from the LVDT output and by that create an inertial signal. This process is called sensor correction.

Figure 3.7.8 shows a block diagram of sensor correction for the AEI-SAS. The LVDTs with transfer function T_R measure the differential motion between optical table and ground. Additionally, a ground motion sensor of the type STS-2 with transfer function T_G measures the ground motion. The STS-2 output is multiplied by a high pass filter H_{sc} in order to filter out the high STS-2 noise at low frequencies. It is added to the LVDT output, such that the feedback signal x_{fb} is described by

$$x_{fb} = (x_i - x_g)T_R C_R T_a + x_{ff} C_R T_a, \quad (3.7.16)$$

where the feedforward signal x_{ff} is described by

$$x_{ff} = x_g T_G H_{sc}. \quad (3.7.17)$$

The LVDT and the STS-2 outputs are both calibrated to units of meter, such that $T_G = T_R := T_s/2$ can be assumed. T_s describes the transfer function of an effective sensor. In the frequency range, where $H_{sc} = 1$, the feedback signal is described by

$$x_{fb} = x_i T_s C_R T_a, \quad (3.7.18)$$

which is independent on x_g and hence provides a feedback signal for inertial isolation. Condition 3.7.18 holds for frequencies above the ripple of the sensor correction high pass filter H_{sc} .

If other noise sources are neglected and the LVDT and STS-2 are calibrated to the same unit, the noise of the plant output n_i is given by

$$n_i = -\frac{G}{1+G}(\tilde{n}_G H_{sc} + \tilde{n}_R). \quad (3.7.19)$$

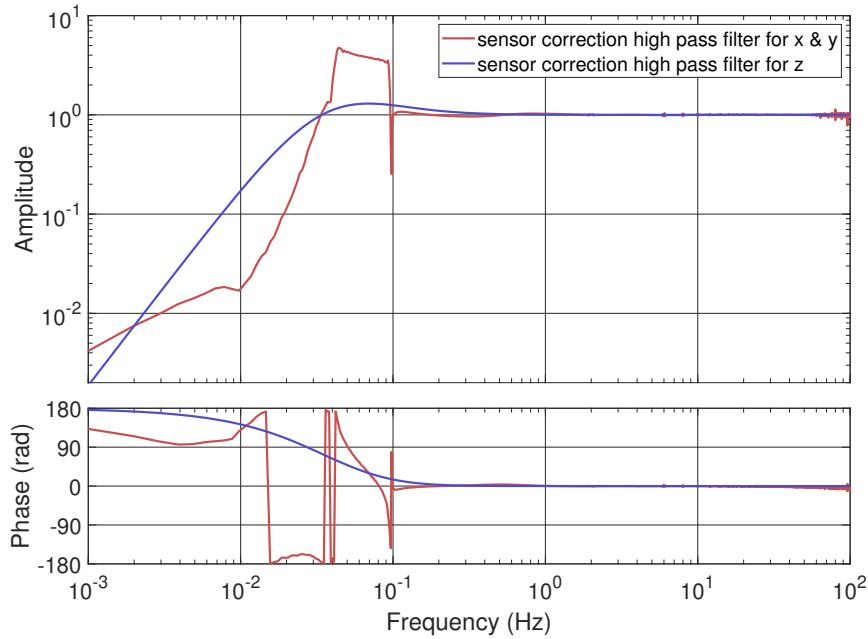


Figure 3.7.9: Bode plot of the sensor correction high pass filters. For x and y a combination of an FIR filter and IIR filters is utilized to obtain a rapid attenuation below the micro seismic peak. For z a standard second order high pass blending filter, as explained in section 3.7.5, is chosen.

The performance of sensor correction strongly depends on coherence between the LVDTs and the STS-2 and on equality of their signal amplitude. At frequencies above ≈ 4 Hz, the large distance between LVDTs and STS-2 in combination with the short wavelength of seismic waves results in incoherence between the sensors; hence, sensor correction above 4 Hz is ineffective. At low frequencies, the STS-2 noise limits the sensor correction. The frequency below which the STS-2 noise significantly contributes to the sensor output varies depending on the magnitude of the seismic. High pass filters are implemented to filter out the sensor noise.

In the z degree of freedom, a second order high pass filter H_{22} with a blending frequency of 0.04 Hz is chosen. For x and y , a more aggressive filter is utilized. Tilt-to-horizontal coupling can contribute noise to the horizontal STS-2 output already below 0.1 Hz. A standard high pass filter with a roll-off starting above 0.1 Hz is not chosen, since this would prevent a sensor correction on the micro-seismic peak; hence, a very steep Finite Impulse Response (FIR) filter [Hua05], modified by Infinite Impulse Response (IIR) filters [Lan12], is utilized. The modification by the IIR filters reduces the computational costs strongly. Figure 3.7.9 shows a bode plot of both high pass filters.

Figures 3.7.10 and 3.7.11 show displacement spectral densities of the optical table motion in x and z with and without sensor correction. The measurements were taken in a “high gain inertial control state”.

Sensor correction reduces the optical table motion in x between 0.1–4 Hz by up to a factor of 10. At low frequencies the improvement is limited by the ripple of the high pass filter as shown in figure 3.7.9, which amplifies the STS-2 noise. At high frequencies, a loss of coherence between the STS-2 and the LVDTs prevent an improvement. The improvement of optical table motion between 0.1–4 Hz is limited by tilt-to-horizontal noise of the accelerometers, which were used as inertial in-loop sensors blended together with the LVDTs. This limitation is not linked to the real performance of sensor correction, masking potentially better results.

In z the optical table motion is reduced by up to a factor 10 between ≈ 0.02 –3 Hz. At low frequencies, it is difficult to determine limitations due to an insufficient res-

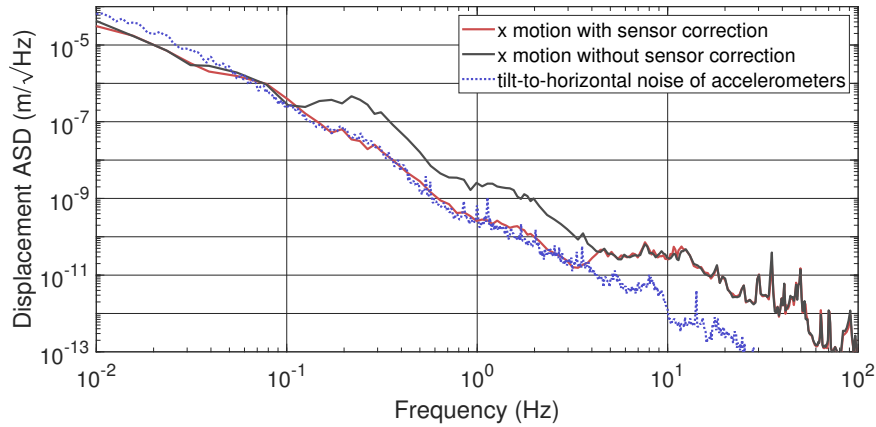


Figure 3.7.10: Amplitude spectral densities of the AEI-SAS optical table motion with and without sensor correction in x . An improvement of up to a factor 10 is measured between 0.1–4 Hz. The improvement is limited by tilt-to-horizontal noise of the accelerometers, which were used as in-loop sensors blended together with the LVDTs; hence, a better sensor correction performance might be achieved but is masked by accelerometer noise.

olution. At high frequencies, the improvement is again prevented by the distance between LVDTs and STS-2, resulting in a loss of coherence and signal equality. It is unclear, what is limiting the improvement in between these frequencies. Readout sensor noise is well below the measured motion, such that the measurement presumably shows the real sensor correction performance.

3.7.7 Controller

All techniques described in sections 3.7.2–3.7.6 aim at generating error signals in each Cartesian degree of freedom with the lowest possible noise, given the available sensors; thereby, the open loop gain G is unaffected. The controller processes these error signals and generates feedback signals for the actuators by adding loop gain.

The loop gain added by the controllers is limited by internal structural resonances of the AEI-SASs above ≈ 5 Hz. These resonances couple to the sensors and enhance the motion strongly, while simultaneously adding a phase shift. If the open loop gain on the resonances exceed unity gain, the control loop can become unstable, as described in section 3.2.3; therefore, the controller filters have to be rolled off to high frequencies. Additional notch filters are applied to decrease the gain directly on the strongest internal resonances.

The west AEI-SAS obtained multiple improvements in order to dampen the internal resonances, decreasing their amplitude and to stiffen the internal structure mechanically, shifting internal resonances to higher frequencies. These improvements are described in detail in [B⁺17] and [Ber18]. They partly enable higher unity gain frequencies.

Figure 3.7.12 shows three measurements of the open loop gain of the west AEI-SAS. Two measurement show the open loop gain in x , one with accelerometers as in-loop sensors and one with L-4C geophones as in-loop sensors. One measurement shows the open loop gain in z . The controller filter for the L-4C control scheme in x has a higher unity gain frequency of 8 Hz, compared to the accelerometers with 1.4 Hz. This leads to a larger overall gain and a larger suppression of motion. This results from strong internal resonances in the mechanically soft springbox, where the accelerometers are located, compared to the comparably stiff optical table, where the L-4Cs are located. The strong resonances in the springbox couple directly to the accelerometers, while they are filtered by the GAS filters and the Viton[®] stage for the geophones. The

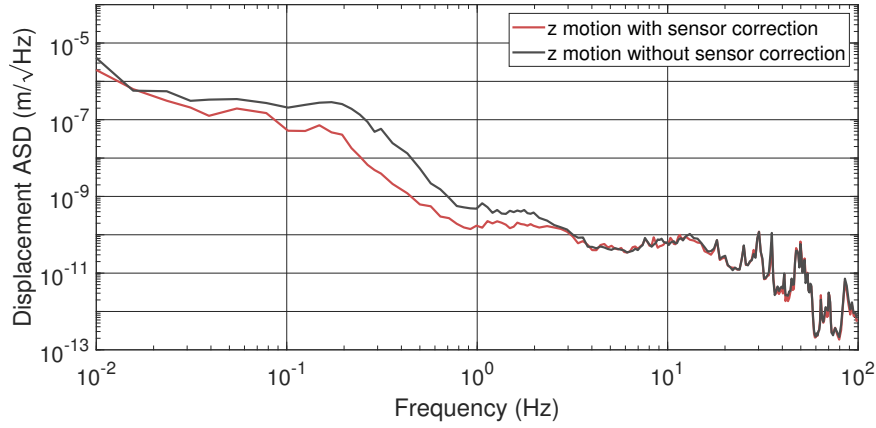


Figure 3.7.11: Amplitude spectral densities of the AEI-SAS optical table motion with and without sensor correction in z . An improvement of up to a factor 10 is achieved between 0.02 – 2.5 Hz.

unity gain frequency in z is even higher with 22.4 Hz.

The open loop gains of the west AEI-SAS in the other degrees of freedom were not directly measured, but calculated by multiplication of the controller filters with the passive transfer functions. The calculated open loop gains in all six degrees of freedom are shown in figure 3.7.13. In x and z the calculations match the direct measurements to a high extent; hence, it is assumed that the calculations are precise in the other degrees of freedom as well.

In a first attempt, the controller filters were designed by eye with a focus on high unity gain frequencies to extend the active isolation band to higher frequencies, which lead to the results shown in figure 3.7.13. Section 3.8.4 discusses requirements for the controller filter design based on simulations, with the result that the filters should be optimized in some degrees of freedom. Possible improvements for the sub-SQL interferometer based on different controller filter designs are analyzed in section 3.9.

The open loop gains for the central and south AEI-SASs were not measured with high precision, because the large actuation could damage the already installed suspensions on the optical table; hence, they are inferred from the passive transfer functions of the west AEI-SAS and the central and south controller filter settings.

3.7.8 Sensor blending optimization

This section describes a new calculation method to identify optimal blending parameters for each degree of freedom, given certain sensors. A simple sensor blending for the local seismic isolation of the AEI-SASs requires the optimization of three blending parameters: the low pass order l , the high pass order h and the blending frequency ω_b . These three parameters are tuned to minimize the cost function $C(\omega_b)$, which, for the local active isolation, is chosen to be the optical table velocity root mean square (rms) $|\dot{X}_{lh}(\omega_b)|_{rms}$.

Minimizing the velocity instead of the displacement has two major benefits. First, it has an increased weighting of the higher frequency band containing the suspension resonances (0.6 – 10 Hz). Pre-isolating the suspensions at their resonances is among the key tasks for the AEI-SASs. Second, scattering noise is proportional to velocity of the object which is hit by the scattered light before re-entering the interferometer (see section 2.7).

The sensor blending optimization is executed, by adding all relevant noise sources, converting them to a velocity, calculating the rms and finding the global minimum. This is done with the equation

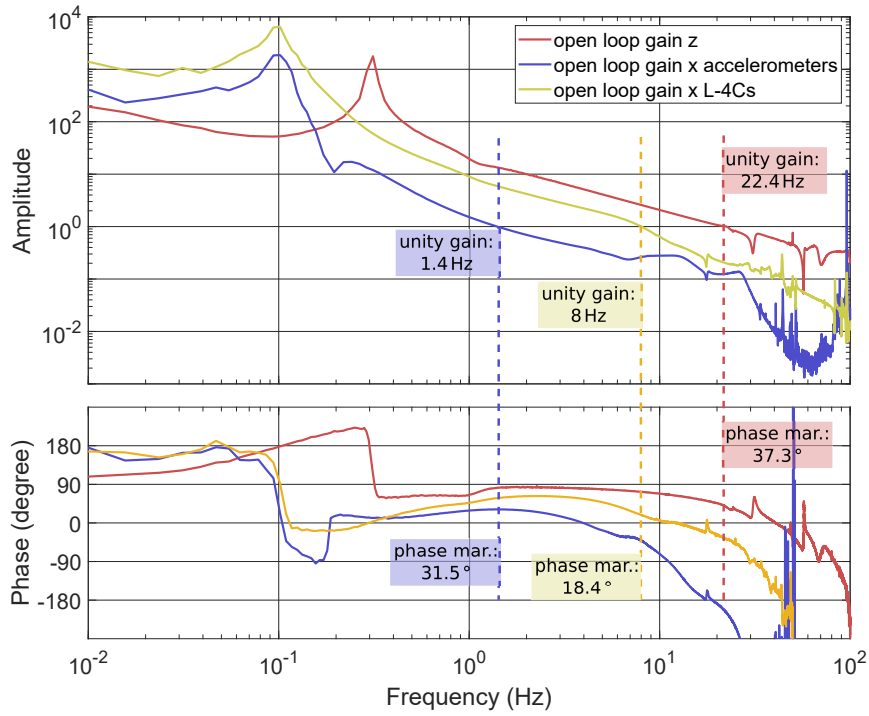


Figure 3.7.12: Open loop gain measurements for the west AEI-SAS. Two measurements show the x degree of freedom, one for in-loop accelerometers and one for in-loop L-4C geophones. The third measurement shows the z degree of freedom. The large gain peak close to 100 Hz and the large phase peaks around 40 Hz in the accelerometer measurement result from a lack of coherence and are not real features of the control loop.

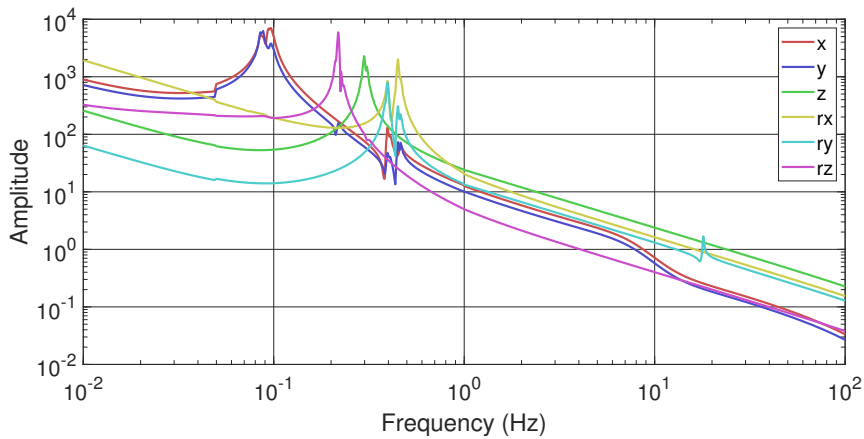


Figure 3.7.13: Open loop gain calculations for the west AEI-SAS in all six degrees of freedom. For the horizontal degrees of freedom, only the L-4C open loop gains are shown. The controller filters were multiplied with the measured passive transfer functions in order to obtain the open loop gain.

Table 3.7.3: Optimal blending parameters and resulting velocity *rms* for all degrees of freedom. The horizontal degrees of freedom are analyzed for accelerometers and horizontal L-4C geophones as in loop sensors.

Degree of freedom	Low pass order	High pass order	f_b (Hz)	Velocity <i>rms</i>
x (accelerometers)	3	2	0.35	3.7e-8 m/s
y (accelerometers)	3	2	0.36	3.6e-8 m/s
rz (accelerometers)	2	2	0.32	3.9e-9 rad/s
x (L-4Cs)	3	4	0.45	5.2e-8 m/s
y (L-4Cs)	3	4	0.45	5.2e-8 m/s
rz (L-4Cs)	2	3	0.43	4.3e-9 rad/s
z	2	3	0.05	1.1e-8 m/s
rx	2	3	0.12	4e-9 rad/s
ry	2	3	0.12	5.1e-9 rad/s

$$\begin{aligned}
 |\dot{X}_{lh}(\omega_b)|_{rms} = & \int_{f=f_{\min}}^{f=f_{\max}} \omega \left([x_{\text{res}}(\omega) + x_{\text{R}}(\omega, \omega_b)L_{lh}(\omega, \omega_b)]^2 \right. \\
 & \left. + \tilde{n}_{\text{R}}^2(\omega)L_{lh}^2(\omega, \omega_b) + \tilde{n}_{\text{I}}^2(\omega)H_{lh}^2(\omega, \omega_b) \right)^{1/2} d\omega. \quad (3.7.20)
 \end{aligned}$$

The integral over the frequency range of interest calculates the *rms* from an amplitude spectral density. The ω converts displacement to velocity. Three terms are added incoherently: $[x_{\text{res}}(\omega) + x_{\text{R}}(\omega, \omega_b)L_{lh}(\omega, \omega_b)]$ describes two paths of ground motion coupling to the optical table. The prior is ground motion that can not be suppressed by the control loop due to insufficient gain. The latter is ground motion coupling to the LVDT, creating noise in the LVDT output, as explained in section 3.4.2. This is filtered by the low pass filter L_{lh} . \tilde{n}_{R} describes the electronic noise of the relative sensor, also filtered by the low pass filter L_{lh} . \tilde{n}_{I} describes the inertial sensor noise, filtered by the high pass filter H_{lh} .

The LVDT noise is split into the two contributions, because the seismic contribution is coherent to x_{res} , while the electronic noise is incoherent. This requires coherent and incoherent addition. x_{res} does not depend on the blending frequency and hence does not influence the optimal blending parameters. It is still included in the calculations, because it gives insight into limitations of the active isolation performance.

Low and high pass filter combinations up to an order of four are investigated for the optimization. A maximum order of four was chosen, because the increased amplitude of the ripple prevents good results for higher orders (see figure 3.7.7).

The optimal blending parameters for a local isolation scheme are calculated for all degrees of freedom, with the results shown in table 3.7.3. The table reveals that horizontal motion is the largest contributor to the overall optical table motion. At the same time, horizontal motion along the longitudinal direction is the most important degree of freedom, emphasizing the need for better horizontal isolation. The analysis for each degree of freedom was done in three steps. This is exemplarily shown for the west AEI-SAS in the x (longitudinal) degree of freedom using accelerometers:

- **Step 1:** Figure 3.7.14 shows the optical table velocity *rms* plotted over the blending frequency for blending filter combinations up to an order of four. The absolute minimum of all curves gives the best possible filter order combination and the optimal blending frequency. In this case, it is a third order low and

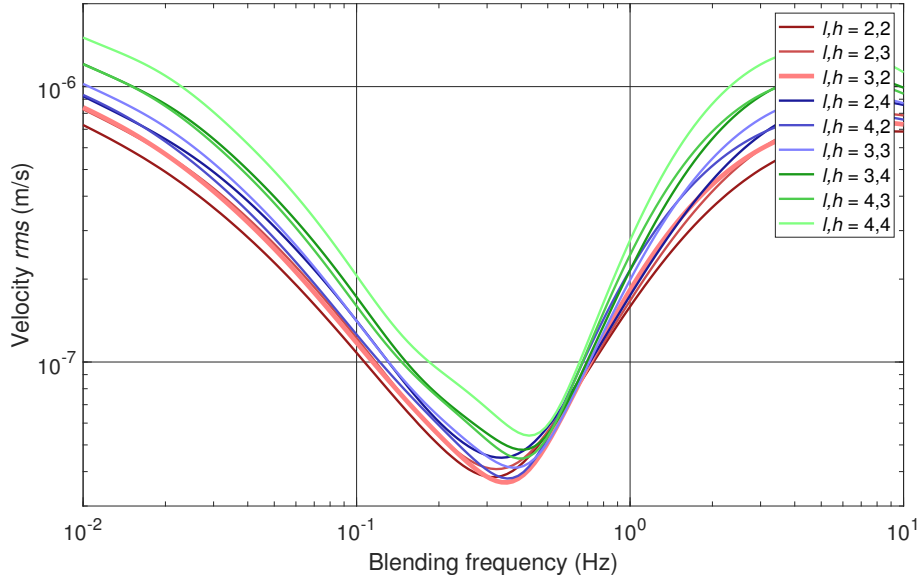


Figure 3.7.14: Velocity *rms* over blending frequency for the west AEI-SAS in *x*, using accelerometers as in loop sensors. *l, h* describe the low and high pass order. The best possible filter order combination is given by a third order low and second order high pass with an optimal blending frequency of 0.35 Hz.

second order high pass combination with a blending frequency of 0.35 Hz. The resulting optical table velocity is $|\dot{X}_{lh}(\omega_b)|_{rms} = 3.7 \times 10^{-8}$ m/s.

- **Step 2:** Figure 3.7.15 shows the individual contributions to the velocity *rms* for the optimal filter order combination of 3,2. The residual, optimally suppressed ground motion and LVDT electronic noise are negligible compared to the ground motion coupling to the LVDT and the accelerometer noise. A lower blending frequency increases the contribution of accelerometer noise and lowers the contribution of LVDT ground motion coupling. A higher blending frequency results in the opposite.
- **Step 3:** Figure 3.7.16 shows velocity spectral densities of the individual contributions for filter orders of 3,2 and a blending frequency of 0.35 Hz. Only the two major contributions of ground motion coupling to the LVDTs and accelerometer noise are included, as well as the total optical table velocity and its *rms*. This figure reveals that the overall *rms* is dominated by motion around the micro seismic peak.
- **Conclusion:** The overall optical table velocity *rms* is limited by ground motion coupling to the LVDTs and by accelerometer noise, which is limited by tilt-to-horizontal noise. The frequency range around the micro seismic peak dominates the overall *rms*.

The LVDT noise contribution could be lowered by a more effective sensor correction; therefore, the equality of the ground sensor signal and the ground motion contribution to the LVDT signal would have to be increased. A possible solution would be to place ground motion sensors onto the baseplate of the AEI-SAS. Downsides of this idea are the high expenses of additional STS-2 and that the sensor correction signal would not be equal for the three AEI-SASs anymore, potentially resulting in larger differential motion.

The accelerometer noise contribution could be lowered by pre-isolating the accelerometers in the tilt degree of freedom. In their current location, inside the springbox, this is not possible. This motivates additional horizontal L-4C

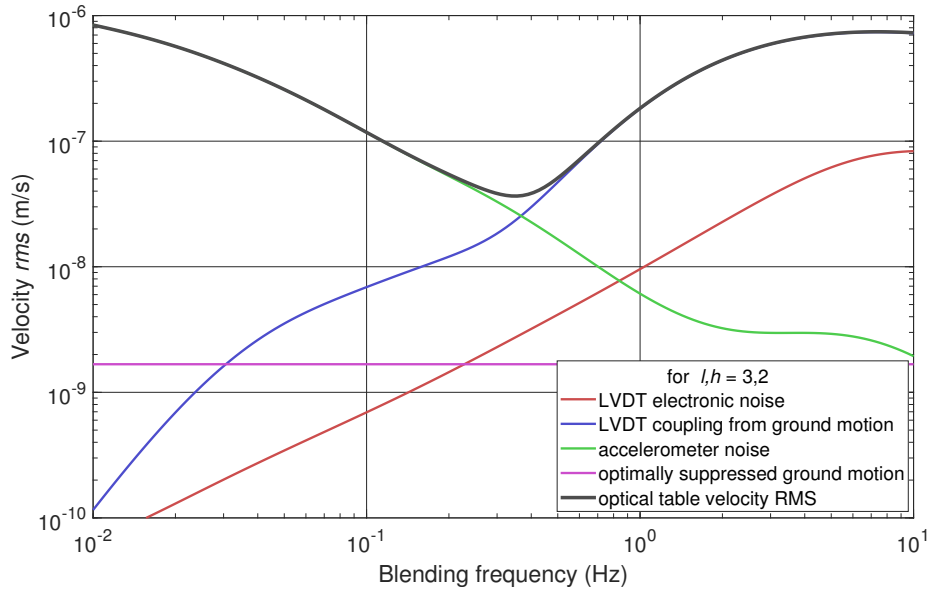


Figure 3.7.15: Velocity *rms* over blending frequency for the west AEI-SAS in *x*, using accelerometers as in loop sensors. The individual contributions for blending filters of order 3,2 are shown. Residual, optimally suppressed ground motion and LVDT electronic noise are negligible compared to the LVDT ground motion coupling and accelerometer noise.

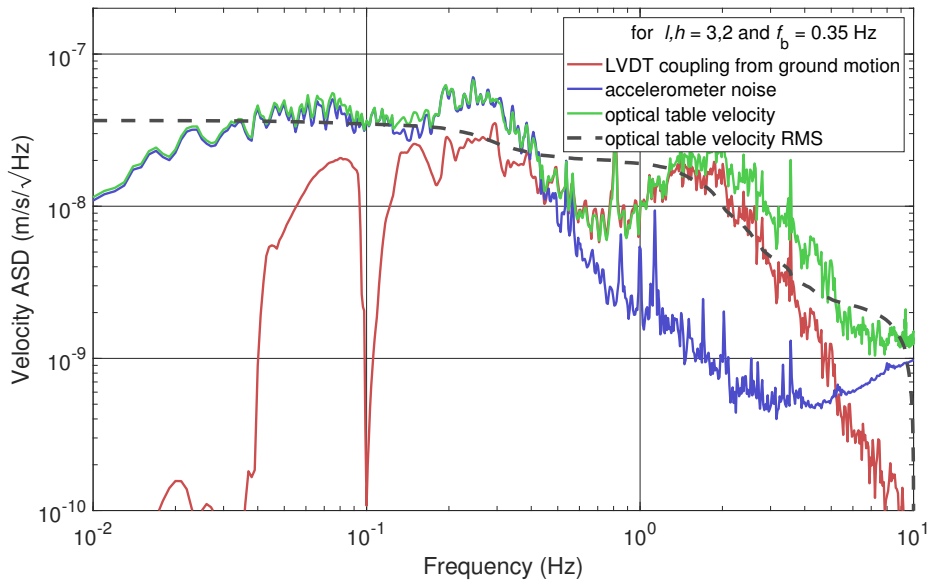


Figure 3.7.16: Velocity spectral densities of the west AEI-SAS in *x*, using accelerometers as in loop sensors. The figure contains the two major contributions of ground motion coupling to the LVDTs and accelerometer noise, as well as the overall optical table velocity and its *rms*. The *rms* is dominated by motion at the micro seismic peak.

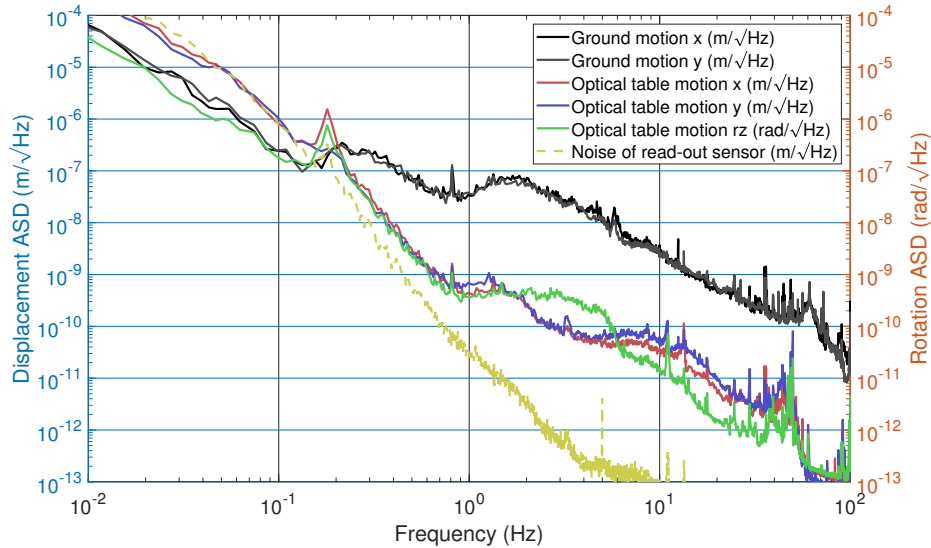


Figure 3.7.17: Horizontal motion of the optical table, horizontal ground motion and readout sensor noise in a “high gain local inertial control state”. The x and y measurements are limited by readout sensor noise below 0.13 Hz. This data is published in [K⁺20].

geophones on the optical table. This section only investigates the local control scheme and neglects optical levers. Without optical levers, the optical table velocity *rms* in tilt is larger than the ground velocity *rms* in tilt; hence, accelerometers are favorable over horizontal L-4C geophones for the local isolation. Section 3.8.3 investigates a sensor blending optimization for a global control scheme including optical levers, with different results.

In the final configuration, the blending parameters will be optimized for global isolation, as shown in section 3.8.3, not for local isolation; nevertheless, the investigations shown here serve as a simplified demonstrator for the more complex global isolation optimizations. Furthermore, the calculations in this section can be used for other seismic isolation systems that are based on local isolation.

3.7.9 Local isolation performance

All local active control techniques described in sections 3.7.1–3.7.8 are utilized to set the AEI-SAS into the “high gain local inertial isolation” state and the resulting inertial optical table motion of the west AEI-SAS is measured with L-4C geophones.

The vertical L-4C geophones were not only used as readout sensors, but also in-loop. This can falsify the measurement data, if the sensor noise is not significantly below the motion signal. For the measurements presented here, the sensor noise is sufficiently low in the frequency range between roughly 0.05–50 Hz. Below and above this range, the measurement might not resemble real motion.

Figure 3.7.17 shows the horizontal optical table motion, the horizontal ground motion and the readout sensor noise. The measurement in x and y is limited by readout sensor noise below roughly 0.13 Hz. Isolation of a factor of about 100 is provided above 1 Hz. The peaks at 0.18 Hz result from unknown effects in the accelerometer control loop and are under investigation.

Figure 3.7.18 shows the vertical optical table motion, the vertical ground motion and the readout sensor noise. The measurements are limited by sensor noise below roughly 0.03 Hz. This noise is not imprinting additional motion onto the optical table because it is attenuated by the sensor blending. An isolation of a factor 100 up to nearly 1000 is provided above 1 Hz.

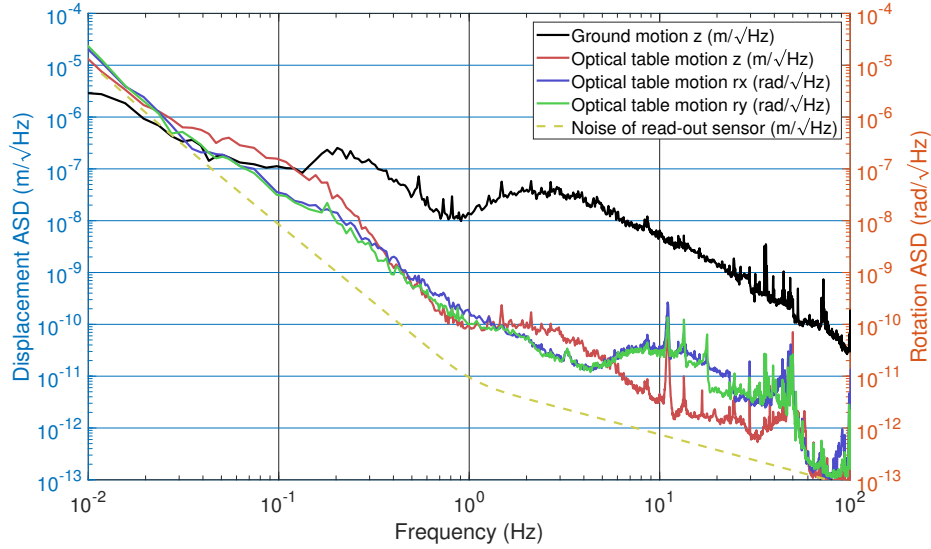


Figure 3.7.18: Vertical motion of the optical table, vertical ground motion and readout sensor noise in a “high gain local inertial control state”. The measurements are limited by readout sensor noise below 0.03 Hz. This data is published in [K⁺20].

3.7.10 Performance analysis

The measured performance of the local inertial isolation was analyzed to understand the limitations; therefore, a model of the AEI-SAS was implemented using SimulinkNb [Wip14]. The inputs to the model are measurements of ground motion and sensor noise. The model contains various transfer functions of AEI-SAS stages in the different degrees of freedom, simulates active control techniques like sensor blending and sensor correction, and includes a closed loop suppression of the inputs. The outputs of the model are expected optical table motion in x , z and rx . The degrees of freedom y and ry are mostly equal to x and rx and are therefore neglected. The rz optical table motion is predominantly created by cross coupling from other degrees of freedom. At the time of writing, this can not be modelled, since the cross coupling mechanisms are mostly unknown.

For this analysis, a “high gain local inertial control state” is chosen, with horizontal L-4C geophones as in-loop sensors instead of accelerometers.

Figures 3.7.19, 3.7.20 and 3.7.21 show the results of the model in comparison to the measured optical table motion and ground motion. All investigated contributions to the total motion are displayed.

The model prediction in x , shown in figure 3.7.19, matches the measurement accurately below roughly 1.5 Hz. Below 0.07 Hz readout sensor noise is limiting, which does not describe the real optical table motion. The real motion is assumed to follow the L-4C noise curve. From 0.07–0.7 Hz readout sensor noise and L-4C sensor noise are limiting. LVDT noise limits the performance from 0.7–4 Hz and coupling from rotational motion of the springbox to translational motion of the optical table (see section 3.3.2) is limiting above 4 Hz. The comparably large deviations between model and measurement above 4 Hz are assumed to result from an imprecise measurement of rotational ground motion, which is utilized to calculate the coupling from rotational springbox motion to translational optical table motion.

The model prediction in z , shown in figure 3.7.20, matches the measurement accurately below roughly 13 Hz. LVDT noise is among the limiting contributions for all frequencies below 13 Hz. It is accompanied by readout sensor noise below 0.03 Hz and residual, optimally suppressed ground motion above 0.4 Hz. Prediction and measurement do not match above 13 Hz, where internal resonances of the AEI-SAS are expected to be limit the performance.

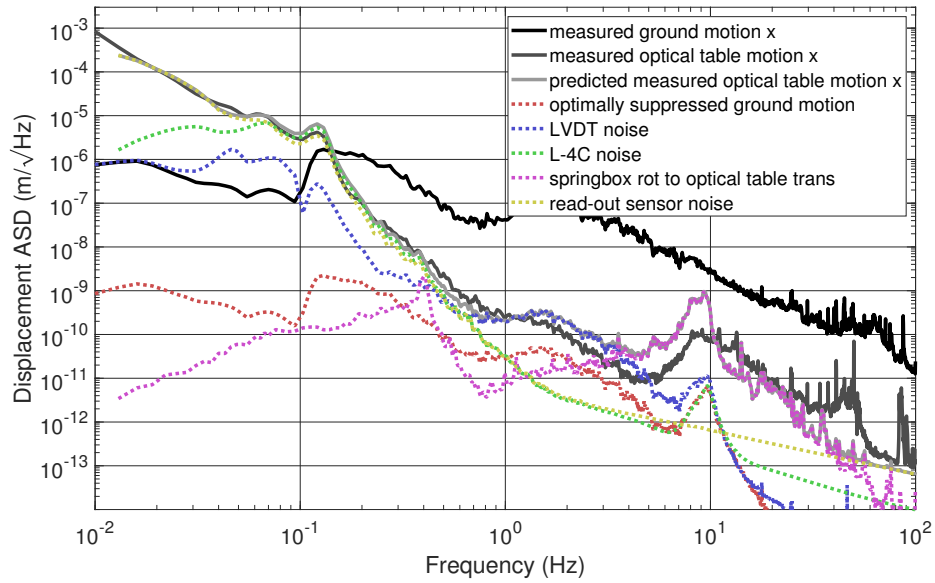


Figure 3.7.19: Modelled and measured optical table motion in x , ground motion in x and all contributions to the modelled motion. Measurement and model match accurately below 1.5 Hz. Larger deviations above 4 Hz are assumed to result from an imprecise measurement of rotational ground motion.

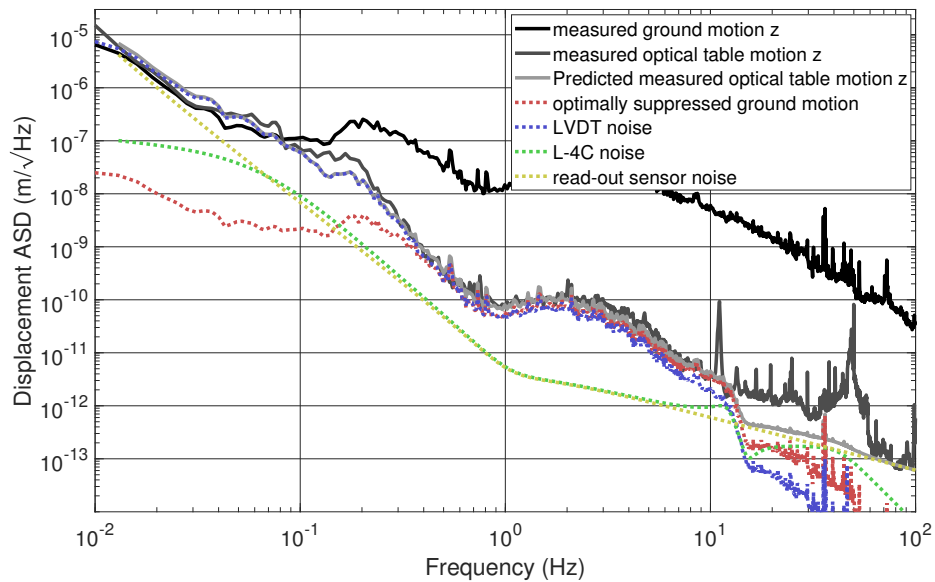


Figure 3.7.20: Modelled and measured optical table motion in z , ground motion in z , and all contributions to the modelled motion. Measurement and model match accurately below 13 Hz. Larger deviations above 13 Hz are assumed to result from internal resonances of the AEI-SAS, which are not included in the model.

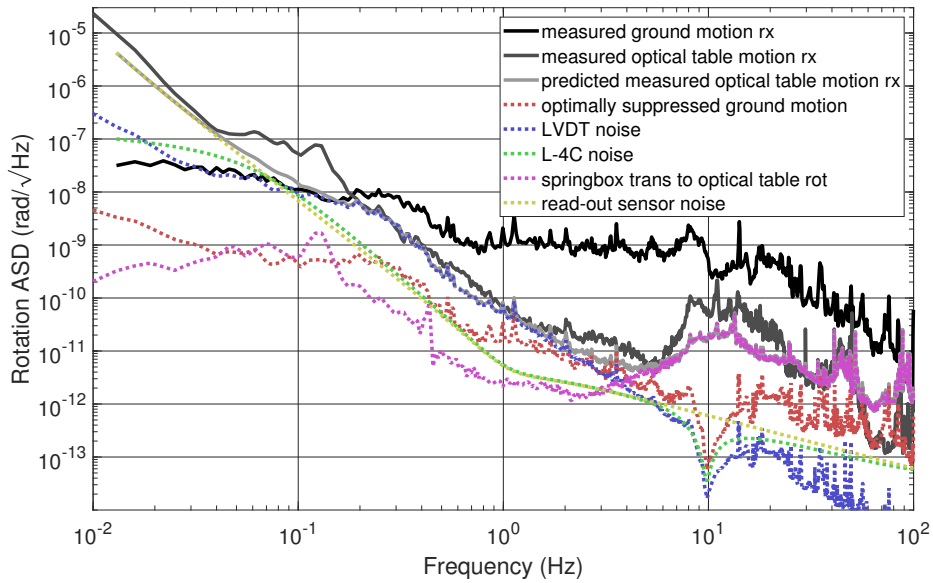


Figure 3.7.21: Modelled and measured optical table motion in rx , ground motion in rx , and all contributions to the modelled motion. Measurement and model match accurately below 6 Hz, with an exception between 0.04–0.2 Hz, presumably caused by cross coupling from x .

Figure 3.7.21 shows the model prediction in rx . Model and measurement match below 6 Hz, except for the frequency range from 0.04–0.2 Hz. In this range, the measurement resembles the shape of optical table motion in x , which leads to the conclusion that the deviation is caused by cross coupling. Below 0.1 Hz readout sensor noise limits the measurement but does not describe the real motion of the optical table. From 0.1–6 Hz LVDT noise is the dominating noise source with optimally suppressed ground motion, contributing significantly between 1–6 Hz. Above 6 Hz coupling of translational motion of the springbox to rotational motion of the optical table (see section 3.3.2) is the main driver for the motion.

Conclusion

The analysis with the AEI-SAS model reveals detailed insight into limitations of the optical table motion. In all degrees of freedom, LVDT noise and L-4C noise limit the active isolation performance in a certain frequency range or over the full range of interest. Closed loop suppression of ground motion offers large space for improvements, which could be exploited with lower sensor noise.

The SPI interferometers and optical levers have significantly lower noise compared to LVDTs and at low frequencies also L-4C geophones, as shown in figures 3.4.39 and 3.4.40. Using these sensors, it is possible to lower the optical table motion drastically and introduce a minimization of differential motion between the optical tables. Detailed descriptions and analyses are described in the following section.

3.8 Global active seismic isolation

Global active isolation, focussing on the minimization of differential mirror motion, is a new and less explored control scheme compared to local active isolation. At the AEI 10 m prototype, it is based on sensors that measure differential motion of two isolation platforms and the resulting minimization of the same. This minimizes the differential motion between interferometer test masses, which is crucial in order to achieve highly sensitive interferometric measurements.

To the author’s knowledge, the global control scheme for the AEI-SASs is the only active isolation scheme in the gravitational wave community that is predominantly based on global isolation techniques. The differential longitudinal motion between the three AEI-SAS is stabilized using the SPIs. The differential pitch and yaw motion is stabilized with pairs of optical levers on two AEI-SAS, as described in more detail in section 3.8.1. The control techniques, like sensor blending and sensor correction, are similar to the local active isolation techniques. The major differences between both isolation schemes are the following:

- **New sensors**, namely the SPI and optical lever, are utilized. These sensors have significantly lower noise, improving the isolation performance in long, pitch and yaw, and consequently also reducing tilt-to-horizontal coupling on the horizontal L-4C geophones.
- The **error signals** to be minimized are partly not limited to motion of one AEI-SAS but describe motion of two AEI-SASs. This requires a different control scheme, which was chosen to be the leader-follower principle at the AEI 10 m prototype. A description of the control scheme is presented in section 3.8.1.
- A new set of coordinates, called **global coordinates**, is introduced. They describe common and differential motion between two AEI-SAS and are utilized in section 3.8.2 to analyze the coupling from optical table motion to the interferometer error signals. 12 global coordinates are required to describe the motion of a combination of two AEI-SASs. The notation used for global isolation within this thesis is defined as:
 - σ for common motion or δ for differential motion,
 - and $x_l, x_s, x_v, rx_p, rx_r, rx_y$ for the mirror degrees of freedom longitudinal (long), side, vertical (vert), pitch, roll and yaw.
- The interconnection of the AEI-SASs results in a **complex coupling from optical table motion to the interferometer error signals**. A detailed analysis is provided in section 3.8.2. This coupling is included in the cost functions for global sensor blending optimization, presented in section 3.8.3.

This section presents the new control schemes, describes the coupling from optical table motion to the interferometer error signals, and presents a revision of sensor blending optimization, with the goal of minimizing the interferometer error signals instead of the optical table velocity. At the end, the global isolation performance is measured, and possible improvements are investigated.

3.8.1 Control scheme

Figure 3.8.1 shows the control scheme for differential longitudinal motion. Ground motion is incident on two different AEI-SASs, labelled “follower plant”, which is the south or west AEI-SAS, and “leader plant”, which is the central AEI-SAS. The differential motion is sensed by the SPI, processed by a controller, and sent to the actuators to control the follower plant. Minimizing the differential motion by acting a force only on one AEI-SAS is called leader-follower principle, where the south and west AEI-SASs follow the central AEI-SAS in their longitudinal directions.

Sensor blending of the SPI with inertial sensors was tested. A blending below the unity gain frequency of the control loop resulted in a poor performance. Presumably, this is because the SPI measures differential motion between two AEI-SASs, while the inertial sensor measures inertial motion of only one AEI-SAS, creating a mismatch between the signals. Above the unity gain frequency, the phasemeter of the SPI was measured to introduce a large phase loss of 11° at 10 Hz, resulting in amplification of motion around the blending frequency. The phase meter was designed for the LISA mission [H⁺04b], which is only interested in frequencies far below 1 Hz. The measurement performance of the SPI for the AEI sub-SQL interferometer is not impaired by

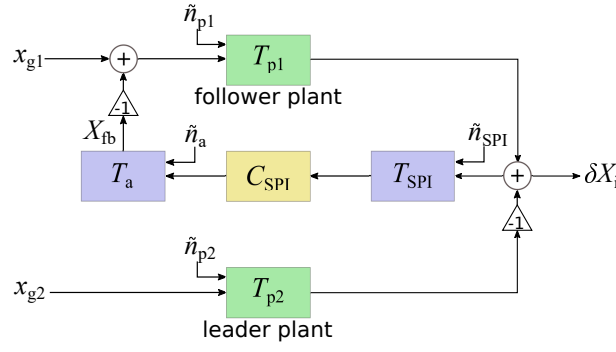


Figure 3.8.1: Control scheme for differential longitudinal motion between two AEI-SASs, sensed by the SPI interferometer. Ground motion x_{g1} and x_{g2} is incident on two different AEI-SASs with transfer functions T_{p1} and T_{p2} . The differential motion is sensed by the SPI with transfer function T_{SPI} , processed by a digital controller and sent to the actuators of one AEI-SAS as a feedback signal. This control scheme is called leader-follower scheme, where the south/west AEI-SAS is forced to follow the central AEI-SAS.

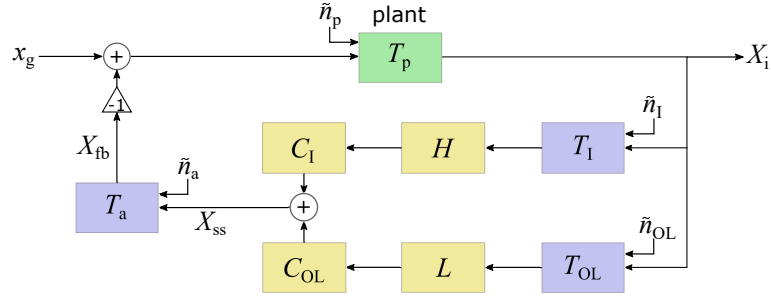


Figure 3.8.2: Control scheme for pitch and yaw motion, including the optical levers. Ground motion x_g is incident on the plant. The plant motion X_i is measured by inertial sensors with transfer function T_I and optical levers with transfer function T_{OL} . Both sensor outputs are blended together, combined to a super sensor output X_{SS} and utilized for feedback suppression of plant motion.

the phase loss, but a successful sensor blending, relying on signals with equal phase at the blending frequency, is impossible.

With the control scheme depicted in figure 3.8.1, differential longitudinal motion δx_1 is only limited by noise of the plants, of the SPI, or by a lack of loop gain. The common longitudinal motion of both AEI-SAS σx_1 is equal to the inertial motion of the central AEI-SAS, which is controlled by LVDTs and inertial sensors. These local sensors have a higher noise compared to the SPI, which is why the common motion is significantly higher, than the differential motion.

Pitch and yaw motion of each AEI-SASs are sensed with optical levers. The central AEI-SAS is part of both interferometer arms; therefore, it has two pitch directions, named pitch to south and pitch to west. The other two AEI-SAS have only one pitch direction. Figure 3.8.2 shows the control scheme for pitch and yaw. It is equal to the local control scheme shown in figure 3.7.1, with optical levers replacing LVDTs.

Active isolation in pitch and yaw is predominantly a local control technique for each AEI-SAS. Global isolation aspects are included as second order effects by the optical lever noise δn_{OL} . Differential vertical or side motion of the two involved AEI-SASs is interpreted as pitch or yaw motion by the optical levers. The control loops enforce a rotation of the optical tables, such that the optical lever beams are centered on the QPDs again. Consequently, the optical tables always face each other, if the loop gain is sufficiently high. This leads to complex couplings between different

Table 3.8.1: Overview of the utilized sensors for controlling the three AEI-SASs. Side and roll are not defined for the central AEI-SAS but are replaced by long to south/west and pitch to south/west.

Degree of freedom	Central AEI-SAS	South/West AEI-SAS
long	LVDT + geophone	SPI
vert	LVDT + geophone	LVDT + geophone
side	–	LVDT + accelerometer
pitch	OL + geophone	OL + geophone
yaw	OL + geophone	OL
roll	–	optical lever + geophone

degrees of freedom, described in section 3.8.2.

Table 3.8.1 gives an overview of the utilized sensors for controlling the three AEI-SASs in the six mirror degrees of freedom. The decision for accelerometers or horizontal L-4C geophones for the horizontal degrees of freedom is motivated in section 3.8.3. In the coordinate system adopted here, side and roll for the central AEI-SAS do not exist, but are replaced by long to south/west and pitch to south/west.

3.8.2 Coupling of AEI-SAS motion to the sub-SQL interferometer

This section describes the coupling of optical table motion of the AEI-SASs to the interferometer error signals via direct mechanical coupling. The focus is put on the interferometer degrees of freedom DARM, pitch and yaw. DARM is the degree of freedom containing the SQL signal and hence requires high attention. Pitch and yaw exhibit high coupling to DARM via the lever of the cavity length. The Advanced LIGO detectors, for example, are partly limited by alignment control at low frequencies (see figure 1.3.3), which results from pitch and yaw motion of the cavity mirrors. Indirect effects like scattering noise and mode mismatch, described in section 3.3.1, are not included. The coupling factors derived within this section will be used in sections 3.8.3 and 3.9 to optimize the sensor blending parameters for global isolation, analyze limitations of the current control system, and derive possible improvements.

All relevant coupling mechanisms are described step-by-step in the following, before they are combined to calculate the entire coupling path from optical table motion to the interferometer error signals.

- Optical table to optical table:

There are two different mechanisms, that couple optical table motion in one degree of freedom to optical table motion in another degree of freedom. Differential vertical motion of the optical tables $\delta x_{tt,v}$ or differential side motion of the optical tables $\delta x_{tt,s}$ are interpreted as pitch or yaw by the optical levers and corrected for by the feedback loops. This results in common pitch $\sigma r x_{tt,p}$ or common yaw motion $\sigma r x_{tt,y}$ of the two involved optical tables. The transfer function for this coupling is described by

$$\frac{\sigma r x_{tt,p}}{\delta x_{tt,v}} = \frac{\sigma r x_{tt,y}}{\delta x_{tt,s}} = \frac{L_{OL}}{d}, \quad (3.8.1)$$

with L_{OL} being the low pass filter of the optical lever and d being the distance between the two AEI-SASs.

The second coupling mechanism results from pitch or roll motion of the optical table, creating tilt-to-horizontal noise in horizontal inertial sensors installed on

the optical table. This noise is interpreted as horizontal motion and corrected for by the feedback loops. The transfer function is described by

$$\frac{x_{tt,l}}{rx_{tt,p}} = \frac{x_{tt,s}}{rx_{tt,r}} = H_I \times T_{tth}, \quad (3.8.2)$$

with H_I being the high pass filter of the inertial sensors and $T_{tth} = g/\omega^2$ being the tilt-to-horizontal coupling.

The central AEI-SAS uses horizontal L-4C geophones for the longitudinal isolation; hence, pitch of the central AEI-SAS always results in tilt-to-horizontal noise and consequently in unwanted longitudinal motion. This longitudinal motion is common for the involved AEI-SASs, because the SPI stabilizes the distance between the optical tables. Pitch of the south or west AEI-SAS does not result in tilt-to-horizontal coupling, since the longitudinal degree of freedom of those two optical tables is controlled by the SPI, not by inertial sensors. A common roll motion leads to common side motion, if horizontal L-4Cs, installed on the optical table, are used for both AEI-SASs. If one of the AEI-SASs uses accelerometers, installed inside the springbox, common roll results in differential side motion. This is because the springbox does not rotate with the optical table and hence, accelerometers are not affected. Differential roll motion results in differential side motion if at least one AEI-SAS uses horizontal L-4C geophones.

- Optical table to suspension point:

Translation motion of the optical table transfers to the exact same motion of the suspension points. The coupling of from optical table motion in pitch, roll and yaw to the suspension points is different, which is explained in figures 3.8.3–3.8.5.

Optical table pitch motion couples to longitudinal and vertical motion of the suspension points, as depicted in figure 3.8.3. The distance between the center of the optical table and the suspension point is labelled with l , having x and z components of l_x and l_z . The optical table is pitched by the angle β , resulting in a larger x component l'_x and a smaller z component l'_z . The difference $\Delta l_x = l'_x - l_x$ is described by

$$\begin{aligned} \Delta l_x &= \cos(\alpha - \beta)l - \cos(\alpha)l, \\ &= [\cos(\alpha)\cos(\beta) + \sin(\alpha)\sin(\beta)]l - \cos(\alpha)l. \end{aligned} \quad (3.8.3)$$

Inserting $\alpha \approx 45^\circ$ and $l \approx 1$ m, and using the small angle approximation for β , leads to the coupling factor c_1 from pitch to longitudinal motion of

$$c_1 = \frac{\Delta l_x}{\beta} \approx \frac{\sqrt{2}}{2} \frac{\text{m}}{\text{rad}}. \quad (3.8.4)$$

Executing the calculation for Δl_z gives the same coupling factor.

Figure 3.8.4 shows a pictorial description of coupling factor c_2 , describing the coupling from optical table roll motion to suspension point side motion. The motion in side is described by

$$\Delta l_y = l_z \sin(\beta) \approx l_z \beta, \quad (3.8.5)$$

with $l_z = 0.7$ m; hence, the coupling factor is given by

$$c_2 = \frac{\Delta l_y}{\beta} \approx 0.7 \frac{\text{m}}{\text{rad}}. \quad (3.8.6)$$

Figure 3.8.5 shows a depiction of the third coupling mechanism from optical table yaw motion to suspension point side motion. The calculation is equal to the second coupling mechanism with $l_x \approx l_z$; hence c_3 is given by

$$c_3 = \frac{\Delta l_y}{\beta} \approx 0.7 \frac{\text{m}}{\text{rad}}. \quad (3.8.7)$$

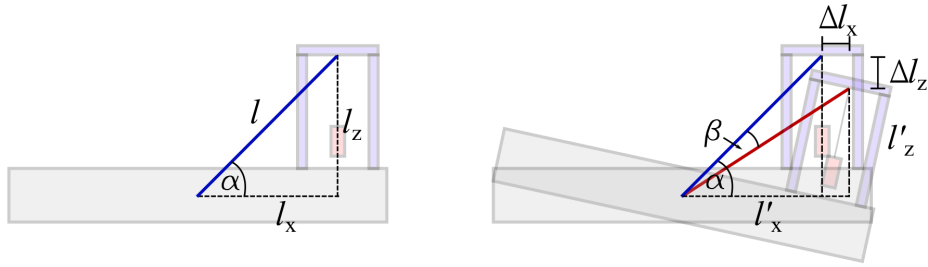


Figure 3.8.3: Pictorial description of coupling factor c_1 , describing the coupling from optical table pitch motion to suspension point long motion. The assembly is shown in the long-vert plane. The left-hand side displays the initial state with l : distance between optical table center and suspension point; l_x and l_z : the x and z component of l and α : the angle spanned by l and l_x . The right-hand side shows the optical table with a pitch by the angle β . l'_x and l'_z are the new x and z components of l , Δl_x and Δl_z are the suspension point displacements in long and vert.

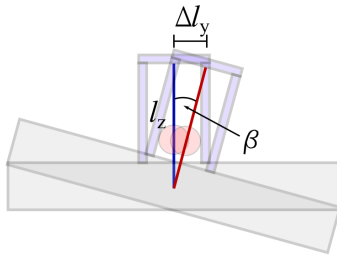


Figure 3.8.4: Pictorial description of coupling factor c_2 , describing the coupling from optical table roll motion to suspension point side motion. The assembly is shown in the side-vert plane. l_z describes the height of the suspension point above the center of the optical table, β is the rotation angle, and Δl_y the resulting displacement of the suspension point in side.

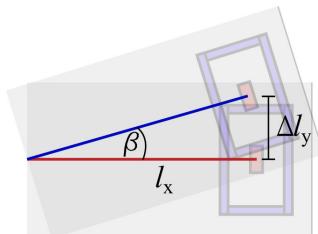


Figure 3.8.5: Pictorial description of coupling factor c_3 , describing the coupling from optical table yaw motion to suspension point side motion. The assembly is shown in the long-side plane. l_x describes the distance between the center of the optical table and the suspension point, β is the rotation angle and Δl_y the resulting displacement of the suspension point in side.

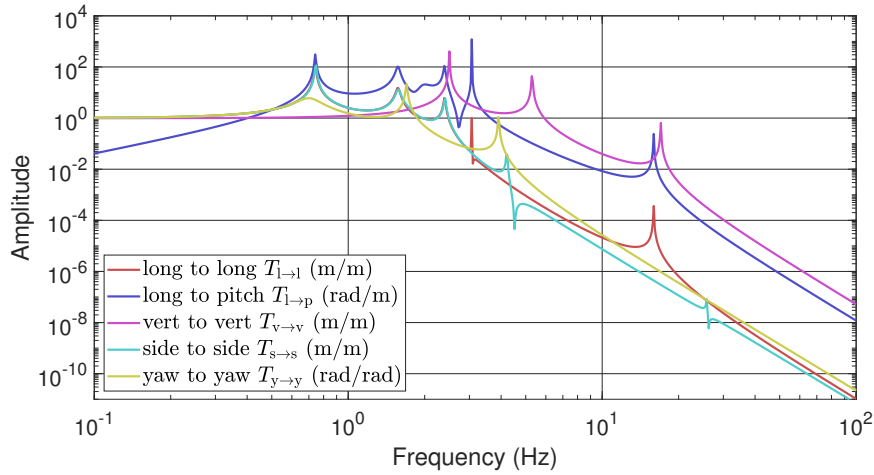


Figure 3.8.6: Transfer function amplitudes of the interferometer mirror suspensions in five different degrees of freedom. The units are provided in the legend. The displayed transfer functions are the relevant transfer functions to describe the coupling from AEI-SAS motion in global coordinates to the interferometer error signals.

- Suspension point to mirror
The transfer functions from suspension point motion to mirror motion are pre-determined by design of the suspensions, which is not presented in detail within this thesis. Figure 3.8.6 shows the transfer functions in the relevant degrees of freedom. The transfer functions are described by the parameters $T_{a \rightarrow b}$, with a, b describing the degree of freedom of the suspension point motion and the resulting mirror motion, respectively.
- Mirror to interferometer
In the last step, the coupling of mirror motion to the interferometer error signals is investigated. A detailed analysis of this coupling is not possible at the time of writing, since information, for example about the interferometer control loops, can only roughly be estimated. The following aspects are included for the calculation of the coupling:
 - Differential longitudinal motion of the mirrors couples to the DARM signal with a coupling factor of 1.
 - Common and differential rotations of the mirrors either rotate the cavity axis or misalign the two mirrors with respect to each other. Both effects are corrected by the auto-alignment (aa) loops of the interferometer. The gain of these control loops is estimated and the resulting coupling to the interferometer pitch or yaw error signals are shown in figure 3.8.7.
 - Differential vertical and side motion also require rotations of the mirrors by the auto-alignment loops to re-align the interferometer. The coupling factor c_4 from mirror displacement to required mirror rotation is derived in figure 3.8.8. The input mirror is displaced with respect to the laser beam and the end test mass by x_m , resulting in a misaligned cavity. The required rotation rx_m to re-align the cavity is calculated by

$$\sin(rx_m) = \frac{2x_m}{l_c}, \quad (3.8.8)$$

where l_c is the length of the cavity. Using the small angle approximation, the coupling factor c_4 from displacement to required rotation is given by

$$c_4 = \frac{rx_m}{x_m} = \frac{2}{l_c} = \frac{1}{5.7}. \quad (3.8.9)$$

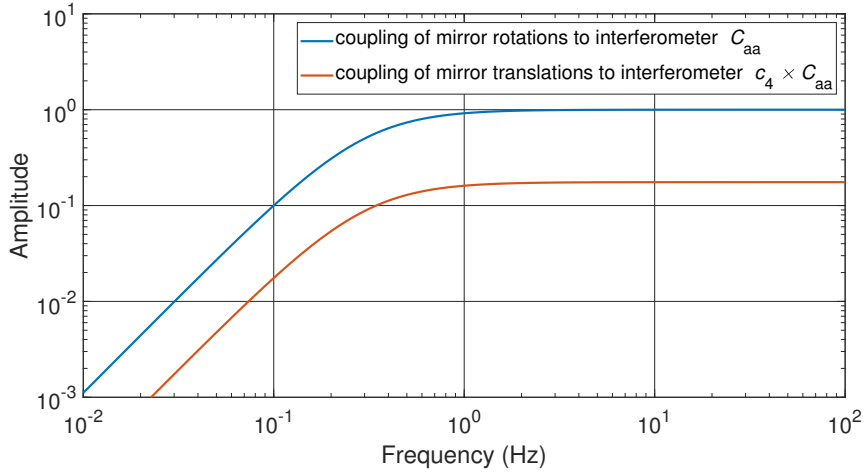


Figure 3.8.7: Transfer functions from mirror motion to the interferometer error signals in pitch and yaw. The coupling of rotational mirror motion is given by C_{aa} , which describes the auto-alignment suppression. The unity gain frequency of the auto-alignment loop is estimated to be at 0.3 Hz. The coupling of mirror translations to the interferometer is smaller compared to the coupling of mirror rotations by the factor c_4

Figure 3.8.7 shows the overall coupling from mirror displacement to the interferometer error signal, including the coupling factor c_4 and the auto-alignment loop suppression.

- Common side motion of two mirrors results in a misalignment of the input laser beam to the cavity. The reason for this misalignment is the low suspension resonance frequency in side of 0.75 Hz. Around and above this frequency, the laser, stiffly connected to the optical table, and the mirrors move differentially. This coupling is as well approximated by the coupling factor c_4 and the auto-alignment suppression, shown in figure 3.8.7.
- Common vertical and longitudinal motion of the mirrors is not assumed to couple to the interferometer error signals. The vertical resonance frequency is at 2.5 Hz; consequently, optical table motion below roughly 2 Hz does not result in differential motion between laser input beam and cavity. Above 2 Hz, optical table motion is already well attenuated; therefore, this coupling is neglected. The longitudinal resonance frequency is at 0.74 Hz, resulting in differential motion between the input laser beam and the cavity in longitudinal direction. This translates the beam waist inside the cavity, which has a weak coupling to the DARM signal; hence, it is neglected as well.

Figures 3.8.9–3.8.22 describe the coupling of optical table motion to the interferometer error signals for each global degree of freedom. The first column depicts illustrations of the investigated optical tables, suspensions and mirrors. The initial motion and subsequent motion of the optical tables are demonstrated in the drawings and by arrows. The second column lists the degree of freedom, in which the motion is present. Columns three to five contain motion of the optical tables, suspension points and mirrors. Column six shows the involved interferometer error signals. All coupling mechanisms and coupling factors described in the list earlier in this section are included by arrows. The overall coupling factors $\bar{T}_{a \rightarrow b}$ can be calculated by following the arrows from the top left to the right.

All variables, parameters and abbreviations are listed in table 3.8.2. Coupling paths without relevance for the interferometer error signals are neglected.

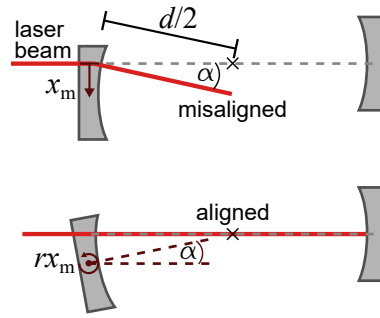


Figure 3.8.8: Pictorial description of the coupling from mirror displacement to the required mirror rotation to re-align the cavity.

Table 3.8.2: Description and values of the variables and abbreviations used in figures 3.8.9–3.8.23.

Variable or abbreviation	Description	Value
$\sigma; \delta$	common; differential	
$x; rx$	translational motion; rotational motion	
tt; sp; m; ifo	table top; suspension point; mirror; interferometer	
l,v,s,p,y,r	long, vert, side, pitch, yaw, roll	
$\bar{T}_{a \rightarrow b}$	transfer function from tt motion in DoF “a” to ifo error signal in DoF “b”	see figures 3.8.24–3.8.26
$T_{a \rightarrow b}$	suspension transfer function from DoF “a” to DoF “b”	see figure 3.8.6
T_{tth}	tilt-to-horizontal coupling factor	g/ω^2
H_I	high pass filter inertial sensors	see section 3.8.3
L_{OL}	low pass filter optical levers	see section 3.8.3
C_{aa}	auto-alignment suppression factor	see figure 3.8.7
d	distance between two AEI-SASs	11.5 m
c_1, c_2, c_3, c_4	geometrical coupling factors	see figures 3.8.3–3.8.5 and 3.8.8

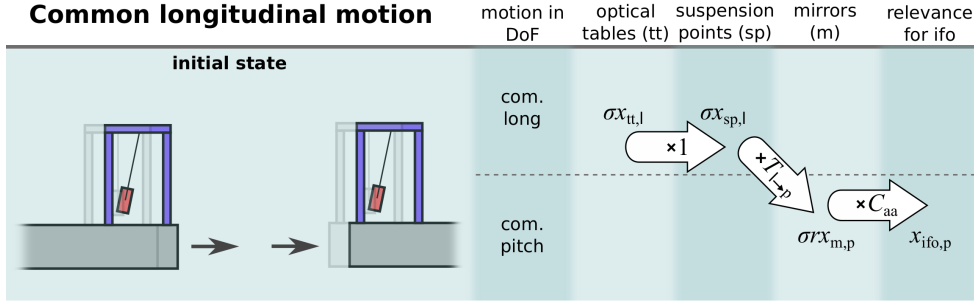


Figure 3.8.9: Coupling path from common longitudinal optical table motion to the interferometer error signal in pitch. The left-hand side shows an illustration of two AEI-SAS optical tables with suspensions and mirrors in the long-vert plane.

Figure 3.8.9 investigates the coupling of common longitudinal motion of the optical tables to the interferometer error signals. Only the pitch error signal is affected significantly, with the transfer function described by

$$\bar{T}_{\sigma l \rightarrow p} = \frac{x_{ifo,p}}{\sigma x_{tt,l}} = T_{l \rightarrow p} C_{aa}. \quad (3.8.10)$$

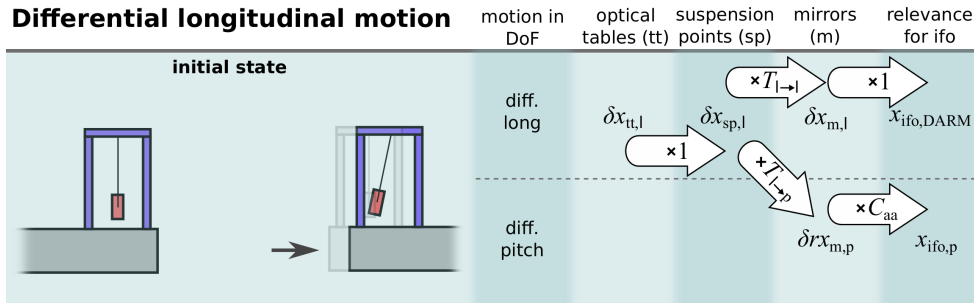


Figure 3.8.10: Coupling path from differential longitudinal optical table motion to the interferometer error signals DARM and pitch. The left-hand side shows an illustration of two AEI-SAS optical tables with suspensions and mirrors in the long-vert plane.

Figure 3.8.10 investigates the coupling of differential longitudinal motion of the optical tables to the interferometer error signals. This motion couples to the DARM and pitch error signals with the transfer functions described by

$$\begin{aligned} \bar{T}_{\delta l \rightarrow DARM} &= \frac{x_{ifo,DARM}}{\delta x_{tt,l}} = T_{l \rightarrow s}, \\ \bar{T}_{\delta l \rightarrow p} &= \frac{x_{ifo,p}}{\delta x_{tt,l}} = T_{l \rightarrow p} C_{aa}. \end{aligned} \quad (3.8.11)$$

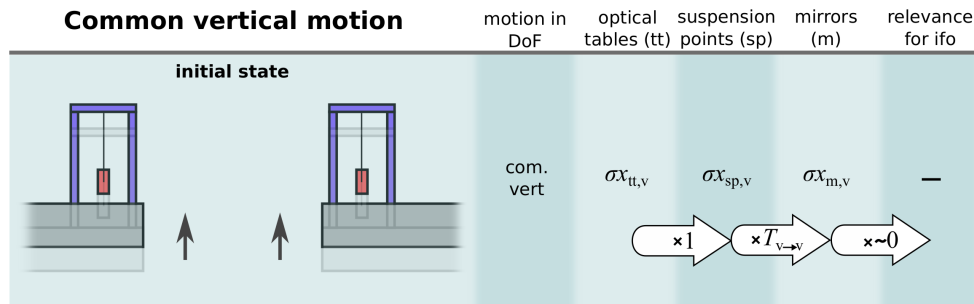


Figure 3.8.11: Coupling path from common vertical optical table motion to the interferometer error signals. The left-hand side shows an illustration of two AEI-SAS optical tables with suspensions and mirrors in the long-vert plane. Motion in this degree of freedom has no relevance for the interferometer error signals.

Figure 3.8.11 investigates the coupling of common vertical motion of the optical tables to the interferometer error signals. Following the coupling mechanisms described at the beginning of this section, common vertical optical table motion has no relevant coupling to the interferometer.

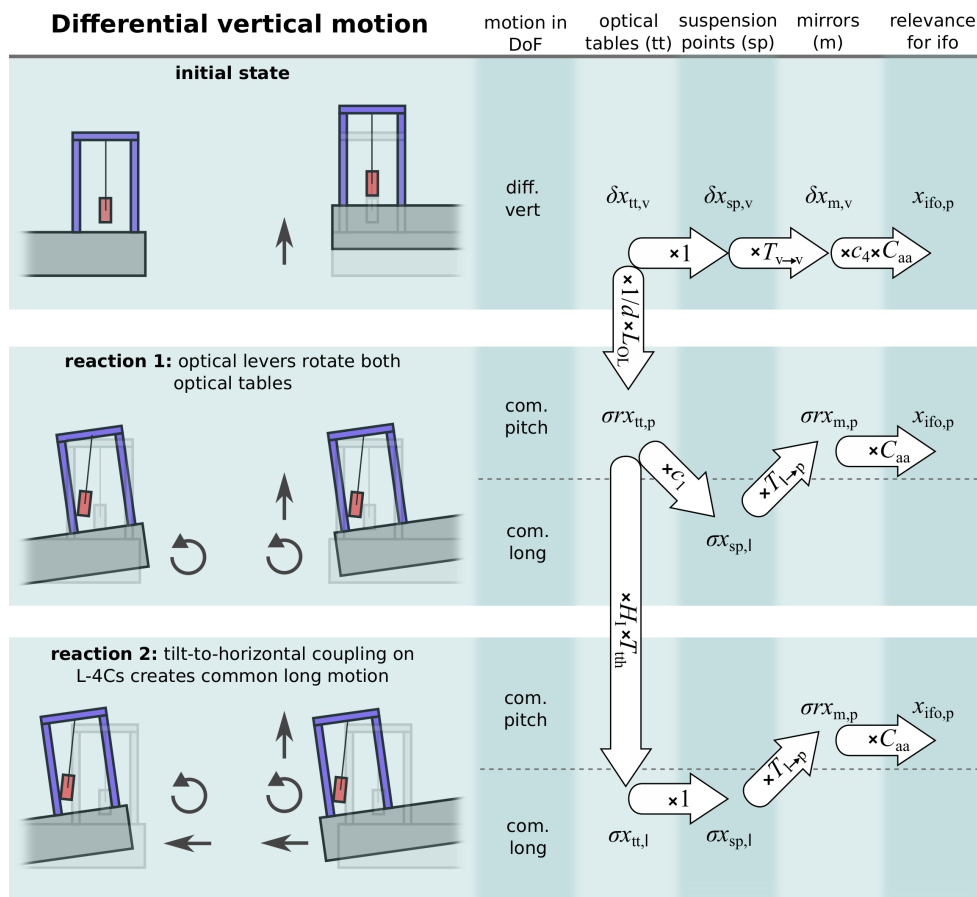


Figure 3.8.12: Coupling path from differential vertical optical table motion to the interferometer error signal in pitch. The left-hand side shows illustrations of two AEI-SAS optical tables with suspensions and mirrors in the long-vert plane.

Figure 3.8.12 investigates the coupling of differential vertical motion of the optical tables to the interferometer error signals. This motion couples to the pitch error signal

on three different paths, summed up to

$$\bar{T}_{\delta v \rightarrow p} = \frac{x_{ifo,p}}{\delta x_{tt,v}} = \left[T_{v \rightarrow v} c_4 + \frac{LOL}{d} (c_1 + H_1 T_{tt}) T_{1 \rightarrow p} \right] C_{aa}. \quad (3.8.12)$$

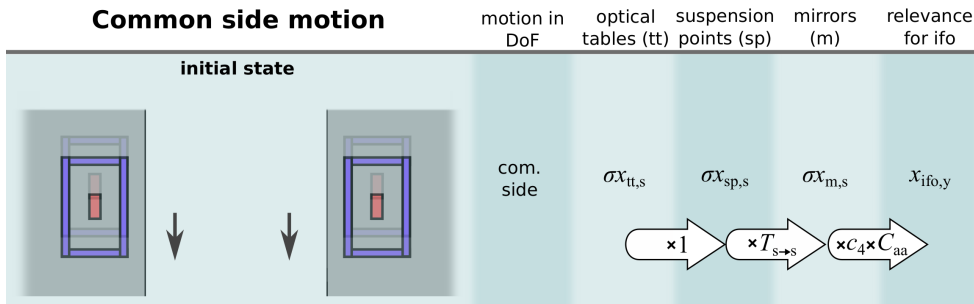


Figure 3.8.13: Coupling path from common side optical table motion to the interferometer error signal in yaw. The left-hand side shows an illustration of two AEI-SAS optical tables with suspensions and mirrors in the long-side plane.

Figure 3.8.13 investigates the coupling of common side motion of the optical tables to the interferometer error signals. Motion in this degree of freedom has a coupling to the interferometer error signal in yaw, described by

$$\bar{T}_{\sigma s \rightarrow y} = \frac{x_{ifo,y}}{\sigma x_{tt,s}} = T_{s \rightarrow s} c_4 C_{aa}. \quad (3.8.13)$$

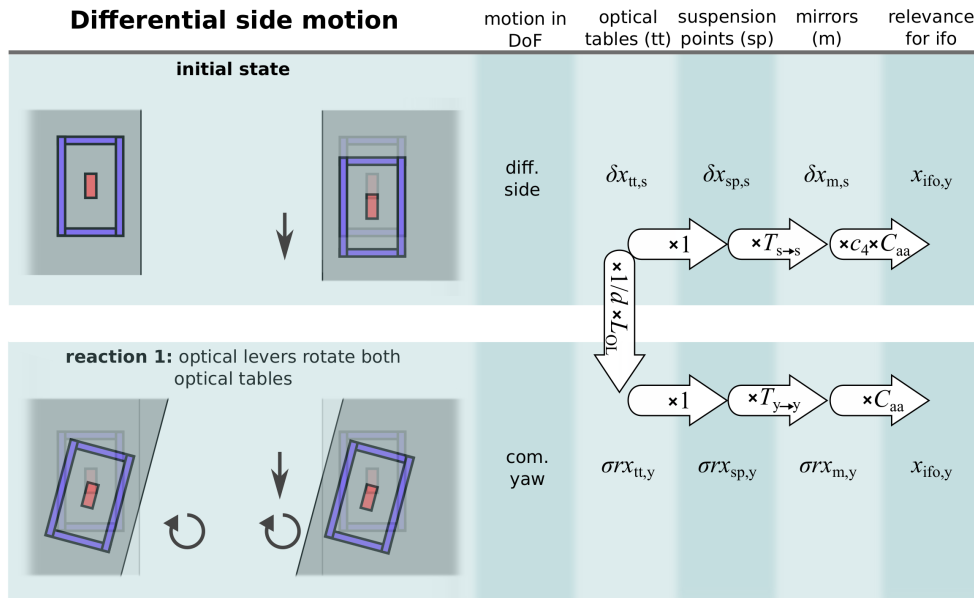


Figure 3.8.14: Coupling path from differential side optical table motion to the interferometer error signal in yaw. The left-hand side shows illustrations of two AEI-SAS optical tables with suspensions and mirrors in the long-side plane.

Figure 3.8.14 investigates the coupling of differential side motion of the optical tables to the interferometer error signals. Motion in this degree of freedom has relevance

for the yaw error signal. An additional coupling path from optical table common yaw motion to suspension point differential side motion (see figure 3.8.5 and equation 3.8.7) exists, but is negligible compared to the other two coupling paths. This results in a transfer function described by

$$\bar{T}_{\delta s \rightarrow y} = \frac{x_{\text{ifo},y}}{\delta x_{\text{tt},s}} = \left(T_{s \rightarrow s} c_4 + \frac{L_{\text{OL}}}{d} T_{y \rightarrow y} \right) C_{\text{aa}}. \quad (3.8.14)$$

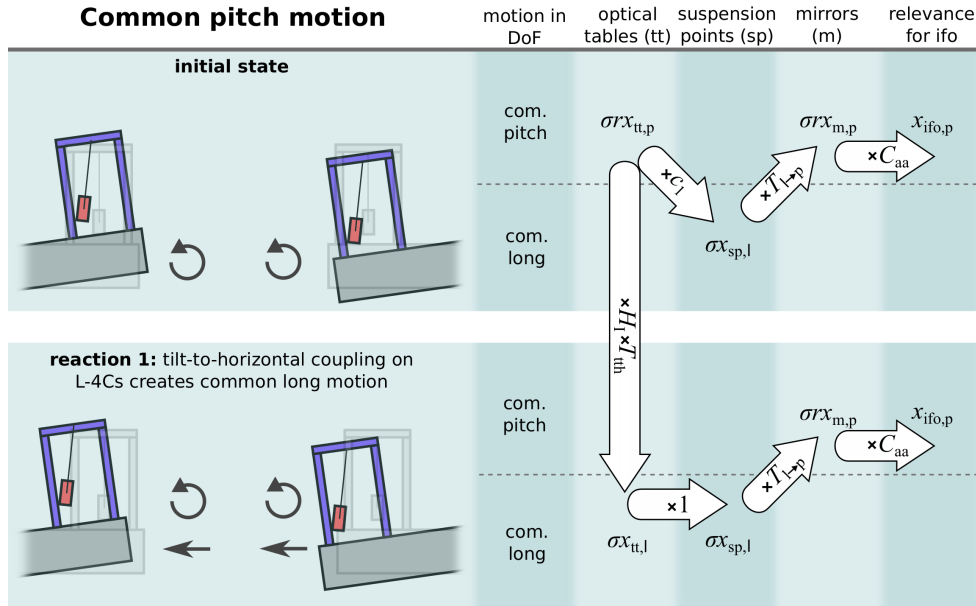


Figure 3.8.15: Coupling path from common pitch optical table motion to the interferometer error signal in pitch. The left-hand side shows illustrations of two AEI-SAS optical tables with suspensions and mirrors in the long-vert plane.

Figure 3.8.15 investigates the coupling of common pitch motion of the optical tables to the interferometer error signals. For this coupling, it is assumed that the central AEI-SAS uses horizontal L-4C geophones for longitudinal isolation; therefore, pitch motion results in tilt-to-horizontal coupling. A common pitch motion of the optical tables couples to the pitch error signal on two paths, described by the transfer function

$$\bar{T}_{\sigma p \rightarrow p} = \frac{x_{\text{ifo},p}}{\sigma x_{\text{tt},p}} = (c_1 + H_1 T_{\text{th}}) T_{l \rightarrow p} C_{\text{aa}}. \quad (3.8.15)$$

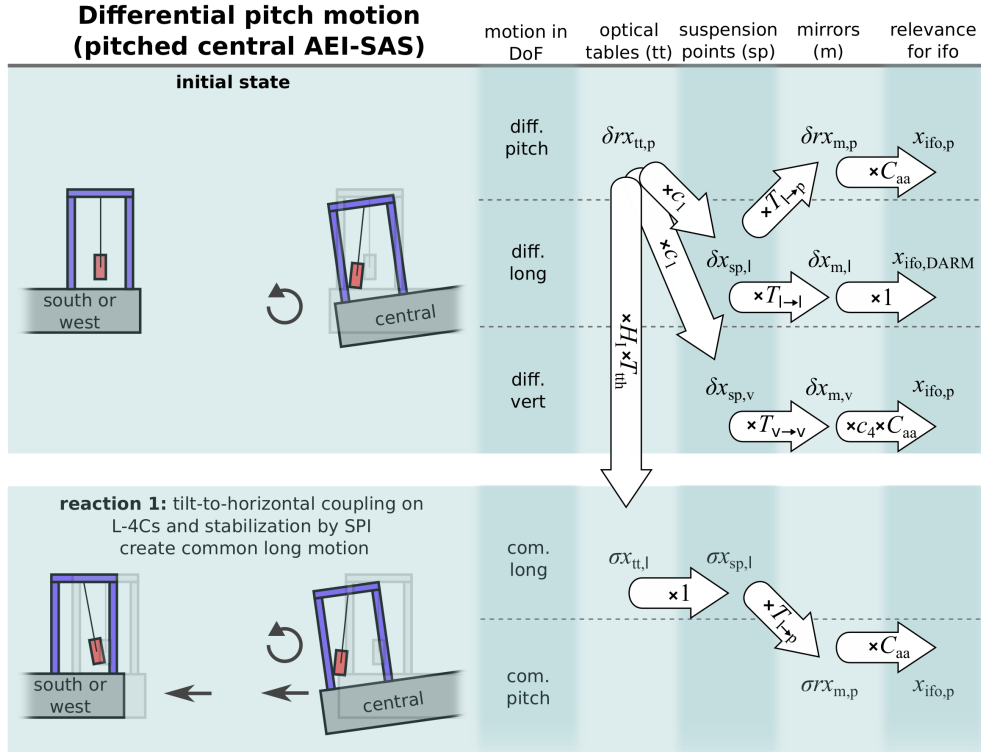


Figure 3.8.16: Coupling path from differential pitch optical table motion to the interferometer error signals in pitch and DARM. This figure investigates the coupling for a pitched central AEI-SAS. The left-hand side shows illustrations of two AEI-SAS optical tables with suspensions and mirrors in the long-vert plane.

Figure 3.8.16 investigates the coupling of differential pitch motion of the optical tables to the interferometer error signals. In this figure, a pitching central AEI-SAS is investigated, while the second AEI-SAS is not pitching. Again, it is assumed that the central AEI-SAS uses horizontal L-4C geophones for longitudinal isolation. There are three different coupling paths to the pitch error signal and one coupling path to the DARM error signal. They are described by

$$\bar{T}_{\delta p \rightarrow p}^C = \frac{x_{ifo,p}}{\delta x_{tt,p}} = [c_1(T_{1 \rightarrow p} + T_{v \rightarrow v}c_4) + H_1 T_{tth} T_{1 \rightarrow p}] C_{aa}, \quad (3.8.16)$$

$$\bar{T}_{\delta p \rightarrow DARM}^C = \frac{x_{ifo,DARM}}{\delta x_{tt,p}} = c_1 T_{1 \rightarrow l}. \quad (3.8.17)$$

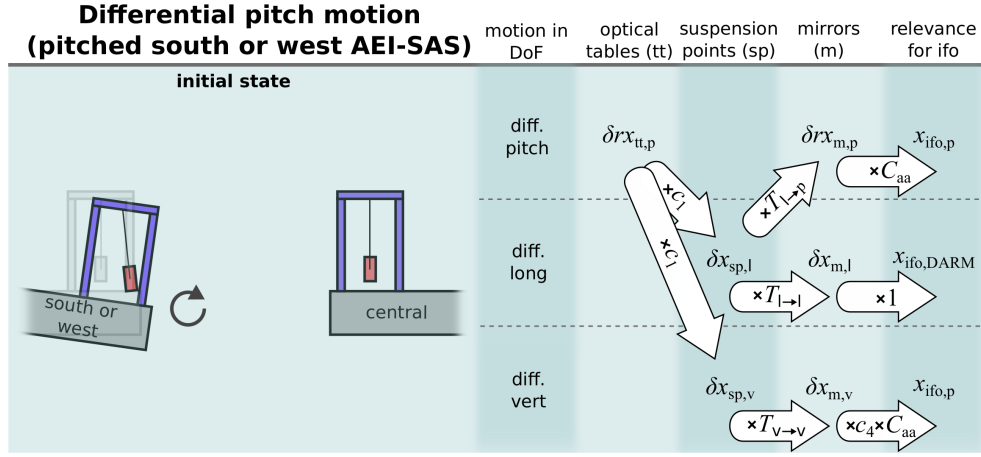


Figure 3.8.17: Coupling path from differential pitch optical table motion to the interferometer error signals in pitch and DARM. This figure investigates the coupling for a pitched south or west AEI-SAS. The left-hand side shows an illustration of two AEI-SAS optical tables with suspensions and mirrors in the long-vert plane.

Figure 3.8.17 investigates the coupling of differential pitch motion of the optical tables to the interferometer error signals. Now, a pitched south or west optical table is investigated, while the central AEI-SAS is not pitched. There is no tilt-to-horizontal coupling, because the south and west AEI-SASs are controlled by the SPI in the longitudinal degree of freedom. In this case, there are two coupling paths to the pitch error signal and one coupling path to the DARM error signal, described by

$$\bar{T}_{\delta p \rightarrow p}^{SW} = \frac{x_{ifo,p}}{\delta x_{tt,p}} = c_1(T_{l \rightarrow p} + T_{v \rightarrow v}c_4)C_{aa}, \quad (3.8.18)$$

$$\bar{T}_{\delta p \rightarrow DARM}^{SW} = \frac{x_{ifo,DARM}}{\delta x_{tt,p}} = c_1T_{l \rightarrow l}. \quad (3.8.19)$$

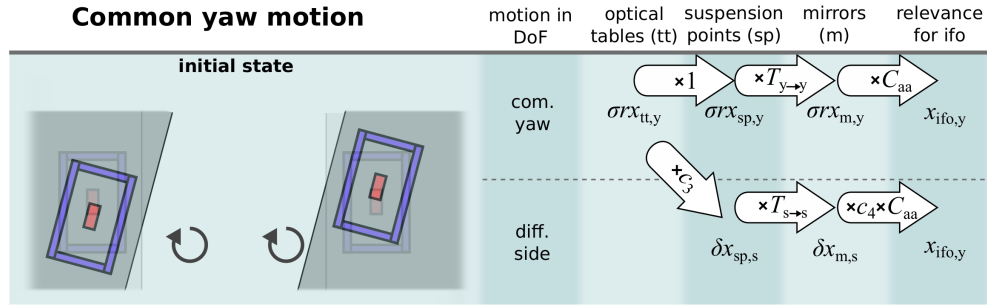


Figure 3.8.18: Coupling path from common yaw optical table motion to the interferometer error signal in yaw. The left-hand side shows an illustration of two AEI-SAS optical tables with suspensions and mirrors in the long-side plane.

Figure 3.8.18 investigates the coupling of common yaw motion of the optical tables to the interferometer error signals. Common yaw motion couples to the interferometer yaw error signal on two paths, described by

$$\bar{T}_{\sigma y \rightarrow y} = \frac{x_{ifo,y}}{\sigma x_{tt,y}} = (T_{y \rightarrow y} + c_3T_{s \rightarrow s}c_4)C_{aa}. \quad (3.8.20)$$

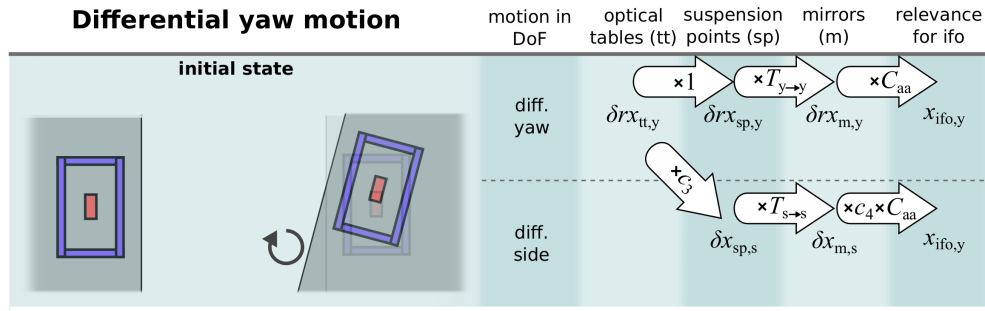


Figure 3.8.19: Coupling path from differential yaw optical table motion to the interferometer error signal in yaw. The left-hand side shows an illustration of two AEI-SAS optical tables with suspensions and mirrors in the long-side plane.

Figure 3.8.19 investigates the coupling of differential yaw motion of the optical tables to the interferometer error signals. The coupling of differential and common yaw motion of the optical tables is identical; hence, the coupling is given by

$$\bar{T}_{\delta y \rightarrow y} = \frac{x_{ifo,y}}{\delta x_{tt,y}} = (T_{y \rightarrow y} + c_3 T_{s \rightarrow s} c_4) C_{aa}. \quad (3.8.21)$$

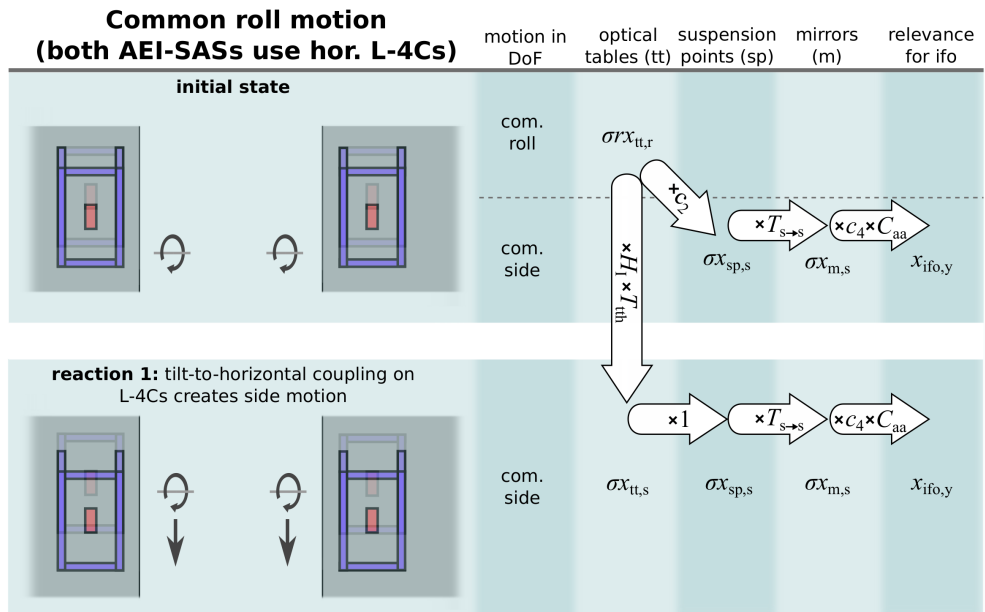


Figure 3.8.20: Coupling path from common roll optical table motion to the interferometer error signal in yaw. For this figure it is assumed that both AEI-SAS use horizontal L-4C geophones, located on the optical table, for the isolation of side. The left-hand side shows illustrations of two AEI-SAS optical tables with suspensions and mirrors in the long-side plane.

Figure 3.8.20 investigates the coupling of common roll motion of the optical tables to the interferometer error signals. In this case, both AEI-SASs use horizontal L-4C geophones on the optical tables instead of accelerometers for the isolation of side motion. A common roll motion of the optical tables couples to the interferometer yaw error signal on two paths, described by

$$\bar{T}_{\sigma r \rightarrow y}^{L4C} = \frac{x_{ifo,y}}{\sigma x_{tt,r}} = (c_2 + H_I T_{tth}) T_{s \rightarrow s} c_4 C_{aa}. \quad (3.8.22)$$

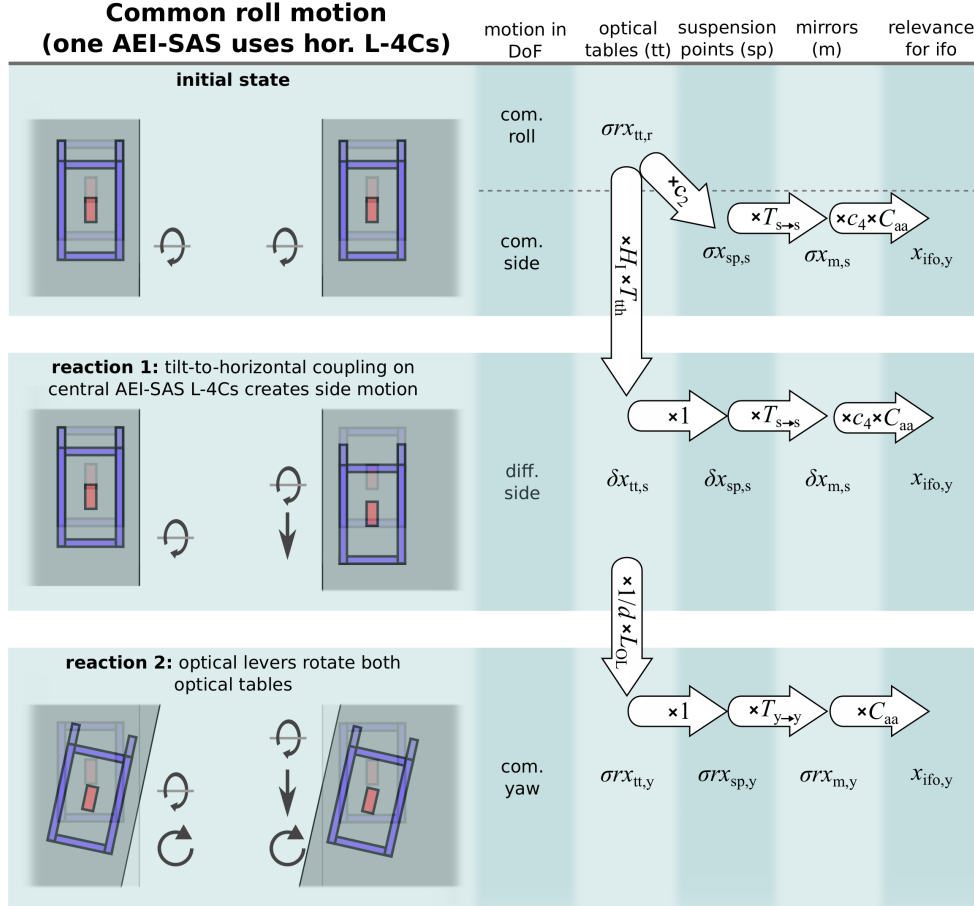


Figure 3.8.21: Coupling path from common roll optical table motion to the interferometer error signal in yaw. For this figure it is assumed that one AEI-SAS uses accelerometers, located in the springbox, while the other AEI-SAS uses horizontal L-4C geophones, located on the optical table. The left-hand side shows illustrations of two AEI-SAS optical tables with suspensions and mirrors in the long-side plane.

Figure 3.8.21 investigates the coupling of common roll motion of the optical tables to the interferometer error signals. Different to the last investigated coupling, only one AEI-SAS uses L-4C geophones on the optical table to control side motion. The second AEI-SAS uses accelerometers, located within the springbox. With this setup, common roll motion has three relevant coupling paths to the interferometer error signal in yaw. In principle, a fourth path exists via coupling from optical table yaw motion to suspension point side motion, explained in figure 3.8.5 and equation 3.8.7, but this path is negligible compared to the other three couplings. The resulting transfer function is given by

$$\bar{T}_{\sigma r 2y}^{acc} = \frac{x_{ifo,y}}{\sigma x_{tt,r}} = \left[c_2 T_{s \rightarrow s} c_4 + H_I T_{tth} \left(T_{s \rightarrow s} c_4 + \frac{L_{OL}}{d} T_{y \rightarrow y} \right) \right] C_{aa}. \quad (3.8.23)$$

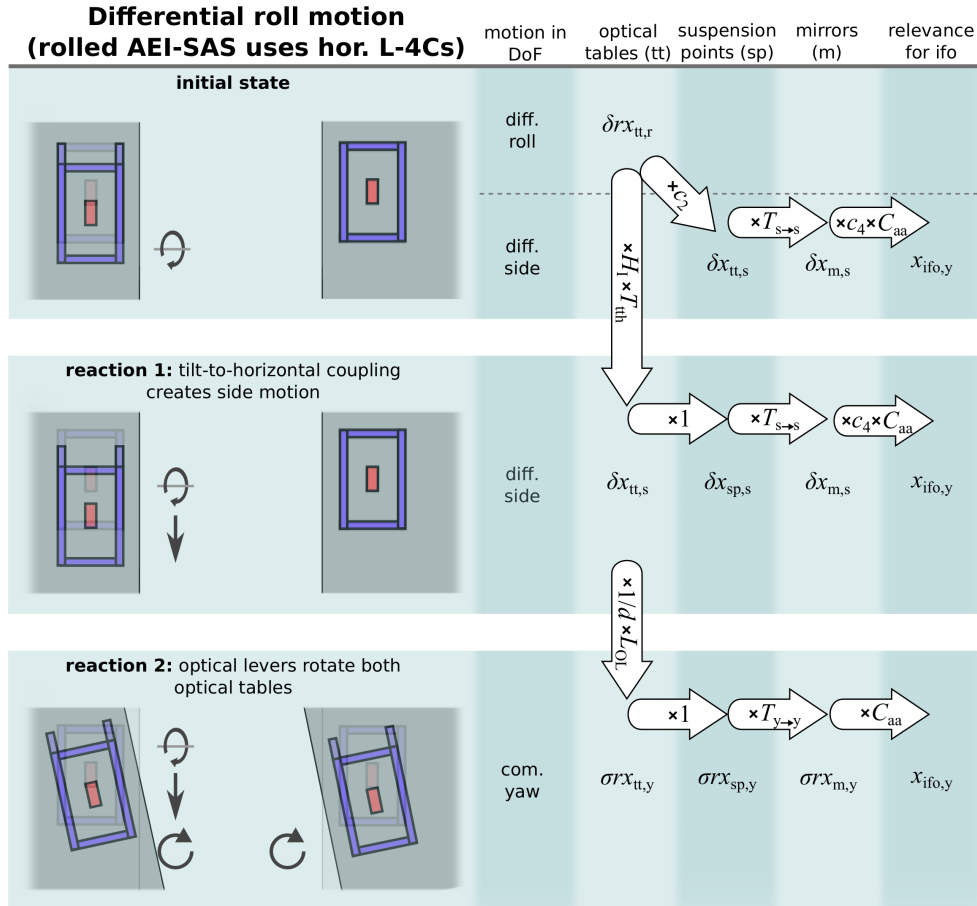


Figure 3.8.22: Coupling path from differential roll optical table motion to the interferometer error signal in yaw. In this figure, it is assumed that the rolled AEI-SAS uses horizontal L-4Cs on the optical table instead of accelerometers. The left-hand side shows illustrations of two AEI-SAS optical tables with suspensions and mirrors in the long-side plane.

Figure 3.8.22 investigates the coupling of differential roll motion to the interferometer error signals. For this figure, it is assumed that the rolled AEI-SAS uses horizontal L-4C geophones located on the optical table to control side motion. There are three relevant coupling paths of optical table motion to the error signal. Same as for the last investigated degree of freedom, a fourth coupling path, resulting from the coupling described in figure 3.8.5 and equation 3.8.7, is negligible. In summary, the coupling can be described by

$$\bar{T}_{\delta r \rightarrow y}^{L4C} = \frac{x_{ifo,y}}{\delta x_{tt,r}} = \left[c_2 T_{s \rightarrow s} c_4 + H_1 T_{tth} \left(T_{s \rightarrow s} c_4 + \frac{L_{OL}}{d} T_{y \rightarrow y} \right) \right] C_{aa}. \quad (3.8.24)$$

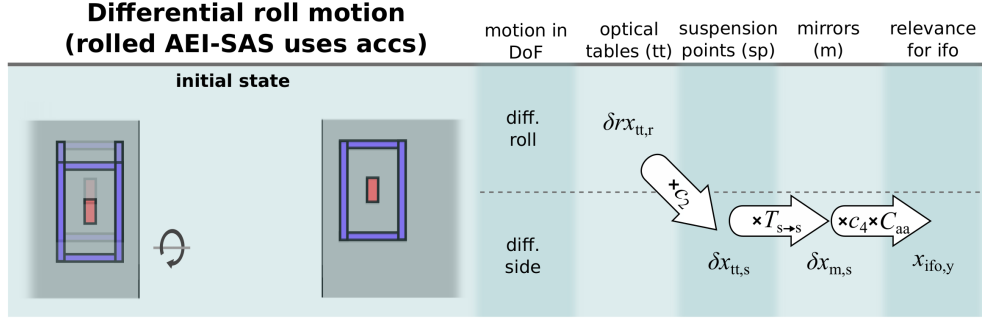


Figure 3.8.23: Coupling path from differential roll optical table motion to the interferometer error signal in yaw. In this figure, it is assumed that the rolled AEI-SAS uses accelerometers within the springbox instead of L-4C geophones. The left-hand side shows illustrations of two AEI-SAS optical tables with suspensions and mirrors in the long-side plane.

Figure 3.8.23 investigates the coupling of differential roll motion of the optical tables to the interferometer error signals. This time, the rolled AEI-SAS uses accelerometers within the springbox instead of L-4C geophones on the optical table to control side motion. In this case, there is only one coupling path to the yaw error signal, described by

$$\bar{T}_{\delta r \rightarrow y}^{acc} = \frac{x_{ifo,y}}{\delta x_{tt,r}} = c_2 T_{s \rightarrow s} c_4 C_{aa}. \quad (3.8.25)$$

All transfer functions \bar{T} from optical table motion to the interferometer error signals are depicted in diagrams 3.8.24–3.8.26. The suspension transfer functions amplify motion significantly between 0.4 and a few Hz, depending on the degree of freedom. This frequency band requires the highest priority, when designing control loops for the AEI-SAS. The transfer functions are utilized in the following section as cost functions to optimize the global sensor blending.

3.8.3 Sensor blending optimization

The sensor blending optimization for global seismic isolation is based on the same principle as the optimization for local isolation, presented in section 3.7.8. Similar to the optimization equation 3.7.20, the sensor blending for global isolation is optimized by the equation

$$|x_{ifo,lh}(\omega_b)|_{rms} = \int_{f=f_{min}}^{f=f_{max}} C([x_{res}(\omega) + x_{low}(\omega)L_{lh}(\omega, \omega_b)]^2 + \tilde{n}_{low}^2(\omega)L_{lh}^2(\omega, \omega_b) + \tilde{n}_{high}^2(\omega)H_{lh}^2(\omega, \omega_b))^{1/2} d\omega. \quad (3.8.26)$$

$|x_{ifo,lh}(\omega_b)|_{rms}$ describes the *rms* of the coupling from optical table motion to the interferometer error signals. C is the cost function. x_{res} labels the residual, optimally suppressed ground motion. The sub-SQL interferometer only requires one measurement at a chosen time to detect the SQL. This measurement will happen at a calm night with low seismic activity; hence, low seismic motion is used for the blending optimization. x_{low} is the coupling of ground motion to the low frequency sensor, and \tilde{n}_{low} is its electronic noise. \tilde{n}_{high} describes the sensor noise of the high frequency sensor and L_{lh} and H_{lh} label the low and high pass filters. There are three main differences to the local sensor blending optimization:

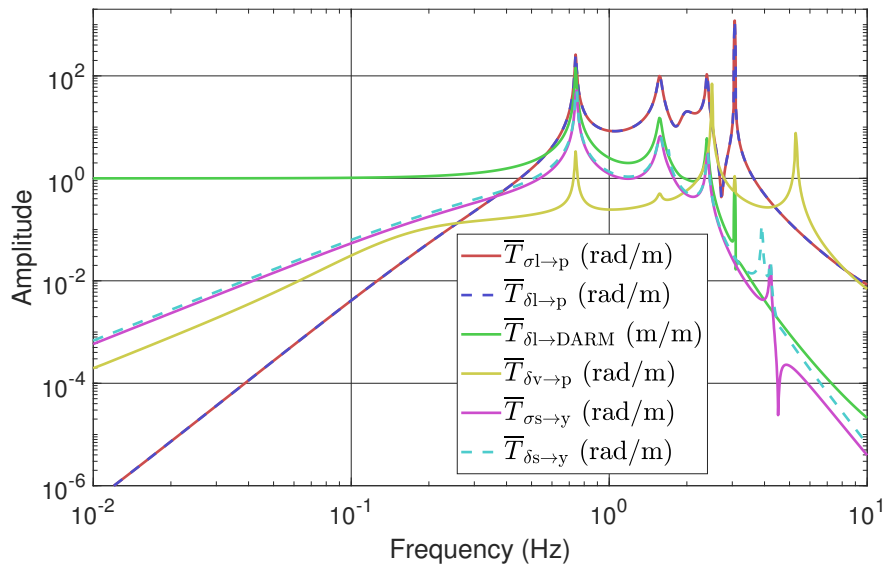


Figure 3.8.24: Transfer function amplitudes from optical table motion to interferometer error signals in different degrees of freedom. The transfer functions are derived in figures 3.8.9–3.8.14.

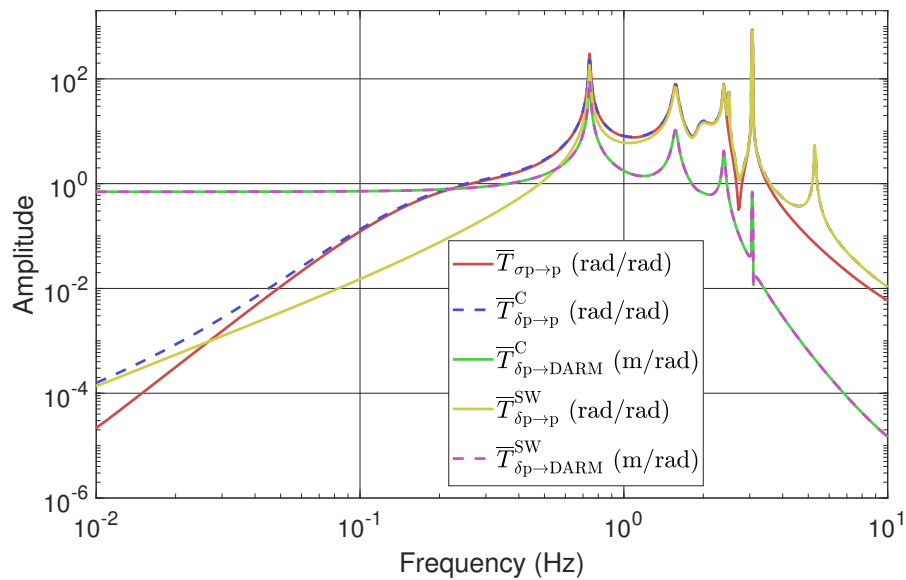


Figure 3.8.25: Transfer function amplitudes from optical table motion to interferometer error signals in different degrees of freedom. The transfer functions are derived in figures 3.8.15–3.8.17.

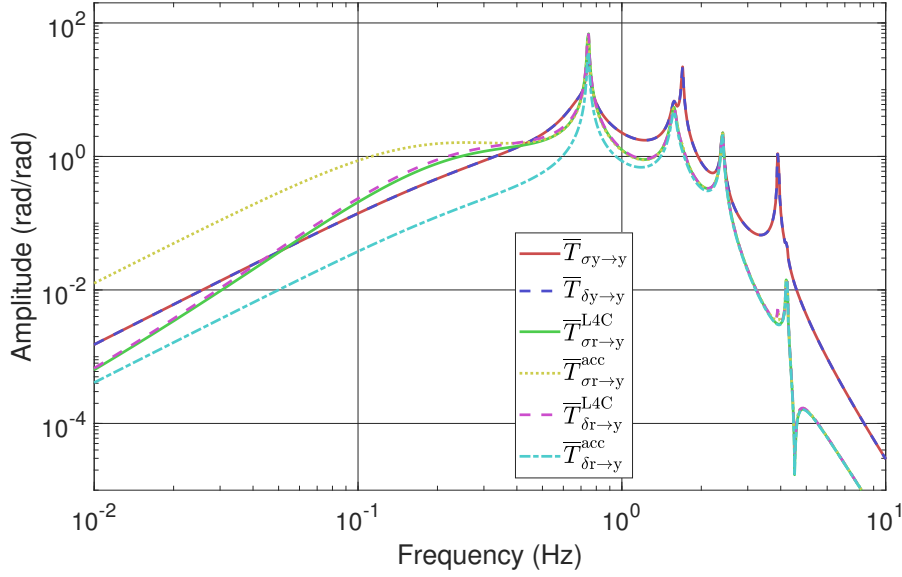


Figure 3.8.26: Transfer function amplitudes from optical table motion to interferometer error signals in different degrees of freedom. The transfer functions are derived in figures 3.8.18 – 3.8.23.

- The sensor blending performance is not optimized to optical table velocity $|\dot{X}_{lh}(\omega_b)|_{rms}$, but the coupling to the interferometer error signals $|x_{ifo, lh}(\omega_b)|_{rms}$ is minimized. This requires various estimations and simplifications, increasing the error bar of the optimization, but also increasing the significance for the overall interferometer performance strongly.
- The cost function C was chosen to be ω for the local optimization, to optimize the optical table velocity. In the global sensor blending optimization, the cost function consists of the transfer function from optical table motion to the interferometer error signal \bar{T} , derived in section 3.8.2, and f , by

$$C = \bar{T} + \eta f. \quad (3.8.27)$$

η defines a weighting between \bar{T} and f . By increasing η , more emphasize is put to the optical table velocity and vice versa.

At the time of writing, it is unclear whether mechanical coupling from the optical tables or second order effects like scattering have more significance for the interferometer performance; hence, it is unclear how to set the weighting factor η . For the optimization in this thesis, η is set to 1. At a later time, when the interferometer is set up and noise contributions are analyzed, the blending optimization can be repeated with a profound choice of η .

The cost functions are defined in global coordinates, while the control loops are designed to stabilize the individual AEI-SASs in local coordinates. This mismatch is resolved by analyzing, whether the AEI-SAS under investigation predominantly moves in common with or independent of the other AEI-SASs for each local degree of freedom.

Common motion between two AEI-SASs is introduced by the SPIs and the optical levers; hence, it is present in longitudinal, pitch and yaw direction. In these degrees of freedom, the common coupling factor $\bar{T}_{\sigma_{a2b}}$ is utilized. The other degrees of freedom use the differential coupling factor $\bar{T}_{\delta_{a2b}}$. By limiting the analysis to these coupling factors, any coupling to the DARM error signal is neglected and only the pitch and yaw error signals have relevance.

Note that in some degrees of freedom \bar{T} depends on the high and low pass filters of other degrees of freedom; therefore, the order for optimization is long→pitch→vert and yaw→side→roll and the results of one optimization are utilized for the cost function of the next.

- Optical levers are included in the control scheme, while they were neglected for local blending optimization; hence, the optical lever noise replaces LVDT noise for optical table motion in pitch and yaw.

The optimization is processed for all three AEI-SASs in all relevant degrees of freedom. The analysis is executed with the same method as the analysis of local sensor blending optimization (see section 3.7.8). The results do not only deliver optimal blending parameters, but at the same time offer insight into possible improvements for the overall isolation performance. The calculations in long, side and yaw are executed for the case of accelerometers and L-4C geophones to determine the better sensor set.

Figures 3.8.27–3.8.36 show the results of the optimizations. Each figure consists of two diagrams with the left-hand side showing the error signal *rms* over the blending frequency and the right-hand side showing amplitude spectral densities over the frequency. With the information of both diagrams, it is possible to derive the optimal blending parameters, analyze limitations of the current performance (see section 3.8.4) and derive possible improvements (see section 3.9).

Optimization in longitudinal direction

Only the central AEI-SAS uses sensor blending in long since the south and west AEI-SAS are isolated using the SPI. In long the goal is to minimize inertial motion since differential motion is stabilized by the SPI; hence, inertial noise of the LVDTs is utilized.

The optimal filter order combination for the isolation in longitudinal direction at the central AEI-SAS is calculated to be $l, h = 4, 2$. A second order high pass is not sufficient for L-4C geophones, since their noise rises with $1/f^3$ for vertical L-4Cs and even stronger for horizontal L-4Cs due to tilt-to-horizontal coupling. This would lead to low frequency drifts exceeding the linear control range. An additional attenuation at frequencies sufficiently below the blending frequency can be used in addition to the blending filter attenuation to retain stability. This is explained in more detail in section 3.9.

Figure 3.8.27 shows the optimization results for the usage of L-4C geophones as in-loop sensors. L-4C noise is relevant for frequencies between 0.01–0.2 Hz. Seismic coupling to the LVDT is the limiting noise contribution between 0.03–0.8 Hz and residual ground motion limits the overall noise above 0.8 Hz. The two first mentioned contributions predominantly limit the overall *rms*.

The optimization was also executed for accelerometers as in-loop sensors, with the result shown in figure 3.8.28. The minimal error signal *rms* is about a factor 1.12 higher than for L-4C geophones. Furthermore, the L-4C geophones, located on the optical table, can be improved more easily compared to accelerometers by reducing the optical table pitch motion; hence, L-4C geophones are favourable for the isolation of the central AEI-SAS in long.

Optimization in vertical direction

In vertical direction, all three AEI-SAS use the same sensors and have roughly equal properties. Figure 3.8.29 shows the optimization results. The limiting noise contributions are L-4C noise below 0.13 Hz, seismic noise coupling to the LVDT between 0.13–0.35 Hz, and residual motion due to insufficient gain above 0.35 Hz. The highest contributions to the *rms* result from the micro-seismic peak around 0.2 Hz and the suspension resonance in vertical direction at 2.5 Hz.

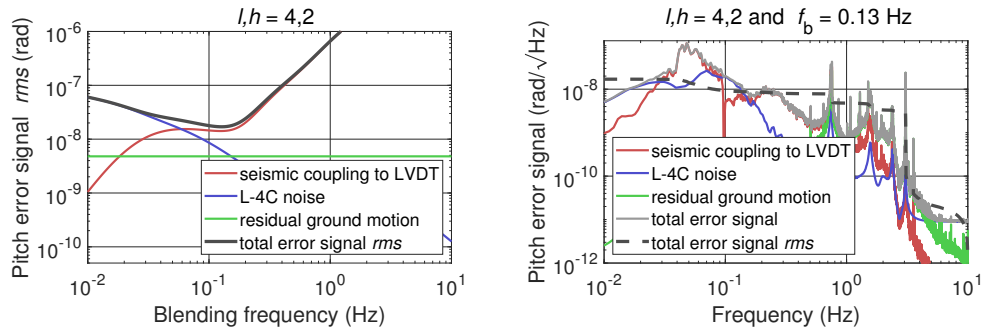


Figure 3.8.27: Blending optimization results in **longitudinal** direction. The diagrams show relevant noise contributions for the central AEI-SAS using L-4C geophones as in-loop sensors.

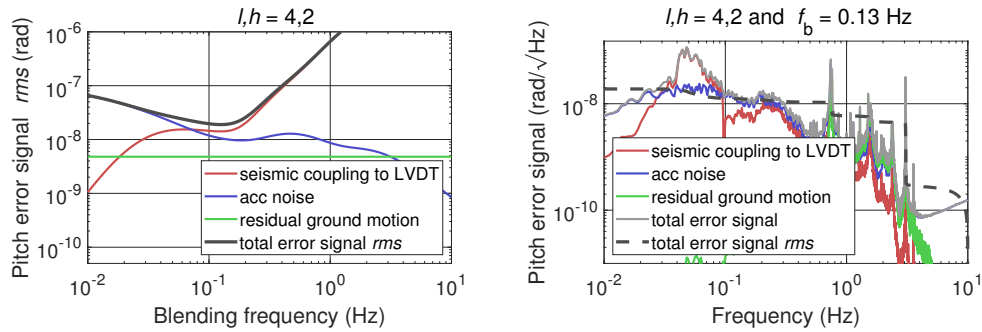


Figure 3.8.28: Blending optimization results in **longitudinal** direction. The diagrams show relevant noise contributions for the central AEI-SAS using accelerometers as in-loop sensors.

Optimization in side

Only the south and west AEI-SASs have a side direction, whereas the central AEI-SAS has two longitudinal direction (long to south and long to west); hence, only the south and west AEI-SASs are investigated in side. Both use the same sensors and have similar properties.

Figure 3.8.30 shows the optimization results for the usage of accelerometers as in-loop sensors. The limiting noise contributions are accelerometer noise below 0.5 Hz and seismic coupling to the LVDT above this frequency. The *rms* is predominantly limited by frequencies below 0.4 Hz and the side suspension resonance at 0.75 Hz.

The optimization was also executed for L-4C geophones as in-loop sensors, with the result shown in figure 3.8.31. The *rms* is a factor 2.5 higher than for accelerometers; hence, accelerometers are chosen for the isolation at the current state. If future improvements to roll motion are executed, tilt-to-horizontal noise of the L-4Cs would be lowered, which could lead to a better isolation performance using the geophones compared to accelerometers.

Optimization in pitch direction

All three AEI-SASs use the same sensors in pitch and have similar properties. Figure 3.8.32 shows the optimization results. The relevant noise contributions are L-4C noise over the entire investigated frequency range from 0.01 – 10 Hz, optical lever noise from 0.13 – 0.3 Hz and optimally suppressed ground motion above 0.8 Hz. The *rms* is predominantly limited by motion around the micro-seismic peak and the longitudinal suspension resonance at 0.74 Hz.

Optimization in yaw direction

Yaw is different for the central AEI-SAS compared to the south and west AEI-SASs,

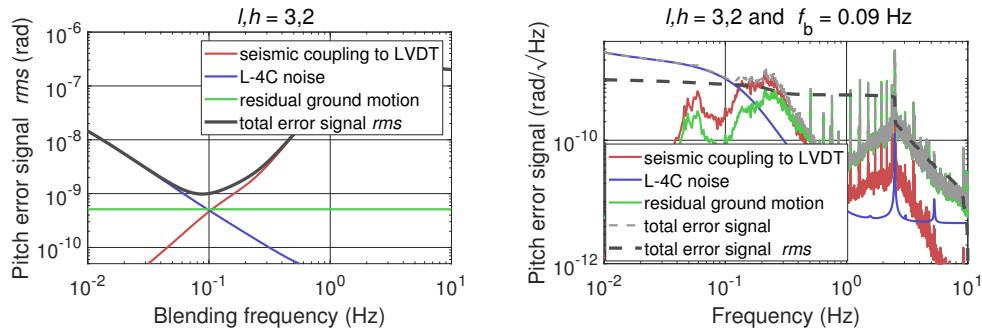


Figure 3.8.29: Blending optimization results in **vertical** direction. The diagrams show relevant noise contributions for all three AEI-SAS. The seismic motion measurement used for the calculation of residual ground motion features various peaks. These peaks are usually not present but do not influence the optimization results significantly.

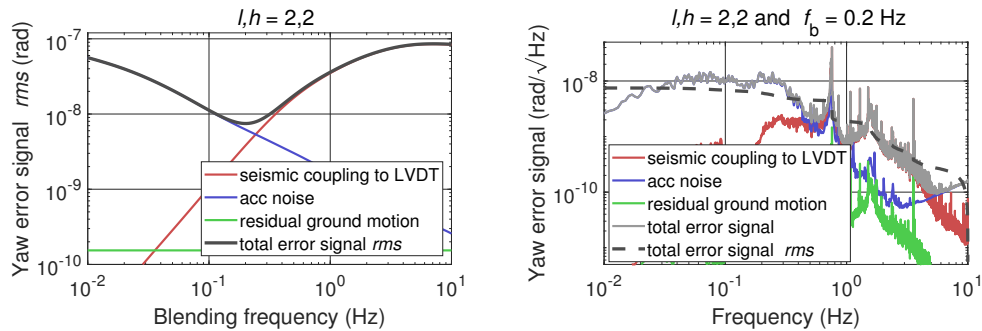


Figure 3.8.30: Blending optimization results in **side** direction. The diagrams show relevant noise contributions for the west and south AEI-SAS using accelerometers as in-loop sensors.

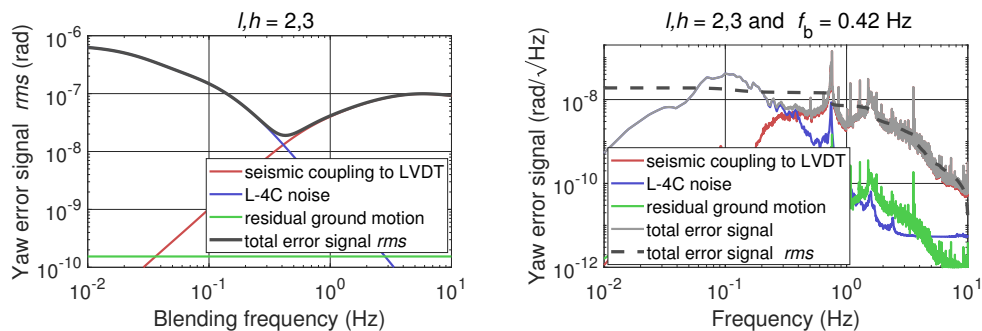


Figure 3.8.31: Blending optimization results in **side** direction. The diagrams show relevant noise contributions for the west and south AEI-SAS using L-4C geophones as in-loop sensors.

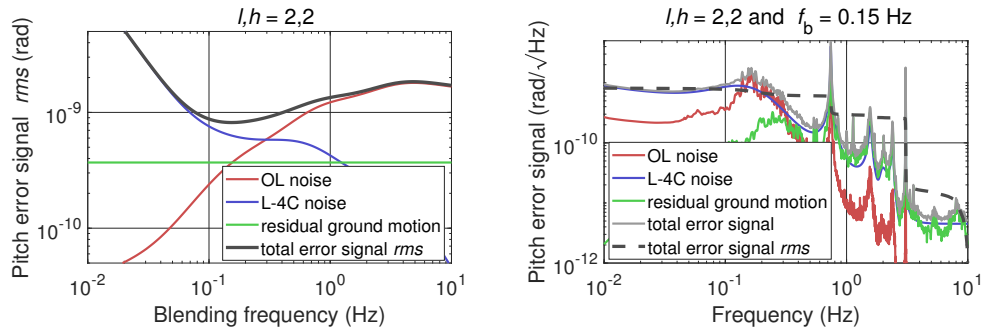


Figure 3.8.32: Blending optimization results in **pitch** direction. The diagrams show relevant noise contributions for all three AEI-SAS.

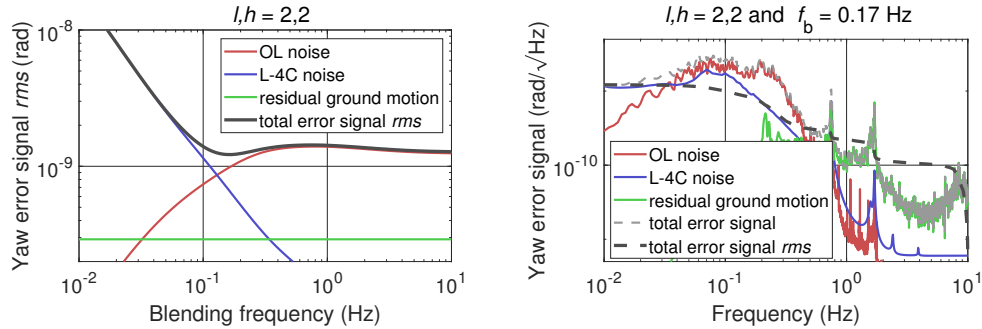


Figure 3.8.33: Blending optimization results in **yaw** direction. The diagrams show relevant noise contributions for the central AEI-SAS using L-4C geophones as in-loop sensors.

because tilt-to-horizontal noise partly couples to the yaw measurement (see section 3.7.3). The central AEI-SAS is controlled by optical levers in pitch to south and pitch to west, while the south and west AEI-SASs only have one optical lever for vertical rotations, resulting in larger tilt-to-horizontal noise.

Figure 3.8.33 shows the optimization results for the central AEI-SAS using L-4C geophones as in-loop sensors. The limiting noise contributions are L-4C noise below roughly 0.04 Hz, optical lever noise between 0.04–0.55 Hz and residual ground motion due to insufficient loop gain above 0.55 Hz. The *rms* is limited by broadband motion below 0.3 Hz.

Figure 3.8.34 shows the optimization results for the south and west AEI-SASs, when using a blending of L-4Cs with optical levers. The diagrams show an optimal blending frequency of 10 Hz, indicating that no blending should be performed. The *rms* is limited by broadband motion below 1 Hz, including the side suspension resonance at 0.76 Hz.

The optimization was also performed for a blending of accelerometers with optical levers. With accelerometers, a differentiation between central, south and west AEI-SAS is not necessary, since tilt-to-horizontal noise for the accelerometers does not depend on the optical table motion but on ground motion. Figure 3.8.35 shows the optimization results for accelerometers. The results are similar to the ones for L-4C geophones on the south and west AEI-SASs, with the conclusion that no sensor blending should be performed.

In summary, the central AEI-SAS optical levers should be blended with L-4C geophones, while for the south and west AEI-SASs the optical levers should be used as stand-alone sensors.

Optimization in roll direction

Roll direction is not defined for the central AEI-SAS; hence, the optimization in roll focuses on the south and west AEI-SASs, which are similar in its properties.

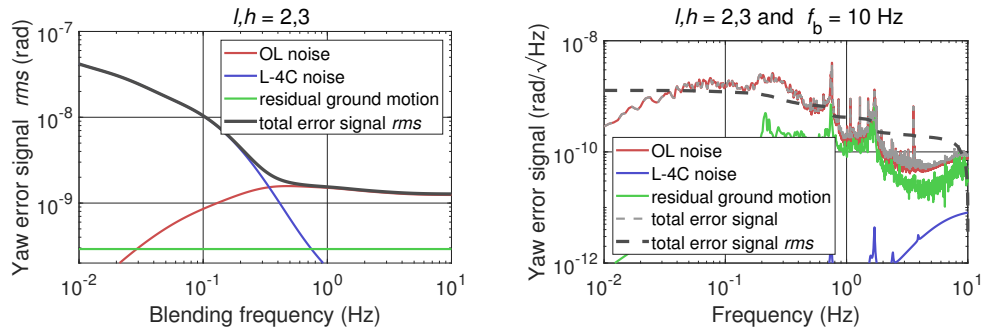


Figure 3.8.34: Blending optimization results in **yaw** direction. The diagrams show relevant noise contributions for the south and west AEI-SAS using L-4C geophones as in-loop sensors. No sensor blending is recommended.

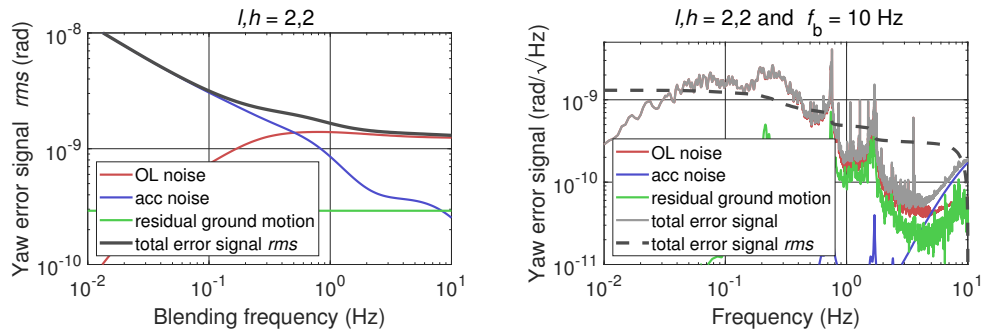


Figure 3.8.35: Blending optimization results in **yaw** direction. The diagrams show relevant noise contributions for all three AEI-SASs using accelerometers as in-loop sensors. No sensor blending is recommended.

Figure 3.8.36 shows the optimization results. The limiting noise contributions are L-4C noise below 0.2 Hz and seismic coupling to the LVDT due to insufficient gain above 0.2 Hz. The *rms* is limited by the side suspension resonance at 0.76 Hz and broadband motion below this frequency.

Conclusion

Table 3.8.3 gives an overview of the optimal blending parameters, the resulting coupling to the interferometer error signals, the affected interferometer degree of freedom and the percentage, with which each degree of freedom contributes to the overall interferometer error signals. The pitch error signal is dominated by common longitudinal optical table motion, with differential vertical optical table motion also contributing significantly. The yaw error signal is predominantly limited by differential side optical table motion.

The following section analyses the error signal limitations in depth and derives requirements for global seismic isolation improvements.

3.8.4 Analysis of performance limitations

The results from the previous section can be utilized to analyze the limitations and identify requirements for improvements of the global isolation system. As concluded in table 3.8.3, longitudinal and vertical motion are the main drivers for the interferometer error signal in pitch, while side motion is the main driver for the yaw error signal; hence, the analysis focuses on these three degrees of freedom.

Common longitudinal motion can be reduced by three different approaches:

- Seismic coupling to the central AEI-SAS LVDTs could be reduced by improving the sensor correction. This would allow the blending frequency to be shifted to

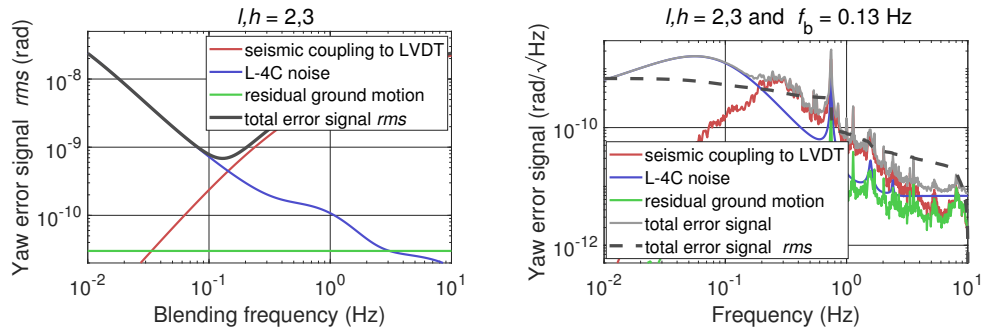


Figure 3.8.36: Blending optimization results in **roll** direction. The diagrams show relevant noise contributions for the south and west AEI-SASs. For this analysis, it is assumed that the south/west AEI-SAS use accelerometers in side direction.

Table 3.8.3: Optimal blending parameters and resulting coupling to the interferometer error signals for all degrees of freedom. For the horizontal degrees of freedom, only the better performing sensor set is included. “DoF” abbreviates the degree of freedom, “C”, “S” and “W” abbreviate the central, south and west AEI-SASs. The “% of total” for yaw is calculated for the higher coupling of the south and west AEI-SASs compared to the central AEI-SAS.

DoF	l, h	f_b (Hz)	Coupling to ifo (rad)	Affected DoF	% of total
long	4,2	0.13	1.70e-8	pitch	62 %
vert	3,2	0.09	9.81e-9	pitch	36 %
side	2,2	0.20	7.48e-9	yaw	79 %
pitch	2,2	0.15	8.18e-10	pitch	3 %
yaw (C)	2,2	0.17	1.22e-9	yaw	14 %
yaw (S,W)	–	–	1.30e-9	yaw	
roll	2,3	0.13	6.84e-10	yaw	7 %

higher frequencies, reducing the coupling of L-4C noise as well. The ripple of the sensor correction high pass filter (see figure 3.7.9) amplifies the LVDT noise significantly. A different filter design could potentially reduce the noise that is coupled in by sensor correction, and will be investigated in section 3.9.1. The sensor correction between 0.1 – 3 Hz is assumed to be limited by tilt-to-horizontal noise of the STS-2 seismometer. A tilt correction of the STS-2 signal requires a ground rotation sensor, like the beam rotation sensor developed for the Advanced LIGO interferometers [VHT⁺14, VHG⁺17], which exceeds the reasonable costs.

- The L-4C noise in longitudinal direction could be reduced by attenuating the tilt-to-horizontal noise, resulting from pitch of the optical table. This would allow for a lower blending frequency. A significant improvement in pitch motion requires a higher gain for the pitch control loop and simultaneously a reduction of sensor noise. A higher gain is required at the suspension resonances at 0.74 Hz, 1.57 Hz and 3.07 Hz. This could be achieved with resonant gain enhancements and is investigated in section 3.9.1. A reduction of sensor noise includes two possibilities:
 - The L-4C noise could be reduced by replacing the L-4Cs in pitch with dedicated rotation sensors, like the beam rotation sensor. This would allow for lower blending frequencies, but exceeds the reasonable costs. The pitch readout could also be improved by installing better vertical sensors, replacing the L-4C geophones.
 - The optical lever noise could be reduced by reducing differential vertical motion between two AEI-SASs. This again requires a higher loop gain in vertical direction and simultaneously a reduction of sensor noise. The increase in loop gain is required on the micro-seismic peak between 0.15 – 0.4 Hz and on the vertical suspension resonance at 2.5 Hz. This is investigated in section 3.9.1. A reduction of LVDT noise requires an improvement in sensor correction on the micro-seismic peak. The limitation for the sensor correction performance in this frequency range is unknown and presumably requires major efforts; hence, it is not further investigated. The vertical L-4C noise can only be reduced by replacing the L-4Cs with better sensors, which is investigated in section 3.9.2.

The latter approach of replacing the vertical L-4C geophones with better sensors does not only reduce the coupling of longitudinal motion to the pitch error signal, but also lowers the second high contribution to the pitch error signal, which is vertical motion.

Differential side motion can as well be reduced by three different options:

- Same as for the longitudinal motion, seismic coupling to the LVDTs could be reduced by improving the sensor correction. Different to longitudinal motion, LVDT noise is not significant at the ripple of the sensor correction filter, but at frequencies above roughly 0.2 Hz. An improvement above 0.2 Hz requires a tilt correction of the STS-2 seismometer, which exceeds the reasonable costs.
- The L-4C geophones on the optical table could be used in-loop, in combination with a reduction of roll motion of the south and west AEI-SASs. This would allow for lower blending frequencies, which would simultaneously lower the coupling of LVDT noise. Roll motion can be reduced in two ways:
 - Seismic coupling to the LVDTs could be reduced and the blending frequency in roll could be lowered. For roll, this is more challenging since no rotational ground sensor is available for sensor correction. One option is a direct measurement of ground rotation, for example with the already mentioned beam rotation sensor, developed for the Advanced LIGO interferometers. This includes high efforts and is not further investigated.

- L-4C noise in roll could be reduced, and the blending frequency could be increased by replacing the L-4Cs with better inertial sensors. This matches the most promising improvement for the pitch error signal and is investigated in section 3.9.2.

In summary, better vertical inertial sensors could reduce both the pitch and yaw error signals significantly. The optimization of digital filters promises for smaller improvements.

3.8.5 Global isolation performance

This section presents measurements for the global isolation performance. The optimal tool for verifying a success of global isolation techniques is a full Michelson interferometer with DARM readout, a pitch error signal and a yaw error signal. Since a full Michelson interferometer is not available at the time of writing, other sensors need to be used to measure the global isolation performance indirectly.

- Sensor 1: LVDTs can be used to track local improvements by optical levers at low frequencies compared to local sensor isolation. A local reduction of motion indicates reduced global motion.
- Sensor 2: Horizontal L-4Cs are limited by tilt-to-horizontal noise at low frequencies and hence provide a measurement of tilt motion to verify local improvements by optical levers.
- Sensor 3: A combination of frequency reference cavity and PMC can be utilized to measure differential motion between central and south AEI-SASs.

The laser frequency is stabilized by locking the laser to the 10m long suspended frequency reference cavity, with the mirrors located on central and south AEI-SASs. Differential longitudinal motion of the optical tables results in length changes of this cavity, which is imprinted onto the locked laser frequency. The PMC is utilized as a readout sensor for frequency noise. With proper calibration, the PMC can read out length changes of the frequency reference cavity, providing information about differential longitudinal motion of the AEI-SASs.

This measurement tool is, in principle, close to one arm of the Michelson interferometer. Both are cavities located on two AEI-SASs and both use triple suspensions. There are three problems that differentiate the two cavities, preventing a precise analysis of global isolation. At first, the frequency reference cavity is located off-axis, at the far side of the optical tables; hence, yaw motion of the AEI-SASs creates high longitudinal motion of the cavity mirrors. The second problem is the different mechanics. The frequency reference cavity is a triangular cavity using different suspension designs with different resonance frequencies and cross couplings. The third problem is the comparably high non-stationary noise of the PMC readout, limiting high frequency measurements above roughly 4 Hz and possibly limiting measurements with high sensitivity below 0.3 Hz.

Because of these three differences, the combination of frequency reference cavity and PMC can only be used to verify large changes and the general behavior of differential longitudinal motion, without providing information on details.

- Sensor 4: The end test mass of the Single Arm Test is equipped with an optical lever to measure test mass pitch and yaw motion. This sensor can be utilized to investigate coupling of optical table motion to rotations of the mirror.

Four different measurements for the global isolation performance are executed:

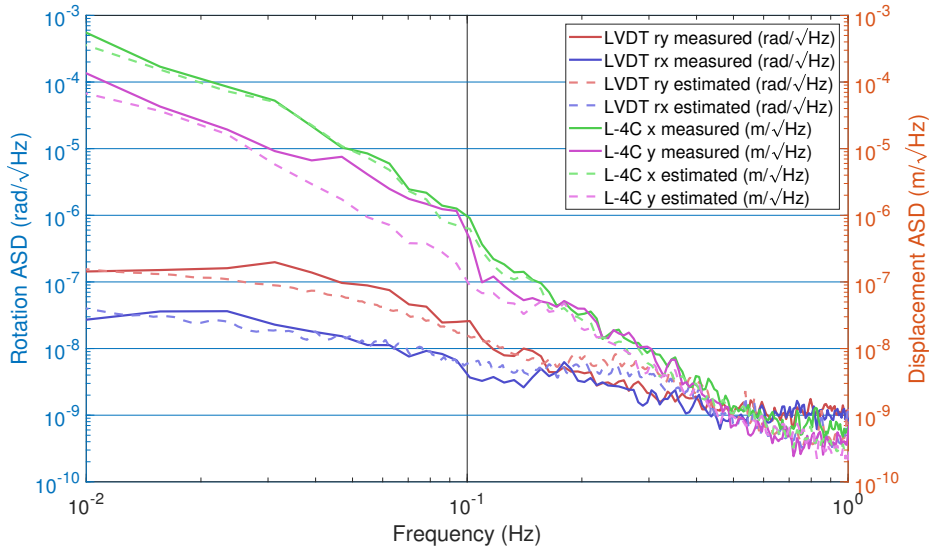


Figure 3.8.37: Central AEI-SAS LVDT outputs in ry and rx and L-4C outputs in x and y . ry is controlled with local sensors and rx is controlled with an optical lever. The better performance of optical levers compared to local sensors is confirmed by the lower rx motion compared to ry and by the lower tilt-to-horizontal noise in y compared to x .

Test 1: Verification of optical lever performance

The central AEI-SAS is controlled using optical levers in yaw and pitch to south and local sensors for all other degrees of freedom. In this control state, pitch to west is significantly larger, being controlled with local sensors, than pitch to south.

Figure 3.8.37 verifies this assumption by showing the measured LVDT outputs in ry (= pitch to west) and rx (= pitch to south). Below 0.16 Hz, rx motion is lower by up to a factor 9. The LVDT outputs were also simulated with a high agreement to the measurement.

The lower rx motion compared to ry leads to a lower tilt-to-horizontal noise for the L-4C geophone output in y compared to x . This is as well verified by measurements shown in figure 3.8.37. The L-4C outputs in x and y show the estimated behavior, with the L-4C y output being significantly lower. The measured LVDT outputs are used to estimate the L-4C outputs with a high overlap to the measurements. Only between 0.04 – 0.1 Hz tilt-to-horizontal noise in y is higher than expected.

Test 2: Verification of SPI performance

The SPI is designed to measure differential optical table motion in longitudinal direction and provide a signal for the suppression of this motion; hence, sensor 3 from the list earlier in this section, measuring length changes of the frequency reference cavity, provides a rough performance readout.

Three different control states are compared. All three control states include optical levers in pitch and yaw using high gain, to minimize cross coupling from these degrees of freedom to differential long.

In a first control state, the optical tables of the central and south AEI-SASs are locked to the ground in all degrees of freedom except for pitch and yaw as explained. This is executed by minimizing the LVDT output with high gain. Ground motion at low frequencies is mostly common for all three AEI-SASs. When locking the optical tables to ground, differential motion at low frequencies between two optical tables is estimated to be low. Above roughly 0.3 Hz, ground motion at two AEI-SASs starts to become uncommon, resulting in a larger differential motion.

In a second control state, only low gain is utilized to dampen the fundamental

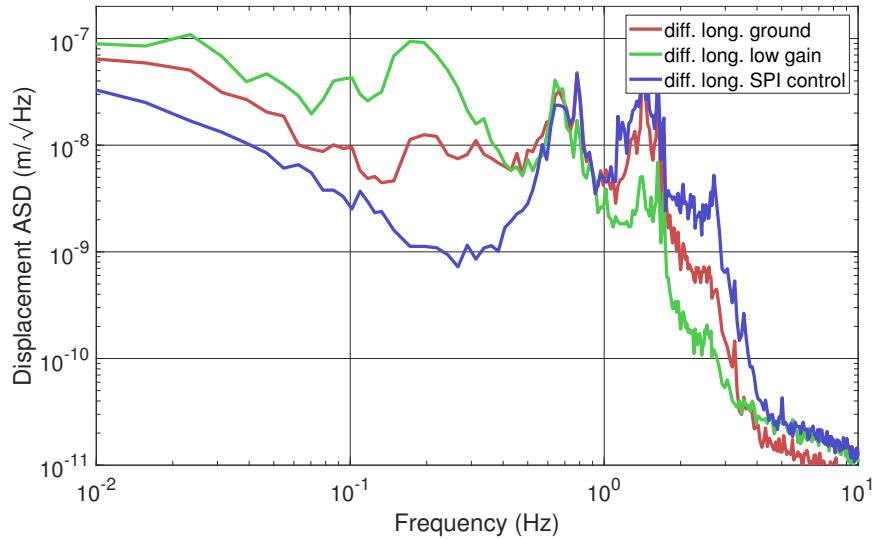


Figure 3.8.38: Reference cavity length changes for three different AEI-SAS control states. For each of the control states, pitch and yaw motion of the optical tables are isolated with optical levers using high gain to minimize cross coupling. “diff. long. ground” describes a control state, where the optical tables are locked to the ground in all other degrees of freedom using LVDTs. “Diff. long. low gain” shows the results for mostly passively isolated optical tables, with active isolation only used to dampen the fundamental resonance frequencies, and in pitch and yaw. “diff. long. SPI control” is similar to the first mentioned control state, but utilizes the SPI to control differential motion.

resonances of the AEI-SASs, while applying as little active isolation as possible. Exceptions are pitch and yaw, as explained earlier. In this control state, differential longitudinal motion is increasing around the fundamental resonance frequency of the AEI-SASs, at 0.1 Hz. This is caused by mechanical differences in the AEI-SASs. Passive isolation well above the resonance frequency reduces differential motion by isolating inertially.

In the third control state, the optical tables are again locked to ground with the LVDTs but now differential longitudinal motion between central and south AEI-SASs is controlled with the SPI. This is estimated to give the lowest differential longitudinal motion of all three compared states in the control band. Close to unity gain, at roughly 3 Hz, the high phase delay of the control loop amplifies differential long motion, as explained in section 3.2.3.

Figure 3.8.38 shows the measurement results for all three control states. As predicted, differential longitudinal motion at low frequencies is highest for a low gain control state. It is reduced significantly when locking the optical tables to ground, and is even lower for an SPI control scheme. Especially on the micro seismic peak, differences are large, with the SPI scheme providing lower motion by a factor of at least 90. A higher factor is possible, but might be masked by PMC noise. Above 1 Hz, the performance is inverse, with the SPI control state exhibiting the largest motion and the low gain control state featuring the lowest motion. This matches the expected behavior.

Test 3: Verification of optical lever and SPI performance

Figure 3.8.39 shows another verification of optical lever and SPI performance as in-loop sensors. The figure compares reference cavity arm length changes (sensor 3 from the list earlier in this section) for three control states: a purely local isolation, a

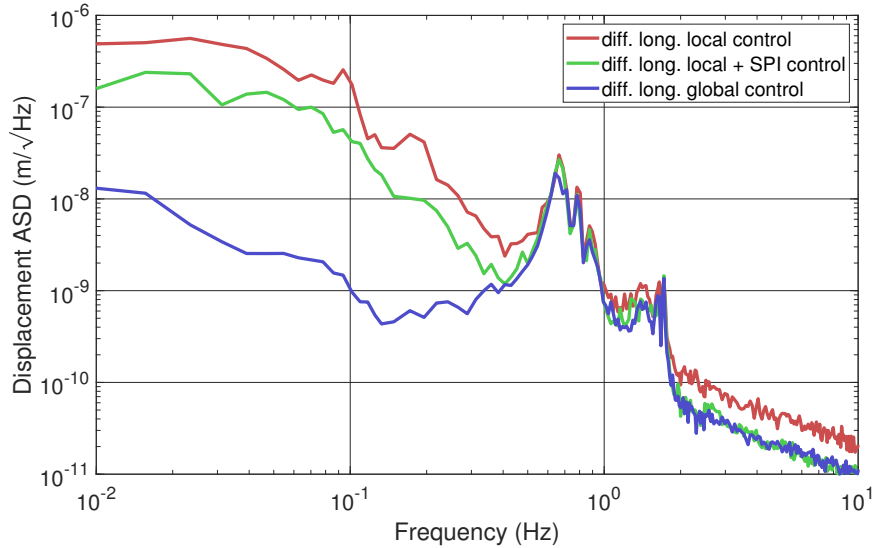


Figure 3.8.39: Reference cavity length changes for three different control states: a purely local isolation, a local isolation with the SPI, controlling differential longitudinal motion, and a full global isolation using the SPI and optical levers. The diagram proves that all global sensors are required to achieve a high performance global isolation.

local isolation but using the SPI to control the differential longitudinal optical table motion, and a global isolation state, using the SPI, all optical levers and local sensors for the other degrees of freedom. A similar measurement was already presented by [Köh18] in 2018. Interim development of the frequency reference cavity results in a higher sensitivity of the current system, resulting in more precise measurements.

It is clearly visible that using the SPI reduces differential motion below 0.5 Hz compared to a fully local isolation. The improvement is roughly a factor 2-3. Adding the optical levers reduces the reference cavity motion further by an additional factor of roughly 50. This shows that longitudinal and rotational motion of the optical tables couple the reference cavity length changes by roughly the same amount. All global sensors are crucial to achieve a high performance global isolation.

The improvement mostly vanishes for frequencies above the reference cavity longitudinal resonance frequency of 0.66 Hz, indicating that common optical table motion is converted to differential mirror motion by differences in the suspensions and by controls noise. The higher noise for local isolation above 2 Hz is caused by the PMC and has no relevance.

Test 4: Verification of simulations for sensor blending optimization

Sections 3.8.3 and 3.8.4 present simulations for a sensor blending optimization that provide information about limitations of the global isolation. One outcome was that longitudinal LVDT noise of the central AEI-SAS is the main driver for the coupling of common longitudinal optical table motion to the interferometer; furthermore, common longitudinal optical table motion is the highest contributor to the pitch error signal of the Michelson interferometer. A measurement of the pitch motion of a cavity mirror should therefore be limited by LVDT noise. This prediction assumes a blending frequency of 0.13 Hz in longitudinal direction, which is calculated to be the optimal blending frequency. In current operation, a higher blending frequency of 0.2 Hz is utilized, which increases the LVDT noise even further.

This prediction by the model is verified in figure 3.8.40. The diagram shows pitch motion of the SAT end test mass for a full global isolation with and without sensor correction. With sensor correction, the shape of the horizontal correction filter, fea-

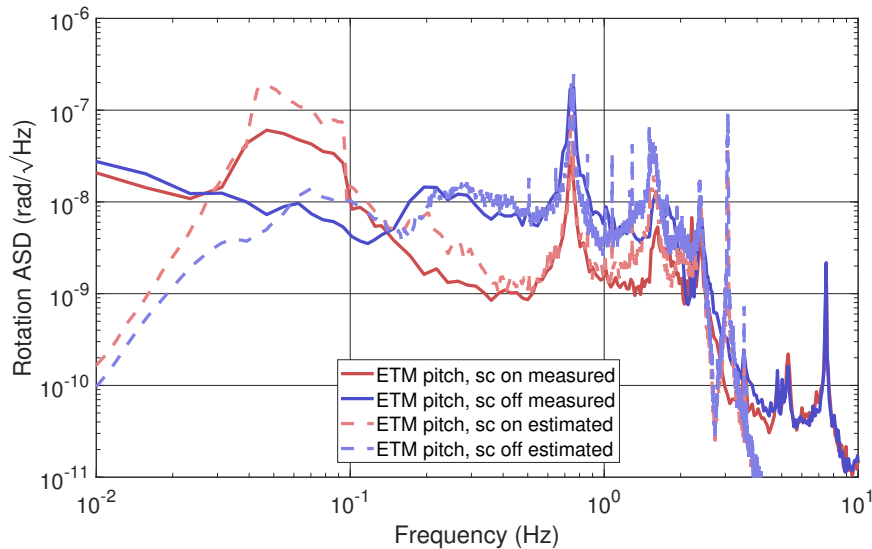


Figure 3.8.40: SAT end test mass motion in pitch for a full global isolation, with and without sensor correction. The figure compares measurements with calculated estimations, featuring a high overlap.

turing a large ripple below 0.1 Hz (see figure 3.7.9), is clearly visible. Without sensor correction, this ripple vanishes. The performance above 0.13 Hz becomes significantly worse, caused by the missing subtraction of ground motion from the LVDT output. This clearly confirms that the mirror pitch motion is dominated by LVDT noise in longitudinal direction.

This behavior matches the estimations calculated with the sensor blending optimization script. The difference between model and measurement at low frequencies is explained by noise of the readout sensor. In particular, it results from translational noise of the optical lever due to differential translational optical table motion (see section 3.4.6). A resonance in the estimations at roughly 3 Hz is shifted to 7.5 Hz for the measurements. This results from different transfer functions of the sub-SQL interferometer suspensions, used for the estimations, compared to the current suspensions. The mismatch between estimation and measurement above 3 Hz is a direct consequence of the shifted resonance. Differences between 0.4 Hz and 3 Hz are assumed to result from vertical cross coupling and imprecise modelling.

3.9 Concepts for improvements

This section discusses two types of possible improvements for the active seismic isolation of the AEI 10 m prototype: optimization of digital filters and implementation of new sensors. The first option is comparably easy to execute due to an easy implementation and testing of filters with CDS. The implementation of new sensors requires more effort because new filters need to be built and/or the control system needs to be adapted. The improvements are evaluated with the principle of global sensor blending optimization, as presented in section 3.8.3.

3.9.1 Optimization of digital filters

At the time of writing, digital filters for the active seismic isolation of gravitational wave detectors are often designed “by eye”, as it was done for the AEI 10 m prototype; hence, the quality of the filters is strongly dependent on the experience of the designers but is also biased by their knowledge. The blending optimization analysis presented in section 3.8.3 and 3.8.4 shows that the first design attempts for filters of

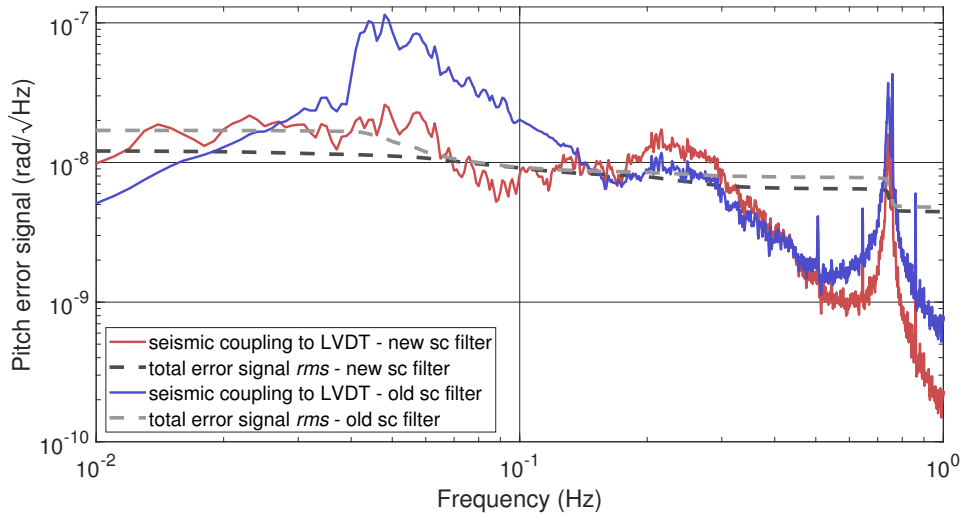


Figure 3.9.1: Coupling of longitudinal optical table motion to the pitch error signal of the interferometer for the old and new sensor correction filters. The old filter amplifies LVDT noise at its ripple below 0.1 Hz which dominates the total error signal *rms*. The new standard second order filter features a significantly lower ripple, lowering the overall error signal.

the AEI-SASs have large room for improvements. These improvements are investigated in the following.

Longitudinal motion

Two possible improvements of digital filters for motion in the longitudinal direction are identified and calculated. The first improvement investigates the sensor correction high pass FIR filter, shown in figure 3.7.9, which features a large ripple below 0.1 Hz. The sensor blending optimization in longitudinal direction, which is presented in figure 3.8.27, shows that LVDT noise being amplified by this ripple limits the overall interferometer error signal *rms* in pitch. Different standard high pass blending filters as presented in section 3.7.5 were tested as replacements for the FIR filter. A second order filter with a blending frequency of 0.06 Hz resulted in the lowest interferometer error signal. Figure 3.9.1 shows the coupling of longitudinal motion to the interferometer error signal with the old and new sensor correction filter. The new filter reduces the coupling of LVDT noise below 0.1 Hz significantly, lowering the overall *rms* by a factor of 1.4. The new filter reduces the sensor correction performance above 0.16 Hz slightly, which is not significant for the overall interferometer *rms*. The lower coupling of LVDT noise above 0.45 Hz results from a lower optimal blending frequency using the new filter.

The second improvement of digital filters in longitudinal direction investigates additional notches in the blending filters. Section 3.7.5 introduces sensor blending filters as complementary filters with very limited numbers of parameters, namely one blending frequency and two filter orders. These types of blending filters were utilized for the optimization within this thesis. Additional features like notches and stronger roll-offs can be implemented in the blending filters to improve the isolation performance. The additional features should only be added at frequencies, where the filter already strongly attenuates the sensor output; hence, they should be added to the low pass filter sufficiently above the blending frequency, and to the high pass filter sufficiently below the blending frequency.

A stronger roll-off is mainly utilized to reduce the coupling of inertial sensor noise at very low frequencies. L-4C noise rises with $1/f^3$ to low frequencies for vertical sensors, horizontal sensor noise rises even stronger, due to tilt-to-horizontal noise.

Accelerometers are also prone to tilt coupling; hence, high pass filters for vertical L-4Cs and accelerometers should have at least a roll-off of f^3 , for horizontal L-4Cs it should be at least f^4 . In order to keep the calculated optimal filter orders, a stronger roll-off can be added significantly below the blending frequency to ensure a long-time stability of the control loops. The blending optimization within this thesis does not include stability considerations; furthermore, it is limited to frequencies above 0.01 Hz. Therefore, the implementation of stronger roll-offs is not discussed within this thesis. Additional notches for the blending filters are investigated in the following.

After adding a feature η to one blending filter, both filters need to be balanced again to remain complementary. The new, balanced blending filters are calculated by

$$\begin{aligned} L' &= L \times \eta, \\ L_{\text{new}} &= \frac{L'}{L' + H}, \\ H_{\text{new}} &= \frac{H}{L' + H}, \end{aligned} \quad (3.9.1)$$

with η being a feature added to the low pass filter L . H is the corresponding high pass filter and L_{new} and H_{new} are the new low and high pass filters.

Figure 3.9.2 shows an example for standard blending filters with a blending frequency of 0.3 Hz and orders of $l, h = 2, 2$, and the same filters but with an additional notch at 0.742 Hz and an according rebalancing. Both filter sets add up to a super sensor with an amplitude of exactly 1. In this example, adding a notch in the low pass filter does not only attenuate the low frequency sensor noise, but also the rebalanced high pass filter has a lower gain at the notch frequency and attenuates the high frequency sensor noise. This is a consequence of the phase difference between low and high pass.

A notch was added to the low pass blending filter in the longitudinal direction at 0.742 Hz to attenuate the coupling of LVDT noise at the fundamental suspension resonance in long. The coupling of longitudinal motion to the interferometer error signal using the old blending filter and the new filter is shown in figure 3.9.3. Both calculations include the optimized sensor correction filter presented earlier in this section. The overall interferometer error signal *rms* reduces slightly, by a factor of 1.1.

The total interferometer pitch error signal reduction due to an optimization of digital filters in longitudinal direction is a factor 1.54.

Vertical motion

In the vertical direction, an optimization of the controller filters promises a reduced coupling to the interferometer error signal and is investigated. Figure 3.9.4 shows transfer functions of the old and new controller filters. The gain above 5 Hz is reduced by a factor 1.27, which reduces the unity gain frequency of the control loop from 22.4 Hz to 18.7 Hz. This provides a higher phase margin, allowing for a significantly higher gain on the vertical suspension resonance at 2.5 Hz and below 1 Hz. The new control loop features roughly the same phase margin at the unity gain frequency as the old control loop with a value of 37° and therefore does not reduce the loop stability.

Figure 3.9.5 shows the coupling of vertical optical table motion to the interferometer error signal in pitch for the old and new controller filters. The coupling is reduced significantly at the vertical suspension resonance at 2.5 Hz and below 1 Hz. The LVDT and L-4C noise are not affected by the new controller filter and limit the overall *rms*; therefore, the reduction of the interferometer *rms* is only a factor of 1.4. The full benefit of the new controller filter can be exploited by reducing the noise of the involved sensors, which is investigated in section 3.9.2.

Side motion

In side direction, one possible improvement was identified to reduce the coupling to the interferometer error signal in yaw. Notches at 0.746 Hz and 1.58 Hz were added

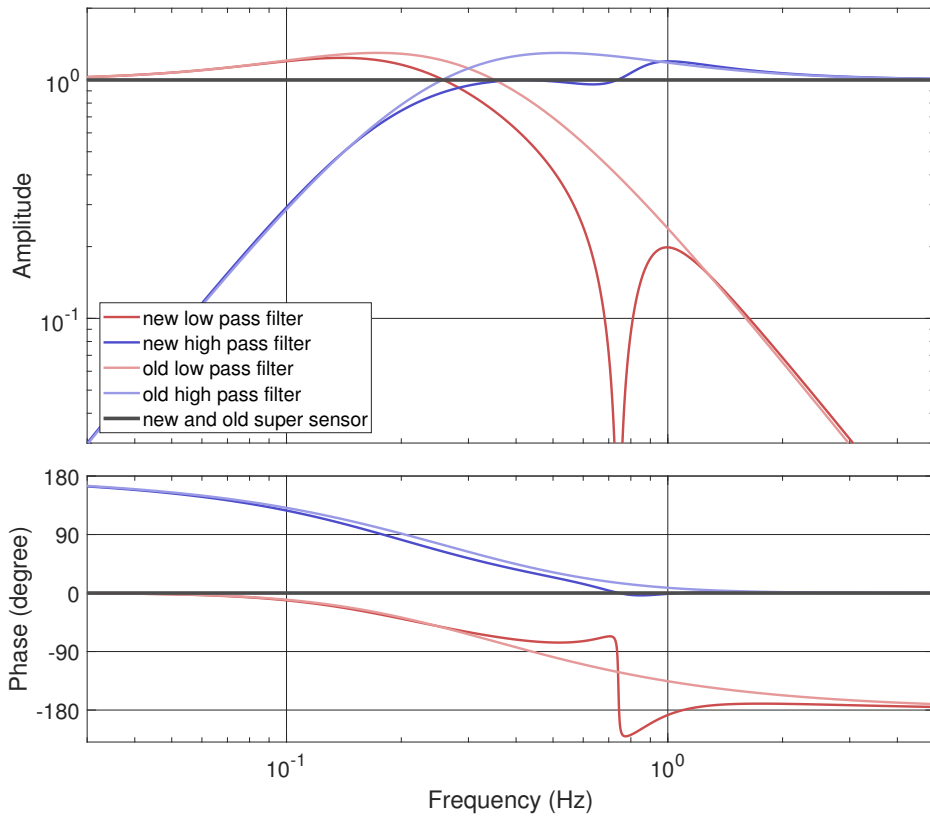


Figure 3.9.2: Bode plot of standard blending filters with a blending frequency of 0.3 Hz and orders of $l, h = 2, 2$, and the same blending filters but with an additional notch at 0.742 Hz and an according re-balancing. The super sensor has an amplitude of exactly 1 for both blending filter sets.

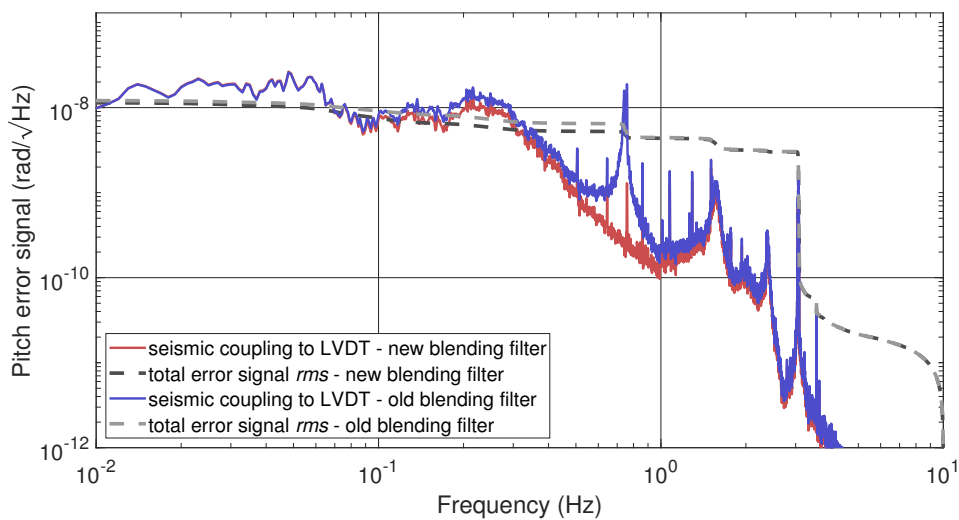


Figure 3.9.3: Coupling of longitudinal optical table motion to the pitch error signal of the interferometer for the old and new blending filters. The new blending filter features a notch at 0.742 Hz, attenuating the coupling of LVDT noise significantly.

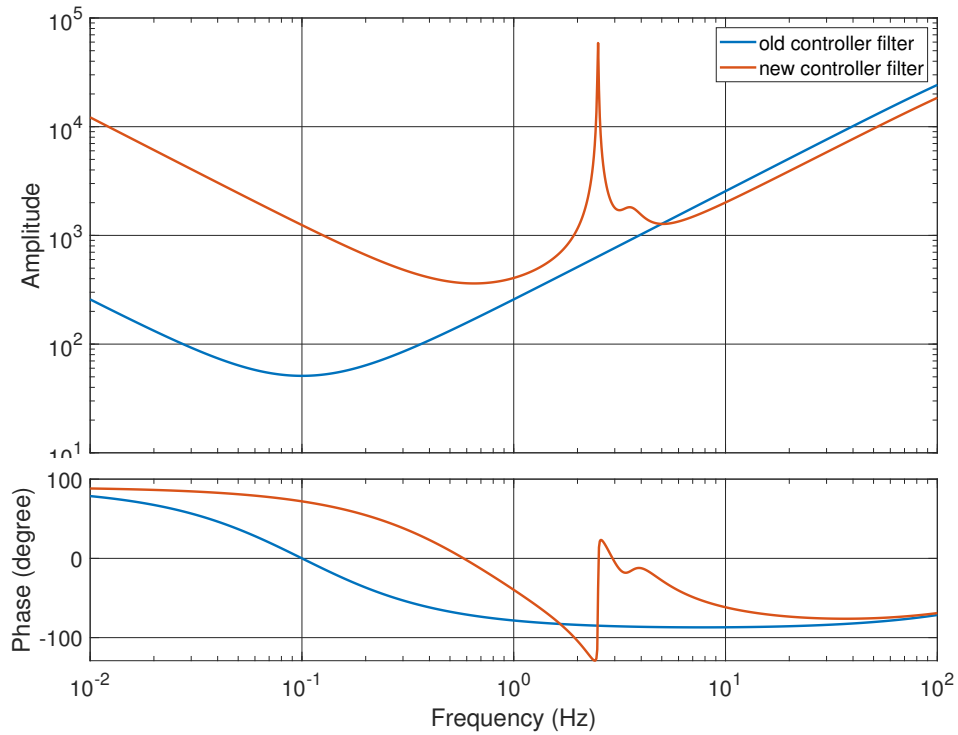


Figure 3.9.4: Bode plot of the old and new controller filter in vertical direction. The gain is slightly lowered above 5 Hz and significantly increased at the vertical suspension resonance at 2.5 Hz and below 1 Hz.

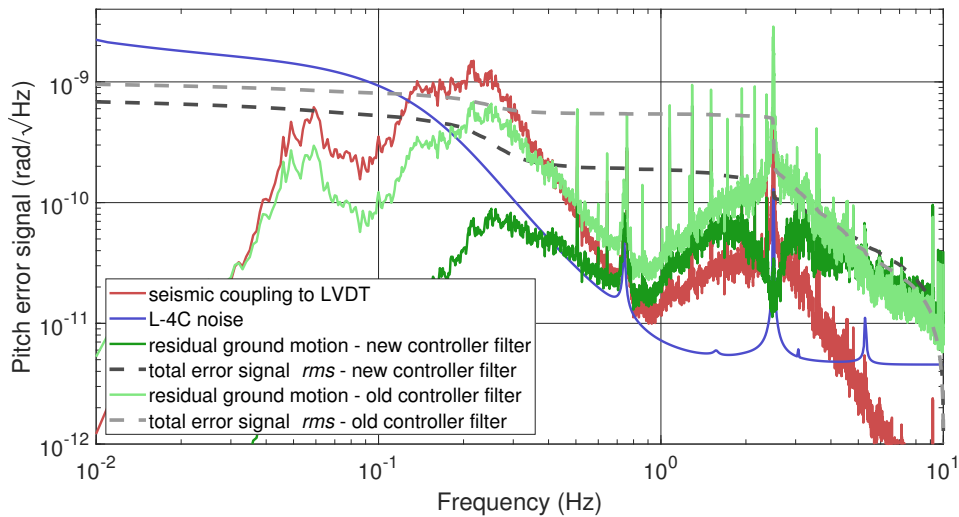


Figure 3.9.5: Coupling of vertical optical table motion to the pitch error signal of the interferometer for the old and new controller filter. The new filter reduces the coupling of residual ground motion to the vertical suspension resonance frequency at 2.5 Hz and below 1 Hz significantly. The coupling of LVDT and L-4C noise is unaffected.

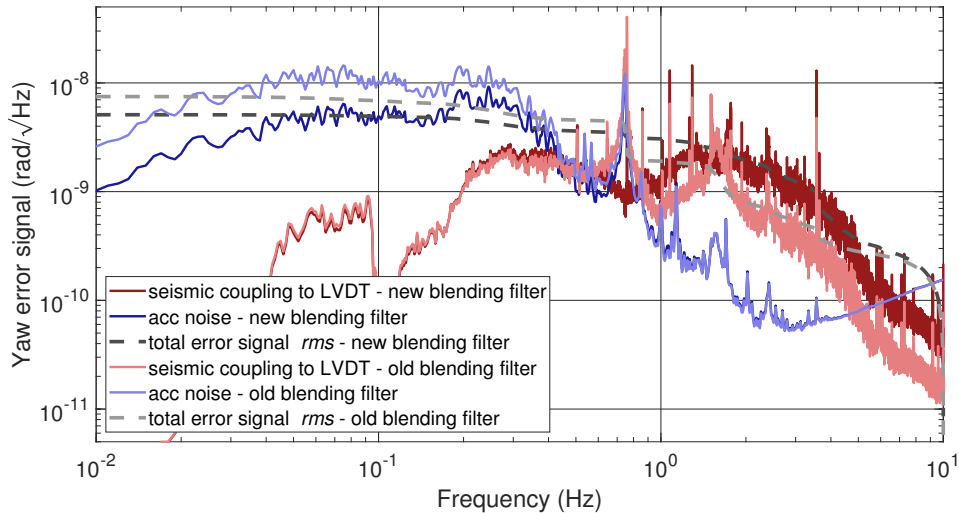


Figure 3.9.6: Coupling of side optical table motion to the yaw error signal of the interferometer for the old and new blending filters. The new filter reduces the coupling of LVDT noise at the two suspension resonances in side at 0.746 Hz and 1.58 Hz. This allows for a higher blending frequency, which reduces the coupling of accelerometer noise.

to the low pass blending filter as explained for longitudinal motion within this section. Figure 3.9.6 shows the coupling of side motion to the interferometer error signal in yaw for the old and new blending filters. The coupling of LVDT noise is reduced significantly on the two suspension resonances. This shifts the optimal blending frequency from 0.2 Hz to 0.34 Hz, reducing the coupling of accelerometer noise at frequencies below 0.4 Hz. The overall interferometer yaw *rms* is reduced by a factor of 1.5.

Pitch motion

Two improvements are investigated to reduce the coupling of pitch motion to the interferometer error signal. A notch is added to the low pass blending filter of the optical levers at the longitudinal suspension resonance at 0.742 Hz. This is described in more detail for the improvement of longitudinal motion earlier in this section. The second improvement is achieved by adding resonant gains to the controller filter, similar to the investigations on vertical motion earlier in this section. Resonant gains are added at the longitudinal suspension resonances at 0.74 Hz, 1.58 Hz and 3.07 Hz, without reducing the phase margin at the unity gain frequency of the loop significantly. Figure 3.9.7 shows the coupling of pitch motion to the interferometer error signal for the old and new filters. The coupling of optical lever noise and residual ground motion is significantly reduced on the longitudinal suspension resonances. The optimal blending frequency is shifted from 0.15 Hz to 0.32 Hz which reduces the coupling of L-4C noise at low frequencies. The overall reduction of the interferometer error signal *rms* is a factor of 1.3.

Yaw motion

In the yaw degree of freedom, no significant improvement by optimizing digital filters was identified. Optical levers are used as stand-alone sensors and limit the *rms*. Neither changes of the controller filter, nor notches in blending filters or a different sensor correction filter can reduce the coupling of optical lever noise to the interferometer. A set of new sensors can improve the isolation in yaw, which is investigated in section 3.9.2.

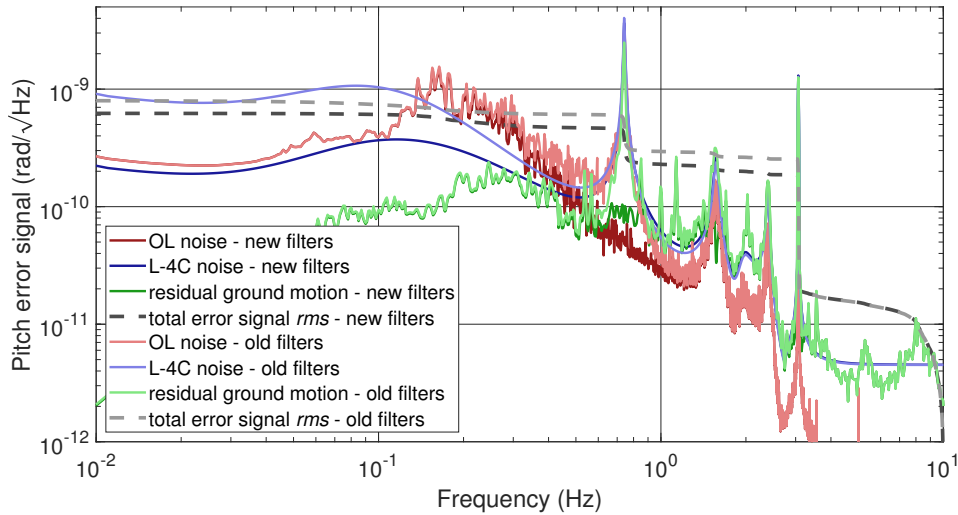


Figure 3.9.7: Coupling of pitch optical table motion to the pitch error signal of the interferometer for the old and new blending and controller filters. The new filters reduce the coupling of optical lever noise at the suspension resonance in long at 0.742 Hz and the coupling of residual ground motion at the longitudinal suspension resonances at 0.74 Hz, 1.58 Hz and 3.07 Hz. The optimal blending frequency is shifted to higher frequencies, reducing the coupling of L-4C noise at low frequencies.

Roll motion

One possible improvement for the roll degree of freedom is investigated, namely adding a notch to the low pass blending filter at 0.746 Hz, as described in more detail for the longitudinal degree of freedom earlier in this section. Figure 3.9.8 shows the coupling of roll motion to the interferometer error signal in yaw. The coupling of LVDT noise is reduced significantly at the suspension side resonance at 0.746 Hz. The optimal blending frequency shifted from 0.13 Hz to 0.18 Hz, reducing the coupling of L-4C noise at low frequencies. The overall reduction of the interferometer error signal *rms* is a factor of 1.3.

The described investigations prove that digital filters designed "by eye" have large potential for improvements. The blending filter optimization introduced in this thesis is an example for a systematic calculation of requirements for digital filters, but only covers a small range of filter designs. Advanced techniques can be utilized to cover a wider range of filter designs, not only for sensor blending, but also for sensor correction and controller filters. One example of an advanced optimization technique is particle swarming, which is presented in [VSS03, CCT⁺20].

Summary optimization of digital filters

Table 3.9.1 summarizes all improvements by optimizing digital filters compared to the current performance presented in table 3.8.3. The analysis proposes a total reduction of the interferometer pitch error signal by a factor of 1.48 and of the interferometer yaw error signal by a factor of 1.39. Especially the improvements in long and side are crucial since long and side were analyzed to dominate the pitch and yaw error signals.

At present, it is not possible to test and verify these improvements, since this requires a Michelson interferometer with error signals in pitch and yaw.

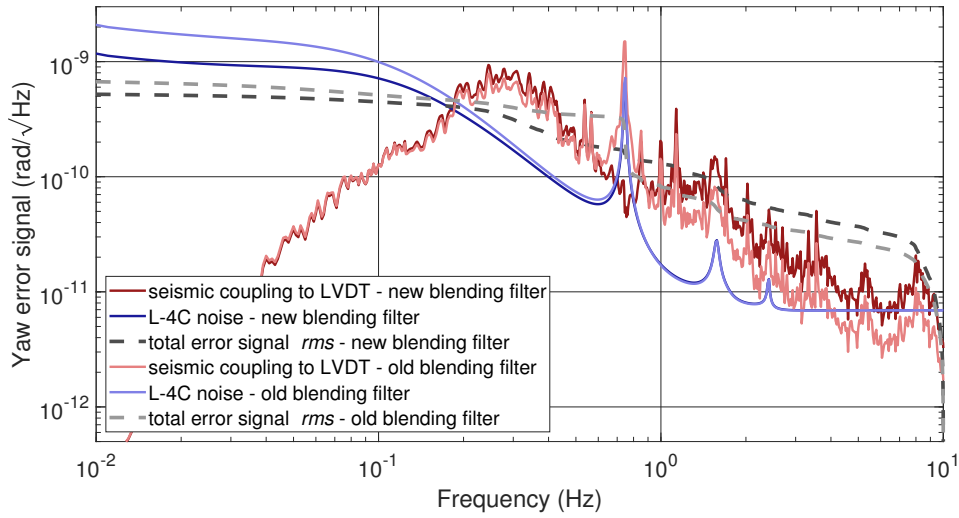


Figure 3.9.8: Coupling of roll optical table motion to the yaw error signal of the interferometer for the old and new blending filters. The new filters reduce the coupling of LVDT noise at the suspension resonance in side at 0.746 Hz. The optimal blending frequency is shifted to higher frequencies, reducing the coupling of L-4C noise at low frequencies.

Table 3.9.1: Summary of all improvements that can be achieved by optimizing digital filters.

Degree of freedom	Optimization of	Improvement by a factor of
long (to ifo pitch)	sensor correction & blending filters	1.54
vert (to ifo pitch)	controller filter	1.4
side (to ifo yaw)	blending filters	1.5
pitch (to ifo pitch)	blending & controller filters	1.3
yaw (to ifo yaw)	–	–
roll (to ifo yaw)	blending filters	1.3
ifo pitch error signal		1.48
ifo yaw error signal		1.39

3.9.2 Implementation of new sensors

The development of new sensors with higher sensitivities is a very active field of research in the gravitational wave community. Some designs are in a preliminary state of development, like the 6D interferometric sensor [MLM19], the Deep Frequency Modulation Interferometric displacement sensor [GI21] and the cryogenic optical accelerometer [vH20]. Other sensors are in their last stages of development and were already tested in small laboratory experiments, like inertial sensors read out with a Homodyne Quadrature Interferometer (HoQI) [CCG⁺18, Coo19] and a similar readout utilized for the inertial sensors HINS and VINS [Din21]. The beam rotation sensor is a newly developed inertial rotation sensor, which is already utilized for the Advanced LIGO interferometers [VHT⁺14, VHG⁺17] for tilt correction of the ground motion sensor.

This subsection investigated how much the AEI sub-SQL interferometer could benefit from installing new sensors. Two scenarios are chosen as examples:

- Having new vertical inertial sensors based on a suspended mass with a HoQI readout.
- Utilizing the already existing but unused yaw optical lever from central to west as a differential side sensor.

For both scenarios, the improved filter designs described in the last subsection 3.9.1 are taken for granted. The listed improvements are additional improvements achieved on top of the improvements by better filters.

Inertial vertical HoQI-based sensors

At the time of writing, a master's student of the group, Luise Kranzhoff, is designing, assembling and testing an inertial vertical sensor based on a HoQI readout. This sensor will have a suspended mass of roughly 1 kg with a quality factor of roughly 100, damped via eddy-current damping. A detailed noise budget, including electronics noise and CDS noise, has not been made yet. For the application in this thesis, readout noise and thermal suspension noise is considered. The prior is fit to the results presented in [Coo19], page 92, while the latter is calculated using equation 2.3.7 for viscous thermal suspension noise. Figure 3.9.9 shows the noise of the HoQI-based sensor and its single contributions, compared to the L-4C noise. The HoQI-based sensor noise is lower by a factor 100 at 0.1 Hz, by a factor 10 at 1 Hz, and by a factor 6 at 10 Hz.

A sensor blending optimization is executed for all degrees of freedom, replacing vertical L-4Cs with vertical HoQI-based sensors. This directly improves the isolation in the three vertical degrees of freedom and indirectly improves the horizontal degrees of freedom due to a lower tilt-to-horizontal noise in the horizontal L-4C geophones and a lower optical lever noise resulting from lower differential translational motion of the optical tables.

Vertical motion

Figure 3.9.10 shows the coupling of vertical optical table motion to the interferometer error signal for the current sensor set and for HoQI-based sensors replacing the L-4C geophones. LVDT noise and L-4C noise below 0.4 Hz dominate the error signal *rms* for the current sensor set, while residual seismic motion does not contribute significantly. With HoQI-based sensors, the optimal blending frequency shifts from 0.1 Hz to 0.02 Hz which significantly lowers the coupling of LVDT noise. Despite using the optimized controller filter from section 3.9.1 for these calculations, residual seismic motion would still dominate the overall *rms*. By installing HoQI-based sensors and re-optimizing the blending parameters, the coupling of vertical optical table motion to the interferometer error signal could be reduced by a factor of 5.7.

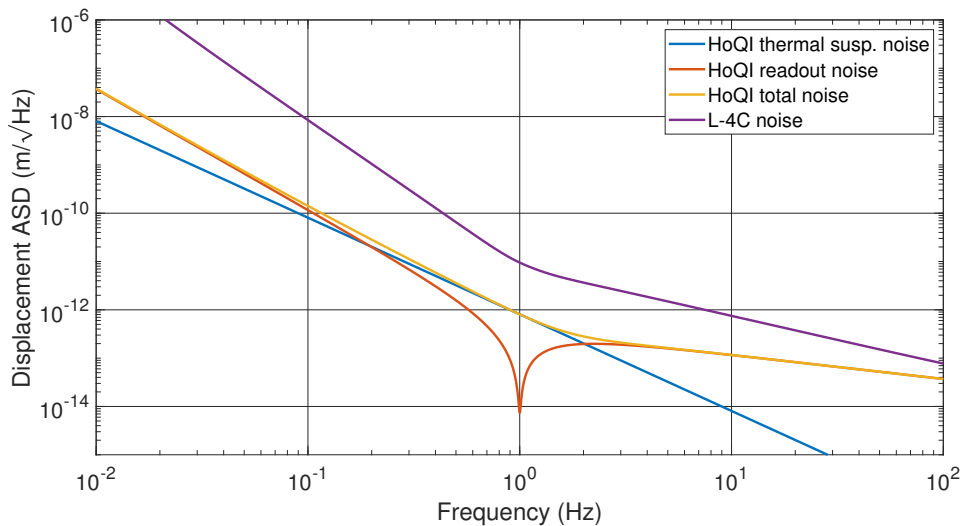


Figure 3.9.9: Displacement spectral densities of the single contributions and the total HoQI-based sensor noise in comparison to the L-4C noise. The HoQI-based sensor noise is an estimate for a sensor that is currently set up at the AEI 10 m prototype.

Pitch motion

The analysis of pitch motion with and without HoQI-based sensors gives a similar overall result as for vertical motion. It is shown in figure 3.9.11. While optical lever and L-4C noise mostly dominate the coupling to the interferometer error signal for the current sensors, residual ground motion becomes the limiting noise source when using HoQI-based sensors instead of vertical L-4C geophones. With the new sensors, the optical levers in pitch would benefit from the improved isolation in the vertical degree of freedom by a reduced differential translational motion noise. The optimal blending frequency would shift from 0.32 Hz to 0.06 Hz. By installing the HoQI-based sensors and re-optimizing the blending parameters, the interferometer error signal *rms* resulting from pitch motion could be reduced by a factor of 4.1.

Roll motion

Using HoQI-based sensors in the roll degree of freedom would also lower the coupling of sensor noise to the interferometer yaw error signal significantly; nevertheless, the HoQI-based sensor noise would still be the limiting noise contribution. This is shown in figure 3.9.12. The optimal blending frequency would be shifted from 0.18 Hz to 0.01 Hz. The coupling of roll motion to the error signal *rms* could be reduced by a factor of 3.7.

Longitudinal motion

Figure 3.9.13 shows the coupling of longitudinal motion to the interferometer error signal in pitch with the current sensors and with HoQI-based sensors. The tilt-to-horizontal coupling to the L-4Cs is reduced significantly, resulting in a lower optimal blending frequency of 0.06 Hz compared to 0.11 Hz for the current sensors. As a result of the lower blending frequency, the coupling of LVDT noise to the interferometer error signal is also reduced. The overall reduction of the interferometer error signal in pitch resulting from longitudinal optical table motion is a factor of 1.5.

Side motion

In side direction, the possible improvement by implementing vertical HoQI-based sensors is based on the same effect as for the longitudinal degree of freedom. A lower roll motion of the optical tables would result in a lower tilt-to-horizontal noise for the horizontal L-4C geophones. These would become favorable over accelerometers.

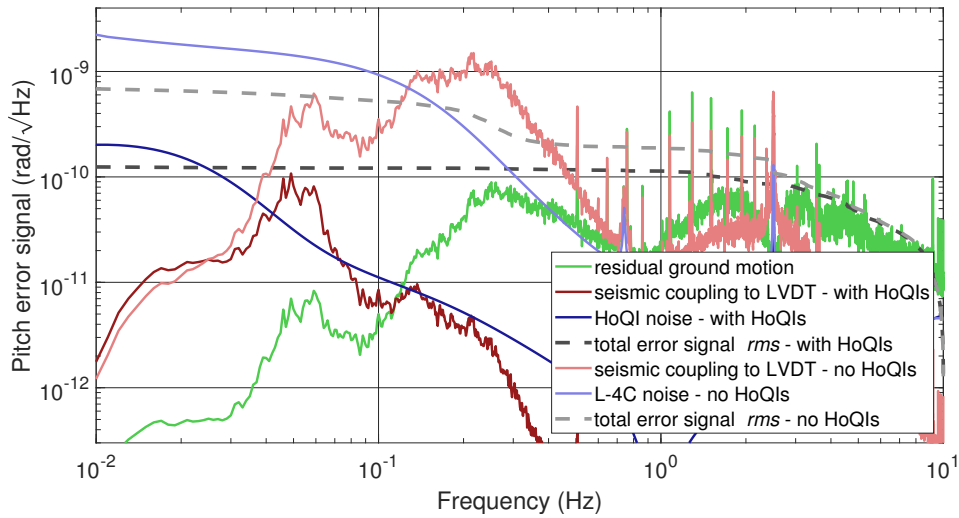


Figure 3.9.10: Coupling of vertical optical table motion to the pitch error signal of the interferometer with the current sensor set and with vertical HoQI-based sensors replacing the L-4Cs. With the new sensors, the sensor noise would be lowered significantly, and residual seismic motion would become the dominating noise source for the error signal *rms*.

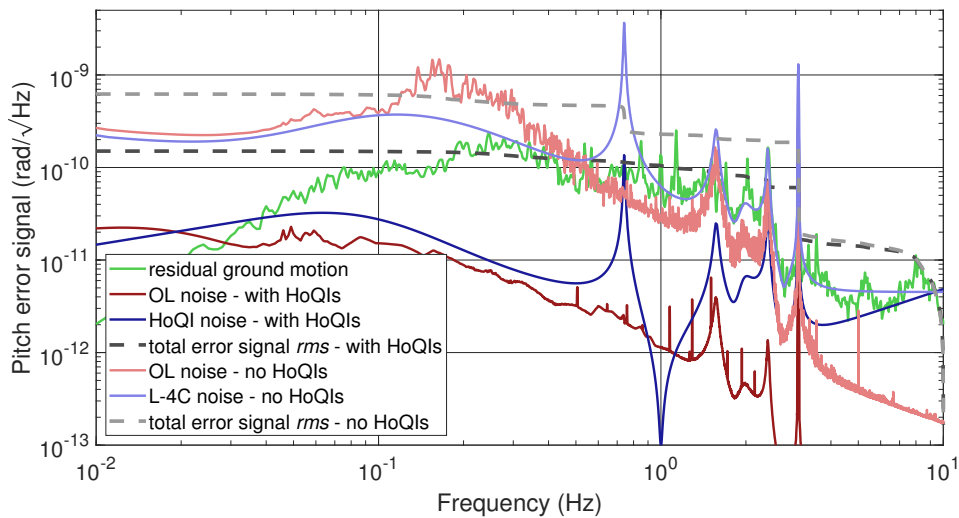


Figure 3.9.11: Coupling of pitch optical table motion to the pitch error signal of the interferometer with the current sensor set and with vertical HoQI-based sensors replacing the L-4Cs. Same as for the vertical degree of freedom, the sensor noise would be lowered significantly, and residual seismic motion would become the dominating noise source for the error signal *rms*.

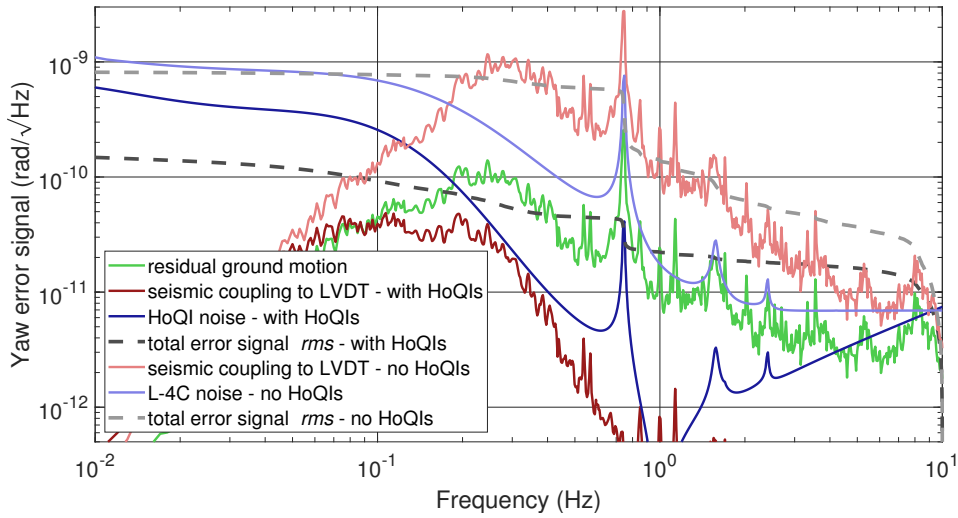


Figure 3.9.12: Coupling of roll optical table motion to the pitch error signal of the interferometer with the current sensor set and with vertical HoQI-based sensors replacing the L-4Cs. The sensor noise contributions would be reduced significantly; nevertheless, the HoQI-based sensor noise would limit the overall interferometer error signal *rms*.

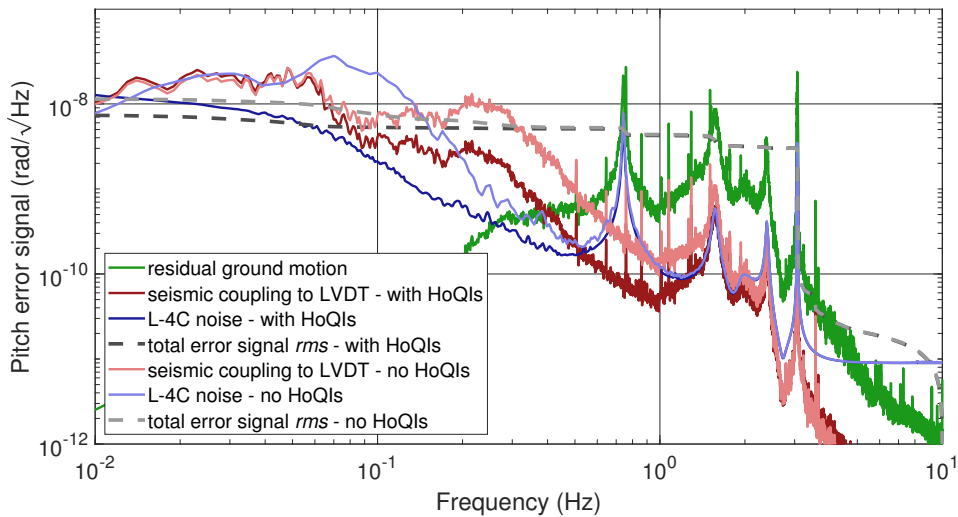


Figure 3.9.13: Coupling of longitudinal optical table motion to the pitch error signal of the interferometer with the current sensor set and with vertical HoQI-based sensors replacing the L-4Cs. The sensor noise contributions would be reduced significantly but still limit the overall interferometer error signal *rms*.

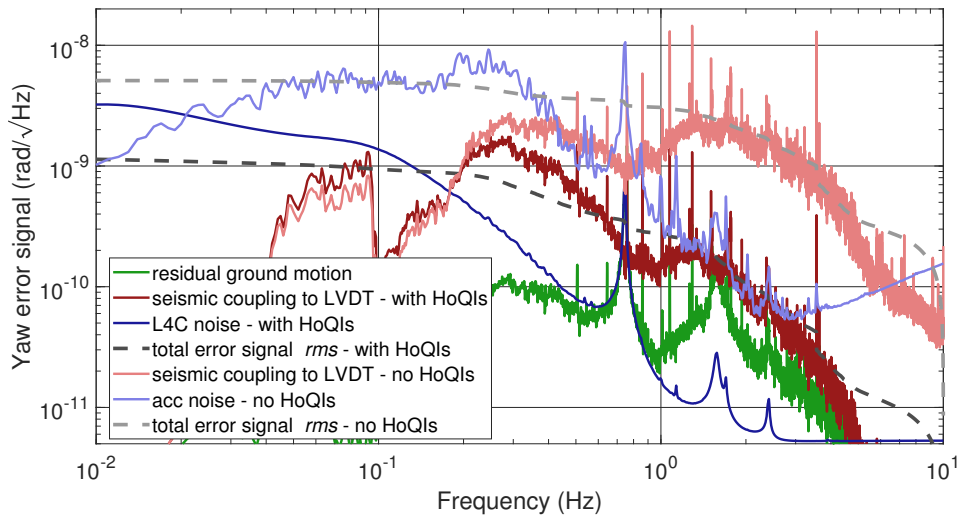


Figure 3.9.14: Coupling of side optical table motion to the yaw error signal of the interferometer with the current sensor set and with vertical HoQI-based sensors replacing the L-4Cs. The sensor noise contributions are reduced significantly; nevertheless, they would still limit the overall interferometer error signal *rms*.

Different to the longitudinal direction, the improvement in side would be a lot larger. This is because pitch is already well isolated by the optical levers, while roll is only isolated using local sensors; therefore, the improvement due to HoQIs in roll would be significantly larger. Figure 3.9.14 shows the coupling of side motion to the interferometer error signal in yaw for the current sensor set, and for HoQI-based sensors replacing the vertical L-4Cs. The horizontal L-4C noise would be reduced significantly, shifting the optimal blending frequency from 0.34 Hz to 0.15 Hz. This would lower the LVDT noise above the resonance frequency strongly. The coupling of side motion to the interferometer error signal could be reduced by a factor of 4.2.

Yaw motion

The implementation of HoQI-based sensors for the vertical degrees of freedom would reduce the coupling of yaw motion to the interferometer by two effects. First, the lower pitch and roll motion would reduce tilt-to-horizontal noise of the horizontal L-4C geophones, and second, the lower side motion would reduce the optical lever noise resulting from differential translational motion. Figure 3.9.15 shows the coupling of optical table yaw motion to the interferometer error signal for the current sensor set and for HoQI-based sensors for the vertical degrees of freedom. The analysis is only executed for the south/west AEI-SAS, which perform worse than the central AEI-SAS with the current sensors. With HoQI-based sensors, the optical levers should not be used as stand-alone sensors in yaw anymore, but should be blended with L-4C geophones at 3.1 Hz. The coupling to the interferometer error signal would be reduced by a factor of 3.4.

Summary inertial vertical HoQI-based sensors

Table 3.9.2 summarizes all improvements by optimizing digital filters and implementing vertical inertial sensors based on a HoQI readout, both with a re-optimization of the blending parameters. The listed improvements are in comparison to the current performance, presented in table 3.8.3. The improvements by HoQI-based sensors build up on the improvements by optimizing digital filters. The total improvement from optimizing digital filters and implementing HoQI-based inertial sensors is also listed. The total interferometer error signal *rms* resulting from optical table motion would be reduced by a factor 3.15 for the pitch error signal and by 5.53 for the yaw

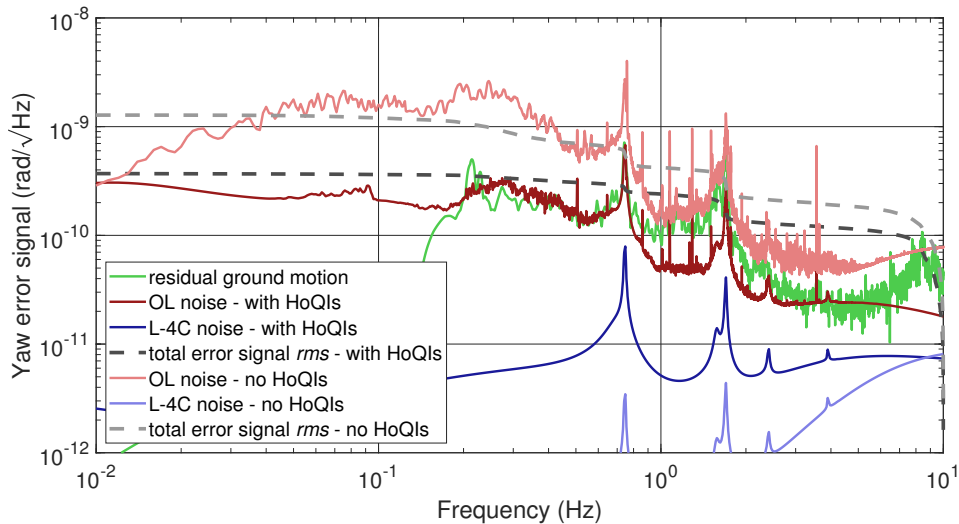


Figure 3.9.15: Coupling of yaw optical table motion to the yaw error signal of the interferometer with the current sensor set and with vertical HoQI-based sensors replacing the L-4Cs. With the new sensors, the optical levers should not be used as stand-alone sensors but should be blended at 3.1 Hz. The *rms* would be limited by residual seismic motion and optical lever noise to roughly the same amount.

error signal. The large improvement for the yaw error signal would predominantly result from a reduced optical table side motion, since side motion is the largest contributor to the yaw error signal (see section 3.8.3).

Optical lever in side for west AEI-SAS

In the current configuration, one optical lever is redundant and not utilized. It points from the central to the west AEI-SAS and, in principle, is predominantly sensitive to yaw motion of the central AEI-SAS. As for all optical levers, differential side motion couples to the optical lever signal with a factor $1/11.5$.

Yaw of the central AEI-SAS is controlled using the optical lever to south. Due to the high optical lever sensitivity, this motion is suppressed very effectively. Side of the west AEI-SAS is controlled by LVDTs and accelerometers. The latter are affected by a large tilt-to-horizontal coupling, with the result that side motion has the largest amplitudes of all degrees of freedom. This side motion is not only large, but also fully differential, since no global sensors are involved. Since the side motion is large and the yaw motion is comparably small, the so far unused optical lever could be utilized to control side motion of the west AEI-SAS. In fact, the coupling of south AEI-SAS side motion to central AEI-SAS yaw motion to west AEI-SAS side motion would result in a situation where the south and west AEI-SAS move in common in side direction.

Figure 3.9.16 demonstrates the global AEI-SASs behavior with and without this additional optical lever. As an example, the reaction of all three AEI-SASs to a side motion of the south AEI-SAS is pictured. The central-to-south arm is fixed by optical levers in both directions; hence, both AEI-SASs rotate such that the optical tables face each other and stay centered to each other. Without the side optical lever, the west AEI-SAS does not follow this motion. Consequently, the central and west AEI-SASs do not face each other and the opening angle between both interferometer arms α changes. In this example, the initial south AEI-SAS side motion has significant coupling to the interferometer, because the interferometer beam propagating to the west is not aligned with the cavity anymore.

In the second example, the additional optical lever (blue arrow) sees the rotation of the central AEI-SAS. Its control loop creates an according reaction, mirroring the south AEI-SAS side motion. The side translation is seen by the optical lever

Table 3.9.2: Summary of all improvements that can be achieved by optimizing digital filters and by installing HoQI-based inertial vertical sensors.

Degree of freedom	Improvement factor digital filters	Improvement factor HoQI-based sensors	Total
long (to ifo pitch)	1.5	1.5	2.3
vert (to ifo pitch)	1.4	5.7	8.0
side (to ifo yaw)	1.5	4.2	6.3
pitch (to ifo pitch)	1.3	4.1	5.3
yaw (to ifo yaw)	–	3.4	3.4
roll (to ifo yaw)	1.3	3.7	4.8
ifo pitch error signal	1.48	2.16	3.15
ifo yaw error signal	1.39	3.98	5.53

pointing from west to central and is corrected by rotation of the west AEI-SAS. In total, the global assembly of all three AEI-SAS becomes “stiff” for horizontal motion. The degree of “stiffness” is given by the optical lever noise floor and residual motion coupling to the optical tables due to insufficient gain.

The investigations on optical table motion coupling to the interferometer, presented in section 3.8.2, is simplified to only look at one interferometer arm. The opening angle between both arms is not included; therefore, improvements achieved by the additional side optical lever can not be investigated adequately with the blending optimization analysis in this thesis. Nevertheless, using the already existing optical lever signal for feedback to the west AEI-SAS side direction is little effort and low costs, and should be investigated. The real benefit of this additional sensor could not be measured at the current state, but would be visible, once the full Michelson interferometer is set up.

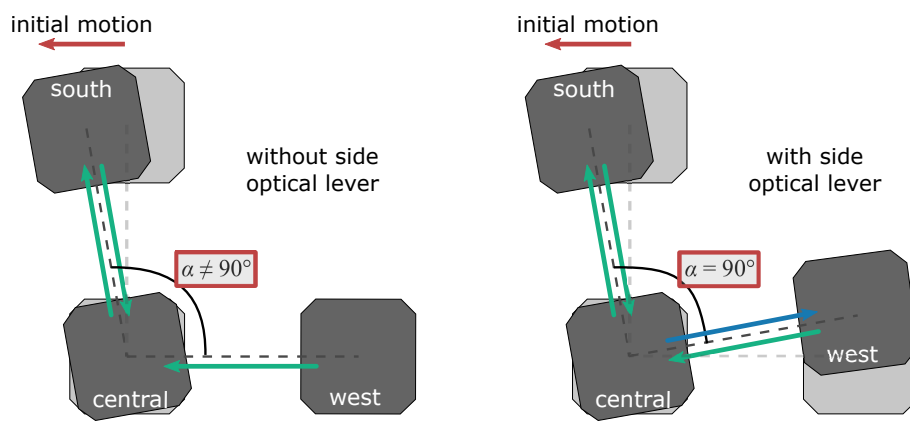


Figure 3.9.16: Schematic description of the global AEI-SASs reaction with and without an additional side optical lever. The already utilized optical levers are depicted by green arrows, the additional optical lever with a blue arrow. In the pictured example, the south AEI-SAS executes a side motion. Without additional side optical lever, there is no according reaction of the west AEI-SAS in side direction, resulting in a changing opening angle α . With an additional side optical lever, the west AEI-SAS mirrors side motion of the south AEI-SAS. This keeps the opening angle constant and reduces the coupling to the interferometer.

Chapter 4

FINESSE simulations

Simulations of optical beam properties in laser interferometers is crucial for both the design and commissioning phases to investigate potential problems and verify the intended functionality. FINESSE [FHL⁺04, Bro16, BF14] is a free-to-use simulation tool that has proven to be useful in both of these phases. It simulates beam parameters in the frequency domain using Hermite-Gauss modes and provides useful commands for plotting various signals. Features like shot noise, radiation pressure noise, mirror surface figures and active loop stabilization are included.

PYKAT [BJR⁺20] is a Python package that provides an interface to FINESSE from within Python, giving the user access to the large variety of available Python functions.

This chapter presents FINESSE simulations using PYKAT to predict a noise budget for the AEI sub-SQL interferometer. It starts with a description of the simplified AEI sub-SQL interferometer model that is utilized. In the following, the jitter noise coupling of the input optics to the interferometer dark port is predicted and compared to the analytic calculations presented in section 2.6. Afterwards the influence of the dark fringe offset on the interferometer dark port output is investigated with a focus on laser power, frequency noise and intensity noise. In the last section, a design for an anti-symmetric port photodetector is presented, and its noise is modelled. For all these noise sources, designs are elaborated to keep the noise sufficiently below the SQL in the measurement band.

4.1 Model of the sub-SQL interferometer

This section presents the sub-SQL interferometer model utilized for all FINESSE investigations within this thesis. The interferometer model includes a DC-offset readout [H⁺09, BBFS17], which will be the initial readout scheme to be used in the AEI sub-SQL interferometer. The setup is described including all relevant parameters, the optical gain is introduced, and noise budgets of the sub-SQL interferometer are presented for different laser input powers.

4.1.1 Setup of the sub-SQL interferometer model

The simplified model of the AEI sub-SQL interferometer is shown in figure 4.1.1. All parameters are listed in table 4.1.1.

Properties of the laser beam are generated using the “gauss” command. This command activates the use of Hermite-Gaussian beam descriptions, rather than plane waves. The spatial distribution of the laser light perpendicular to the direction of propagation is described by Transverse Electro Magnetic (TEM) modes, which are simulated up to a radial and angular mode number of 4.

The interferometer path between laser source and IMC is denoted by l_1 . It includes the optical fiber guiding the laser beam into the vacuum system, the PMC as a first filter for higher order modes and steering mirrors and mode-matching for the PMC

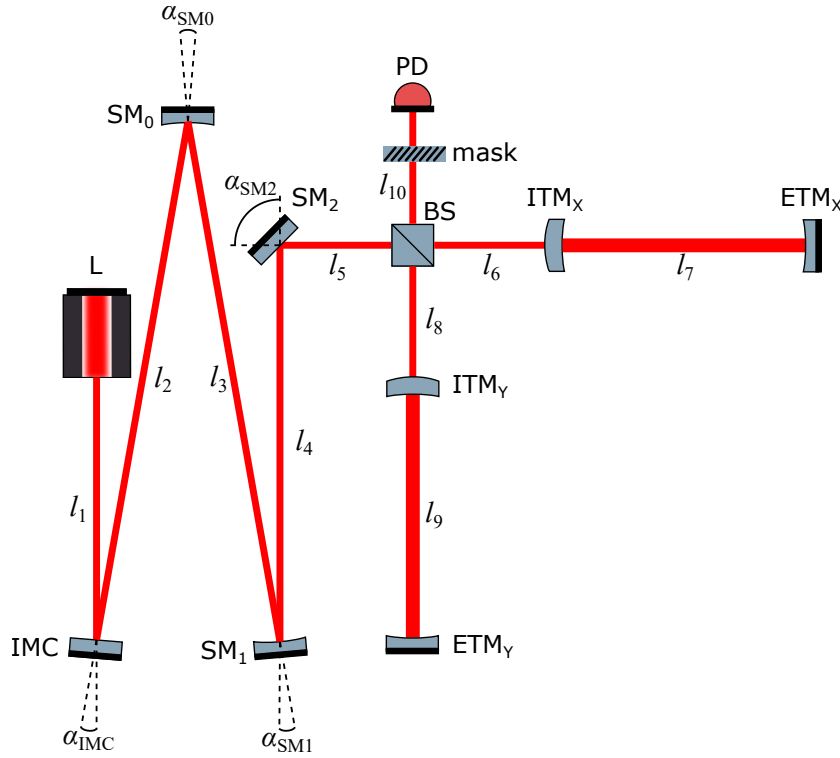


Figure 4.1.1: Setup of the AEI sub-SQL interferometer as modelled in FINESSE. Input and output path are simplified for the purpose of this thesis.

and IMC. This simplification is possible since none of the components prior to the IMC have significance for the simulations that follow. The IMC is only relevant for jitter noise simulations described in section 4.2. Since the IMC is a linear cavity, it is simulated as a single mirror hit under $\alpha_{\text{IMC}} = 0^\circ$. The mode-matching optics SM_0 and SM_1 have a Radius of Curvature (RoC) of 8 m and are hit under 4° to minimize astigmatism. The steering mirror SM_2 is hit under 45° and is flat.

The beam splitter splits the beam into both interferometer arms. The ITMs and End Test Mass (ETM)s are simulated to be suspended using simplified transfer functions of the triple suspensions. The distances to the ITMs are macroscopically different, with $l_6 = 0.525$ m and $l_8 = 0.475$ m; this is intentional and known as the Schnupp asymmetry [Sch88, TjMMK94]. This technique is used to enable a side-band extraction for an interferometer control at the anti-symmetric port of the interferometer, while keeping it in destructive interference. The two arm cavities are microscopically detuned differentially; this is called the dark fringe offset and enables the DC-offset readout. The detuning provides some DC carrier power for the signal to beat with at the anti-symmetric port. For simplicity, the anti-symmetric output of the interferometer is filtered using “masks” instead of including the OMC. All higher order TEM modes are masked to generate the TEM_{00} mode signal, which is the signal of interest. Table 4.1.1 provides more detailed properties of the distances and optics.

4.1.2 Optical gain

The FINESSE model simulates how actuation of various interferometer components couple to the carrier laser power at the anti-symmetric port. These transfer functions can be multiplied by the amplitudes of the noise at the ports at which they enter to project the noise to the output of the interferometer in units of $\text{W}/\sqrt{\text{Hz}}$.

The optical gain of an interferometer describes the response of the laser power at

Table 4.1.1: Description and values for all abbreviations and parameters used for the FINESSE model of the AEI sub-SQL interferometer.

Abbreviation	Description	
L	laser	
IMC	input mode cleaner	
SM	steering mirror	
BS	beam splitter	
ITM _{x,y}	input test mass x- or y-arm	
ETM _{x,y}	end test mass x- or y-arm	
PD	photodetector	

Parameter	Description	Value
P_L	laser power	variable
λ_L	laser frequency	1064 nm
l_1	length L – IMC	1 m
α_{IMC}	incidence angle IMC	0°
l_2	length IMC – SM ₀	10.912 m
α_{SM_0}	incidence angle SM ₀	4°
RoC_{SM_0}	radius of curvature SM ₀	8 m
l_3	length SM ₀ – SM ₁	10.329 m
α_{SM_1}	incidence angle SM ₁	4°
RoC_{SM_1}	radius of curvature SM ₁	8 m
l_4	length SM ₁ – SM ₂	11 m
α_{SM_2}	incidence angle SM ₂	45°
l_5	length SM ₂ – BS	0.4 m
δ_{BS}	power loss BS	15 ppm
l_6	length BS – ITM _x	0.525 m
l_8	length BS – ITM _y	0.475 m
RoC_{ITMAR}	radius of curvature anti-reflective surface ITMs	1.776 m
T_{ITM}	Transmittance both ITM	8220 ppm
δ_{ITM}	loss both ITMs	15 ppm
d_{ITM}	thickness both ITMs	24.46 mm
RoC_{ITMHR}	radius of curvature high-reflective surface ITMs	5.7 m
m_{ITM}	mass both ITMs	0.1 kg
I_{ITM}	moment of inertia both ITMs	$15 \times 10^{-6} \text{ kg m}^2$
$l_7; l_9$	length of arm cavities	11.3673 m
T_{ETM}	Transmittance both ETMs	15 ppm
RoC_{ETM}	radius of curvature both ETMs	5.7 m
m_{ETM}	mass both ETMs	0.1 kg
I_{ETM}	moment of inertia both ETMs	$15 \times 10^{-6} \text{ kg m}^2$
l_{10}	length BS – PD	1 m

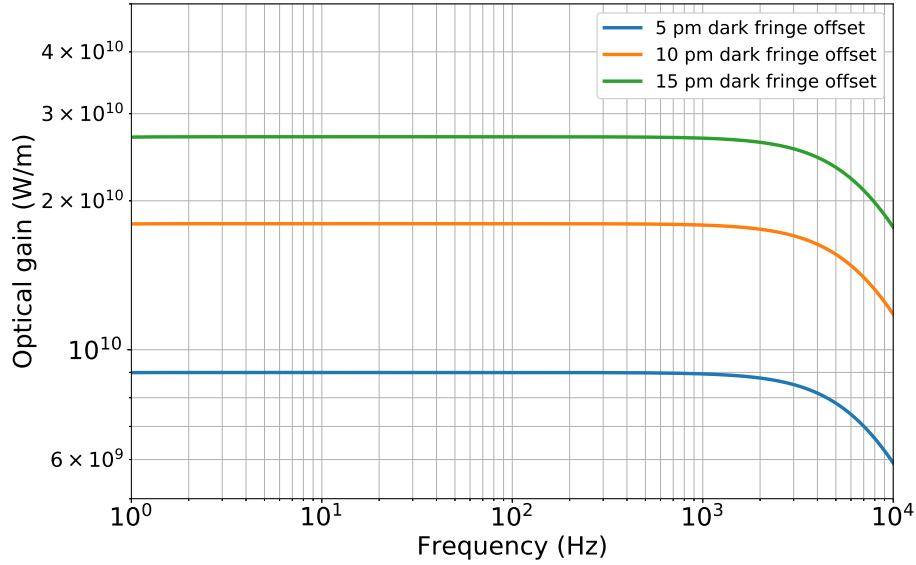


Figure 4.1.2: Optical gain of the sub-SQL interferometer for different dark fringe offsets.

the anti-symmetric port for a DARM length change in units of W/m . This quantity is utilized to calibrate the interferometer output to units of $\text{m}/\sqrt{\text{Hz}}$. Figure 4.1.2 shows the optical gain of the sub-SQL interferometer simulated with FINESSE for dark fringe offsets of 5 pm, 10 pm and 15 pm. Between 1–1000 Hz the optical gain is flat and scales linearly in amplitude with the dark fringe offset. Above 1000 Hz the arm cavities have their cavity poles, calculated by

$$f_{\text{pole}} = \frac{1}{4\pi\tau_{\text{stor}}}, \quad (4.1.1)$$

with τ_{stor} being the light storage time inside the cavities, calculated by

$$\tau_{\text{stor}} = \frac{L\sqrt{r_1 r_2}}{c_0(1 - r_1 r_2)}. \quad (4.1.2)$$

L describes the cavity length, $r_1 = \sqrt{1 - T_{\text{ITM}}}$ and $r_2 = \sqrt{1 - T_{\text{ETM}}}$ the reflection coefficients of the ITM and ETM and c_0 the speed of light in vacuum. Inserting the values from table 4.1.1 results in a cavity pole at $f_{\text{pole}} = 8683 \text{ Hz}$, matching figure 4.1.2.

4.1.3 Noise budget

Figure 4.1.3 shows three noise budgets for laser input powers of 0.5 W in diagram a), 3 W in diagram b) and 10 W in diagram c), respectively. Noise of the individual interferometer components are mostly calculated with an adapted version of the Gravitational Wave Interferometer Noise Calculator (gwinc) [gwi], originally developed for the LIGO detectors. The individual noise is multiplied with the relevant interferometer response to it, calculated with FINESSE, and calibrated to displacement equivalent noise by dividing by the optical gain.

The diagrams show single noise contributions, the SQL, the total classical noise, and the total noise including quantum noise. A box located at the top center provides relevant information on:

- the input power to the interferometer from the laser,
- the respective output power at the dark port,
- the dark fringe offset,
- the probe frequency, at which quantum noise and SQL are equal for the utilized input power,
- and the amplitude ratio of the SQL and classical noise at the probe frequency, which is the signal-to-noise ratio for the sub-SQL interferometer.

A comparison of the three diagrams shows that the SQL touching frequency increases with input power due to increasing quantum noise. The signal-to-noise ratio is higher at low frequencies, with a value of 3.9 for 0.5 W input power and 1.7 for 10 W. Classical noise is dominated by seismic noise and intensity noise (for 3 W and higher input powers) below 20 Hz and coating Brownian noise above 20 Hz.

The pictured noise budgets are preliminary results and ignore some relevant noise contributions like controls noise, described in section 3.3.1, jitter noise of optics in the input and output path and noise of the anti-symmetric port photodetector. The latter two are investigated in the following sections. At the time of writing, controls noise can not be predicted adequately, since relevant control schemes are not designed. It is not expected to be the dominating noise contribution in the interferometer's most sensitive band.

4.2 Jitter noise of input path optics

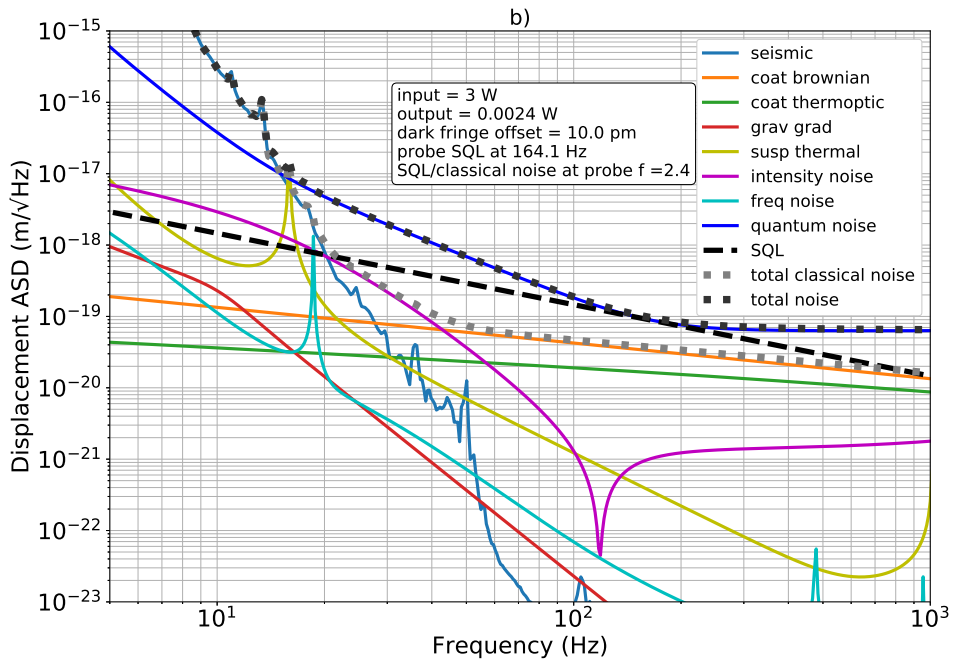
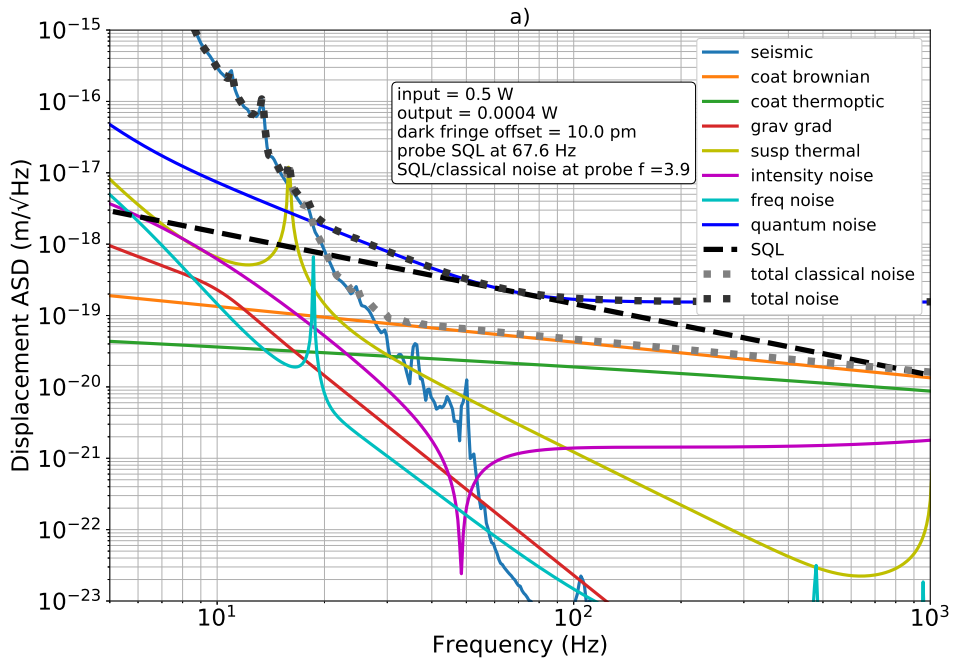
In this section the coupling of jitter noise from the optics in the input path to the output power is investigated. The calculation of jitter noise in units of $\text{m}/\sqrt{\text{Hz}}$ is executed following the methods described in section 4.1.2.

The transfer functions for input optics jitter to the output power depends on misalignment of the ITMs and ETMs; therefore, the following section investigates, how different ITM and ETM pitch and yaw misalignments influence the jitter transfer functions in detail and determines the worst case combinations. The subsequent section shows worst case simulations of jitter noise.

4.2.1 Influence of test mass misalignments on jitter noise

To investigate the influence of test mass misalignment on the jitter transfer functions, two different types of parameters are varied: the amplitude of test mass rotation and the direction (positive or negative) of test mass rotation. For these simulations an input power of 0.5 W is chosen since this low input power corresponds to a low SQL probing frequency and jitter noise is mostly relevant at the lower end of the measurement band.

Figure 4.2.1 shows example transfer functions from jitter of SM_0 in yaw to the dark port output power of the TEM_{00} mode. For these simulations, the ITMs and ETMs are all misaligned into the same direction relative to the global reference frame in yaw by 1 nrad, 10 nrad, 30 nrad and 50 nrad. The coupling increases non-linearly for higher misalignment amplitudes, with several peaks and dips, changing their frequency. The pole-zero pairs around 5 Hz and 20 Hz result from an optical spring. For 50 nrad misalignment, the spring is shifted to lower frequencies and is hence not shown. Optical springs are described in general in [SGML⁺04, DK12, Gor15] and in context of the AEI sub-SQL interferometer in [Ady18]. They result from oscillating energy exchange between optical power inside a detuned cavity and potential energy of the mirrors being displaced in the presence of restoring forces. A second smaller zero-pole pair is present between 1–2 Hz. This results from angular oscillations of the cavity mirrors. For the other input optics these transfer functions look differently but show a similar behavior; therefore, 50 nrad misalignment is chosen for the following



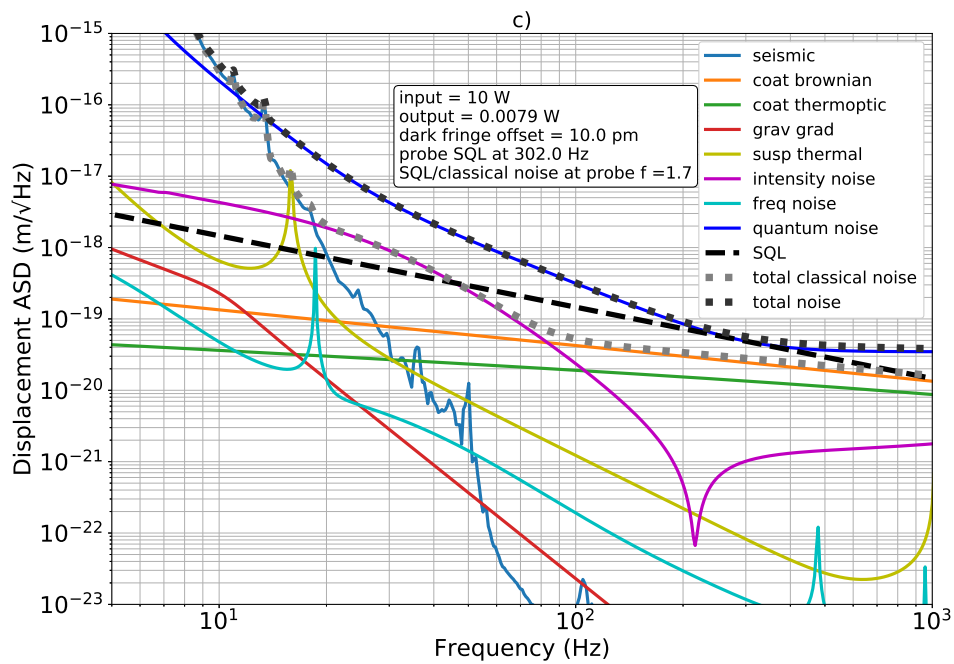


Figure 4.1.3: Noise budgets of the AEI sub-SQL interferometer based on FINESSE simulations for input powers of 0.5 W in diagram a), 3 W in diagram b) and 10 W in diagram c). The noise budgets include individual noise contributions, the SQL, the total classical noise and the total noise including quantum noise. The information box provides information on the laser input power, the corresponding laser output power, the dark fringe offset, the probe frequency of the SQL, where quantum noise and SQL are equal, and the signal-to-noise ratio of the SQL over classical noise at the probe frequency.

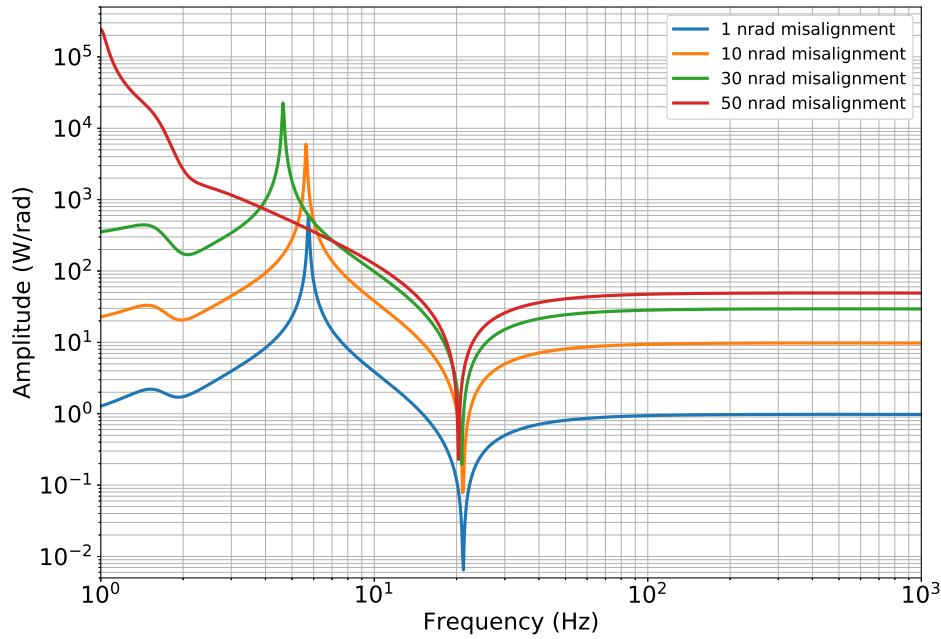


Figure 4.2.1: Transfer function amplitude from SM_0 jitter in yaw to the output power of the TEM_{00} mode for different misalignment amplitudes of the ITMs and ETMs. For these simulations the input power is chosen to be 0.5 W and all ITMs and ETMs are misaligned into the same direction in yaw by different amplitudes.

simulations. This is expected to be the worst case *rms* misalignment of the ITMs and ETMs in final operation.

Figure 4.2.2 investigates misalignment of the ITMs and ETMs into different directions. As before, the response from SM_0 jitter in yaw to the TEM_{00} mode power at the dark port is shown. The input laser power is 0.5 W and the misalignment has an amplitude of 50 nrad. All possible misalignment combinations of the ITMs and ETMs are examined. Half of the combinations are redundant because they have the same transfer function as another combination. This is the case if all four signs are flipped. An example referring to the notation in the legend is: “+-+” $\hat{=}$ “-+-”.

The figure shows that for different frequency regimes, different misalignment combinations result in the highest coupling of jitter motion to the TEM_{00} mode dark port power. Depending on the combination, an optical spring between 5–6 Hz appears.

This analysis was performed for all input optics in yaw and pitch. For each optic, the transfer functions featuring the highest coupling at 68 Hz are compared in figure 4.2.3. A frequency of 68 Hz is chosen since this is the probe frequency of the SQL for an input power of 0.5 W. In yaw, a misalignment of all ITMs and ETMs into the same direction gives the highest coupling for all input optics. In pitch, the highest coupling is present, if ITM and ETM of one arm are aligned into the opposite direction than for the other arm cavity. At 68 Hz, SM_0 features the highest coupling, followed by SM_1 and SM_2 . Coupling of the IMC is significantly lower. This is presumably related to the fact that the IMC output mirror is located exactly at the beam waist.

These investigations only cover the very specific situation of 0.5 W input power, 50 nrad misalignment amplitude, 10 pm dark fringe offset and only misalignment in either yaw or pitch. Varying any of these parameters gives new results, making it impossible to give an exact prediction of jitter noise. The results shown in figure 4.2.3 serve as a reasonable prediction for the worst case and are thus utilized for further investigations.

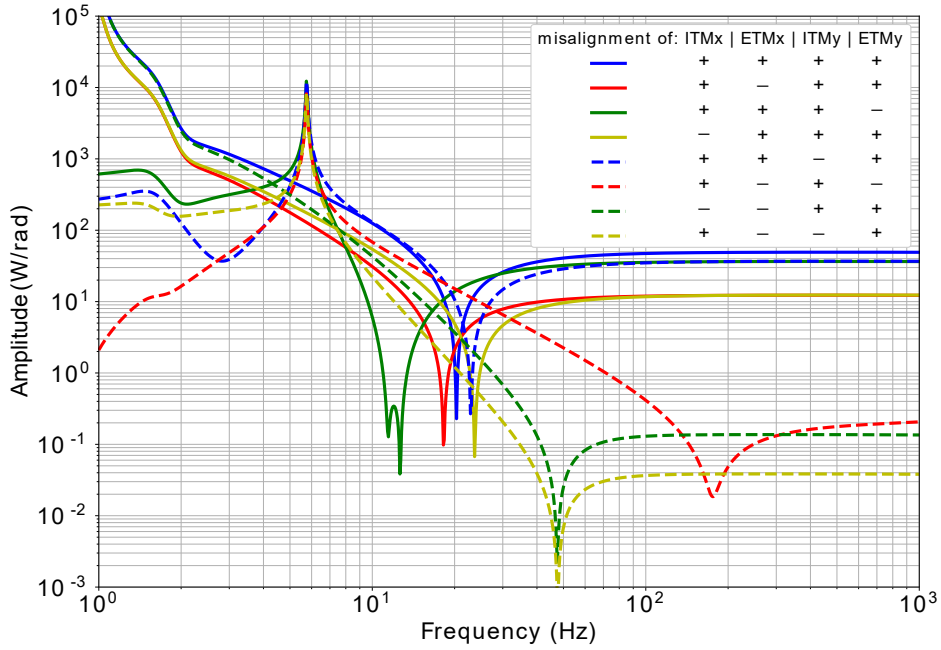


Figure 4.2.2: Transfer function amplitude of SM_0 jitter in yaw to the output power of the TEM_{00} mode for different misalignment of the ITMs and ETMs. The input power is 0.5 W and all ITMs and ETMs were misaligned in yaw by 50 nrad into positive and negative directions, indicated by the signs in the legend.

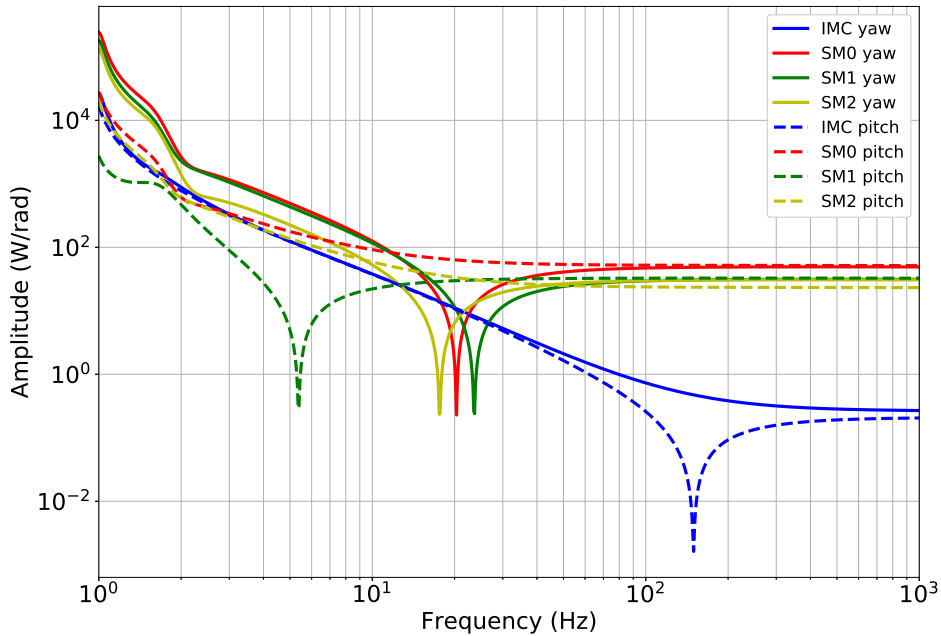


Figure 4.2.3: Transfer function amplitudes of the worst case jitter coupling of all input optics in yaw and pitch. The input power is 0.5 W, resulting in a probe frequency of the SQL of 68 Hz. At this frequency, the jitter transfer functions for all ITM and ETM misalignment combinations are compared for each input optic, and the one with the highest amplitude is shown.

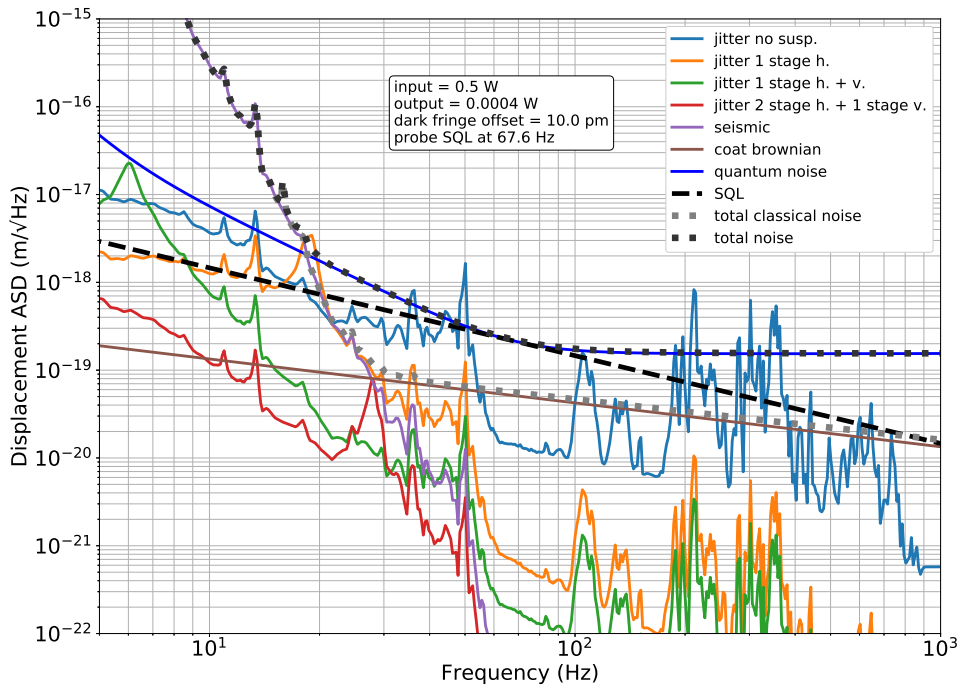


Figure 4.2.4: Noise budget for the AEI sub-SQL interferometer showing the most relevant noise sources compared to jitter noise for four scenarios: without suspending the input optics, with currently installed one-stage suspensions, with new one-stage suspensions featuring an additional vertical suspension stage, and with two-stage suspensions featuring one stage of vertical isolation. Requirement for jitter noise is to be a factor 10 below all other classical noise sources. Above 60 Hz, this is met with the current suspensions. The total classical noise does not include jitter noise in this diagram.

4.2.2 Noise budget

The transfer functions from jitter of input optics to the TEM_{00} mode power at the interferometer output are multiplied with the expected jitter motion and calibrated to units of $\text{m}/\sqrt{\text{Hz}}$. The resulting noise of all input optics is added incoherently to calculate the total jitter noise. Incoherent addition is applicable due to mechanical differences in the suspensions and different ground motion for the different AEI-SAS in the relevant frequency regime. Four different scenarios are investigated: no additional suspensions for the input optics, the currently installed one-stage suspension without vertical isolation, new one-stage suspensions with vertical isolation and two-stage suspensions with one stage of vertical isolation. All the scenarios assume an isolation by the AEI-SASs.

Figure 4.2.4 shows the resulting total jitter noise for the four scenarios compared to the other most relevant noise sources. The requirement for jitter noise is to be below the sum of all other classical noise sources, summarized as “total classical noise”. Above 60 Hz, jitter noise with the current one-stage suspensions is sufficiently below the other classical noise sources. Between 5–50 Hz jitter noise would contribute significantly.

Proceeding with current input optic suspensions and investigating jitter noise with measurements, once a full Michelson interferometer is available, is recommended. The analytically calculated coupling of jitter noise to the interferometer output power, as

presented in section 2.6, roughly matches the FINESSE simulation. The requirement for the analytical calculation was set to be equal to the ISS requirements, since the exact coupling to the interferometer output power was unknown. This resulted in the need for a double-stage suspensions, which is confirmed by the FINESSE simulation, if the requirements were the same.

4.3 Dark fringe offset

For the simulations within this thesis, the dark fringe offset manifests as a detuning of the interferometer arms. Both ETMs are displaced anti-symmetrically, such that one cavity is elongated while the other is shortened. This detuning results in non-optimal destructive interference of the carrier beam at the beam splitter, coupling light to the anti-symmetric interferometer output. This carrier light serves as a local oscillator for the signal sidebands created by e. g. gravitational waves or quantum noise; hence, it enables the resulting beat signal to be detected as a variation in the light power upon a photodetector placed at the output port.

Allowing carrier light to couple to the output port of the interferometer has the downside of increased laser frequency and intensity noise coupling, potentially masking the signal to be measured. This section investigates the influence of the dark fringe offset on both laser noise sources for the AEI sub-SQL interferometer and concludes with a maximal acceptable offset while maintaining the overall interferometer sensitivity.

Figure 4.3.1 shows intensity and frequency noise for laser input powers of 0.5 W in diagram a), 3 W in diagram b) and 10 W in diagram c). Each diagram shows the two laser noise sources for four different dark fringe offsets of 5 pm, 15 pm, 30 pm and 50 pm. The figures also show the sum of all other classical noise sources, the SQL, and a vertical line marking the probe frequency of the SQL for the given input power.

The intensity and frequency noise is below the sum of all other classical noise contributions for all chosen dark fringe offsets; hence, all dark fringe offsets are acceptable, although a low offset is favorable.

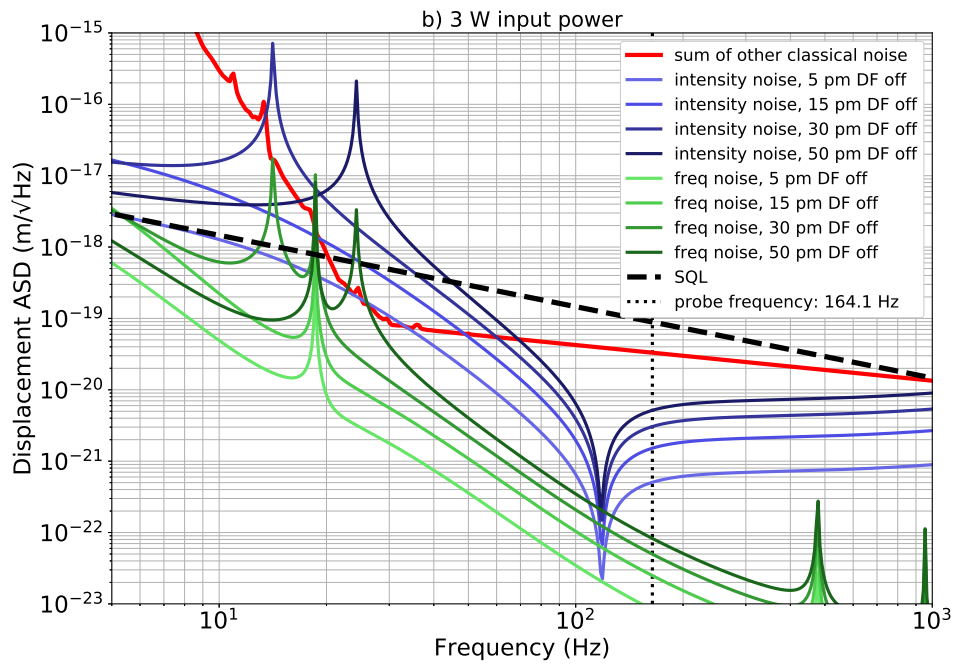
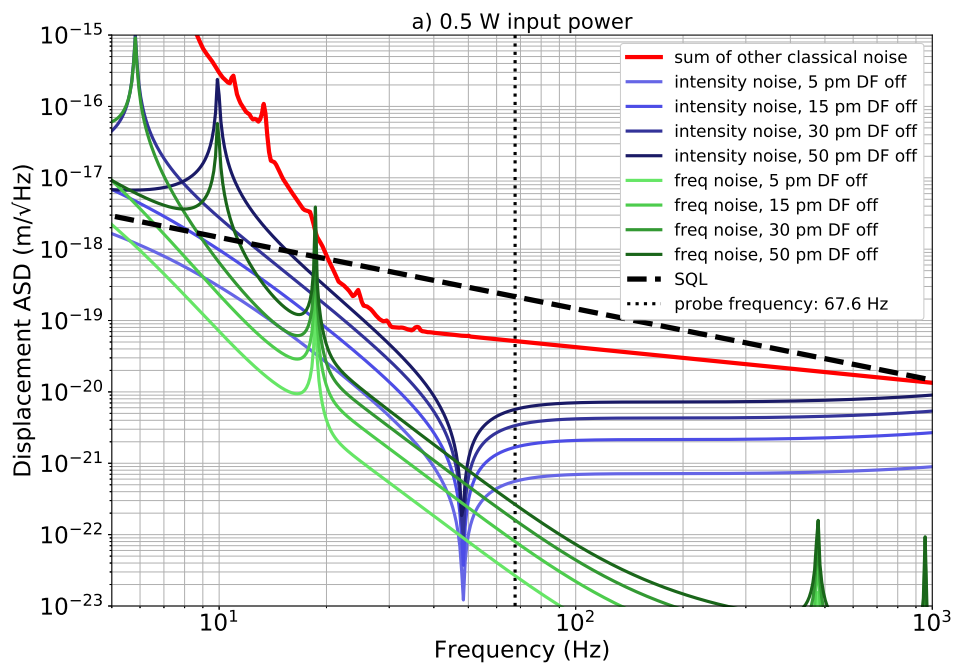
Table 4.3.1 lists the output powers of the TEM_{00} mode for the four investigated dark fringe offsets and the three investigated laser input powers. A higher dark fringe offset results in higher output powers, which complicates the design of the anti-symmetric port photodetector. A low dark fringe offset reduces the signal, and hence increases the noise-to-signal ratio. In principle, it is possible to use different dark fringe offsets for different laser input powers to keep the output power roughly constant. This would simplify requirements on the anti-symmetric port photodetector, but involves redesigning interferometer control loops; hence, a constant dark fringe offset is preferable.

As a compromise between the level of frequency and intensity noise, the complexity of the anti-symmetric port photodetector, and the noise-to-signal ratio, a dark fringe offset of 15 pm is reasonable. The following section discusses a possible design for the anti-symmetric port photodetector.

4.4 Anti-symmetric port photodetector

The requirement for the photodetector is to be capable of detecting the SQL with the maximal and minimal intended laser input powers, while keeping the dark fringe offset constant. In particular, the photodetector must be able to detect the maximum TEM_{00} mode output power for 10 W input and its noise needs to be sufficiently below quantum noise in case of 0.5 W input power.

The light filtered by the OMC is split onto two photodiodes. Assuming a dark fringe offset of 15 pm as derived in the prior section, each photodiode will have about 9 mW incident light power. The Indium Gallium Arsenide (InGaAs) photodiode IG17X3000G1i from Laser Components [Las20] was chosen, having a responsivity



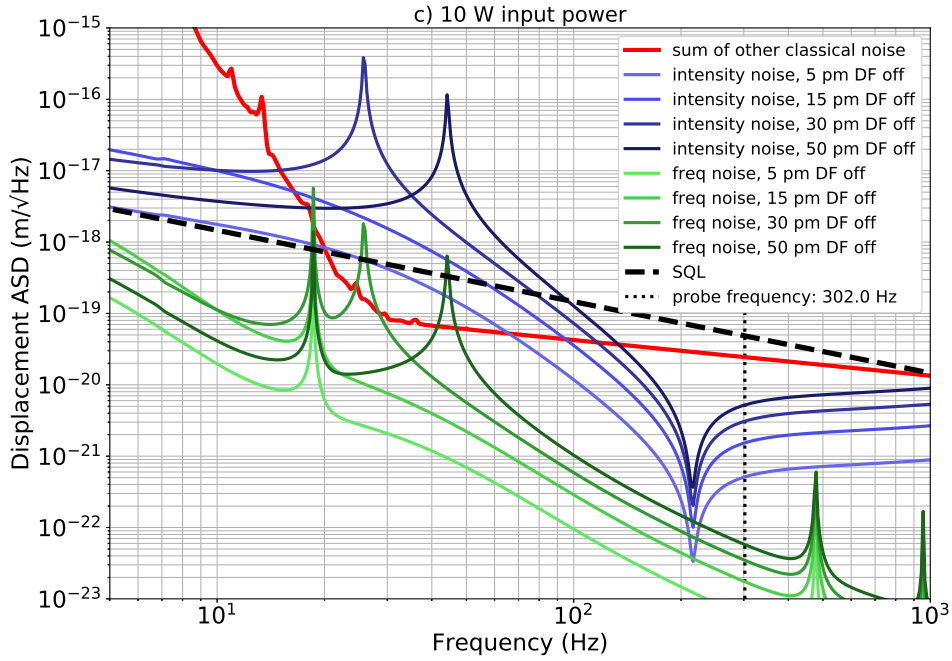


Figure 4.3.1: Displacement equivalent frequency and intensity noise of the AEI sub-SQL interferometer for different dark fringe offsets and laser input powers of 0.5 W in diagram a), 3 W in diagram b) and 10 W in diagram c). For comparison, the SQL, the sum of all other classical noise sources and the probe frequency of the SQL is shown.

Table 4.3.1: Output power of the interferometer at the anti-symmetric port for different dark fringe offsets and different input powers.

Dark fringe offset in [pm]	Output power in [mW] for input powers of:		
	0.5 W	3 W	10 W
5	0.1	0.6	2.0
15	0.9	5.3	17.7
30	3.5	21.2	70.8
50	9.8	58.6	195.4

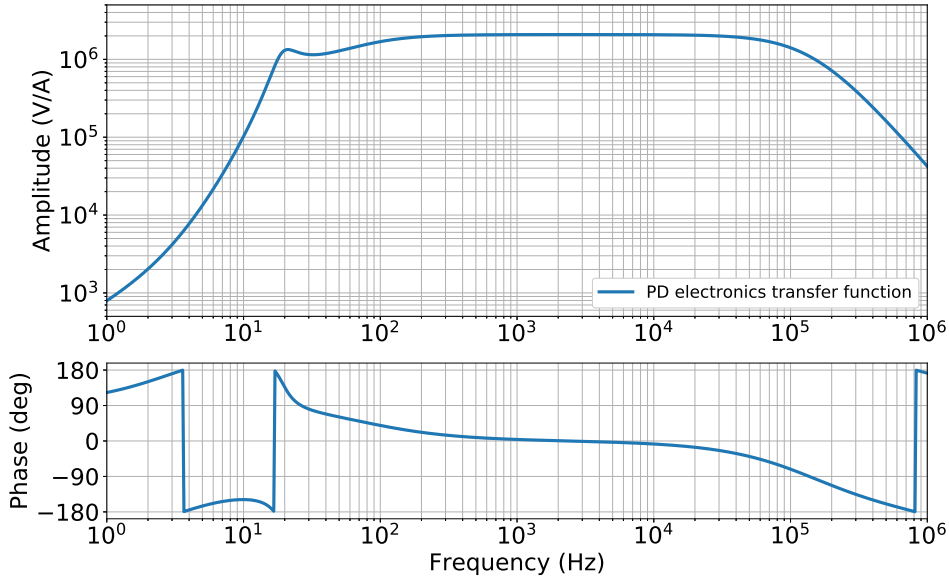


Figure 4.4.1: Bode diagram of the anti-symmetric port photodetector electronics. The transfer function reaches values of 10^6 V/A at 20 Hz and 2×10^6 V/A between 100 – 50 kHz, providing high amplification in the sub-SQL interferometer measurement band.

of 0.8 A/W; therefore, the maximum current to be generated is 7.2 mA. The photodiode bias is limited to currents below 10 mA granting sufficient safety margin. This fulfills the first requirement for the maximum power to be detected.

The design of the electronics is adapted from a so far unpublished design for a future Advanced LIGO plus photodetector [Gro]. It is similar to the schematics presented in [G⁺16]. The electronics consist of a trans-impedance amplifier, two whitening stages and a differential output stage. Figure 4.4.1 shows the response of the electronics. In the measurement band of the AEI sub-SQL interferometer, the electronics provide a gain of at least 10^6 V/A.

The displacement equivalent noise of the photodetector electronics is included into the sub-SQL interferometer noise budget for 0.5 W input power and 15 pm dark fringe offset, shown in figure 4.4.2. At the probe frequency of 67.6 Hz, the photodetector noise is a factor of 5 below the total classical noise, satisfying the second requirement.

Concluding these investigations, a photodetector design, including trans-impedance electronics, is found that allows for a constant dark fringe offset of 15 pm for laser input powers of 0.5 – 10 W.

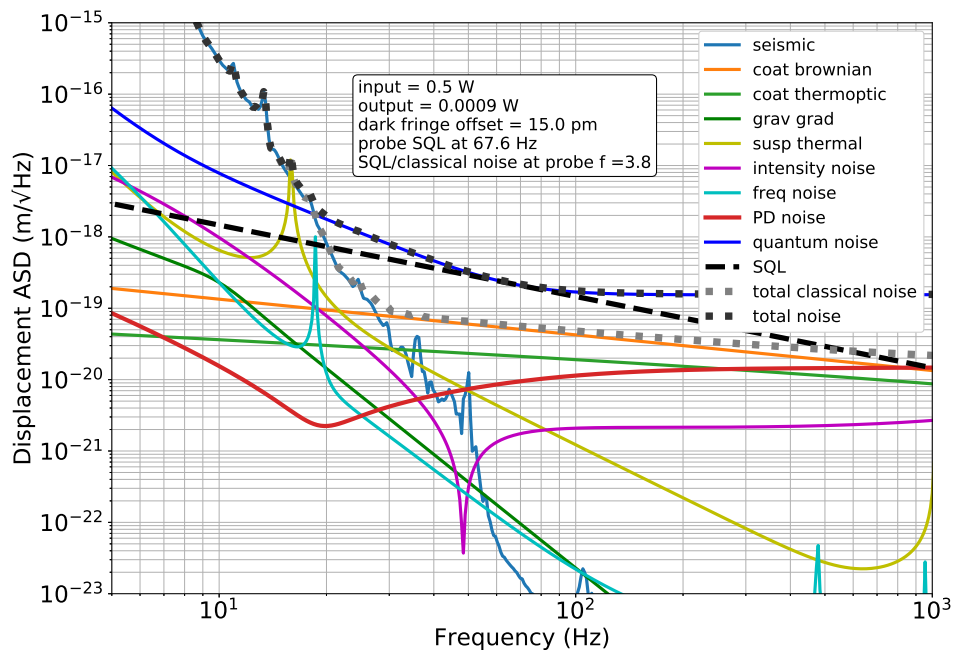


Figure 4.4.2: Noise budget of the sub-SQL interferometer for 0.5 W input power and a dark fringe offset of 15 pm. The photodetector noise is a factor 5 below the total classical noise at the SQL probe frequency.

Chapter 5

Summary and outlook

In the scope of this thesis, an active seismic isolation system for the AEI 10 m prototype was developed, analyzed and characterized. The system's passive isolation was mostly implemented prior to this thesis, but was optimized in its performance and characterization. A careful tuning of the GAS-filter and inverted pendulum stiffness for the west AEI-SAS lead to significantly reduced unwanted drifts during ventilation of the vacuum system compared to the central and south AEI-SAS by up to a factor 12 in amplitude. An analysis on the coupling between horizontal and tilt motion of the springbox and optical table improved the understanding of the system's isolation performance above 3 Hz significantly.

The functionality and noise performance of all involved sensors and actuators was described. The signal-to-noise performances were compared as a function of frequency, showing different optimal frequency bands for each sensor. The discovered high noise of previously installed L-22D geophones lead to the decision to replace them with L-4C geophones with revised amplifier electronics, featuring lower noise by a factor 10 at 1 Hz and 100 at 0.01 Hz.

The calculated noise was compared to huddle test measurements. Excellent agreement between calculation and measurement provided deep insight into sensitivity limitations of the sensors. The ratio between measurement and calculation for the L-4C geophones, for example, is mostly within a factor of 2. This enables a precise characterization of the entire isolation system and provides valuable information for any research group world-wide using these sensors. The number of reference sensors and the seismic pre-isolation were identified to have a great impact on the precision of huddle tests. The AEI-SAS, providing large seismic pre-isolation and a variety of reference sensors stiffly connected via the optical table, provides an excellent environment for these tests.

Commonly utilized local isolation techniques were described and improved using novel approaches, also applicable to other experiments. A new technique for the determination of transformation matrix entries was described, based on the sensor response to a well characterized actuation. The cross-coupling between different degrees of freedom was significantly reduced, which manifested in a lower tilt-to-horizontal noise in the rz signal by roughly a factor of 3 below 0.3 Hz.

The influence of sensor positioning and alignment on the sensitivity in Cartesian coordinates was derived using a novel method. The results improved the characterization of the AEI-SAS and can help other research groups to optimize their sensor positioning and alignment to their requirements.

The sensor blending parameters were optimized for each degree of freedom to find the minimal optical table velocity *rms* by varying the blending filter orders and the blending frequencies. This calculation serves as a simple alternative for the determination of blending parameters by eye or more advanced optimization processes, like particle swarming.

The local isolation performance with all the presented techniques was measured and compared to a model, with a high level of agreement. The simulation provides deep insight into limitations, showing that the x and y degrees of freedom are limited by sensor noise up to 4 Hz. The z degree of freedom is limited by sensor noise below 0.4 Hz, while sensor noise and gain limited motion jointly dominate the motion from 0.4–13 Hz. Vertical rotations in rx and ry are dominated by sensor noise below 1 Hz and by sensor noise and gain limited motion from 1–6 Hz.

Global seismic isolation of the AEI 10 m prototype was introduced as a novel isolation scheme including optical levers and suspension platform interferometers. The interconnection of the AEI-SASs by these sensors leads to complex coupling mechanisms between motion in the different degrees of freedom. Transfer functions from optical table motion to the interferometer error signals were derived, giving deep insight into these coupling mechanisms. They provide valuable knowledge for future upgrades of or newly designed seismic isolation systems that include global sensors.

A new optimization of sensor blending parameters, including these transfer functions, was executed to minimize the interferometer error signal *rms* in pitch and yaw. The results provided valuable knowledge about significant contributions to the error signals. Common longitudinal motion of the AEI-SASs appears to dominate the pitch error signal, while the yaw error signal appears to be dominated by differential side motion. These calculations are used to demonstrate concrete possibilities for improvements of the isolation performance. Changes to the sensor correction filters, the controller filters and additional features in the blending filters are calculated to reduce the pitch error signal by a factor 1.48 and the yaw error signal by a factor 1.39. A future implementation of new inertial vertical sensors based on a HoQI readout is calculated to further reduce the pitch and yaw error signals by factors of 3.15 and 5.53, respectively. It was concluded that the changes to digital filters should be made, due to their easy testing and implementation. The new vertical sensors would require a significantly higher effort to install and may be further investigated if major seismic isolation improvements are needed in the future.

The principles of global isolation were verified by measurements. These measurements served as rough demonstrations, since the optimal measurement tool, a Michelson interferometer, has, as of writing, not yet been assembled.

A noise budget of the AEI sub-SQL interferometer was constructed with FINESSE. This was used to find requirements for the seismic pre-isolation of the input optics by simulating the effect of jitter noise from those optics on the interferometer sensitivity. One-stage suspensions in horizontal and vertical direction were identified to provide sufficient pre-isolation. With this tool, the optimal dark fringe offset was calculated to be 15 pm, with particular focus being placed on intensity and frequency noise and the resulting TEM₀₀ mode laser power at the anti-symmetric port of the interferometer. This simulation lead to requirements for the anti-symmetric port photodetector, a possible design of which was presented. Its noise was shown to be sufficiently below the SQL.

With the work presented in this thesis, the active seismic isolation of the AEI 10 m prototype can be considered to be fully operational and able to provide excellent performance. It is expected to be sufficient for the main interferometer to reach and later surpass the SQL without being limited by seismic noise. In the short term, the presented changes of digital filters will be implemented to optimize the isolation performance. Two scenarios involving the installation of new sensors will be investigated if, contrary to the expectations, larger improvements of seismic isolation are required. A fully installed Michelson interferometer will likely provide enough useful information for a thorough performance analysis to be conducted. This will be useful to assess the validity of the assumptions made for the global sensor blending optimization and the presented improvements.

The seismically isolated, well characterized optical tables in vacuum will continue

to serve as an excellent environment for future testing of sensors. In the short term, HoQI-based vertical inertial sensors will be characterized, and huddle tests will provide valuable information on their noise. HoQI sensors will later be installed and tested at the interferometer beam splitter intermediate mass to prove their functionality in a full Michelson interferometer before being considered for implementation at LIGO.

The FINESSE models developed during the course of this work will continue to be useful for the understanding of the performance of the Michelson interferometer once operational. While being used for calculation of requirements in this thesis, the simulation will serve for the characterization of the interferometer post installation, analyzing limitations and possible malfunction of subsystems.

The simulated dependence of the anti-symmetric port laser power, the frequency noise, and the intensity noise on the dark fringe offset will be compared to measurements once the Michelson interferometer is operational. The anti-symmetric port photodetector is currently assembled and characterized. It will soon be installed on the OMC breadboards and implemented in the vacuum system.



Appendix A

Overview of further seismic isolation systems

Seismic isolation is required for every gravitational wave detector and every sophisticated prototype for gravitational wave detectors. [Ber18] gives a detailed overview of the different pre-isolation systems with a focus on their mechanical setup and passive isolation techniques. Different approaches of active isolation strategies were developed within the gravitational wave community and are now utilized. This section reviews various of these seismic isolation systems, with a strong focus on active isolation techniques.

A.1 Active seismic isolation of GEO600

GEO600 is an operating gravitational wave detector of the first generation and is located in Sarstedt, Germany [L⁺97, D⁺15]. Its seismic isolation system is mostly passive and consists of a triple suspension supported by passive pre-isolation [PTH⁺00, Goß04]. Active pre-isolation was intended but is not utilized in current operation [L⁺].

Figure A.1.1 shows a schematic overview of one GEO600 seismic isolation system. The triple suspension hangs from a rotational stage, which provides coarse rotational pre-alignment. Suspension motion is sensed by shadow sensors called Birmingham Optical Sensor and Electro-Magnetic Actuators (BOSEMs) [CAC⁺12] and damped locally at the upper mass by simple feedback loops. Actuators are utilized to exert additional damping at the intermediate and test mass. They are seismically isolated by a reaction pendulum in order not to significantly couple ground motion to the test mass via the exerted force. The rotational stage and stack stabilizer are pre-isolated passively in vertical and horizontal directions by a layer of graphite-loaded silicon rubber (RTV 615).

The initially planned active pre-isolation included feedback and feedforward techniques. The feedback signal was supposed to be provided by a set of L-22D geophones, while an STS-2 seismometer was installed to measure ground motion for feedforward. Three degrees of freedom piezo actuators were intended to apply the actuation signals with a large range of 25 μm (see [Goß04], page 51). Failures occurred in full range operation, limiting the range of the actuators strongly. Operating the active isolation during high seismic activity became impossible. Further problems, like high electronic noise of the geophone readout beyond the specifications, lead to the decision of relinquishing the active pre-isolation [L⁺].

A.2 Active seismic isolation of Advanced LIGO

The Advanced LIGO detectors include different seismic isolation systems for different optics and interferometer subsystems. The suspension systems range from quadruple suspensions for the main interferometer optics [A⁺12], to single stage suspensions for

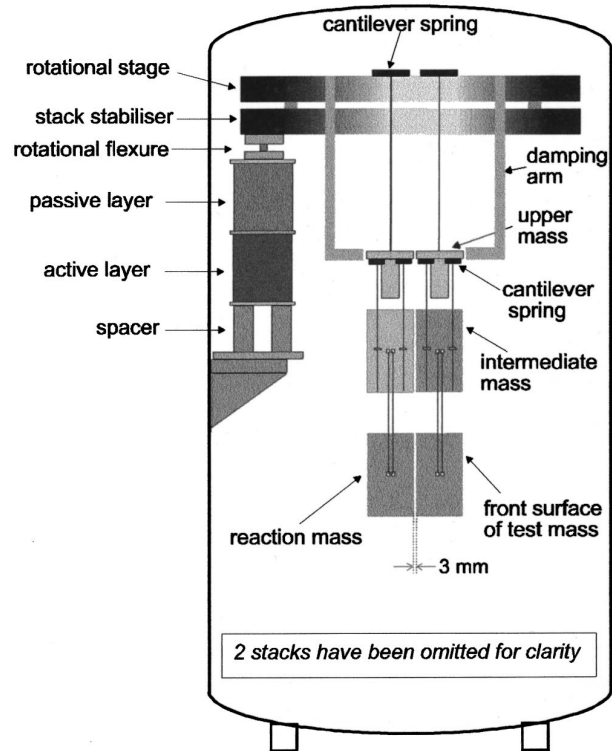


Figure A.1.1: Seismic isolation system of the GEO600 gravitational wave detector. The core isolation system is a mostly passive triple suspension with damping of resonances. It was intended to be supported by passive and active pre-isolation, while only the passive pre-isolation is utilized in current operation. Reproduced from [PTH⁺00], with the permission of AIP Publishing.

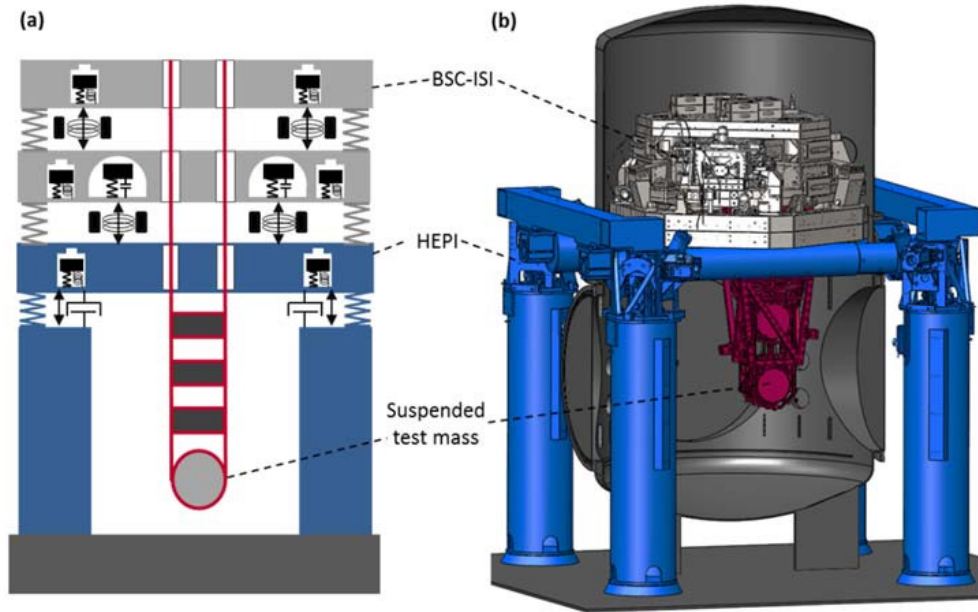


Figure A.2.1: a) Schematic drawing of the HEPI system, the BSC-ISI and the quadruple suspensions for main interferometer optics in side-vert view. The BSC-ISI consists of two actively isolated stages. b) CAD drawing of the HEPI system, the BSC-ISI and the quadruple suspensions. The figure is taken from [M⁺15b].

auxiliary optics [A⁺15]. Three different pre-isolation systems were developed for the Advanced LIGO detectors. Their isolation is mainly based on active seismic isolation.

- The **Hydraulic External Pre-Isolator (HEPI)** system serves as a seismic pre-isolator of further in-vacuum pre-isolation systems mentioned below [W⁺14, M⁺15b].
- The **Basic Symmetric Chambers - Internal Seismic Isolation (BSC-ISI)** is located inside the vacuum tanks to pre-isolate the main interferometer mirror suspensions [M⁺15b, M⁺15a].
- The **Horizontal Access Module - Internal Seismic Isolation (HAM-ISI)** is located inside the vacuum tanks to pre-isolate auxiliary optic suspensions [KL08, M⁺15b].

Figures A.2.1 and A.2.2 show schematic drawings of the HEPI system, supporting a BSC-ISI and a HAM-ISI. The BSC-ISI consists of two active isolation stages, while the HAM-ISI consists of one.

[DeR14] and [M⁺15b] give detailed analyses of these active isolation systems. A summary is provided in the following.

HEPI

The HEPI system serves as the first active isolation stage for all interferometer components inside the vacuum system, including the BSC-ISI and the HAM-ISI. It utilizes hydraulic actuators operating in the laminar flow regime to minimize noise from turbulences [HAD⁺01, H⁺04a] and is equipped with different sensors. Position sensors of the type DIT-5200 from KAMAN [KAM] are blended with L-4C geophones to provide feedback signals. STS-2 seismometers measure ground motion for a sensor correction of the position sensors.

Figure A.2.3 shows an exemplary block diagram of the control system (a), an example of open loop gain (b), and a performance example (c). The figure is copied from [M⁺15b]. The control scheme and filter designs vary for the pre-isolation of the

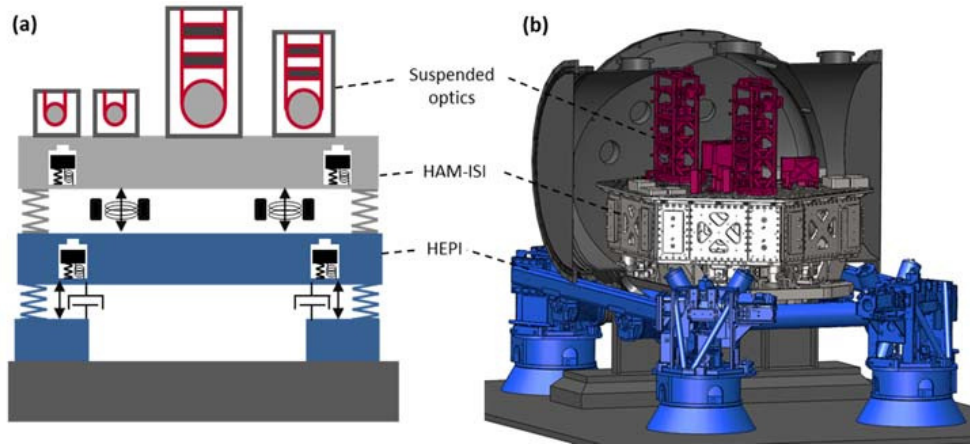


Figure A.2.2: a) Schematic drawing of the HEPI system, the HAM-ISI and 1-3 stage suspensions for auxiliary interferometer optics in side-view. The HAM-ISI consists of one active isolation stage. b) CAD drawing of the HEPI system, the HAM-ISI and auxiliary suspensions. The figure is taken from [M⁺15b].

HAM-ISI and BSC-ISI and for different degrees of freedom. Details are provided in [W⁺14]. The pictured control system is mostly equal to the local seismic isolation system of the AEI-SAS (see section 3.7.1). Differences only occur in the type of position sensors and the filter shapes. The feedback loop has a unity gain frequency of 10 Hz and a value of 1000 at 0.1 Hz. The performance result shows that large isolation is achieved between 0.1–5 Hz with a value of up to 100 providing excellent pre-isolation at low frequencies.

The HEPI system was first installed in initial LIGO at Livingston, which was impaired by large differential motion of the test masses during science run 3. The installation of the HEPI system increased the duty cycle from 21.8% to 66.7% in science run 5. It was installed at LIGO Hanford in a modified design during the upgrade to Advanced LIGO.

HAM-ISI

The HAM-ISI pre-isolates suspensions for auxiliary interferometer components like input and output optics. It consists of two stages, named stage 0 and stage 1. Stage 0 is stiffly connected to and pre-isolated by the HEPI system. Stage 1 is suspended from stage 0 by vertically soft blades and horizontally soft flexures. The resonance frequencies of the whole system are in between 0.9–1.8 Hz. Stage 0 carries STS-2 seismometers and L-4C geophones, while stage 1 is equipped with Capacitive Position Sensors (CPSs) from MicroSense and GS13 geophones [Ins], having slightly lower noise than L-4C geophones but an increased total mass.

Figure A.2.4 shows a) the transfer function from an applied force to the optical table motion for all degrees of freedom, b) an exemplary block diagram of the active control scheme, and c) the open loop gain and its components. The transfer functions resemble a perfect, damped harmonic oscillator up to 100 Hz to a high extent, not showing any internal resonances. The control scheme is similar to the local active isolation of the AEI-SAS (see section 3.7.1) featuring four differences. CPSs are utilized instead of LVDTs, and GS13 geophones replace the L-4C geophones. Furthermore, there is an additional damping path and a damping filter D , which uses the GS13 signal to dampen internal resonances of the system. The fourth difference is the use of L-4C geophones on stage 0 to provide a feedforward signal, suppressing residual motion of the optical table. The unity gain frequency of the feedback loop is at 35 Hz. At 0.1 Hz the loop features a large gain of 10^6 .

Figure A.2.5 shows the isolation results for the horizontal degrees of freedom. At low frequencies, tilt-to-horizontal coupling prevents significant isolation. At 1 Hz, the

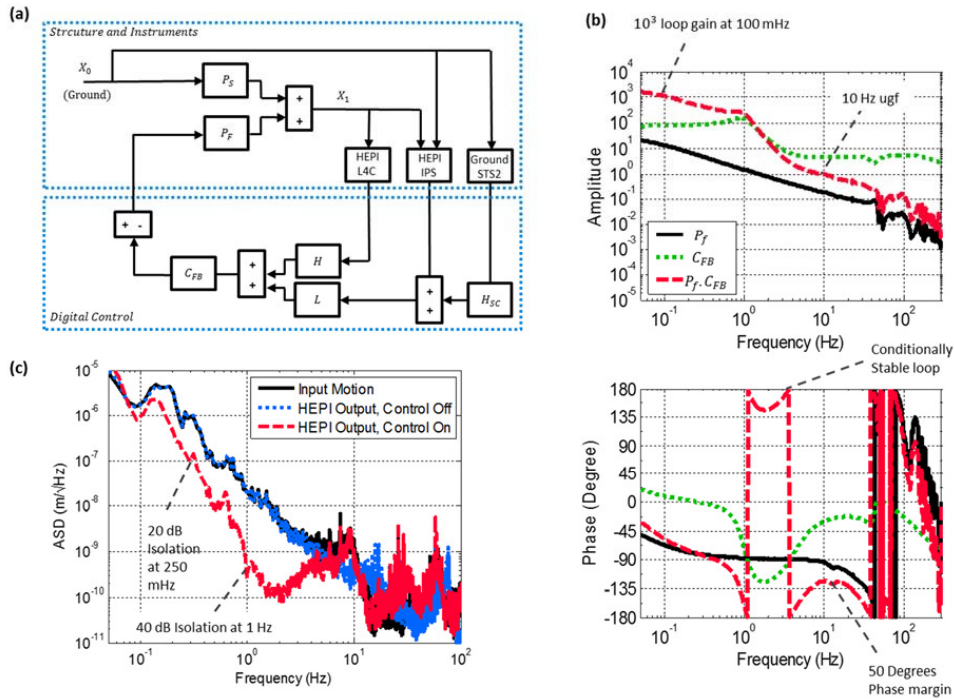


Figure A.2.3: a) Block diagram of the control system for the HEPI. It is similar to the local isolation system of the AEI-SAS (see section 3.7.1). A feedback loop provides suppression of ground motion. Position sensors (IPS) are sensor corrected by STS-2 seismometers and blended with L-4C geophones. b) Exemplary gain of the controller filter C_{FB} , the plant response to a force P_F , and their product being equal to the open loop gain with a unity gain frequency of 10 Hz. c) Performance example of the HEPI system. The figure is taken from [M⁺15b].

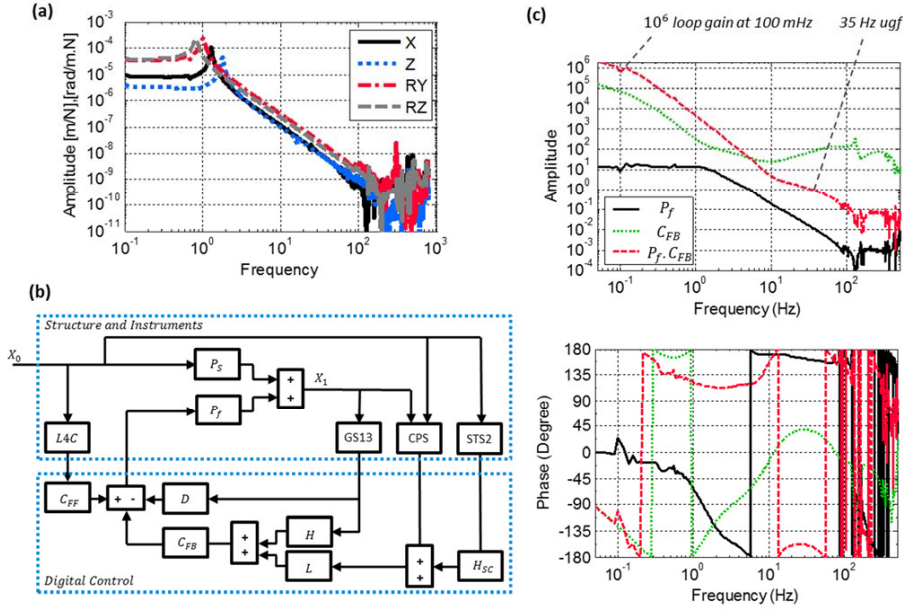


Figure A.2.4: a) Transfer function of the HAM-ISI for the degrees of freedom x , z , rx and rz . The resonance frequencies are between 0.9–1.8 Hz. The first internal resonances occur above 100 Hz. b) Block diagram of the active control scheme. The scheme includes standard sensor correction and sensor blending, an additional damping (filter D) of rigid body modes and a feedforward path to suppress residual seismic noise. c) Exemplary gain of the controller filter C_{FB} , the plant response to a force P_F , and their product being equal to the open loop gain. The unity gain frequency is at 35 Hz. The figure is taken from [M⁺15b].

isolation reaches a factor of 1000, which is reduced to about 100 above 3 Hz.

BSC-ISI

The BSC-ISI supports the suspensions for the most critical interferometer optics and isolates in all six degrees of freedom. It consists of three stages, named stage 0–2. Stage 0 is stiffly connected to and isolated by the HEPI system. It supports stage 1 via vertically soft blades and horizontally soft flexures. Stage 1 supports stage 2 via a similar set of blades and flexures. Active seismic isolation is provided between stage 0 and 1 and between stage 1 and 2. Together with the HEPI system, this results in 3 stages of active pre-isolation.

The motion of stage 0 is measured with L-4C geophones and STS-2 seismometers. Stage 1 supports CPSs, L-4C geophones and T240 seismometers [Pas], being similar to STS-2 seismometers in every aspect of performance. Stage 2 carries CPSs and a set of GS13 geophones.

Figure A.2.6 shows the control schemes of stage 1 and 2 and an example of the open loop gain of stage 1. The figure is copied from [M⁺15b]. Stage 2 has a similar loop gain to the HAM-ISI. Control schemes and loop gain vary slightly for different degrees of freedom and different vacuum chambers. Stage 1 is similar to the local AEI-SAS control scheme in some aspects, but also features differences. Capacitive position sensors are utilized instead of LVDTs. They are sensor corrected as described in this thesis. Three sets of sensors are blended together, namely the CPSs at low frequencies, T240 seismometers in the mid-frequency range, and L-4C geophones at high frequencies. The L-4C geophones are also used to dampen internal resonances on a separate control path via filter D . L-4Cs positioned on stage 0 provide feedforward isolation for otherwise unsuppressed seismic motion coupling to stage 1. The active control scheme of stage 2 is similar to stage 1, but only features a blending between

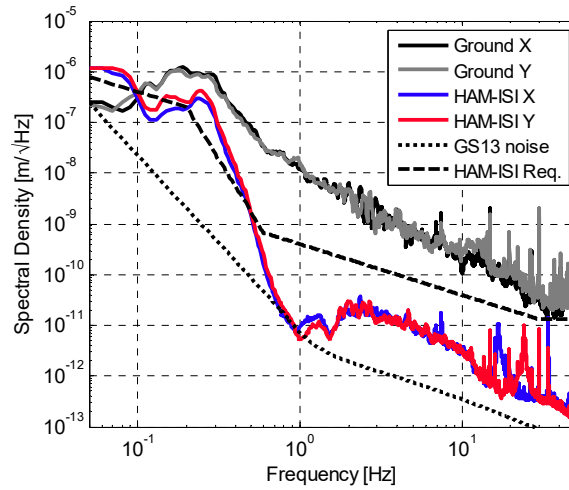


Figure A.2.5: Performance of the HAM-ISI, pre-isolated by the HEPI system. A maximum isolation of a factor 1000 is achieved at 1 Hz. At low frequencies, tilt-to-horizontal coupling limits the isolation performance. Above 3 Hz, the isolation is a factor of 100. The figure is taken from [M⁺15b].

two sensor sets of the CPSs and the GS13 geophones. The open loop gain of stage 1 features a unity gain frequency of 40 Hz.

Figure A.2.7 shows a typical performance of the BSC-ISI in combination with the HEPI system in the longitudinal degree of freedom. The figure is taken from [M⁺15b]. The optical table motion was measured with in-loop GS13 geophones. Between 0.9–5 Hz, the measurement shows a smaller value than the GS13 noise; hence, the data does not resemble the real motion in this frequency regime, but indicates a sensor noise limited performance.

A.3 Active seismic isolation of Advanced Virgo

While Advanced LIGO focuses on active seismic pre-isolation, the Advanced Virgo pre-isolation systems mostly rely on passive isolation. Three different pre-isolators are utilized for Advanced Virgo, each with a different isolation performance. The choice of pre-isolator is determined by the isolation requirements for different interferometer components.

- The **Superattenuator** [DDG⁺87, B⁺05, A⁺10b] is located inside the vacuum system and incorporates pre-isolation system and suspension for the main interferometer mirrors in one.
- The **Multistage Seismic Attenuation System (MultiSAS)** [vBH⁺19, Bek13] is a pre-isolation system for auxiliary interferometer components located inside the vacuum system.
- The **External Injection Bench - Seismic Attenuation System (EIB-SAS)** [BBv⁺12, BBB⁺13, BBb⁺15] is utilized outside the vacuum system to pre-isolate auxiliary components that require less seismic pre-isolation and no vacuum system.

An overview of these three pre-isolation systems is provided in the following.

Superattenuator

Figure A.3.1 shows a schematic drawing of the Virgo Superattenuator. It consists of a seven-stage pendulum, supported by 6 m long inverted pendulums. The upper five masses of the suspension chain are made of mechanical filters that provide

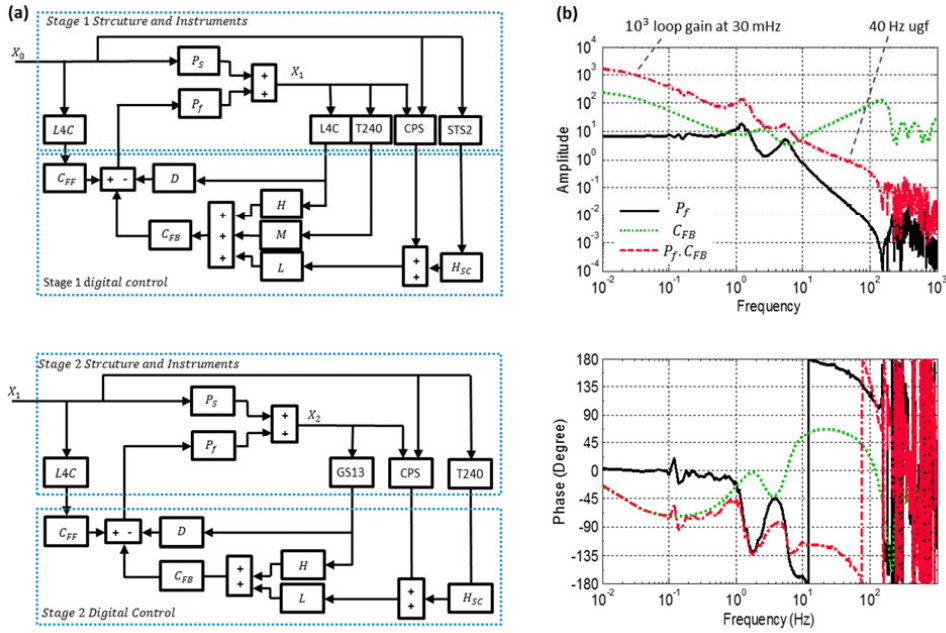


Figure A.2.6: a) Block diagram of the control system for the first and second isolation stage of the BSC-ISI. Both are based on feedback loops. Stage 1 includes a standard sensor correction, a sensor blending between three sensors, an additional damping (filter D) of rigid body modes, and a feedforward path to suppress residual seismic noise. Active isolation of stage 2 is similar, but with only two sensors being blended together. b) Exemplary gain of the controller filter C_{FB} , the plant response to a force P_F , and their product being equal to the open loop gain with a unity gain frequency of 40 Hz. The figure is taken from [M⁺15b].

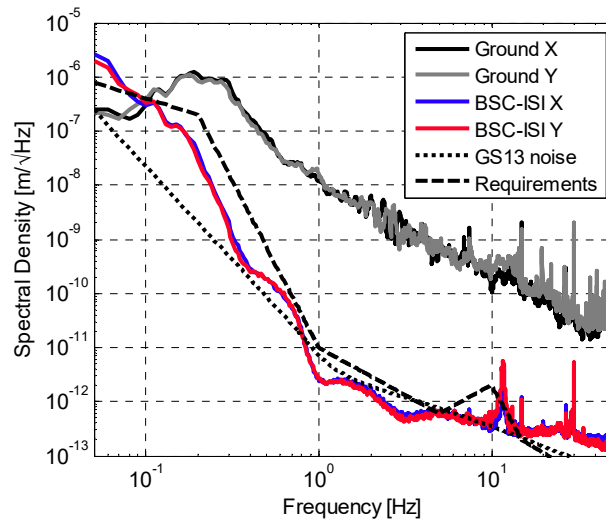


Figure A.2.7: Performance of the BSC-ISI, pre-isolated by the HEPI system. Between 0.9–5 Hz the measurement does not resemble the real motion, which is limited by GS13 sensor noise (dotted line). A total isolation of a factor of roughly 1000 is achieved between 1–10 Hz. The figure is taken from [M⁺15b].

vertical isolation [B⁺97]. They are similar to the GAS filters, but instead of generating a mechanical anti-restoring force, they rely on a magnetic anti-spring effect. The second last suspended mass is called Marionette [BMP⁺99]. The test mass and a reference mass are suspended in parallel to each other from the Marionette. All fundamental suspension resonance frequencies in vertical direction are below 2 Hz, while in horizontal direction they are below 2.5 Hz. This provides extremely high isolation performance above a few Hz. The inverted pendulum resonance frequency is at 0.04 Hz, providing large pre-isolation of the suspension resonances in the horizontal directions. [L⁺01] presents isolation results for the top stage of the inverted pendulums with a reduction of *rms* motion of 100 at 0.1 Hz. The overall transfer function of the Superattenuator is shown in figure A.3.2.

[A⁺10b] presents measurements in which injection lines are introduced at the inverted pendulum stage by the LVDTs, and the response of the test mass is measured. Already at 4.1 Hz, no peak was distinguishable from the interferometer noise floor after several hours of measuring. This sets an upper limit for the transfer function to a few 10^{-8} . The authors conclude that already at 4.1 Hz mirror thermal noise is larger than the coupling of seismic noise to the test mass.

Active seismic isolation of the Superattenuator is described in [L⁺01, LPR06, Tro18]. It is predominantly utilized for positioning and damping of the mechanical resonances; therefore, a hierarchical control strategy is adopted. At first, accelerometers and LVDTs, similar to the ones used in the AEI-SAS, measure motion on top of the inverted pendulum stage. Their signal is blended and utilized in combination with coil-magnet actuators to form feedback loops.

Secondly, the test mass underlies large drifts of hundreds of micrometers below 10 mHz, measured by the main laser. This signal is fed to the coil-magnet actuators on top of the inverted pendulum stage to reduce the drifts.

A third step of active isolation is introduced by the Marionette. Optical levers measure the motion of the Marionette and the test mass. Their signals are sent to electromagnetic actuators within the Marionette to reduce so far unsuppressed seismic motion.

A fourth and last stage of active isolation is exerted between reference mass and test mass. Since noise of this actuation signal is directly applied to the test mass, the actuation only compensates for a few nano meter above a few Hz [A⁺10b]. The unity gain frequency of the overall active control system is at roughly 5 Hz.

MultiSAS

Figure A.3.3 displays a drawing of the MultiSAS. The figure is taken from [vBH⁺19]. It consists of an inverted pendulum stage supporting the top stage. A first GAS filter is mounted inside the top stage, carrying a second GAS filter, which suspends an optical table, all via fiber connections. The optical table supports auxiliary interferometer components.

The resonance frequencies of the horizontal and vertical suspension stages are in the range of 0.1–1.8 Hz. Three horizontal suspension stages result in an isolation of $1/f^6$ above resonances, while the two stages isolate vertically with $1/f^4$.

Sets of three horizontal LVDTs, horizontal L-4C geophones, horizontal voice-coil actuators and one T240 seismometer provide signals for horizontal feedback loops, including sensor blending and sensor correction. In vertical direction, only LVDTs and voice-coil actuators are installed to dampen vertical resonances. Figure A.3.4 is taken from [vBH⁺19] and shows the isolation performance in longitudinal direction for open loop operation and closed loop operation. Large passive isolation by the multiple pendulum system is well visible, while active isolation mainly provides a reduction of motion on the mechanical resonance frequencies. More details about the MultiSAS are provided in [Bek13].

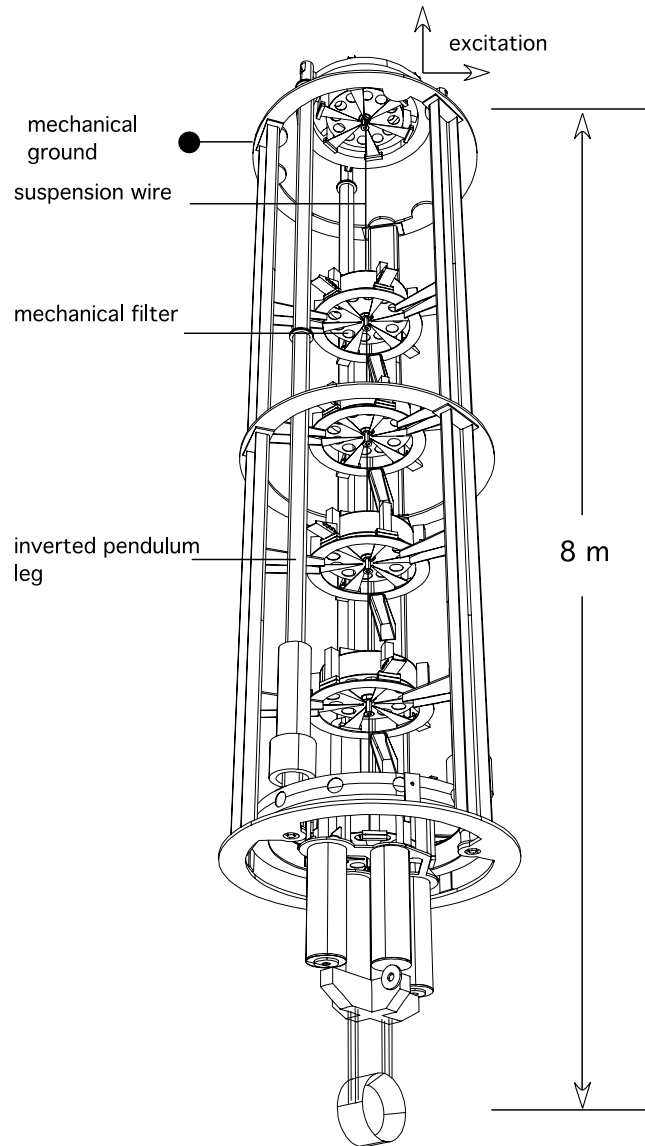


Figure A.3.1: Schematic drawing of the Virgo Superattenuator. It consists of an inverted pendulum stage, supporting an 8 m long 7-stage suspension. The Superattenuator combines pre-isolation system and mirror suspension in one and is utilized for the main interferometer optics. The figure is taken from [B⁺05].

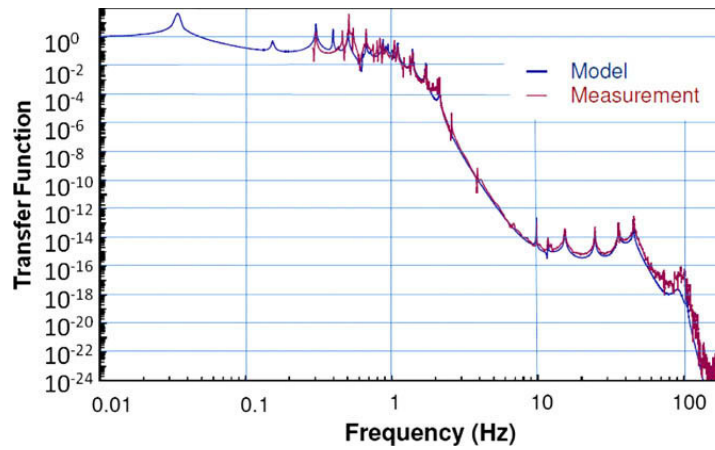


Figure A.3.2: Modelled and measured transfer function of the Virgo Superattenuator. The measurement is extrapolated from stage-by-stage transfer function measurements. The figure is taken from [A⁺10b].

EIB-SAS

The EIB-SAS is closely related to the AEI-SAS, both being adapted versions of the HAM-SAS [BDF⁺05, S⁺09]. It is designed to isolate auxiliary interferometer components that do not require to be installed inside the vacuum system. The operation in air relaxes the material restrictions but requires a more robust isolation strategy to cope with air turbulences.

The EIB-SAS consists of an inverted pendulum stage carrying a GAS filter stage, which supports the optical table. The resonance frequencies are tuned to 0.22 Hz in horizontal direction and 0.39 Hz in vertical direction. Equal to the AEI-SAS, it is equipped with 6 LVDTs, 6 geophones, 6 voice-coil actuators and 7 motorized springs. LVDT and geophone signals are combined in a sensor blending. Geophones measuring ground motion are utilized for a sensor correction of the LVDTs.

Active isolation of the EIB-SAS has the goals of providing long time stability and damping of the mechanical resonances of the passive isolators. The open loop gain of the EIB-SAS is about a factor 100-1000 lower compared to the AEI-SAS open loop gain. Only at roughly 16 Hz, it peaks through unity gain again to dampen resonances. With this scheme, the mechanical resonances are effectively damped, as shown in [BBB⁺13, BBb⁺15].

A.4 Active seismic isolation of KAGRA

The Kamioka Gravitational Wave Detector includes four different seismic isolation systems, which rely on the same principles as the Virgo Superattenuator. They are shown in figure A.4.1, which is taken from [A⁺21b]. The Type-A isolator is used for the main interferometer mirrors. The Type-B isolator suspends the beam splitter and signal recycling mirrors. The Type-Bp isolator provides isolation for the power recycling mirrors, and the Type-C isolator decouples the input mode cleaner and other input optics from seismic motion. Each of the isolation systems combines pre-isolation and mirror suspension in one system. The detector is located underground, which reduces seismic motion of the surroundings at frequencies above 1 Hz significantly, relaxing the requirements on the suspension systems. A more detailed description of each suspension type is provided in the following.

Type-A suspension

The Type-A suspension is described in the papers [HSKT14, M⁺17, Ush21] and discussed in more detail in the theses [Fuj19, Oku19]. Figure A.4.2 shows the setup in a CAD drawing and a schematic drawing. It is taken from [Fuj19], page 91. Different

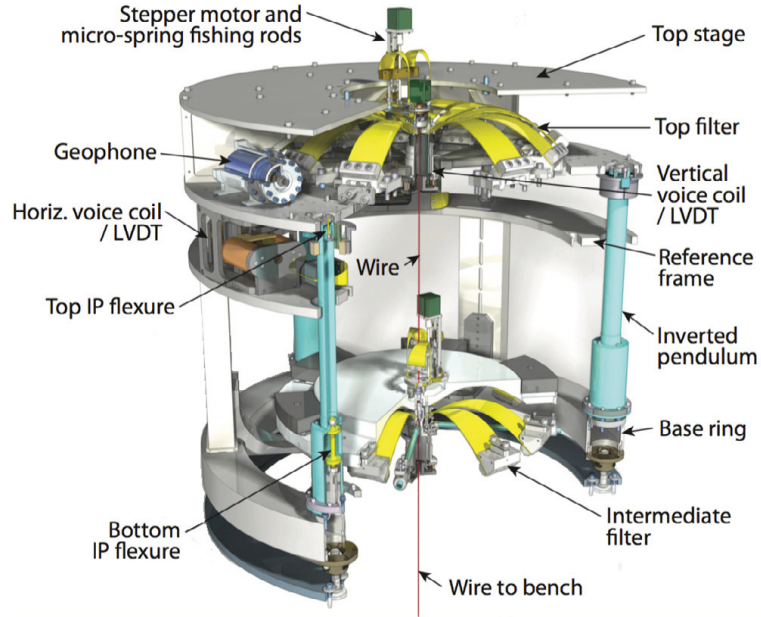


Figure A.3.3: Schematic drawing of the Virgo MultiSAS. It consists of an inverted pendulum stage, two suspension stages for horizontal isolation and two GAS filters, implemented as upper and intermediate suspension masses, for vertical isolation. Various sensors and actuators are installed on top of the inverted pendulum stage to measure the motion and provide active isolation. The MultiSAS supports an optical bench, carrying auxiliary interferometer components. The figure is taken from [vBH⁺19].

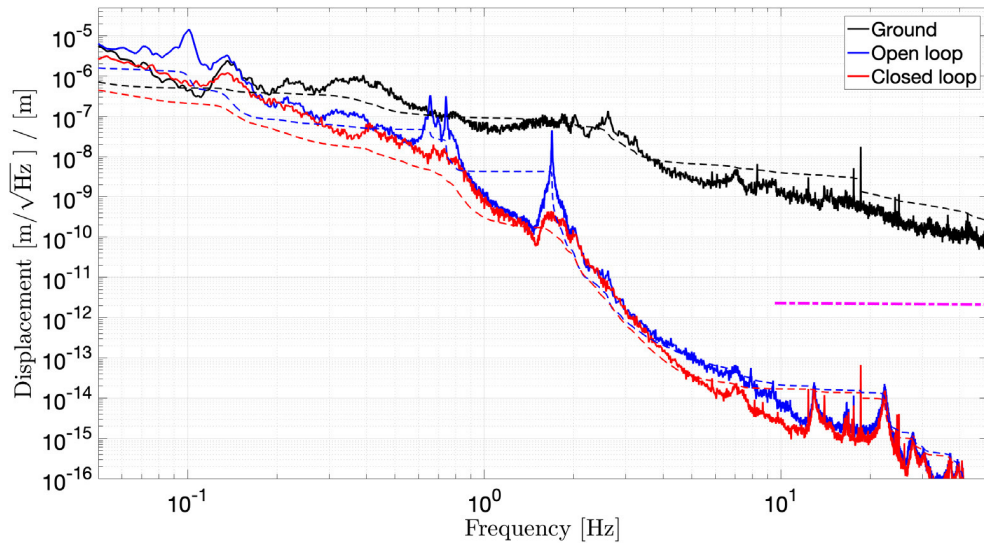


Figure A.3.4: Amplitude spectral densities and *rms* values of the MultiSAS optical bench motion in longitudinal direction in comparison to the ground motion. The optical bench motion is displayed with passive isolation only and with closed loop isolation. The figure is taken from [vBH⁺19].

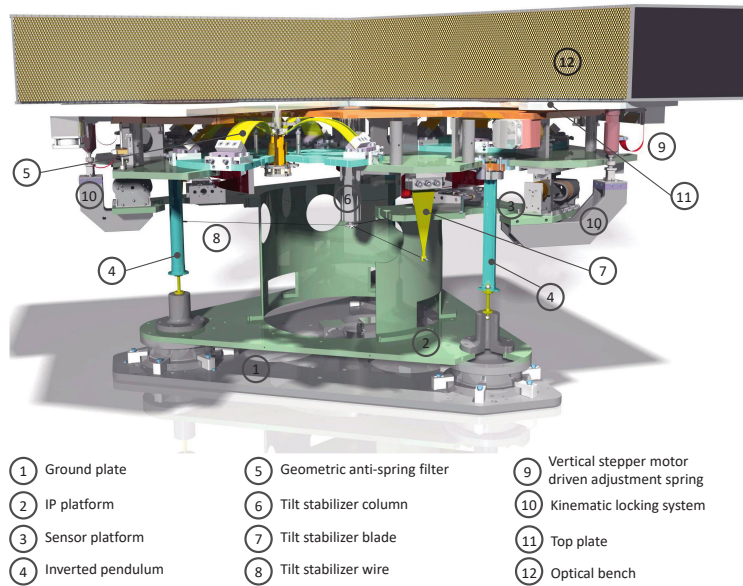


Figure A.3.5: Schematic drawing of the EIB-SAS. The design is similar to the AEI-SAS design. It consists of an inverted pendulum stage supporting a GAS filter stage, which carries an optical table. Various sensors and actuators are installed to provide active isolation. The EIB-SAS isolates auxiliary interferometer components located outside the vacuum system. The figure is taken from [BBb⁺15].

to all other currently existing seismic isolation systems within the gravitational wave community, the last four stages of this system are cryogenic. Horizontal isolation consists of one inverted pendulum stage and eight suspension stages. Vertical isolation is based on five GAS filters utilized as suspension masses, accompanied by two blade spring stages in the cryogenic bottom part. A three stage reaction pendulum is suspended in parallel to the last three stages to provide low noise actuation signals.

Figure A.4.2 shows the sensors and actuators implemented in the Type-A suspension. These are utilized to provide damping and low frequency drift stabilization for the individual stages. Sensor correction is applied at the inverted pendulum stage. The inertial sensors are L-4C geophones and were intended to provide inertial isolation. In current operation, they are not used due to insufficient noise performance [Fuj19], page 125.

Cryogenic cooling is achieved by thermal radiation and by heat conductivity; therefore, the cryogenic parts are surrounded by a cooling shield at a temperature of 8 K. Heat links create a connection from this shield to the Marionette and from there to the other cryogenic components, except for the test mass. An additional triple suspension is used to create a soft connection between the shield and the Marionette via the heat links [Oku19]. [Fuj19], page 103, provides a simulation, stating that seismic coupling via the heat links dominates the overall seismic noise above roughly 10 Hz. This is shown in figure A.4.3.

The active isolation is separated into three phases: the calm-down phase, the lock-acquisition phase, and the observation phase. In the calm-down and lock-acquisition phase, noise of the control loops is of minor interest; hence, more aggressive servo filters are applied to dampen the resonances. In the observation phase, the gain reduced, especially in the measurement band. To the author's knowledge, the Type-A suspensions are not run in their intended configuration at the time of writing. GAS filters had to be locked mechanically in all Type-A suspensions in order to maintain the mirror operating points [Fuj19], page 195.

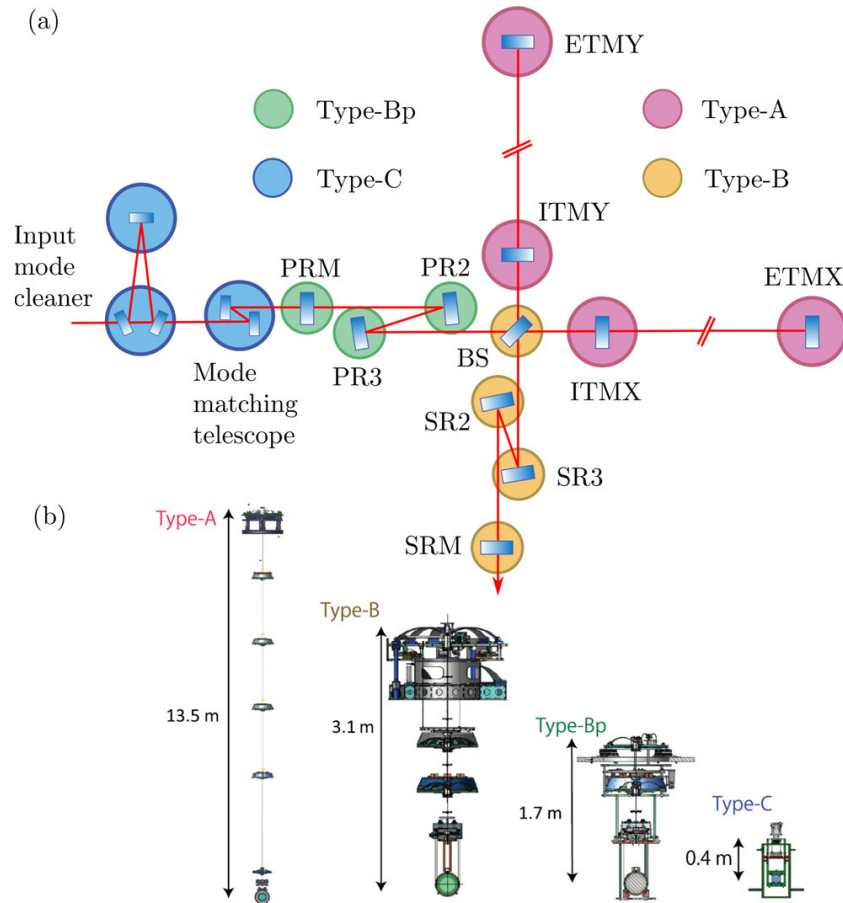


Figure A.4.1: a) Overview on the applications of the four different KAGRA isolation systems in the detector and b), overview on their mechanical setup. The figure is taken from [A⁺21b].

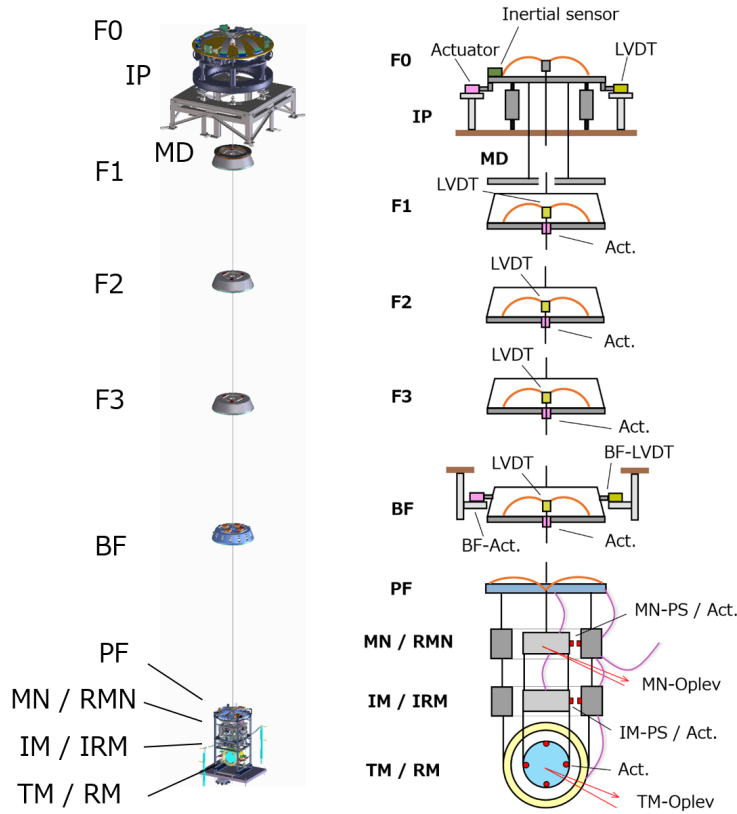


Figure A.4.2: left: CAD drawing and right: schematic setup of the KAGRA Type-A suspension. The first suspension stage consists of three short inverted pendulum (IP) legs, followed by the top GAS filter (F0). Four more GAS filters and the cryogenic part are suspended with wires from F0. The first of these GAS filters (F1) includes an additional magnetic damper (MD) ring. The fourth GAS filter is named bottom filter (BF). The upper stage of the cryogenic part is called platform (PF) and suspends a Marionette (MN) and a recoil-Marionette (RMN), followed by an intermediate mass (IM) and an intermediate-recoil-mass (IRM). The last stage consists of the test mass (TM) and recoil-mass (RM). Actuators (Act.), inertial sensors, LVDTs, photo sensors (PS) and optical levers (Oplev) are labelled. The figure is taken from [Fuj19], page 91.

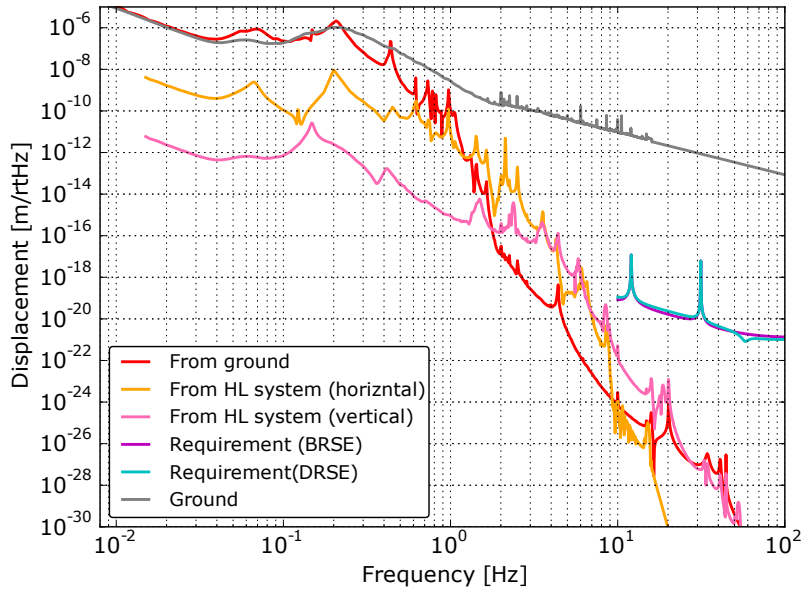


Figure A.4.3: Expected vibration isolation performance of the Type-A system. The figure shows direct seismic coupling via the whole suspension chain and seismic coupling via the heat links (HL). A coupling from vertical to horizontal motion of 1% was assumed. The two requirements refer to two different detection modes, namely Broadband Resonant Sideband Extraction (BRSE) and Detuned Resonant Sideband Extraction (DRSE). The figure is taken from [Fuj19], page 103.

Type-B

The Type-B suspension is described in [A⁺21b, F⁺16] and shown in figure A.4.4. While the top stage is similar to the Type-A suspension, the Type-B suspension only includes three GAS-filters instead of five. It has no platform and Marionette, and the last stages are at room temperature. The intermediate mass is utilized as a replacement for the Marionette and provides similar control capabilities. An intermediate-recoil-mass is suspended from the last GAS filter in parallel to the intermediate mass, to provide low noise actuation forces. A recoil-test-mass is suspended in parallel to the test mass from the intermediate mass for the same purpose. The implementation of sensors and actuators in all stages is very similar to the Type-A suspension.

In total, the suspension system provides five stages of horizontal isolation and three stages of vertical isolation for the test mass.

As in the Type-A suspension, active isolation has the goal of damping the suspension resonances and providing a low frequency positioning to compensate for drifts. [A⁺21b] describes that the inverted pendulum stage and the three GAS filter stages use local feedback loops, based on sensors and actuators within the single stages. Sensor blending and sensor correction is planned to be utilized in the inverted pendulum stage, but is not yet implemented. The intermediate mass actuators receive signals from local sensors and also low frequency signals from the optical lever measurement on the test mass; hence, no large forces need to be applied directly to the test mass. The last stage of actuation is again provided by actuators attached to the recoil-test-mass, to compensate for small, so far unsuppressed seismic vibrations.

Figure A.4.5 shows the simulated final performance of the Type-B suspension with and without active control. The suspension resonances at 0.4 Hz and 0.65 Hz are sufficiently damped, but control noise is introduced between 0.06–0.35 Hz. At the time of writing, this performance is not achieved, but improvements are undertaken.

Type-Bp

The KAGRA Type-Bp suspension is described in [A⁺19b] and shown in figure

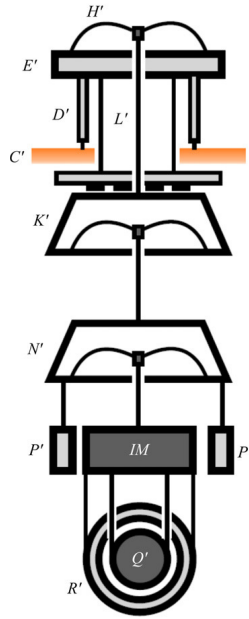


Figure A.4.4: Schematic setup of the KAGRA Type-B suspension. The first suspension stage consists of three short inverted pendulum legs (D') followed by the top GAS filter (H'). Two more GAS filters (K' and N'), the intermediate mass (IM), and the test mass (Q') are suspended from the first GAS filter with wires. An intermediate-recoil-mass (P') is suspended in parallel to the intermediate mass. A recoil-test-mass (R') is suspended in parallel to the test mass. The figure is taken from [A⁺21b].

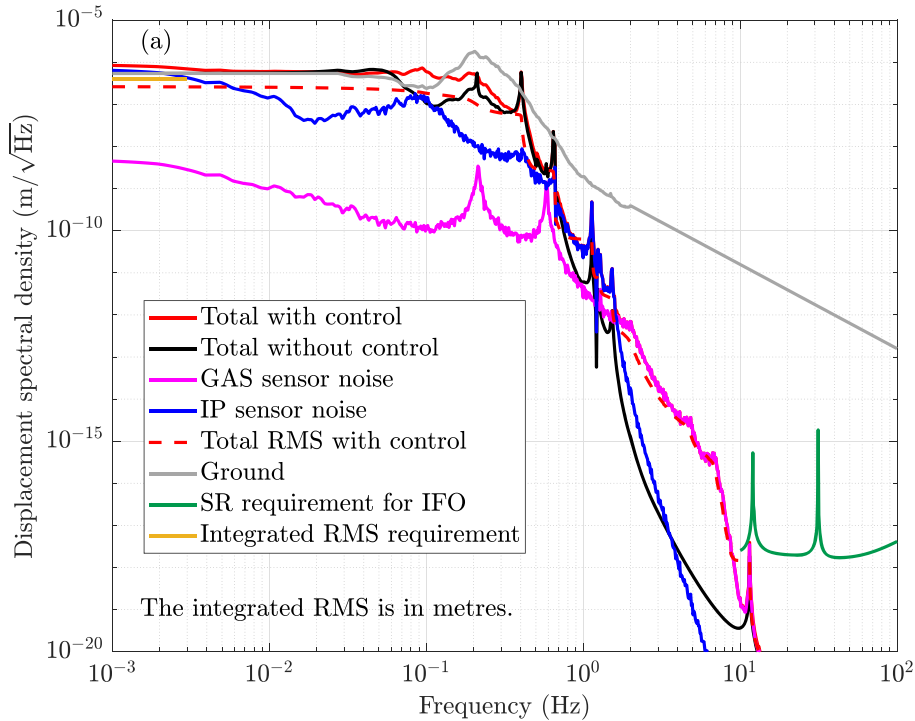


Figure A.4.5: Simulated displacement spectral densities of the Type-B suspension performance with and without active isolation. The limitations, ground motion and the requirements are shown for comparison. The figure is taken from [A⁺21b].

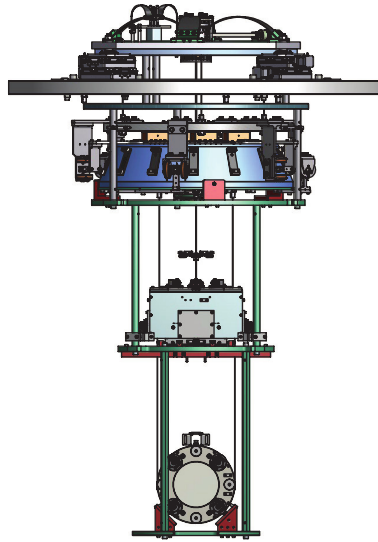


Figure A.4.6: Setup of the Type-Bp suspension. It consists of two GAS filters, an intermediate mass and a test mass. Each stage is equipped with sensors and actuators. The figure is taken and slightly adapted from [A⁺19b].

A.4.6, which is taken and modified from [A⁺19b]. This type of suspension does not have inverted pendulums and consists of two GAS filters, an intermediate mass and the test mass. A reference mass is suspended in parallel to the second GAS filter to enable low noise damping. In total, the system includes three horizontal isolation stages and two vertical isolation stages.

The active control principles are equal to the Type-B suspension: Each stage has a local feedback control using local sensors and actuators. Additionally, the intermediate mass feedback uses low frequency signals from the optical lever on the test mass. The test mass actuators only apply small forces in order not to introduce additional noise.

Type-C

The KAGRA Type-C suspension is a modified version of the suspensions of the first generation gravitational wave detector TAMA300 [T⁺02a]. It consists of a three-stage vibration isolation stack followed by a two-stage suspension. This setup is similar to the GEO600 suspensions.

Active isolation is applied as damping of the suspension resonances. More information about the Type-C suspension is provided in [M⁺17].

A.5 Global seismic isolation outside the AEI 10 m prototype

This section gives an overview of global seismic pre-isolation techniques that are currently utilized or under discussion for use in gravitational wave detectors.

Global seismic isolation of Advanced LIGO

Two global seismic isolation techniques are currently utilized for the Advanced LIGO detectors. In the first scheme, local L-4C measurements are used in feedforward to local actuators. This control path is already described in section A.2. The global aspect is included by minimizing cavity error signals instead of local motion signals. The technique was already utilized for initial LIGO and is presented in [DDA⁺12].

The second global isolation technique has the purpose of increasing the robustness to

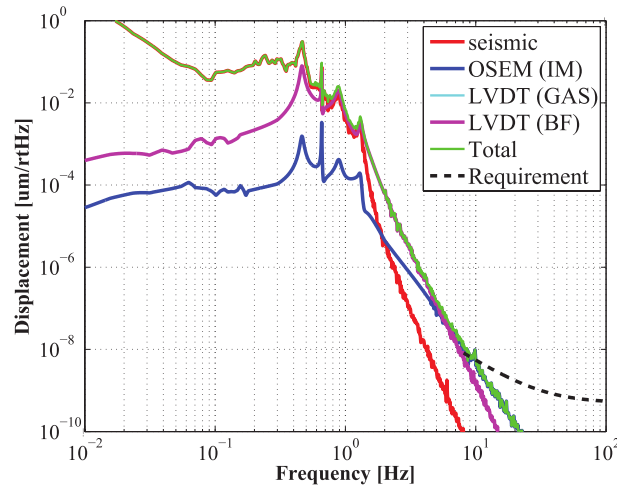


Figure A.4.7: Performance of the Type-Bp suspension, the individual contributions and the requirements. The figure is taken and from [A⁺19b].

earthquakes and is called EQ mode [S⁺20]. It includes two changes to the standard control scheme, with one of them introducing global aspects. They are automatically activated in presence of an earthquake.

Earthquakes have a peak intensity around 0.05 Hz. This frequency coincides with the ripple of the utilized sensor correction filter of Advanced LIGO, resulting in amplification of the already large ground motion. This commonly leads to a loss of interferometer lock, requiring significant downtime for re-locking; hence, the first change to the control scheme in presence of an earthquake is a shift of the sensor correction corner frequency from 0.05 Hz to 0.02 Hz.

Even without amplification by the filter ripple, the amplitude of the earthquake can result in saturation of the actuators, trying to preserve inertially quite platforms. A saturation of actuators also results in a loss of the interferometer lock. This issue is solved by redefining the input for the actuators. While ground motion of the central and end stations is usually uncommon, studies show that during earthquakes common motion exceeds differential motion by a factor 5-6. Common motion at frequencies of 0.05 Hz translates to common test mass motion and barely harms the interferometer operation. Instead of minimizing inertial motion of the isolation platforms, differential motion is minimized during earthquakes. The differential motion signal is obtained by combining seismometer measurements from central and end stations and is applied to the pre-isolation systems for ITMs and ETMs.

Two additional global isolation techniques for Advanced LIGO are currently investigated. Both rely on a leader-follower scheme, as utilized for the AEI sub-SQL interferometer.

- [DiF20a, DiF20b] discuss the possibility of locking pre-isolation systems within the same station together using both relative and inertial sensors; therefore, existing cavity error signals would be used as feedback signals for one isolation system to lock it to a second one.
- The second idea is to implement AEI-SAS-like optical levers and SPIs. They are intended to lock pre-isolation systems within one station onto each other and reduce differential motion [Köh21].

Global seismic isolation of Advanced Virgo

[Maj17] presents two global seismic isolation techniques designed for initial Virgo, which are now utilized for Advanced Virgo. Both techniques aim to reduce differential mirror motion by applying forces to the top stages of the seismic isolation systems. This reduces differential low frequency motion of mirrors, which simplifies the lock

acquisition. A second benefit is the reduction of required forces within the suspension chains that are insufficiently filtered by the reduced number of suspension stages to the test masses.

Motion at the micro seismic peak is coherent within the central station of Advanced Virgo; hence, it is possible to apply a coherent control signal to multiple seismic isolation system within the central station. The applied signal is corrected for the different transmissibilities of the isolation systems, such that differential mirror motion is reduced. This technique, called μ Seism-Free reconstruction, is applied to the isolation systems of both ITMs, the beam splitter and the power recycling mirror.

Seismic motion at the end stations is not sufficiently coherent to the central station; hence, another technique, called the Global Inverted Pendulum Control, is applied. Error signals of the arm cavities are utilized to lock the upper stages of the Superattenuators for the ITMs and ETMs onto each other, reducing the differential mirror motion.

A.6 Comparison to the AEI-SAS

The global isolation of the AEI sub-SQL interferometer combines active and passive isolation to a similar extent and is unique in the field of seismic isolation systems.

The GEO600 suspensions, Virgo Superattenuator, and all KAGRA systems combine the pre-isolation with the mirror suspension and mostly rely on passive isolation techniques. Active isolation is mostly used for damping of the suspension resonances and for positioning of the test masses. Active techniques like sensor blending and sensor correction are partly utilized but feature a significantly lower open loop gain compared to the AEI-SAS; hence, they mostly improve the resonance damping, without attenuating seismic motion over large frequency ranges.

The Virgo MultiSAS design is more similar to the AEI-SAS by suspending an optical table instead of a single mirror; nevertheless, the mechanical setup features large differences. The optical table is suspended from above by two suspension stages, using two GAS filters. The MultiSAS features similar sets of local sensors, actuators and active isolation techniques, although active isolation is predominantly used for damping and positioning.

The BSC-ISI occupies the opposite position to the prior mentioned systems, featuring high passive resonance frequencies but a largely extended active isolation. Some basic active techniques are similar to the AEI-SAS, including sensor blending and sensor correction, but there are also large differences to the AEI-SAS local active isolation. A first large difference is based on the significantly more rigid structure, allowing for strongly increased loop gain. A second difference is the multiple stage configuration, where two layers of active isolation are provided within the BSC-ISI, supported by low frequency isolation of the HEPI system.

The HAM-ISI is more similar to the AEI-SAS, but still with a stronger focus on active isolation. It features one main isolation stage, like the AEI-SAS, but is still supported by the HEPI system at low frequencies. Just as with the BSC-ISI, the significantly more rigid structure allows for a strongly increased loop gain. Furthermore, it features some additional active isolation techniques, like a feedforward path.

The Virgo EIB-SAS is the most similar isolation system to the AEI-SAS in terms of its mechanical setup, with only minor differences. This results from the fact that both system designs are based on the HAM-SAS design, proposed for the Advanced LIGO seismic isolation. The key difference with respect to local active isolation is its operation in air, which requires very robust control loops in order to ensure stability. This leads to a lower extent of active isolation usage.

One aspect makes the AEI-SAS a unique system among all other seismic isolation systems. This is its exceptional global seismic isolation based on the SPI and optical levers. There is no seismic isolation system worldwide that operates a global isolation

scheme to the same extent, locking optical tables to each other over a wide frequency range and multiple degrees of freedom. The great benefits of such a control scheme lead to first efforts of the Advanced LIGO group to install similar sensors, as described in section A.5.

Appendix B

Schematics of amplifier electronics

This appendix displays the schematics of all amplifier electronics. The electronic design shown in figure B.0.1 is shared by LVDTs, accelerometers and voice-coil actuators, with some components having different values. These are listed in table B.0.1.

Table B.0.1: Component values for the LVDT, accelerometer and voice-coil actuator electronics. “np” abbreviates not populated components.

Component	Vertical LVDT or voice-coil actuator	Horizontal LVDT or voice-coil actuator	Accelerometer
r3 (Ω)	1 k	1 k	np
r6 (Ω)	200	200	50
r16 (Ω)	330	330	np
r17 (Ω)	3.3 k	1.2 k	0
r18 (Ω)	0	0	5.62 k
r19 (Ω)	np	np	301
r20 (Ω)	10 k	10 k	0
r21 (Ω)	3.01 k	14.7 k	np
r22 (Ω)	22.6	10	1325
c1 (F)	np	np	4.7 n
c5 (F)	10 n	10 n	2.2 n
c10 (F)	np	np	220 n

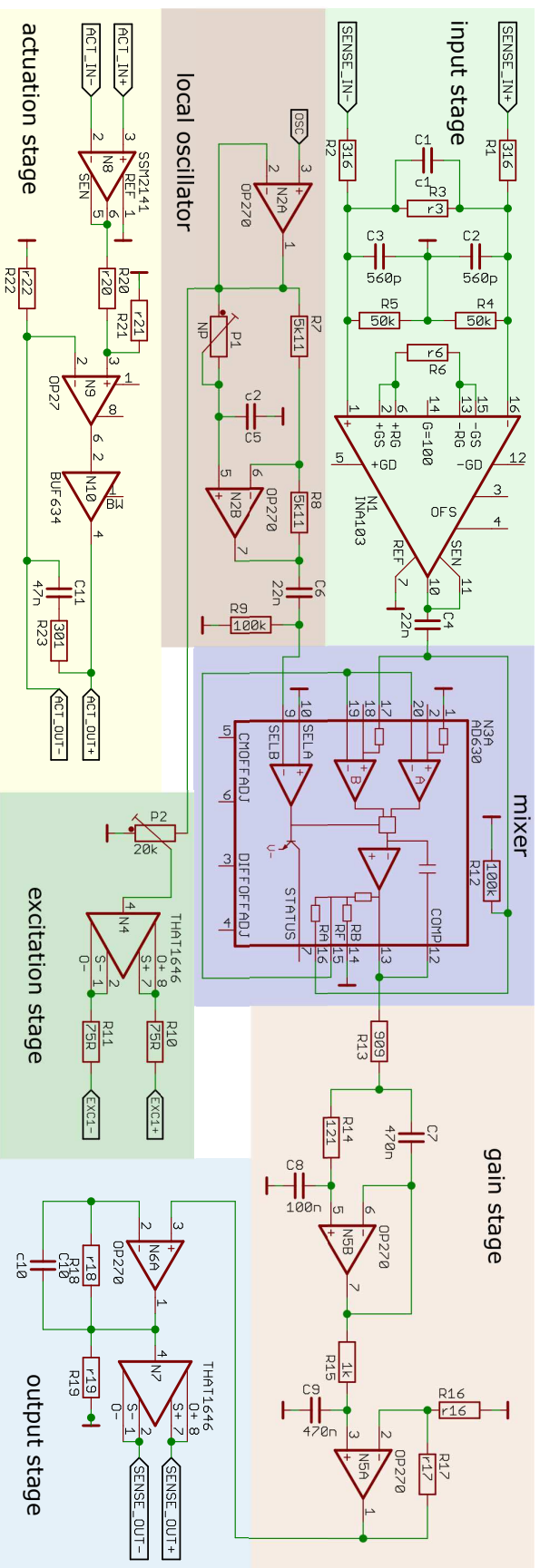


Figure B.0.1: Schematics of the vertical and horizontal LVDI, the accelerometer and the voice-coil actuator electronics. The actuation stage either provides a force-feedback signal for the accelerometers or an actuation signal for the voice-coil actuators. Diagnostic channels and power supply for amplifiers are not shown. The electronics feature an input stage, amplifying the modulated input signals. A local oscillator stage sends excitation signals via the excitation stage to the emitter coil and provides the signal for the mixer to demodulate the input signals. A gain stage and output stage prepare the signal for acquisition with CDS. Components with different values for the different devices show an “r” or “c”. They are listed in table B.0.1.

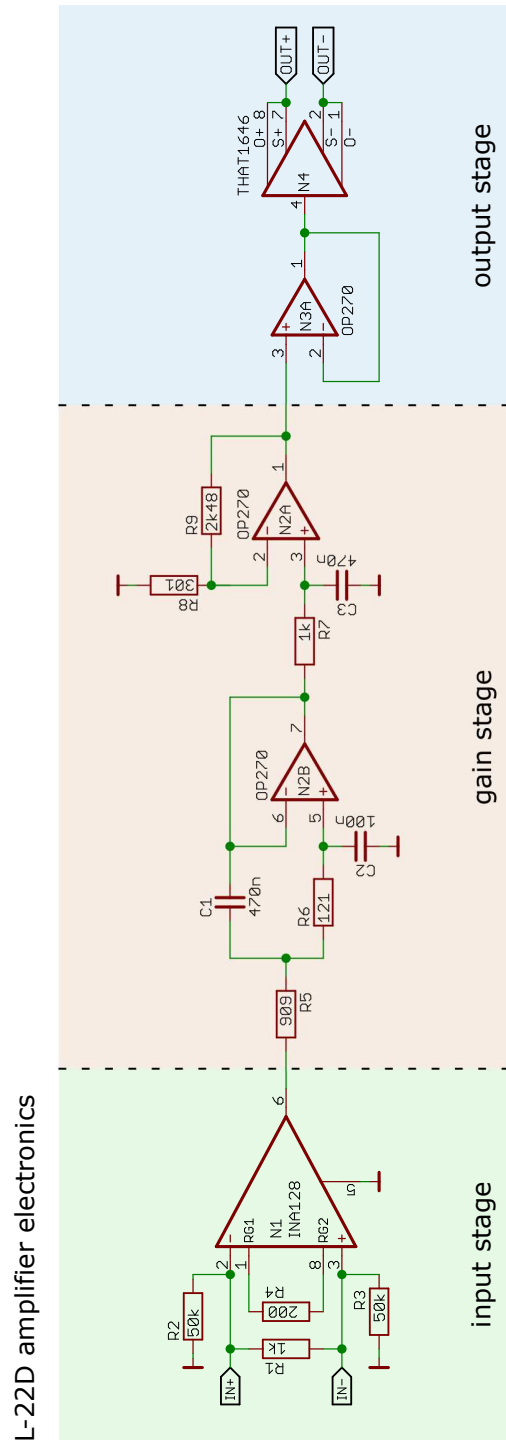


Figure B.0.2: Schematics of the L-22D amplifier electronics. Redundant components and the power supply for the amplifiers are not shown.

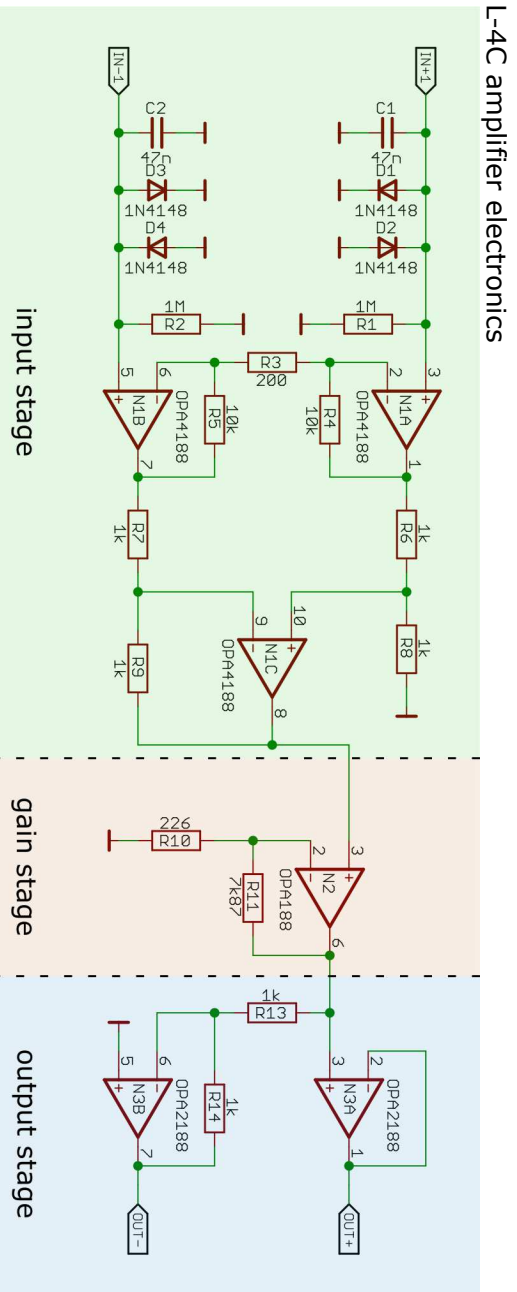


Figure B.0.3: Schematics of the L-4C amplifier electronics. Redundant components and the power supply for the amplifiers are not shown.

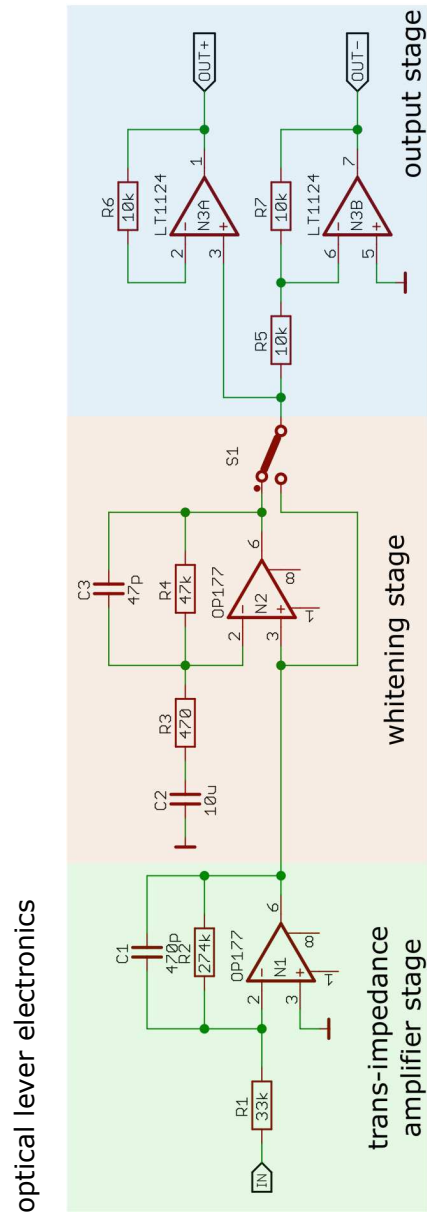


Figure B.0.4: Schematics of the optical lever amplifier electronics. Redundant components and the power supply for the amplifiers are not shown. Switch S1 can be used to activate or deactivate the whitening stage.

Appendix C

Removal of L-22D geophones

The AEI-SASs were designed to utilize L-22D geophones for vertical inertial isolation, but L-4C geophones were retrofitted to improve the sensitivity. Each L-22D geophone was installed in a heavy stainless steel chamber to provide vacuum compatibility. The chamber itself weighs about 10.5 kg each.

During installation and further planning of the AEI sub-SQL interferometer, it became evident that the available payload mass on the central AEI-SAS is scarce. Despite the fact that L-4C geophones are significantly larger than L-22D geophones, the vacuum chamber of L-4C geophones was designed to be significantly lighter, with about 1.5 kg each.

Although having lightweight L-4C chambers, possibilities to remove the L-22Ds were investigated. The L-22Ds were positioned above the GAS filters inside the optical table honey-comb structure. They were installed from the bottom through large holes during the setup of the AEI-SASs. These large holes are covered once the optical table is installed onto the intermediate plate. The vacuum chambers of the L-22Ds are too large to fit through the sides of the optical tables, even if the cans were disassembled inside the optical table.

Different possibilities for an L-22D removal were considered:

- Lifting the optical tables would require opening the 10 m prototype vacuum system, possibly increasing dirt inside. Furthermore, it would require extended realignment of all installed interferometer components and suspensions.
- To remove their mass load, the L-22D cans could be lifted inside the optical tables. This could be done from above by suspending from the vacuum system lid, or from below by utilizing a supporting structure from the baseplate through small holes. Both versions include high risk of mechanical shortcut of the optical tables to ground.
- The holes at the sides of the optical tables could be enlarged. Each L-22D has to pass two equally large holes. This requires heavy work with potential to damage suspensions and the risk of contamination of the vacuum system.

Option three was investigated in more detail. Figure C.0.1 shows the largest part of the L-22D can centered in front of the largest available hole in the honeycomb structure. The right-hand side depicts a zoom into the upper left corner, showing that only a very small cutout is required to fit the part through the hole. The total volume to be milled away is roughly 1.5 mm^3 .

It was decided to remove some material in two corners of the honey-comb structures by milling. A small box was designed that is pushed onto the stainless steel honey-comb plate. It has an adapter for a vacuum cleaner hose and an elongated hole for a milling tool. Chips produced by milling are sucked in to ensure cleanliness. The left-hand side of figure C.0.2 shows the small box attached to the outer stainless steel plate of the honey-comb structure. The right-hand side shows the milling result and the still installed L-22D geophone.

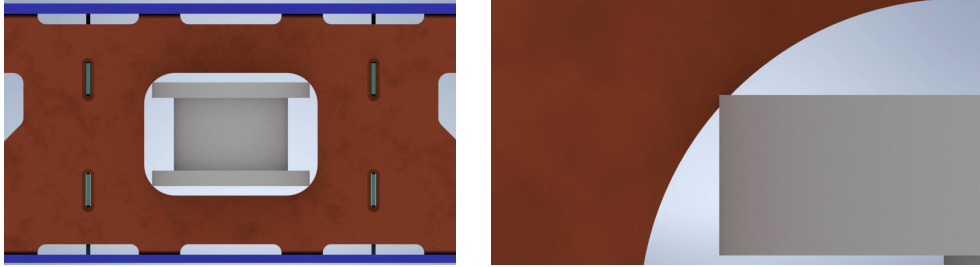


Figure C.0.1: Largest part of the L-22D vacuum can, centered in front of the largest available hole of the optical table honey-comb structure. The left drawing shows the whole part of the can, the right drawing shows a zoom into the upper left corner. It is apparent that only a small cutout is required to fit the part through the hole.

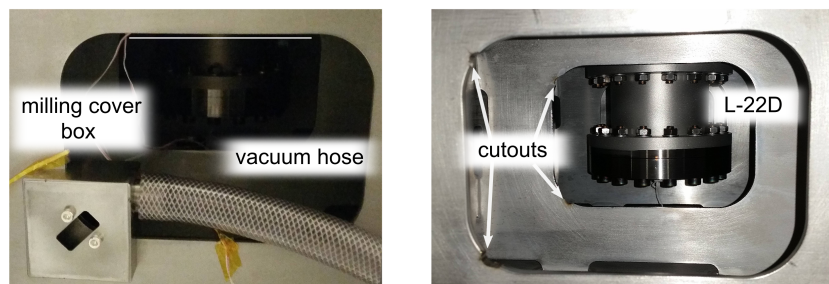


Figure C.0.2: Left: Cover box with attached vacuum hose to suck in all metal chips produced by milling. Right: Milling results with four cutouts at the lower and upper left corner of both holes inside the honey-comb structure. The L-22D is still installed inside the optical table.

The L-22D geophones of the central AEI-SAS were disassembled inside the optical table and all parts were removed. The total removed mass weighs about 32.4 kg, enabling significantly more payload from additional interferometer components to be installed. The west AEI-SAS was never equipped with L-22D geophones. The south AEI-SAS still supports all three L-22Ds. They were not removed, because it is assumed that the residual payload mass suffices. The L-22Ds can be removed following the same procedure, if unanticipated heavy interferometer components need to be installed on the south AEI-SAS in the future.

Appendix D

Positioning of L-4C geophones

Most of the sensors and actuators within the AEI-SASs were included in the AEI-SAS design phase and hence have a dedicated position, presented in section 3.4. The vertical and horizontal L-4C geophones were retrofitted in the process of commissioning, since lower noise sensors were required; hence, their positioning was constrained by all other components on the optical tables. Figure D.0.1 shows the positioning of all L-4Cs on the central, south and west AEI-SAS and gives the distances d to the x and y axes. The in-loop L-4Cs are labelled with V for vertical and H for horizontal, while witness L-4Cs are labelled with V_W and H_W .

The central AEI-SAS is not equipped with witness L-4Cs since current and future interferometer components demand the full payload mass. The south AEI-SAS is not equipped with horizontal L-4Cs, because the current operation utilizes accelerometers. If future upgrades of the seismic isolation system reduce the tilt of the optical table, horizontal L-4Cs are favorable and can be installed. This is described and motivated in section 3.9.2. The west AEI-SAS serves as a demonstrator for horizontal L-4C control schemes; hence, it is equipped with horizontal in-loop and witness L-4Cs to verify their performance.

All in-loop L-4Cs are positioned inside the optical tables in their honey-comb structures. Space is available there and interferometer components are not impaired. Only the witness L-4Cs are positioned on top of the optical tables, above the corresponding main sensors, in order to have a roughly equal transformation matrix and sensitivity.

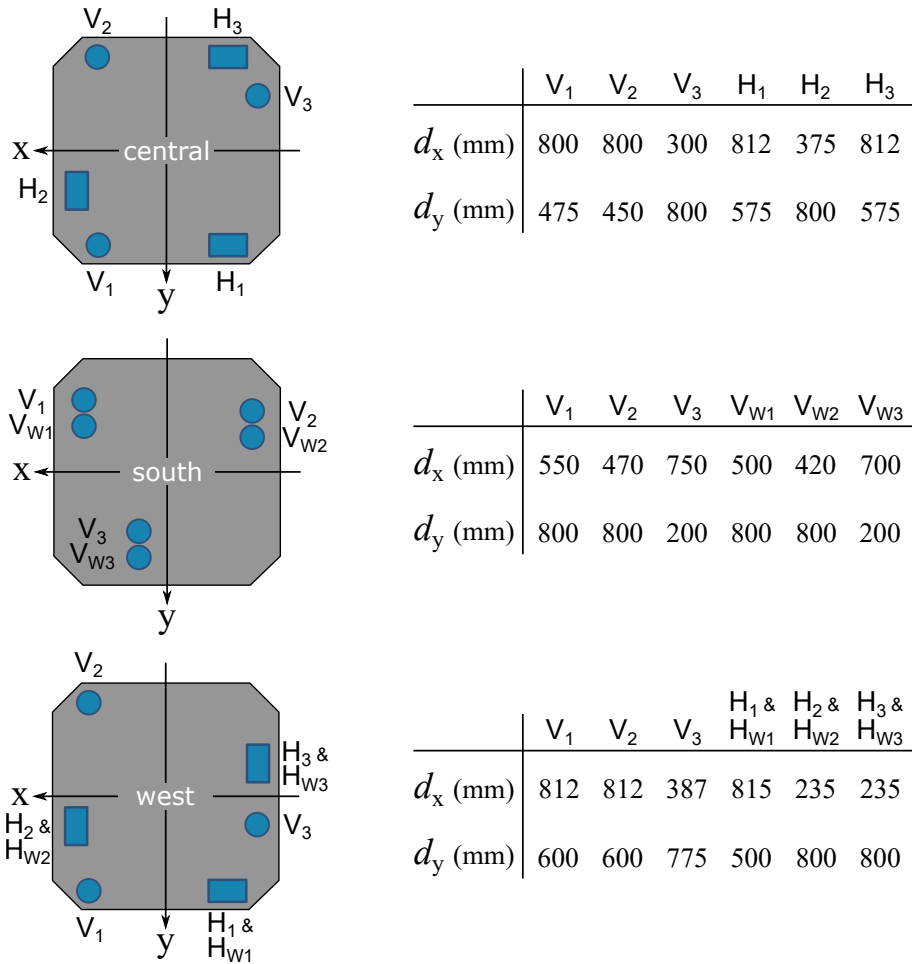


Figure D.0.1: Positioning of the L-4C geophones on all three AEI-SASs. V and H label the main sensors, while V_W and H_W label the witness sensors. The main sensors are positioned inside the optical table honey-comb structures, the witness L-4Cs are installed on top of the optical table.

Appendix E

Sensor blending filter calculation

This appendix describes the calculation of sensor blending filters. The super sensor, having an amplitude of 1, can be substituted with a polynomial expression. Numerator and denominator have the form $(\alpha + s)^{l+h-1}$, with $\alpha \in \mathbb{R}$, s being the Laplace variable and l and h being the low and high pass filter orders. This results in

$$1 = L_{lh}(s) + H_{lh}(s) = \frac{(\alpha + s)^{l+h-1}}{(\alpha + s)^{l+h-1}}, \quad (\text{E.0.1})$$

with L and H being the low and high pass filters. These are calculated exemplarily for a second order low and second order high pass. Therefore, the nominator is expanded and split into its h lower and l higher orders of s , such that

$$\begin{aligned} L_{22}(s) + H_{22}(s) &= \frac{\alpha^3 + 3\alpha^2s + 3\alpha s^2 + s^3}{(s + \alpha)^3}, \\ L_{22}(s) &= \frac{\alpha^3 + 3\alpha^2s}{(s + \alpha)^3}, \\ H_{22}(s) &= \frac{3\alpha s^2 + s^3}{(s + \alpha)^3}. \end{aligned} \quad (\text{E.0.2})$$

α is determined by evaluating the frequency response at the blending frequency $s = i\omega_b$. By definition, the low and high pass filters are equal in amplitude at the blending frequency, resulting in

$$\begin{aligned} |L_{22}(s)|_{s=i\omega_b} &= |H_{22}(s)|_{s=i\omega_b}, \\ |\alpha^3 + 3\alpha^2s|_{s=i\omega_b} &= |3\alpha s^2 + s^3|_{s=i\omega_b}, \\ (\alpha^3)^2 + (3\alpha^2\omega_b)^2 &= (3\alpha\omega_b^2)^2 + (\omega_b^3)^2. \end{aligned} \quad (\text{E.0.3})$$

The non-trivial solution of equation E.0.3 is

$$\alpha = \pm\omega_b. \quad (\text{E.0.4})$$

Hence, by setting α to the desired blending frequency, equations E.0.2 give the according second order low and high pass filters. Equation E.0.4 holds for all combinations of low and high pass filters with equal orders. For unequal order filters, an additional factor C_{lh} needs to be introduced. This is exemplarily shown for a second order low pass and third order high pass filter combination:

$$\begin{aligned} L_{23}(s) + H_{23}(s) &= \frac{\alpha^4 + 4\alpha^3s + 6\alpha^2s^2 + 4\alpha s^3 + s^4}{(s + \alpha)^4}, \\ L_{23}(s) &= \frac{\alpha^4 + 4\alpha^3s + 6\alpha^2s^2}{(s + \alpha)^4}, \\ H_{23}(s) &= \frac{4\alpha s^3 + s^4}{(s + \alpha)^4}. \end{aligned} \quad (\text{E.0.5})$$

Table E.0.1: Correction factors for the calculation of blending filters up to an order of four. The missing correction factors are calculated by $C_{lh} = (C_{hl})^{-1}$.

C_{23}	C_{24}	C_{34}
0.6896	0.5329	0.7773

To determine α , the frequency response is again evaluated at the blending frequency, resulting in

$$(\alpha^4)^2 + (4\alpha^3\omega_b)^2 + (6\alpha^2\omega_b^2)^2 = (4\alpha\omega_b^3)^2 + (\omega_b^4)^2. \quad (\text{E.0.6})$$

In this case, the non-trivial solution is

$$\alpha = \omega_b \times C_{23}, \quad (\text{E.0.7})$$

with C being a correction factor that depends on l and h . Table E.0.1 gives a list of correction factors up to a filter order of four, which were calculated numerically. The missing correction factors can be calculated by

$$C_{lh} = (C_{hl})^{-1}. \quad (\text{E.0.8})$$

Three examples of blending filter pairs are shown in section 3.7.5.

Appendix F

FINESSE script

This appendix shows the basic FINESSE script, written in the PYKAT environment, that was used for all simulations within this thesis. The script for calculating the optical gain is also provided as an example for manipulation of parameters. The calculations of transfer functions for jitter, intensity, and frequency noise follow the same principle.

- Import packages:

```
from pykat import finesse
from pykat.commands import *
import numpy as np
import matplotlib
import matplotlib.pyplot as plt
import pickle
import cmath as cm
import scipy.io as sc
from scipy import signal
from scipy.interpolate import interp1d
```

- Set a list of laser input powers "pwr" and a dark fringe offset "DF_off" in units of meters, which is afterwards calibrated to degrees:

```
pwr = [0.5, 3, 10]
DF_off = 10e-12
DF_offset = DF_off/(1064e-9)*360
```

- Basic FINESSE script defining the interferometer:

```
base_michelson = finesse.kat()
base_code = """

# define laser
l laser 10 0 n0
gauss gauss1 IMC nIMCrefl 386.11e-6 34.84m
s sltoIMC 1 n0 nIMCin

# define input path
bs1 IMC 0 0 0 0 nIMCin nIMCrefl n1 n2
s sIMCtoSM0 10.912 nIMCrefl nSM0in
bs1 SM0 0 0 0 4 nSM0in nSM0refl n3 n4
attr SM0 Rc 8
s sSM0toSM1 10.329 nSM0refl nSM1in
bs1 SM1 0 0 0 4 nSM1in nSM1refl n5 n6
attr SM1 Rc 8
s sSM1toSM2 11 nSM1refl nSM2in
bs1 SM2 0 0 0 45 nSM2in nSM2refl n7 n8
```

```

s sSM2toBS 0.4 nSM2refl nBSin

# define beam splitter
bs1 BS 0.5 15u 0 45 nBSin nBSX nBSY nBSDP
attr BS mass 1.5 zmech sus3long
attr BS Ix 15u rxmech sus3pitch
attr BS Iy 15u rymech sus3yaw

# define x-arm
s sBStoITMX 525m nBSX nITMXARin
m2 ITMXAR 0 0 0 nITMXARin nITMXARout
attr ITMXAR Rc -1776m
s sITMXARtoITMXHR 24.46m $nsilica nITMXARout nITMXHRin
m1 ITMXHR 8220u 15u 0 nITMXHRin nITMXHRout
attr ITMXHR Rc -5700m
attr ITMXHR mass 0.1
attr ITMXHR zmech sus3long
attr ITMXHR Ix 15u
attr ITMXHR rxmech sus3yaw
attr ITMXHR Iy 15u
attr ITMXHR rymech sus3pitch
s sXarm 11.3673 nITMXHRout nETMXin
m1 ETMX 15u 0 0 nETMXin nETMXout
attr ETMX Rc 5700m
attr ETMX mass 0.1
attr ETMX zmech sus3long
attr ETMX Ix 15u
attr ETMX rxmech sus3yaw
attr ETMX Iy 15u
attr ETMX rymech sus3pitch

# define y-arm
s sBStoITMY 475m nBSY nITMYARin
m2 ITMYAR 0 0 0 nITMYARin nITMYARout
attr ITMYAR Rc -1776m
s sITMYARtoITMYHR 24.46m $nsilica nITMYARout nITMYHRin
m1 ITMYHR 8220u 15u 0 nITMYHRin nITMYHRout
attr ITMYHR Rc -5700m
attr ITMYHR mass 0.1
attr ITMYHR zmech sus3long
attr ITMYHR Ix 15u
attr ITMYHR rxmech sus3yaw
attr ITMYHR Iy 15u
attr ITMYHR rymech sus3pitch
s sYarm 11.3673 nITMYHRout nETMYin
m1 ETMY 15u 0 0 nETMYin nETMYout
attr ETMY Rc 5700m
attr ETMY mass 0.1
attr ETMY zmech sus3long
attr ETMY Ix 15u
attr ETMY rxmech sus3yaw
attr ETMY Iy 15u
attr ETMY rymech sus3pitch

# define dark port
s sDP 1 nBSDP nDP

```

```

# define suspension transfer functions, arm cavities, maximum TEM-
order and the diffraction coefficient of fused silica
tf2 sus3long 1 0 0.0628,0.1+4.65i 0.000628
tf2 sus3yaw 1 0 0.1+1.225i,1.885 0.000628
tf2 sus3pitch 1 0 0.1+1.225i,1.885 0.000628
cav cavXARM ITMXHR nITMXHRout ETMX nETMXin
cav cavYARM ITMYHR nITMYHRout ETMY nETMYin
maxtem 4
const nsilica 1.449631

"""
base_michelson.parse(base_code)

```

- Simulate the optical gain for the three laser input powers. The mass and moment of inertia of the mirrors is set to a high value to eliminate the influence of mirror dynamics:

```

detector_michelson = deepcopy(base_michelson)
opt_gain = np.zeros(len(pwr),dtype=object)

detector_michelson.ITMXHR.mass = 1000000
detector_michelson.ITMYHR.mass = 1000000
detector_michelson.ETMX.mass = 1000000
detector_michelson.ETMY.mass = 1000000
detector_michelson.ITMXHR.Ix = 1000000
detector_michelson.ITMYHR.Iy = 1000000
detector_michelson.ETMX.Ix = 1000000
detector_michelson.ETMY.Iy = 1000000
detector_michelson.ITMXHR.Ix = 1000000
detector_michelson.ITMYHR.Iy = 1000000
detector_michelson.ETMX.Ix = 1000000
detector_michelson.ETMY.Iy = 1000000
detector_michelson.ITMXHR.phi = 90
detector_michelson.ETMX.phi = 90 + DF_offset/2
detector_michelson.ETMY.phi = 0 - DF_offset/2

for i in range(len(pwr)):
    detector_michelson.laser.P = pwr[i]
    detector_code = """

# define photodiode
fsig sig sXarm phase 1 0
pd1 pd.00 1 nDP
mask pd.00 0 1 0
mask pd.00 1 0 0
mask pd.00 1 1 0
mask pd.00 2 0 0
mask pd.00 0 2 0
mask pd.00 2 1 0
mask pd.00 1 2 0
mask pd.00 2 2 0
mask pd.00 3 0 0
mask pd.00 3 1 0
mask pd.00 1 3 0
mask pd.00 0 3 0
put pd.00 f1 $x1

# execute simulation

```

```
    xaxis* sig f log 0.1 10000 1000
    yaxis log abs:deg
    """

    detector_michelson.parse(detector_code)
    opt_gain[i] = detector_michelson.run()
```

Bibliography

- [A⁺02] M Ando et al. Current status of TAMA. *Classical and Quantum Gravity*, 19(7):1409, March 2002. doi:10.1088/0264-9381/19/7/324.
- [A⁺07] F Acernese et al. Status of Virgo detector. *Classical and Quantum Gravity*, 24(19):S381, September 2007. doi:10.1088/0264-9381/24/19/S01.
- [A⁺09] B P Abbott et al. LIGO: the laser interferometer gravitational-wave observatory. *Reports on Progress in Physics*, 72(7):076901, June 2009. doi:10.1088/0034-4885/72/7/076901.
- [A⁺10a] T. Accadia et al. Noise from scattered light in Virgo's second science run data. *Classical and Quantum Gravity*, 27(19):194011, 2010. URL: <https://doi.org/10.1088/0264-9381/27/19/194011>.
- [A⁺10b] F Acernese et al. Measurements of Superattenuator seismic isolation by Virgo interferometer. *Astroparticle Physics*, 33(3):182–189, April 2010. doi:10.1016/j.astropartphys.2010.01.006.
- [A⁺12] S M Aston et al. Update on quadruple suspension design for Advanced LIGO. *Classical and Quantum Gravity*, 29(23):235004, October 2012. doi:10.1088/0264-9381/29/23/235004.
- [A⁺13] Y Aso et al. Interferometer design of the KAGRA gravitational wave detector. *Physical Review D*, 88(4):043007, August 2013. doi:10.1103/PhysRevD.88.043007.
- [A⁺14] F Acernese et al. Advanced Virgo: a second-generation interferometric gravitational wave detector. *Classical and Quantum Gravity*, 32(2):024001, December 2014. doi:10.1088/0264-9381/32/2/024001.
- [A⁺15] J Aasi et al. Advanced LIGO. *Classical and Quantum Gravity*, 32(7):074001, March 2015. doi:10.1088/0264-9381/32/7/074001.
- [A⁺16a] B P Abbott et al. Improved analysis of GW150914 using a fully spin-precessing waveform model. *Physical Review X*, 6(4):041014, October 2016. doi:10.1103/PhysRevX.6.041014.
- [A⁺16b] B P Abbott et al. Observation of gravitational waves from a binary black hole merger. *Physical Review Letters*, 116(6):061102, February 2016. doi:10.1103/PhysRevLett.116.061102.
- [A⁺16c] T Akutsu et al. Vacuum and cryogenic compatible black surface for large optical baffles in advanced gravitational-wave telescopes. *Optical Materials Express*, 6(5):1613–1626, May 2016. doi:10.1364/OME.6.001613.
- [A⁺17a] B P Abbott et al. GW170817: Observation of gravitational waves from a binary neutron star inspiral. *Physical Review Letters*, 119(16):161101, October 2017. doi:10.1103/PhysRevLett.119.161101.

- [A⁺17b] B P Abbott et al. Multi-messenger observations of a binary neutron star merger. *The Astrophysical Journal Letters*, 848(2), October 2017. doi:10.3847/2041-8213/aa91c9.
- [A⁺19a] B P Abbott et al. GWTC-1: A gravitational-wave transient catalog of compact binary mergers observed by LIGO and Virgo during the first and second observing runs. *Physical Review X*, 9(3):031040, September 2019. doi:10.1103/PhysRevX.9.031040.
- [A⁺19b] Y Akiyama et al. Vibration isolation system with a compact damping system for power recycling mirrors of KAGRA. *Classical and Quantum Gravity*, 36(9):095015, April 2019. doi:10.1088/1361-6382/ab0fcb.
- [A⁺20a] R Abbott et al. GW190521: A binary black hole merger with a total mass of 150 solar masses. *Physical Review Letters*, 125(10):101102, September 2020. doi:10.1103/PhysRevLett.125.101102.
- [A⁺20b] R Abbott et al. Properties and astrophysical implications of the 150 solar mass binary black hole merger GW190521. *The Astrophysical Journal letters*, 900(1):L13, September 2020. doi:10.3847/2041-8213/aba493.
- [A⁺20c] R X Adhikari et al. A cryogenic silicon interferometer for gravitational-wave detection. *Classical and Quantum Gravity*, 37(16):165003, July 2020. doi:10.1088/1361-6382/ab9143.
- [A⁺21a] R Abbott et al. GWTC-2: Compact binary coalescences observed by LIGO and Virgo during the first half of the third observing run. *arXiv:2010.14527v3 [gr-qc]*, March 2021. URL: <https://arxiv.org/abs/2010.14527>.
- [A⁺21b] T Akutsu et al. Vibration isolation systems for the beam splitter and signal recycling mirrors of the KAGRA gravitational wave detector. *Classical and Quantum Gravity*, 38(6):065011, March 2021. doi:10.1088/1361-6382/abd922.
- [AC00] A Abramovici and J Chapsky. *Feedback Control Systems - A Fast-Track Guide for Scientists and Engineers*. Springer, 2000. doi:10.1007/978-1-4615-4345-9.
- [Ady18] V Adya. *Ways to stop mirrors from moving unnecessarily: design of advanced gravitational wave detectors*. PhD thesis, Leibniz Universität Hannover, 2018. doi:10.15488/3430.
- [AG95] Streckeisen AG. *Portable Very-Broad-Band Tri-Axial Seismometer*, May 1995. URL: https://www.pascal.nmt.edu/webfm_send/488.
- [AHO99] B Allen, W Hua, and A Ottewill. Automatic cross-talk removal from multi-channel data. *arXiv:gr-qc/9909083*, September 1999. URL: <https://arxiv.org/abs/gr-qc/9909083>.
- [Ali13] Thimotheus Alig. Charakterisierung und unterdrückung der strahlgeometriefluktuationen des fasergekoppelten 35 W lasers für das AEI 10 m prototypinterferometer. Master's thesis, Leibniz Universität Hannover, 2013.
- [Ana07] Analog Devices. Datasheet - SSM2141 high common-mode rejection differential line receiver, 2007. review C. URL: <https://www.analog.com/media/en/technical-documentation/data-sheets/SSM2141.pdf>.
- [Ana15] Analog Devices. Datasheet - OP270 operational amplifier, 2001-2015. URL: <https://www.analog.com/media/en/technical-documentation/data-sheets/OP270.pdf>.

- [Ana16a] Analog Devices. Datasheet - OP177 operational amplifier, 1995-2016. URL: <https://www.analog.com/media/en/technical-documentation/data-sheets/OP177.pdf>.
- [Ana16b] Analog Devices. Datasheet - AD630 balanced modulator/demodulator, 2015-2016. URL: <https://www.analog.com/media/en/technical-documentation/data-sheets/AD630.pdf>.
- [And84] D Z Anderson. Alignment of resonant optical cavities. *Applied Optics*, 23(17):2944–2949, September 1984. doi:10.1364/AO.23.002944.
- [AS⁺17] P Amaro-Seoane et al. Laser interferometer space antenna. *arXiv:1702.00786 [astro-ph.IM]*, February 2017. URL: <https://arxiv.org/abs/1702.00786>.
- [B⁺97] M Beccaria et al. Extending the VIRGO gravitational wave detection band down to a few hz: metal blade springs and magnetic antisprings. *Nuclear Instruments and Methods in Physics Research A*, 394(3):397–408, July 1997. doi:10.1016/S0168-9002(97)00661-X.
- [B⁺05] S Braccini et al. Measurement of the seismic attenuation performance of the VIRGO Superattenuator. *Astroparticle Physics*, 23(6):557–565, July 2005. doi:10.1016/j.astropartphys.2005.04.002.
- [B⁺17] G Bergmann et al. Passive-performance, analysis, and upgrades of a 1-ton seismic attenuation system. *Classical and Quantum Gravity*, 34(6):065002, February 2017. doi:10.1088/1361-6382/aa5e1f.
- [B⁺20] A Buikema et al. Sensitivity and performance of the Advanced LIGO detectors in the third observing run. *Physical Review D*, 102(6):062003, September 2020. doi:10.1103/PhysRevD.102.062003.
- [BABH01] R. Bork, R. Abbott, D. Barker, and J. Heefner. An overview of the LIGO control and data acquisition system. *arXiv:physics/0111077 [physics.ins-det]*, 2001. URL: <https://arxiv.org/abs/physics/0111077>.
- [Bar15] S Barke. *Inter-spacecraft frequency distribution for future gravitational wave observatories*. PhD thesis, Gottfried Wilhelm Leibniz Universität Hannover, 2015. doi:10.15488/8405.
- [Bar18] L Barsotti. The A+ upgrade for Advanced LIGO. In *Bulletin of the American Physical Society*, 2018. URL: <http://meetings.aps.org/link/BAPS.2018.APR.S14.2>.
- [BBB⁺13] M R Blom, M G Beker, A Bertolini, J F J van den Brand, H J Bulten, E Hennes, F A Mul, D S Rabeling, and A Schimmel. Seismic attenuation system for the external injection bench of the Advanced Virgo gravitational wave detector. *Nuclear Instruments and Methods in Physics Research Section A*, 718:466–470, 2013. doi:10.1016/j.nima.2012.11.108.
- [BBb⁺15] M R Blom, M G Beker, A bertolini, J F J van den Brand, H J Bulten, M Doets, E Hennes, F A Mul, D S Rabeling, and A Schimmel. Vertical and horizontal seismic isolation performance of the Advanced Virgo external injection bench seismic attenuation system. *Physics Procedia*, 61:641–647, 2015. doi:10.1016/j.phpro.2014.12.064.
- [BBFS17] C Bond, D Brown, A Freise, and K Strain. Interferometer techniques for gravitational-wave detection. *Living Reviews in Relativity*, 19(3), February 2017. doi:10.1007/s41114-016-0002-8.

- [BBv⁺12] M G Beker, M Blom, J F J van den Brand, H J Bulten, E Hennes, and D S Rabeling. Seismic attenuation technology for the Advanced Virgo gravitational wave detector. *Physics Procedia*, 37:1389–1397, October 2012. doi:10.1016/j.phpro.2012.03.741.
- [BDF⁺05] A. Bertolini, R. DeSalvo, F. Fidecaro, M. Francesconi, S. Marka, V. Sannibale, D. Simonetti, A. Takamori, and H. Tariq. Mechanical design of a single-axis monolithic accelerometer for advanced seismic attenuation systems. *Nuclear Instruments and Methods in Physics Research Section A*, 556(2):616–623, January 2005. doi:10.1016/j.nima.2005.10.117.
- [BDG⁺06] A Bertolini, R DeSalvo, C Galli, G Gennaro, M Mantovani, S Márka, V Sannibale, A Takamori, and C Torrie. Design and prototype tests of a seismic attenuation system for the advanced-LIGO output mode cleaner. *Classical and Quantum Gravity*, 23(8):S111, March 2006. doi:10.1088/0264-9381/23/8/S15.
- [Bek13] M G Beker. *Low-frequency sensitivity of next generation gravitational wave detectors*. PhD thesis, Vrije Universiteit Amsterdam, June 2013. URL: <https://s3.cern.ch/inspire-prod-files-c/c7e5547b789925aa0b82bea7d78c20c5>.
- [Ber01] A Bertolini. *High sensitivity accelerometers for gravity experiments*. PhD thesis, University of Pisa, 2001. URL: <http://citeseerx.ist.psu.edu/viewdoc/download?doi=10.1.1.383.8784&rep=rep1&type=pdf>.
- [Ber18] G Bergmann. *Improving the seismic isolation for the AEI 10 m prototype*. PhD thesis, Leibniz Universität Hannover, 2018. doi:10.15488/3329.
- [BF14] D D Brown and A Freise. FINESSE - download. Zenodo, May 2014. doi:10.5281/zenodo.821364.
- [BJR⁺20] D D Brown, P Jones, S Rowlinson, S Leavey, A C Green, D Töyrä, and A Freise. PYKAT: Python package for modelling precision optical interferometers. *SoftwareX*, 12:100613, December 2020. doi:10.1016/j.softx.2020.100613.
- [BMP⁺99] A Bernardini, E Majorana, P Puppo, P Rapagnani, F Ricci, and G Testi. Suspension last stages for the mirrors of the Virgo interferometric gravitational wave antenna. *Review of Scientific Instruments*, 70(8):3463, May 1999. doi:10.1063/1.1149938.
- [BMR⁺79] H Billing, K Maischberger, A Rüdiger, R Schilling, L Schnupp, and W Winkler. An argon laser interferometer for the detection of gravitational radiation. *Journal of Physics E: Scientific Instruments*, 12(11):1043, 1979. doi:10.1088/0022-3735/12/11/010.
- [BP10] J Bendat and A Piersol. *Random data : analysis and measurement procedures*. John Wiley & Sons, 4 edition, September 2010. URL: <https://www.wiley.com/en-us/RandomData:AnalysisandMeasurementProcedures,4thEdition-p-9781118210826>.
- [Bro16] D D Brown. *Interactions of light and mirrors: Advanced techniques for modelling future gravitational wave detectors*. PhD thesis, University of Birmingham, 2016. URL: <https://etheses.bham.ac.uk//id/eprint/6500/>.
- [BWS⁺81] H Billing, W Winkler, R Schilling, A Rüdiger, K Maischberger, and L Schnupp. *Quantum Optics, Experimental Gravitation and Measurement Theory*, volume 94 of *NATO Advanced Science Institutes Series*, chapter The Munich Gravitational Wave Detector Using

- Laser Interferometry, pages 533–543. Springer, 1981. doi:10.1007/978-1-4613-3712-6_23.
- [BYZ17] G Billingsley, H Yamamoto, and L Zhang. Characterization of the Advanced LIGO core optics. Technical report, LIGO Laboratory, 2017. URL: <https://dcc.ligo.org/LIGO-P1700029/public>.
- [C⁺12] A V Cumming et al. Design and development of the advanced LIGO monolithic fused silica suspension. *Classical and Quantum Gravity*, 29(3):035003, January 2012. doi:10.1088/0264-9381/29/3/035003.
- [CAC⁺12] L Carbone, S M Aston, R M Cutler, A Freise, J Greenhalgh, J Heefner, D Hoyland, N A Lockerbie, D Lodhia, N A Robertson, C C Speake, K A Strain, and A Vecchio. Sensors and actuators for the Advanced LIGO mirror suspensions. *Classical and Quantum Gravity*, 29(11):115005, May 2012. doi:10.1088/0264-9381/29/11/115005.
- [CCG⁺18] S J Cooper, C J Collins, A C Green, D Hoyland, C C Speake, A Freise, and C M Mow-Lowry. A compact, large-range interferometer for precision measurement and inertial sensing. *Classical and Quantum Gravity*, 35(9):095007, March 2018. doi:10.1088/1361-6382/aab2e9.
- [CCT⁺20] J J Carter, S J Cooper, E Thrift, J Briggs, J Warner, M P Ross, and C M Mow-Lowry. Particle swarming of sensor correction filters. *Classical and Quantum Gravity*, 37(20):205009, September 2020. doi:10.1088/1361-6382/abb32a.
- [CG52] H B Callen and R F Greene. On a theorem of irreversible thermodynamics. *Physical Review Journals Archive*, 86(5):702, June 1952. doi:10.1103/PhysRev.86.702.
- [CJFC⁺12] C Collette, S Janssens, P Fernandez-Carmona, K Artoos, M Guinchard, C Hauviller, and P Preumont. Review: Inertial sensors for low-frequency seismic vibration measurement. *Bulletin of the Seismological Society of America*, 102(4):1289–1300, August 2012. doi:10.1785/0120110223.
- [CM04] T Corbitt and N Mavalvala. Review: Quantum noise in gravitational-wave interferometers. *Journal of Physics B: Quantum and Semiclassical Optics*, 6(8):S675, July 2004. doi:10.1088/1464-4266/6/8/008.
- [Coo19] S J Cooper. *Breaking the seismic wall: how to improve gravitational wave detectors at low frequency*. PhD thesis, University of Birmingham, 2019. URL: <http://etheses.bham.ac.uk/id/eprint/9903>.
- [CW51] H B Callen and T A Welton. Irreversibility and generalized noise. *Physical Review Journals Archive*, 83(1):34, July 1951. doi:10.1103/PhysRev.83.34.
- [CZM⁺13] G D Cole, W Zhang, M J Martin, J Ye, and M Aspelmeyer. Tenfold reduction of brownian noise in high-reflectivity optical coatings. *Nature Photonics*, 7(8):644–650, July 2013. doi:10.1038/nphoton.2013.174.
- [D⁺15] K L Dooley et al. Status of GEO 600. *Journal of Physics: Conference Series*, 610:012015, 2015. doi:10.1088/1742-6596/610/1/012015.
- [Dah13] K Dahl. *From design to operation: a suspension platform interferometer for the AEI 10 m prototype*. PhD thesis, Leibniz Universität Hannover, 2013. doi:10.15488/8033.
- [DDA⁺12] R DeRosa, J C Driggers, D Atkinson, H Miao, V Frolov, M Landry, J A Giaime, and R X Adhikari. Global feed-forward vibration isolation in a km scale interferometer. *Classical and Quantum Gravity*, 29(21):215008, October 2012. doi:10.1088/0264-9381/29/21/215008.

- [DDG⁺87] R Del Fabbro, A Di Virgilio, A Giazotto, H Kautzky, V Montelatici, and D Passuello. Three-dimensional seismic super-attenuator for low frequency gravitational wave detection. *Physics Letters A*, 124(4-5):253–257, July 1987. doi:10.1016/0375-9601(87)90632-3.
- [DeR14] R T DeRosa. *Performance of Active Vibration Isolation in the Advanced LIGO Detectors*. PhD thesis, Louisiana State University and Agricultural and Mechanical College, December 2014. URL: https://digitalcommons.lsu.edu/gradschool_dissertations/3464/.
- [DHW⁺12] K Dahl, G Heinzl, B Willke, K A Strain, S Goßler, and K Danzmann. Suspension platform interferometer for the AEI 10 m prototype: concept, design and optical layout. *Classical and Quantum Gravity*, 29(9):095024, April 2012. doi:10.1088/0264-9381/29/9/095024.
- [DiF20a] C DiFronzo. Reducing differential motion of Advanced LIGO seismic platforms to improve interferometer control signals: analysis of feasibility. Internal dokument, University of Birmingham, June 2020. URL: <https://dcc.ligo.org/LIGO-T2000365>.
- [DiF20b] C DiFronzo. Reducing differential motion of Advanced LIGO seismic platforms to improve interferometer control signals: block diagrams and maths. Internal dokument, University of Birmingham, February 2020. URL: <https://dcc.ligo.org/LIGO-T2000108>.
- [Din21] B Ding. *Development of High Resolution Interferometric Inertial Sensors*. PhD thesis, Vrije Universiteit Brussels, January 2021. URL: <http://hdl.handle.net/2013/ULB-DIPOT:oai:dipot.ulb.ac.be:2013/317532>.
- [DK12] S L Danilishin and F Y Khalili. Quantum measurement theory in gravitational-wave detectors. *Living Reviews in Relativity*, 15(5), April 2012. doi:10.12942/lrr-2012-5.
- [DPPS20] R DeSalvo, G Pelosi, I M Pinto, and S Selleri. Stepped beam pipes and helical baffles for scattered light absorption in future gravitational wave detectors. *Review of Scientific Instruments*, 91(5):054505, May 2020. doi:10.1063/1.5144862.
- [DR03] K Danzmann and A Rüdiger. LISA technology - concept, status, prospects. *Classical and Quantum Gravity*, 20(10):S1, April 2003. doi:10.1088/0264-9381/20/10/301.
- [EG] F Elavsky and A Geller. Masses in the stellar graveyard. Visualization: LIGO -Virgo / Frank Elavsky, Aaron Geller / Northwestern. URL: <https://media.ligo.northwestern.edu/gallery/mass-plot>.
- [Ein16] A Einstein. Die grundlage der allgemeinen relativitätstheorie. *Annalen der Physik*, 354(7):769–822, 1916. doi:10.1002/andp.19163540702.
- [ET 20] ET Steering Committee Editorial Team. Design report update 2020 for the Einstein Telescope. Technical report, 2020. URL: <https://apps.et-gw.eu/tds/q1/?c=15418>.
- [F⁺16] Y Fujii et al. Active damping performance of the KAGRA seismic attenuation system prototype. *Journal of Physics: Conference Series*, 716:012022, May 2016. doi:10.1088/1742-6596/716/1/012022.
- [Fai09] S Fairhurst. Triangulation of gravitational wave sources with a network of detectors. *New Journal of Physics*, 11:123006, December 2009. doi:10.1088/1367-2630/11/12/123006.

- [Fai11a] S Fairhurst. Improved source localization with LIGO-India. *Journal of Physics: Conference Series*, 484:012007, 2011. doi:10.1088/1742-6596/484/1/012007.
- [Fai11b] S Fairhurst. Source localization with an advanced gravitational wave detector network. *Classical and Quantum Gravity*, 28(10):105021, April 2011. doi:10.1088/0264-9381/28/10/105021.
- [FHL⁺04] A Freise, G Heinzl, H Lück, R Schilling, B Willke, and K Danzmann. Frequency-domain interferometer simulation with higher-order spatial modes. *Classical and Quantum Gravity*, 21(5):S1067, February 2004. doi:10.1088/0264-9381/21/5/102.
- [Fis17] P J Fish. *Electronic Noise and Low Noise Design*. Macmillan new electronics series. Macmillan International Higher Education, March 2017. URL: <https://books.google.de/books?id=-EldDwAAQBAJ>.
- [FMF⁺09] J Franc, N Morgado, R Flaminio, R Nawrodt, I Marin, L Cunningham, A Cumming, S Rowan, and J Hough. Mirror thermal noise in laser interferometer gravitational wave detectors operating at room and cryogenic temperature. *arXiv: 0912.0107 [gr-qc]*, (ET-02109), December 2009. URL: <https://arxiv.org/abs/0912.0107>.
- [FSW⁺07] M Frede, B Schulz, R Wilhelm, P Kwee, F Seifert, B Willke, and D Kracht. Fundamental mode, single-frequency laser amplifier for gravitational wave detectors. *Optics Express*, 15(2):459–465, 2007. doi:10.1364/OE.15.000459.
- [FTW95] I Freitag, A Tünnermann, and H Welling. Power scaling of diode-pumped monolithic Nd:YAG lasers to output powers of several watts. *Optics Communications*, 115(5-6):511–515, April 1995. doi:10.1016/0030-4018(95)00020-9.
- [Fuj19] Y Fujii. *Fast localization of coalescing binaries with gravitational wave detectors and low frequency vibration isolation for KAGRA*. PhD thesis, Institute for Cosmic Ray Research - University of Tokyo, 2019. URL: <https://gwdoc.icrr.u-tokyo.ac.jp/cgi-bin/DocDB/ShowDocument?docid=11137&version=4>.
- [G⁺16] H Grote et al. High power and ultra-low-noise photodetector for squeezed-light enhanced gravitational wave detectors. *Optics Express*, 24(18):20107–20118, 2016. doi:10.1364/OE.24.020107.
- [G⁺20] M Granata et al. Amorphous optical coatings of present gravitational-wave interferometers. *Classical Quantum Gravity*, 37(9):095004, April 2020. doi:10.1088/1361-6382/ab77e9.
- [GI21] O Gerberding and K.-S. Isleif. Ghost beam suppression in deep frequency modulation interferometry for compact on-axis optical heads. *MDPI - sensors*, 21(5):1708, March 2021. doi:10.3390/s21051708.
- [Gon00] G Gonzalez. Suspensions thermal noise in the LIGO gravitational wave detector. *Classical Quantum Gravity*, 17(21):4409–2235, November 2000. doi:10.1088/0264-9381/17/21/305.
- [Gor08] M L Gorodetsky. Thermal noises and noise compensation in high-reflection multilayer coating. *arXiv: 0809.0438 [cond-mat.mtrl-sci]*, September 2008. doi:10.1016/j.physleta.2008.09.056.
- [Gor15] N A Gordon. *Characterisation and control of coupled optical springs for future gravitational wave detector*. PhD thesis, University of Glasgow, 2015. URL: <http://theses.gla.ac.uk/id/eprint/6532>.

- [Goß04] Stefan Goßler. *The suspension systems of the interferometric gravitational-wave detector GEO 600*. PhD thesis, Leibniz Universität Hannover, 2004. doi:10.15488/6350.
- [Gro] H Grote. personal communication.
- [gwi] Gravitational wave interferometer noise calculator - download. GitLab. URL: <https://git.ligo.org/gwinc>.
- [H⁺04a] C Hardham et al. Multi-DOF isolation and alignment with quiet hydraulic actuators, 2004. URL: http://www.faludidesign.com/work/publications/Hardham_2004--Multi-DOF_Isolation_and_Alignment_with_Quiet_Hydraulic_Actuators.pdf.
- [H⁺04b] G Heinzel et al. The LTP interferometer and phasemeter. *Classical and Quantum Gravity*, 21(5):S581, February 2004. doi:10.1088/0264-9381/21/5/029.
- [H⁺09] S Hild et al. DC-readout of a signal-recycled gravitational wave detector. *Classical and Quantum Gravity*, 26(5):055012, February 2009. doi:10.1088/0264-9381/26/5/055012.
- [HAD⁺01] C T Hardham, G S Allen, D B DeBra, B Dan, W Hua, B T Lantz, and J G Nichol. Quiet hydraulic actuators for the laser interferometer gravitational wave observatory (LIGO), 2001.
- [Han18] M Hanke. *Laser frequency stabilization for the sub-SQL interferometer*. PhD thesis, Leibniz Universität Hannover, 2018. doi:10.15488/3895.
- [Hei83] W Heisenberg. *Quantum Theory and Measurement*, chapter The Physical Content of Quantum Kinematics and Mechanics, pages 62–84. Princeton Series in Physics, 1983.
- [HHP14] G Hammond, S Hild, and M Pitkin. Advanced technologies for future ground-based, laser-interferometric gravitational wave detectors. *Journal of Modern Physics*, 61(sup1):S10–S45, February 2014. doi:10.1080/09500340.2014.920934.
- [Hoy16] David Hoyland. Op-amp noise test results. Technical report, University of Birmingham, 2016. URL: <https://dcc.ligo.org/LIGO-T1600206/public>.
- [HSKT14] E Hirose, T Sekiguchi, R Kumar, and R Takahashi. Update on the development of cryogenic sapphire mirrors and their seismic attenuation system for KAGRA. *Classical and Quantum Gravity*, 31(22):224004, November 2014. doi:10.1088/0264-9381/31/22/224004.
- [HT75] R A Hulse and J H Taylor. Discovery of a pulsar in a binary system. *Astrophysical Journal*, 195:L51–L53, January 1975. doi:10.1086/181708.
- [Hua05] Wensheng Hua. *Low Frequency Vibration Isolation and Alignment System for Advanced LIGO*. PhD thesis, Stanford University, June 2005. URL: https://labcit.ligo.caltech.edu/~rana/docs/Theses/hua_thesis.pdf.
- [Ins] Geotech Instruments. datasheet - GS13. URL: <http://www.geoinstr.com/s-13.htm>.
- [JOW17] J Junker, P Oppermann, and B Willke. Shot-noise-limited laser power stabilization for the AEI 10 m prototype interferometer. *Optics Letters*, 42(4):755–758, 2017. doi:10.1364/OL.42.000755.

- [K⁺09] F Kawazoe et al. Designs of the frequency reference cavity for the AEI 10 m prototype interferometer. *Journal of Physics: Conference Series*, 228:012028, June 2009. doi:10.1088/1742-6596/228/1/012028.
- [K⁺17] R Kirchhoff et al. Huddle test measurement of a near johnson noise limited geophone. *AIP - Review of Scientific Instruments*, 88(11):115008, November 2017. doi:10.1063/1.5000592.
- [K⁺20] R Kirchhoff et al. Local active isolation of the AEI-SAS for the AEI 10 m prototype facility. *Classical and Quantum Gravity*, 37(11):115004, May 2020. doi:10.1088/1361-6382/ab857e.
- [KAM] KAMAN. Datasheet - DIT-5200. URL: <https://www.kamansensors.com/product/dit-5200/>.
- [KB85] T J Kane and R L Byer. Monolithic, unidirectional single-mode Nd:YAG ring laser. *Optics Letters*, 10(2):65-67, 1985. doi:10.1364/OL.10.000065.
- [KGG11] N M Kondratiev, A G Gurkovsky, and M L Gorodetsky. Thermal noise and coating optimization in multilayer dielectric mirrors. *Physical Review D*, 84(2):022001, July 2011. doi:10.1103/PhysRevD.84.022001.
- [KL08] J Kissel and B Lantz. Enhanced LIGO HAM ISI prototype - preliminary performance review. Technical report, Louisiana State University, October 2008. URL: <https://dcc.ligo.org/public/0028/T080251/000/T080251-01.pdf>.
- [Köh18] S Köhlenbeck. *Towards the SQL Interferometer Length Stabilization at the AEI 10 m-Prototype*. PhD thesis, Gottfried Wilhelm Leibniz Universität Hannover, 2018. doi:10.15488/3567.
- [Köh21] S M Köhlenbeck. A seismic platform interferometer in the aLIGO infrastructure? internal document, 2021. conference talk. URL: <https://dcc.ligo.org/LIGO-G2100582>.
- [KW08] P Kwee and B Willke. Automatic laser beam characterization of monolithic Nd:YAG nonplanar ring lasers. *Applied Optics*, 47(32):6022-6032, November 2008. doi:10.1364/AO.47.006022.
- [KWD09] P Kwee, B Willke, and K Danzmann. Shot-noise-limited laser power stabilization with a high-power photodiode array. *Optics Letters*, 34(19):2912-1914, October 2009. doi:10.1364/OL.34.002912.
- [L[̈]] H Lück. personal communication.
- [L⁺97] H Lück et al. The GEO600 project. *Classical and Quantum Gravity*, 14(6):1471, August 1997. doi:10.1088/0264-9381/14/6/012.
- [L⁺01] G Losurdo et al. Inertial control of the mirror suspensions of the Virgo interferometer for gravitational wave detection. *Review of Scientific Instruments*, 72(9):3653, August 2001. doi:10.1063/1.1394189.
- [Lan05] Brian Lantz. Some calculations for the GS-13 readout and performance. Technical report, Stanford University, 2005. URL: <https://dcc.ligo.org/LIGO-T050137/public>.
- [Lan12] Brian Lantz. Description of the sensor correction FIR and IIR filter components. Technical report, Stanford University, 2012. URL: <https://dcc.ligo.org/LIGO-T1200285/public>.

- [Las20] Laser Components. Datasheet - InGaAs PD IG17X3000G1i, 2020. URL: https://www.lasercomponents.com/fileadmin/user_upload/home/Datasheets/lc-ingaas/ig17-series.pdf.
- [LBP⁺20] A Longo, S Bianchi, W Plastino, N Arnaud, A Chiummo, I Fiori, B Swinkels, and M Was. Scattered light noise characterisation at the Virgo interferometer with tvf-EMD adaptive algorithm. *Classical and Quantum Gravity*, 37(14):145011, July 2020. doi:10.1088/1361-6382/ab9719.
- [LIG20] LIGO Scientific Collaboration. Instrument science white paper 2020. Technical report, LIGO Collaboration, 2020. URL: <https://dcc.ligo.org/LIGO-T2000407/public>.
- [Lin92] Linear Technology Corporation. Datasheet - LT1124 low noise, high speed precision op amps, 1992. URL: <https://www.analog.com/media/en/technical-documentation/data-sheets/11245ff.pdf>.
- [LN17] A Le Tiec and J Novak. *An Overview of Gravitational Waves*, chapter 1. Theory of Gravitational Waves, pages 1–41. World Scientific, April 2017. doi:10.1142/10082.
- [LPR06] G Losurdo, D Passuello, and P Ruggi. The control of the Virgo Superattenuator revised (i). Technical report, INFN Firenze, April 2006. VIR-NOT-FIR-1390-318. URL: <http://citeseerx.ist.psu.edu/viewdoc/similar?doi=10.1.1.580.6331&type=cc>.
- [M⁺15a] F Matichard et al. Advanced LIGO two-stage twelve-axis vibration isolation and positioning platform. Part 1: Design and production overview. *Precision Engineering*, 40:273–286, April 2015. doi:10.1016/j.precisioneng.2014.09.010.
- [M⁺15b] F Matichard et al. Seismic isolation of Advanced LIGO: review of strategy, instrumentation and performance. *Classical and Quantum Gravity*, 32(18):185003, August 2015. doi:10.1088/0264-9381/32/18/185003.
- [M⁺17] Y Michimura et al. Mirror actuation design for the interferometer control of the KAGRA gravitational wave telescope. *Classical and Quantum Gravity*, 34(22):225001, October 2017. doi:10.1088/1361-6382/aa90e3.
- [Maj17] E Majorana. Ruggi’s global inverted pendulum control. In *conference paper*, 2017. URL: <https://dcc.ligo.org/LIGO-G1700891/public>.
- [MCB14] C Moore, R H Cole, and C P L Berry. Gravitational-wave sensitivity curves. *arXiv:1408.0740 [gr-qc]*, August 2014. URL: <https://arxiv.org/abs/1408.0740>.
- [MCB18] C Moore, R H Cole, and C P L Berry. Gravitational wave detectors and sources, 2018. URL: <http://www.sr.bham.ac.uk/~cplb/GWplotter/>.
- [ME15] F Matichard and M Evans. Review: Tilt-free low-noise seismometry. *Bulletin of the Seismological Society of America*, 105(2A):497–510, April 2015. doi:10.1785/0120140200.
- [Mil95] E Milotti. Linear processes that produce 1/f or flicker noise. *Physical Review E*, 51(4):3087, April 1995. doi:10.1103/PhysRevE.51.3087.
- [MLM19] C M Mow-Lowry and Denis Martynov. A 6D interferometric inertial isolation system. *Classical and Quantum Gravity*, 36(24):245006, November 2019. doi:10.1088/1361-6382/ab4e01.

- [MVF⁺15] J Miller, S Vitale, P Fritschel, M Evans, and D Sigg. Prospects for doubling the range of Advanced LIGO. *Physical Review D*, 91(6):062005, March 2015. doi:10.1103/PhysRevD.91.062005.
- [OFW12] D J Ottaway, P Fritschel, and S J Waldman. Impact of upconverted scattered light on advanced interferometric gravitational wave detectors. *Optics Express*, 20(8):8329–8336, March 2012. doi:10.1364/OE.20.008329.
- [Oku19] Koki Okutomi. *Development of 13.5-meter-tall Vibration Isolation System for the Main Mirrors in KAGRA*. PhD thesis, Institute for Cosmic Ray Research - University of Tokyo, 2019. URL: <http://id.nii.ac.jp/1013/00005650/>.
- [O’R21] B O’Reilly. LIGO-Virgo cumulative event rate plot o1-o3a (added a separate plot to include O3b public alerts). LIGO public file server (dcc), 2021. URL: <https://dcc.ligo.org/LIGO-G2001862/public>.
- [P⁺17] L Pinard et al. Mirrors used in the LIGO interferometers for first detection of gravitational waves. *Applied Optics*, 56(4):C11–C15, February 2017. doi:10.1364/AO.56.000C11.
- [Pas] Passcal. Datasheet - T240. URL: <https://www.passcal.nmt.edu/content/instrumentation/sensors/broadband-sensors/t240-bb-sensor>.
- [PTH⁺00] M V Plissi, C I Torrie, M E Husman, N A Robertson, K A Strain, H Ward, H Lück, and J Hough. GEO 600 triple pendulum suspension system: Seismic isolation and control. *Review of Scientific Instruments*, 71(6):2539 – 2545, February 2000. doi:10.1063/1.1150645.
- [R⁺19] D Reitze et al. Cosmic Explorer: the U.S. contribution to gravitational-wave astronomy beyond LIGO. *arXiv:1907.04833 [astro-ph.IM]*, July 2019. URL: <https://arxiv.org/abs/1907.04833>.
- [RG05] D Ristau and T Gross. Ion beam sputter coatings for laser technology. In Claude Amra, Norbert Kaiser, and H. Angus Macleod, editors, *Advances in Optical Thin Films II*, volume 5963, pages 315 – 326. International Society for Optics and Photonics, SPIE, 2005. doi:10.1117/12.624772.
- [RSHG14] A T Ringler, R Sleeman, C R Hutt, and L S Gee. *Encyclopedia of Earthquake Engineering*, chapter Seismometer Self-Noise and Measuring Methods. Springer, January 2014. doi:10.1007/978-3-642-36197-5.
- [RSS⁺81] A Rüdiger, R Schilling, L Schnupp, W Winkler, H Billing, and K Maischberger. A mode selector to suppress fluctuations in laser beam geometry. *Optica Acta: International Journal of Optics*, 28(5):641–658, November 1981. doi:10.1080/713820609.
- [S⁺09] A. Stochino et al. The seismic attenuation system (SAS) for the Advanced LIGO gravitational wave interferometric detectors. *Nuclear Instruments and Methods in Physics Research Section A*, 598(3):737–753, 2009. URL: <https://doi.org/10.1016/j.nima.2008.10.023>.
- [S⁺20] E Schwartz et al. Improving the robustness of the advanced LIGO detectors to earthquakes. *Classical and Quantum Gravity*, 37(23):235007, November 2020. doi:10.1088/1361-6382/abbc8c.
- [S⁺21] M Saleem et al. The science case for LIGO-India. *arXiv:2105.01716 [gr-qc]*, May 2021. URL: <https://arxiv.org/abs/2105.01716>.

- [Sau90] P R Saulson. Thermal noise in mechanical experiments. *Physical Review D: Particles and Fields*, 42(8):2437–2445, October 1990. doi:10.1103/PhysRevD.42.2437.
- [Sch88] L Schnupp. Talk at european collaboration meeting on interferometric detection of gravitational waves, Sorrento, Italy. In *conference paper*, page 31, 1988.
- [Sch18] H Schmid. *Circuits at the Nanoscale: Communications, Imaging, and Sensing*, chapter 7. Offset, Flicker Noise, and Ways to Deal with Them. CRC Press, October 2018. URL: <https://books.google.de/books?id=hH50DwAAQBAJ>.
- [SCKM06] K Somiya, Y Chen, S Kawamura, and N Mio. Frequency noise and intensity noise of next-generation gravitational-wave detectors with RF/DC readout schemes. *Physical Review D*, 73(12):122005, June 2006. doi:10.1103/PhysRevD.73.122005.
- [Ser18] Sercel. Geophones specifications, 2018. URL: <http://www.sercel.com/products/Pages/seismometers.aspx>.
- [SGML⁺04] B S Sheard, M B Gray, C M Mow-Lowry, D E McClelland, and S E Whitcomb. Observation and characterization of an optical spring. *Physical Review A*, 69(5):051801, May 2004. doi:10.1103/PhysRevA.69.051801.
- [SKP09] M Scholz, E Kovalchuk, and A Peters. Frequency characteristics of an inherently stable Nd:YAG laser operated at liquid helium temperature. *Applied optics*, 48(20):3938–3942, July 2009. doi:10.1364/AO.48.003938.
- [SRK⁺17] T Souradeep, S Raja, Z Khan, C S Unnikrishnan, and B Iyer. LIGO-India - a unique adventure in Indian science. *Current Science*, 113(4):672–677, August 2017. URL: <https://www.jstor.org/stable/26293908>.
- [T⁺02a] A Takamori et al. Mirror suspension system for the TAMA SAS. *Classical and Quantum Gravity*, 19(7):1615, March 2002. doi:10.1088/0264-9381/19/7/352.
- [T⁺02b] H Tariq et al. The linear variable differential transformer (LVDT) position sensor for gravitational wave interferometer low-frequency controls. *Nuclear Instruments and Methods in Physics Research Section A*, 489(1-3):570–576, August 2002. doi:10.1016/S0168-9002(02)00802-1.
- [Tex95] Texas Instruments Incorporated. Datasheet - INA12x precision, low-power instrumentation amplifiers, 1995. revised 2018. URL: <http://www.ti.com/lit/ds/symlink/ina128.pdf>.
- [Tex98a] Texas Instruments Incorporated. Datasheet - DRV13x audio-balanced line drivers, 1998. revised 2014. URL: <http://www.ti.com/lit/ds/symlink/drv134.pdf>.
- [Tex98b] Texas Instruments Incorporated. Datasheet - INA103 low noise, low distortion instrumentation amplifier, 1998. revised 2000. URL: <https://www.ti.com/lit/ds/symlink/ina103.pdf?ts=1602745206676>.
- [Tex13] Texas Instruments Incorporated. Datasheet - OPA188 operational amplifier, 2013. revised 2016. URL: <http://www.ti.com/lit/ds/symlink/opa188.pdf>.
- [THA15] THAT Corporation. Datasheet - THAT1646 balanced line driver ics, 2015. Document 600078 Rev. 07. URL: http://www.thatcorp.com/datashts/THAT_1606-1646_Datasheet.pdf.

- [TjMMK94] R Takahashi, j Mizuno, S Miyoki, and N Kawashima. Control of a 10 m delay-line laser interferometer using the pre-modulation method. *Physics Letters A*, 187(2):157–162, April 1994. doi:10.1016/0375-9601(94)90054-X.
- [Tro18] L Trozzo. *Low Frequency Optimization and Performance of Advanced Virgo Seismic Isolation System*. PhD thesis, Università di Siena, 2018. URL: <https://usiena-air.unisi.it/handle/11365/1052744?mode=full.1443#.YFh5UNwo9hE>.
- [TSS⁺04] R Takahashi, Y Saito, Y Sato, T Kubo, T Tomaru, M Tokunari, T Sumiya, K Kakasugi, and Y Naito. Application of diamond-like carbon (DLC) coatings for gravitational wave detectors. *Vacuum*, 73(2):145–148, March 2004. doi:10.1016/j.vacuum.2003.12.014.
- [Ush21] T Ushiba. Cryogenic suspension design for a kilometer-scale gravitational-wave detector. *Classical and Quantum Gravity*, 38(8):085013, March 2021. doi:10.1088/1361-6382/abe9f3.
- [Vas06a] G Vasilescu. *Electronic Noise and Interfering Signals: Principles and Applications*, chapter 3. Physical Noise Sources, pages 45–68. Springer, January 2006. URL: <https://books.google.de/books?id=uQ1Er5iW0dUC&hl>.
- [Vas06b] G Vasilescu. *Electronic Noise and Interfering Signals: Principles and Applications*, chapter 13. Low-Noise Circuit Design, pages 413–442. Springer, January 2006. URL: <https://books.google.de/books?id=uQ1Er5iW0dUC&hl>.
- [VBB96] J.-Y. Vinet, V Brisson, and S Braccini. Scattered light noise in gravitational wave interferometric detectors: Coherent effects. *Physical Review D*, 54(2):1276, July 1996. doi:10.1103/PhysRevD.54.1276.
- [vBH⁺19] J V van Heijningen, A Bertolini, E Hennes, M G Beker, M Doets, H J Bulten, K Agatsuma, T Sekiguchi, and J F J van den Brand. A multi-stage vibration isolation system for Advanced Virgo suspended optical benches. *Classical and Quantum Gravity*, 36(7):075007, March 2019. doi:10.1088/1361-6382/ab075e.
- [vH20] J V van Heijningen. A fifty-fold improvement of thermal noise limited inertial sensitivity by operating at cryogenic temperatures. *Journal of Instrumentation*, 15:P06034, June 2020. doi:10.1088/1748-0221/15/06/P06034.
- [VHG⁺17] K Venkateswara, C A Hagedorn, J H Grundlach, J Kissel, J Warner, H Radkins, T Shaffer, B Lantz, R Mittleman, F Matichard, and R Schofield. Subtracting tilt from a horizontal seismometer using a ground rotation sensor. *Bulletin of the Seismological Society of America*, 107(2):709 – 717, March 2017. doi:10.1785/0120160310.
- [VHT⁺14] K Venkateswara, C A Hagedorn, M D Turner, T Arp, and J H Grundlach. A high-precision mechanical absolute-rotation sensor. *AIP - Review of Scientific Instruments*, 85(1):015005, January 2014. doi:10.1063/1.4862816.
- [VSS03] G Venter and J Sobieszczanski-Sobieski. Particle swarm optimization. *AIAA Journal*, 8(8):1583, 2003. doi:10.2514/2.2111.
- [W⁺07] B Willke et al. GEO600: status and plans. *Classical and Quantum Gravity*, 24(19):S389, September 2007. doi:10.1088/0264-9381/24/19/S02.

- [W⁺12] T Westphal et al. Design of the 10 m AEI prototype facility for interferometry studies. *Applied Physics B*, 106:551–557, February 2012. doi:10.1007/s00340-012-4878-z.
- [W⁺14] S Wen et al. Hydraulic external pre-isolator system for LIGO. *Classical and Quantum Gravity*, 31(23):235001, November 2014. doi:10.1088/0264-9381/31/23/235001.
- [Wan13] A Wanner. *Seismic Attenuation System (AEI-SAS) for the AEI 10 m Prototype*. PhD thesis, Leibniz Universität Hannover, 2013. doi:10.15488/8194.
- [Wes16] T Westphal. *A Coating Thermal Noise Interferometer for the AEI 10m Prototype facility*. PhD thesis, Leibniz Universität Hannover, 2016. doi:10.15488/8896.
- [Wie12] E Wielandt. *New Manual of Seismological Observatory Practise 2*, volume 2, chapter 5. Seismic Sensors and their Calibration, pages 20–21. Deutsches GeoForschungsZentrum Potsdam, August 2012. doi:10.2312/GFZ.NMSOP-2_ch5.
- [Wip14] C. Wipf. Noise budgeting for advanced detectors, 2014. URL: <https://dcc.ligo.org/LIGO-G1400587/public>.
- [WTD⁺02] C. Wang, H. Tariq, R. DeSalvo, Y. Iida, S. Marka, Y. Nishi, V. Sannibale, and A. Takamori. Constant force actuator for gravitational wave detectors seismic attenuation systems (SAS). *Nuclear Instruments and Methods in Physics Research Section A*, 489(1-3):563–569, February 2002. doi:10.1016/S0168-9002(02)00801-X.
- [ZATA19] S Zeidler, T Akutsu, Y Torii, and Y Aso. Measuring scattering light distributions on high-absorptive surfaces for stray-light reduction in gravitational-wave detectors. *Optics Express*, 27(12):16890–16910, June 2019. doi:10.1364/OE.27.016890.

Acknowledgements

First of all I would like to thank Prof. Dr. Karsten Danzmann for giving me the opportunity to write my thesis at the AEI. The institute and its infrastructure, including the laboratories, offices, IT systems, workshops and many more, is an outstanding place to do great science.

My time in the AEI 10 m prototype group was enriching not only for my career, but also for my life, and I want to thank Harald for taking me as a bachelor student and giving me the possibility to stay in the group until now. The atmosphere in the group and the whole institute was always supportive and enjoyable. I want to thank everyone who accompanied me through this time of my life, for the scientific support, and also for the non-scientific fun we had.

I want to thank Harald and Ken for the exceptional supervision of the project, with all the fruitful discussions in the meetings, the lunch breaks and in the offices. I also want to thank Conor for the scientific help and the successful cooperation, which improved my thesis significantly.

Thanks to Gerald for introducing me to the AEI-SAS, to Conor for teaching me active isolation, and to Alex for the support, even after he left the group. Many thanks go to Johannes for all the teamwork on the AEI-SAS and the full AEI 10 m prototype.

Many thanks go to the secretaries, the IT team, the members of the workshops, and the whole institute staff, without whose work and support my project would not have been possible.

I am thankful to the whole prototype group for proofreading my thesis and providing very helpful comments and discussions.

Finally, special thanks go to my wife, Jenny, for always supporting me in stressful times, for being part of my life, and for our daughter, Malina, who has made my private life as exciting and fascinating as it can be.

Curriculum vitae

Persönliche Daten

Name Robin Kirchhoff
Adresse Bergkrug 3a
31691 Helpsen
Geburtsort Bückeburg
Geburtsdatum 13.11.1991

Berufserfahrung

11/2016 - 12/2021 **Promotion** am Albert-Einstein-Institut für Gravitationsphysik Hannover
12/2018 - 02/2019 **Nebenjob** bei Siegfried PharmaChemikalien Minden GmbH
12/2014 - 10/2016 **Hilfswissenschaftler** am Albert-Einstein-Institut für Gravitationsphysik Hannover

Studium

09/2015 - 10/2016 **Masterarbeit Physik** am Albert-Einstein-Institut für Gravitationsphysik Hannover
04/2014 - 11/2014 **Bachelorarbeit Physik** am Albert-Einstein-Institut für Gravitationsphysik Hannover
10/2011 - 12/2021 **Physikstudium** an der Leibniz Universität Hannover

Schulische Ausbildung

08/2004 - 06/2011 **Allgemeine Hochschulreife** am Wilhelm Busch Gymnasium Stadthagen
08/2008 - 02/2009 **Auslandsaufenthalt** in Kanada, British Columbia

Publications with direct contribution

- [1] G Bergmann et al. Passive-performance, analysis, and upgrades of a 1-ton seismic attenuation system. *Classical and Quantum Gravity*, 34(6):065002, February 2017.
- [2] R Kirchhoff et al. Huddle test measurement of a near johnson noise limited geophone. *AIP - Review of Scientific Instruments*, 88(11):115008, November 2017.
- [3] R Kirchhoff et al. Local active isolation of the AEI-SAS for the AEI 10 m prototype facility. *Classical and Quantum Gravity*, 37(11):115004, May 2020.
- [4] P Koch et al. Thickness uniformity measurements and damage threshold tests of large-area GaAs/AlGaAs crystalline coatings for precision interferometry. *Optics Express*, 27(25):36731–36740, December 2019.